Molecular mechanisms governing Hexokinase 2 nuclear shuttling and resistance to 2-deoxyglucose

by

Mitchell Allen Lesko

Bachelor of Science, Kent State University, 2019

Submitted to the Graduate Faculty of the

Dietrich School of Arts and Sciences in partial fulfillment

of the requirements for the degree of

Doctor of Philosophy

University of Pittsburgh

2024

UNIVERSITY OF PITTSBURGH

DIETRICH SCHOOL OF ARTS AND SCIENCES

This dissertation was presented

by

Mitchell Allen Lesko

It was defended on

February 21, 2024

and approved by

Andrea J. Berman, Ph.D., Associate Professor, Department of Biological Sciences

Jeffrey L. Brodsky, Ph.D., Professor, Department of Biological Sciences

Jon P. Boyle, Ph.D., Professor, Department of Biological Sciences

Martin C. Schmidt, Ph.D., Professor, Department of Microbiology and Molecular Genetics

Thesis Advisor/Dissertation Director: Allyson F. O'Donnell, Ph.D., Assistant Professor, Department of Biological Sciences

Thesis Advisor/Dissertation Director: Jacob D. Durrant, Ph.D., Associate Professor, Department of Biological Sciences

Molecular mechanisms governing Hexokinase 2 nuclear shuttling and resistance to 2-deoxyglucose

Mitchell Allen Lesko, PhD

University of Pittsburgh, 2024

Hexokinases represent the gateway enzyme of glucose metabolism by regulating cellular glucose uptake and glycolytic rate. Interestingly, some mammalian hexokinase isoforms shuttle into the nucleus in response to nutrient starvation, necessitating further investigation into the regulation and function of nuclear hexokinases. Here, using *Saccharomyces cerevisiae* and quantitative live-cell imaging, we gain insight into this phenomenon. In agreement with current mammalian models, we demonstrate nuclear accumulation of hexokinase 2 (Hxk2) in response to glucose starvation. Through this approach, we identify a NUAK-family kinase, Tda1, as crucial for inducing Hxk2 nuclear accumulation. Additionally, we identify a lysine residue located in the Hxk2 N-terminal tail, that maintains nuclear exclusion in glucose-replete conditions. This study advances our understanding of the mechanisms regulating hexokinase nuclear accumulation, with potential implications for disease, as increased hexokinase expression is linked to cancer progression, making hexokinases promising drug targets. 2-deoxyglucose (2DG) is a hexokinase inhibitor that elicits a starvation response in cancer cells. Despite its therapeutic potential, cancer cells gain resistance to 2DG by suppressing hexokinase activity. Yeast studies show that spontaneous loss-of-function mutations in the *HXK2* gene confer 2DG resistance. To understand how Hxk2 mutations confer 2DG resistance we conducted lab evolution of wild-type yeast, identifying a novel *HXK2* mutation ($Hxk2^{G238V}$) in resistant cells. Biochemical and phenotypic analyses reveal this mutant encodes a loss-of-function allele, though the affected residue does not

interact with substrates. Molecular dynamics simulations predict that Hxk2^{G238V} impedes glucose binding by altering the stability of the glucose binding pocket and large-scale domain closures required for catalysis. In past screens, we identified the Hxk2^{G55V} allele that also conferred 2DG resistance. Hxk2^{G55V} encodes an unstable enzyme that accumulates in the nucleus regardless of glucose availability. Though far from the enzymatic pocket, this mutation impacted the dynamics of a key "hinge-point," influencing Hxk2 domain closures and hindering stable glucose binding. Collectively, these findings present the first atomistic models describing the impact of Hxk2 mutations on enzyme dynamics and advance our understanding of substrate-induced conformational changes in hexokinases.

Table of Contents

List of Tables

List of Figures

List of Abbreviations

Below is a list of abbreviations used in this dissertation, with common abbreviations (i.e., DNA, ATP, etc.) omitted.

2DG: 2-deoxyglucose
AMPK: AMP-activated Protein Kinase
a.u: Arbitrary Units
BCC: Betweenness Centrality
CHX: Cycloheximide
CMAC: 7-amino-4-chloromethylcoumarin
Co-IP: Co-Immunoprecipitation
DCC: Dynamic Cross-Correlation
ER: Endoplasmic Reticulum
ERAD: ER-Associated Degradation
ESCRT: Endosomal Sorting Complex Required for Transport
FRAP: Fluorescence Recovery After Photobleaching
GBM: Glioblastoma Multiforme
GFP: Green Fluorescent Protein
GLUT: Glucose Transporter
HXT: Hexose Transporter
INQ: Intranuclear Quality Control Compartment
IPOD: Insoluble Protein Deposit
JUNQ: Juxtanuclear Quality Control Compartment
kDa: Kilodalton
MAM: Mitochondria-Associated Membrane
MAPK: Mitogen-activated Protein Kinase
MBD: Mitochondrial Binding Domain
MD: Molecular Dynamics
MODY2: Maturity Onset Diabetes of the Young Type 2
mPTP: Mitochondrial Permeability Transition Pore
mTORC1: Mammalian Target of Rapamycin Complex 1
NLS: Nuclear Localization Signal
n.s.: Not Significant
NucPQC: Nuclear Protein Quality Control
NVJ: Nuclear-Vacuolar Junction
OD: Optical Density
OMM: Outer Mitochondrial Membrane
OXPHOS: Oxidative Phosphorylation
PCR: Polymerase Chain Reaction
PHHI: Persistent Hyperinsulinemic Hypoglycemia of Infancy
PNDM: Permanent Neonatal Diabetes Mellitus

PP1: Protein Phosphatase 1
PPP: Pentose Phosphate Pathway
RMSD: Root-Mean-Square Deviation
RMSF: Root-Mean-Square Fluctuation
RoG: Radius of Gyration
ROS: Reactive Oxygen Species
Snf1: Sucrose Non-Fermenting 1
Tda1: Topoisomerase Damage Associated 1
tpm: Transcripts Per Million
VDAC1: Voltage-Dependent Anion Channel 1
WESTPA: Weighted Ensemble Simulation Toolkit with Parallelization and Analysis

1.0 Introduction

1.1 Glucose

Glucose is the main carbon source that most cells use to generate energy and support cell function. Additionally, glucose is a building block for important cellular structures and macromolecules, such as fatty acids, cholesterol, nucleic acids, and amino acids [1]. Therefore, microorganisms such as yeast and complex multicellular organisms such as mammals possess regulatory networks that control glucose uptake and metabolism aimed at supporting the needs of the cell. Here, I summarize glucose metabolic pathways and the mechanisms of glucose homeostasis in mammals and yeast.

1.1.1 Metabolism of glucose

Glucose is a hydrophilic molecule and will not penetrate the lipid bilayer of cells without the help of transporters. The transport of glucose down its concentration gradient is mediated by 5 glucose transporters (GLUTs; GLUT1-5) in mammals or 7 hexose transporters (HXTs; HXT1-7) in yeast [2]. Once inside the cell glucose must be “trapped” otherwise it can diffuse back out through the glucose transporters. To “trap” glucose in cells, the action of enzymes called hexokinases or glucokinases transfers a phosphate group from ATP to the C6 carbon of glucose. The resulting metabolite, glucose-6-phosphate (G6P), has four possible fates through which it acts as a substrate (Figure 1) [3].

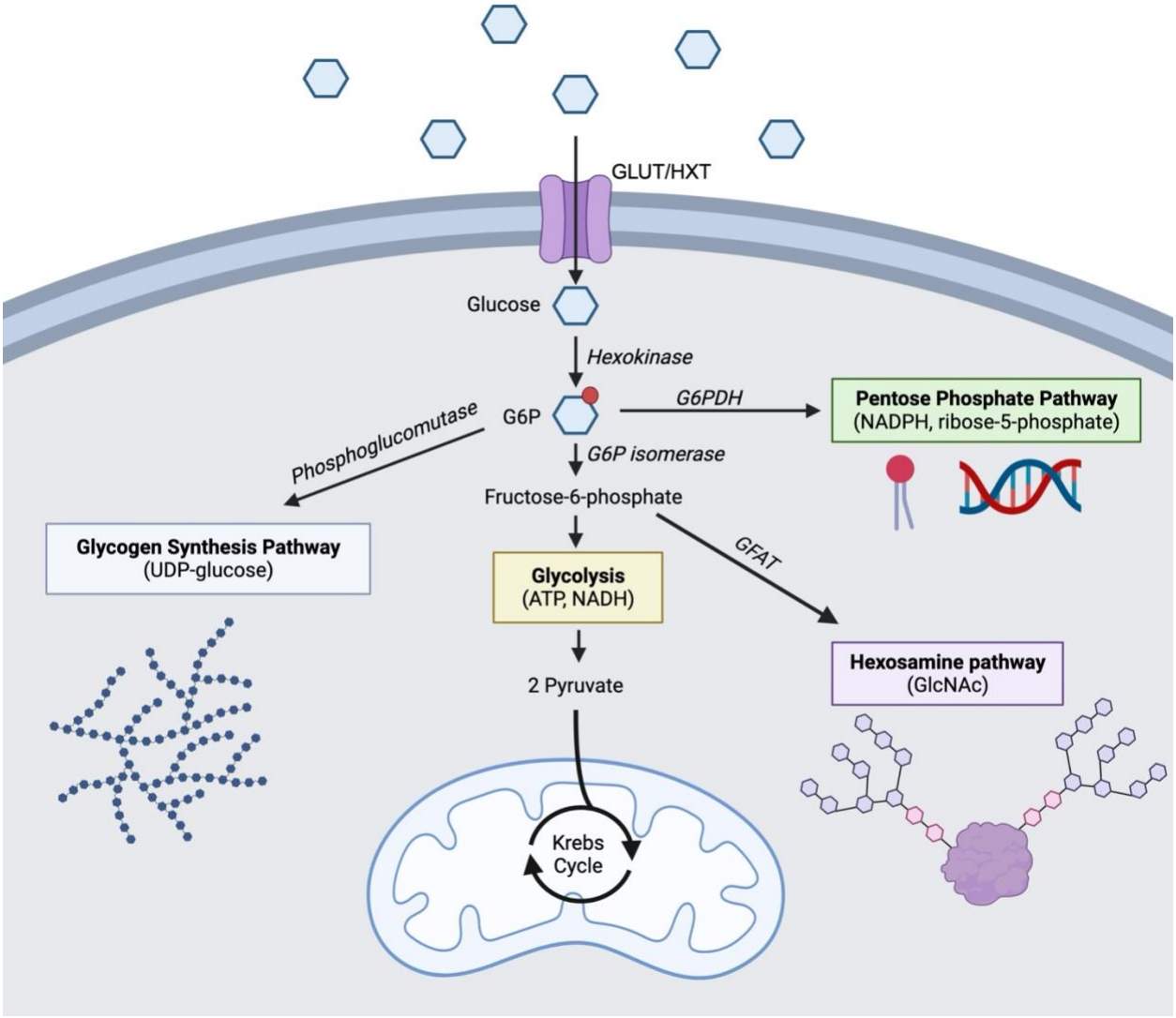

Figure 1. Metabolic fates of glucose.

Glucose is phosphorylated by hexokinases and converted to glucose-6-phosphate. G6P is a substrate for four different metabolic pathways. First, G6P is used to generate ATP and NADH, the latter of which is used in OXPHOS to generate even more ATP. Glycolysis generates two pyruvate molecules per G6P that enter the Krebs cycle. Secondly, G6P serves as a substrate for the pentose phosphate pathway. It is utilized to generate reducing agents for reductive biosynthesis and to counteract the build-up of ROS species. Additionally, it is used to make substrates for DNA synthesis. Third, G6P is converted to N-acetylglucosamine by the hexosamine biosynthetic pathway where it is incorporated into glycan chains used in protein modifications. Finally, G6P can be stored in the form of glycogen.

First, G6P can enter the glycolysis pathway that uses a series of enzymatic reactions to convert G6P into two pyruvate molecules. From this pathway, the cell yields useable energy in the form of ATP and reducing agents in the form of NADH that can be used for further energy production in the electron transport chain. The resulting pyruvate molecules are metabolized through aerobic oxidative phosphorylation or anaerobic fermentation to generate more ATP and reducing agents NADH and $FADH_2$. Second, G6P can enter the pentose phosphate pathway (PPP). Here, G6P is oxidized to generate NADPH and ribose-5-phosphate – a substrate for lipid biosynthesis and structural component of nucleotides, respectively [4]. Third, G6P can proceed one step further in glycolysis and be converted to fructose-6-phosphate which is a substrate for the hexosamine biosynthesis pathway. The first committed step of this pathway involves the glutamine fructose-6-phosphate aminotransferase 1-catalyzed production of glucosamine-6-phosphate from fructose-6-phosphate and glutamine. The resulting product, N-acetylglucosamine (GlcNAc) is a substrate for N- and O-linked glycosylation of proteins [5]. Finally, G6P serves as a precursor for glycogenesis. This pathway is triggered in the liver in response to insulin signaling when blood glucose levels rise after a meal. UDP-glucose is generated from G6P and used by glycogen synthase to assemble glycogen chains that are kept for storage until blood glucose levels drop [3].

1.1.2 Glucose homeostasis and signaling in mammals

An intricate regulatory network controls blood glucose levels in mammals. The pancreas and liver play central roles in maintaining blood glucose levels and regulation of glucose uptake by adipose and muscle tissue cells [6]. Blood glucose levels are kept at ~5 mM which is maintained by hormonal signaling originating in the pancreas [6]. Specifically, insulin is released by pancreatic β-cells to facilitate cellular glucose uptake by muscle and adipose cells while glucagon

released by pancreatic α-cells stimulates hepatic glucose production thereby increasing blood glucose levels [7]. For example, after a meal rising blood glucose levels are detected by pancreatic β-cells, inducing insulin release into the bloodstream. Insulin binds to insulin receptors expressed on the surface of muscle and adipose cells. Binding to these receptors activates downstream intracellular signaling pathways, such as the Ras-MAPK pathway and the AKT pathway [8]. Ras-MAPK and AKT activation promotes anabolic pathways, increases glucose metabolism, and leads to expression and translocation of glucose transporters to the cell surface [7,8]. Muscle and adipocytes express an insulin-sensitive glucose transporter known as GLUT4 [9]. In the absence of insulin, GLUT4 is localized in intracellular vesicles known as GLUT4 storage vesicles. Insulin signaling promotes activates the AKT pathway and this triggers fusion of the GLUT4 storage vesicles to the plasma membrane [10,11]. Uptake of glucose through GLUT4 allows muscle and adipocytes to stockpile post-prandial glucose. At the same time, the liver uptakes excess bloodstream glucose and stores it in the form of glycogen [7]. It should be noted that mammalian diets contain many different sugars other than glucose, including fructose and galactose. Both sugars are almost completely cleared from the bloodstream in one passage through the liver thanks to fructo- and galacto-kinases [12,13]. When blood glucose levels fall below 5 mM, pancreatic α-cells secrete glucagon to counteract the effects of insulin [14]. Glucagon signaling initiates i) the breakdown of liver glycogen stores and ii) the generation of glucose via gluconeogenesis in the liver, each of which increases the release of glucose into blood circulation [14]. Though muscle cells do not express glucagon receptors, they benefit indirectly from glucose released by the liver [14]. In contrast, in adipocytes, binding of glucagon to receptors initiates lipid breakdown and release of fatty acids, which can also be used as a fuel source [15].

Mammalian cells control their rate of energy consumption based on the availability of nutrients and capacity to generate ATP from glucose or other sources. Two key players, the AMP-activated protein kinase (AMPK) and mammalian target of rapamycin complex 1 (mTORC1), are opposing, master regulators of cell metabolic processes that sense nutrient and energy availability [16]. mTORC1 is positively regulated by intracellular nutrients (glucose, amino acids, etc.), high ATP levels, and extracellular growth factors (insulin and insulin-like growth factor 1) [16–19]. In response to these activating cues, mTORC1 is recruited to lysosomes (equivalent of yeast vacuole) where it promotes anabolic metabolism and cell growth by inducing processes such as protein, lipid, and nucleotide synthesis [16–19]. AMPK acts oppositely to mTORC1 and is activated in response to energy depletion and stress [20,21]. In these conditions, the LKB1 kinase phosphorylates the AMPK activation loop at T172, allowing AMPK to become a functional kinase [22,23]. AMPK is further allosterically activated by AMP, a breakdown product of ATP hydrolysis, and therefore AMPK directly senses and responds to the cellular energy balance [24].

In addition, more recently a non-canonical activation of AMPK activation by the degree of glycolytic flux has been proposed. This mechanism requires fructose-1,6-bisphosphate (FBP), a substrate for the enzyme aldolase [25–27]. When aldolase is left unoccupied by FBP, it recruits LKB1 to the lysosome in complex with the adaptor proteins AXIN1 and AXIN2 [25]. This brings LKB1 into proximity of lysosomal AMPK, allowing LKB1 promotion of AMPK phosphorylation and activation [25]. Activated AMPK redirects cellular metabolism, favoring catabolism and decreasing anabolism by altering the activation of downstream proteins in several pathways, including mTORC1 itself [20]. AMPK deactivates mTORC1 signaling and phosphorylates its upstream regulator TSC2 and mTORC1 subunit RAPTOR in response to energy stress [20]. Therefore, AMPK and mTORC1 represent master regulatory circuits of metabolism.

1.1.3 Glucose homeostasis and signaling in yeast

The budding yeast *Saccharomyces cerevisiae* is an important model organism that has been instrumental in helping scientists to understand basic biological processes and human disease states. Like most cells on the planet, yeast cells prefer glucose as a carbon source. However, they utilize glucose differently than most cells, preferring to get most of their energy from glycolysis with a limited contribution from respiration even with sufficient oxygen, a phenomenon known as the Crabtree effect [28]. This metabolism is driven by the fact that glucose inhibits transcription of genes that promote catabolism of other carbon sources, but also genes involved in respiration and oxidative phosphorylation [29]. Though less efficient at generating ATP, the Crabtree effect provides some competitive advantage for yeast cells [30,31]. First, yeast's glycolysis-based metabolism relies on the rapid uptake of glucose from the environment which may diminish glucose supply to non-yeast cells in the area that consume glucose more slowly [30,31]. Second, at the end of yeast's glycolysis, the pyruvate produced is fermented to ethanol [30,31]. This provides an advantage because it restricts this carbon source from organisms that cannot metabolize ethanol and prevents ethanol-sensitive organisms from growing [30,31]. In addition, when glucose becomes limiting, yeast can begin expressing cellular respiratory genes and utilize ethanol for energy production [30,31].

Central to this metabolic preference is the glucose repression pathway (Figure 2). Activation of this pathway is dependent on the yeast AMPK ortholog, Snf1 [32,33]. Snf1 functions as a heterotrimeric complex composed of the Snf1 catalytic subunit, the γ regulatory subunit, Snf4, and one of three β-subunits encoded by *GAL83*, *SIP1*, or *SIP2* [32,33]. Association with each β-subunit subcellular localization of the Snf1 complex, which in turn is thought to dictate substrate

specificity [34–36]. Sip1 directs the AMPK complex to the vacuole while Sip2 promotes its cytosolic localization and Gal83 directs AMPK to the nucleus [34–36]. Like in mammalian cells, yeast Snf1 mainly responds to glucose limitation, nutrient, and other cellular stressors [32,33,36–38]. Once active, Snf1 signals a shift in metabolism from aerobic glycolysis to respiratory metabolism, glycogen synthesis, gluconeogenesis, autophagy, glyoxylate cycle, and the use of alternative carbon sources [29,32,33,39]. Like mammalian AMPK, activation of Snf1 in low glucose conditions is achieved through phosphorylation of a conserved threonine residue (T210) within its activation loop [38,40–42]. This phospho-activation is carried out by one of three upstream kinases -- Sak1, Tos3, and Elm1 [43–45]. Unlike in mammals, Snf1 is not allosterically activated by ADP rather than AMP [46], but this still allows direct coupling of Snf1 activity with cellular energy status. In rich glucose conditions, phosphorylation of Snf1 is counter-acted by the Glc7/Reg1 PP1 phosphatase complex [38,41,47–49]. Dephosphorylation by Reg1/Glc7 is proposed to be the primary means by which Snf1 phosphorylation is regulated as none of the upstream kinases responds to changing glucose levels [41].

Upon activation, Snf1 phosphorylates several transcription factors [29]. Mig1, is a well-characterized downstream target of Snf1-dependent phosphorylation [36,50–52]. In glucose-rich environments, Mig1 is dephosphorylated in the cytosol by the Glc7/Reg1 phosphatase, which allows Mig1 import into the nucleus where it acts as a transcription repressor that suppresses glucose-repressed genes [41,50,53]. In glucose starvation conditions, active Snf1 phosphorylates Mig1, causing it to become nuclear-excluded and thereby mitigating its role as a transcription repressor [50,54]. This allows for the activation of genes needed to for use of alternative carbon sources, thereby lifting glucose repression of gene expression [50,54]. In addition to Mig1, Snf1 phosphorylates the transcription activator Cat8 [55]. Phosphorylated Cat8 binds to carbon-source

responsive elements in the promoters of genes involved in gluconeogenesis, glyoxylate cycle, and utilization of nonfermentable carbon sources including fructose-1,6-bisphosphatase (FBP1; gluconeogenesis), malate synthase (MLS1; glyoxylate cycle), and isocitrate lyase (ICL1; glyoxylate cycle) [56–59].

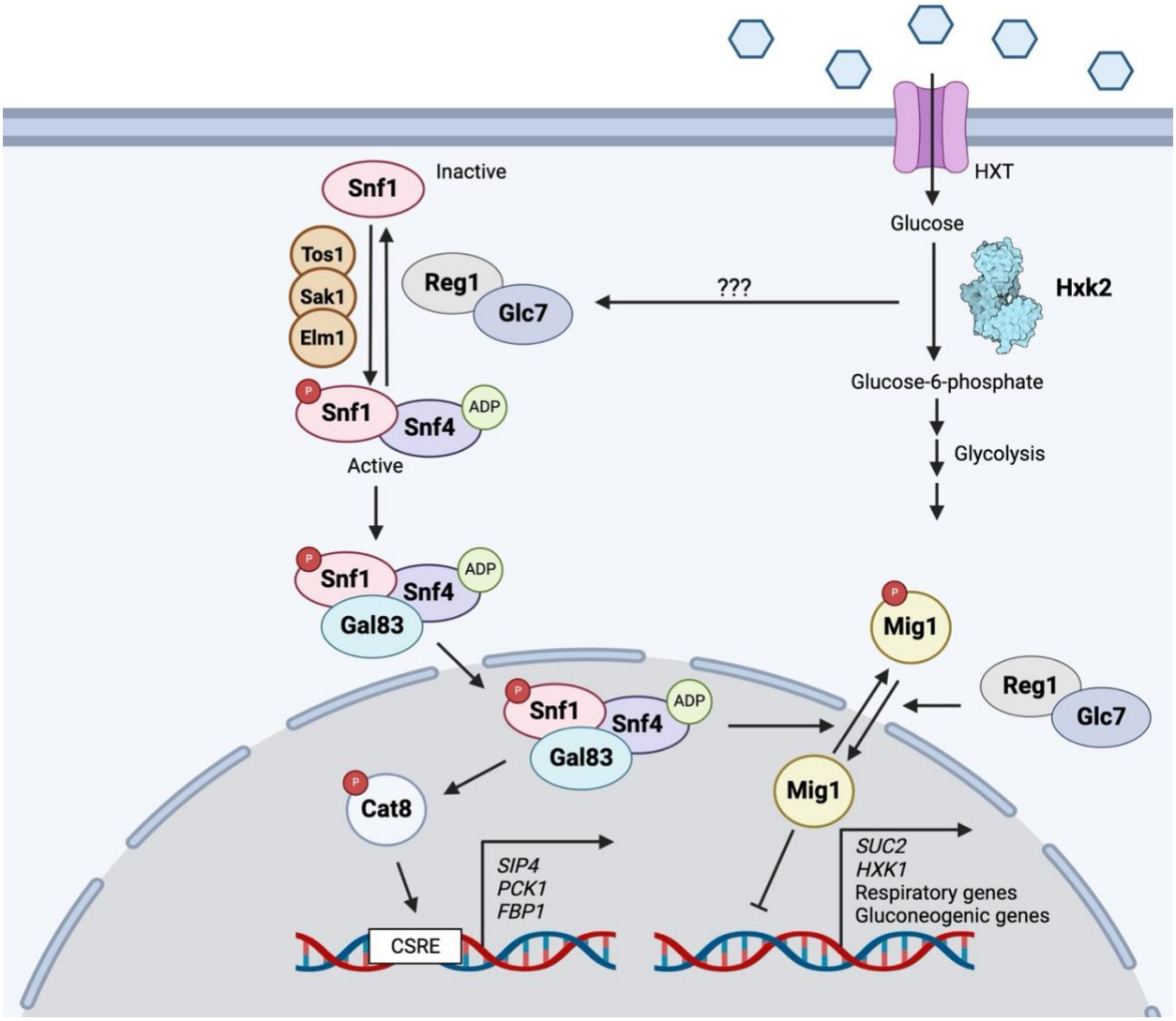

Figure 2. Yeast glucose repression pathway.

The Snf1 kinase coordinates the use of alternative carbon sources by releasing glucose repression. Three upstream kinases, Sak1, Tos1, and Elm1 are responsible for phosphorylating and activating Snf1, while the Glc7/Reg1 phosphatase dephosphorylates it in glucose-replete conditions. The glucose-sensing mechanism requires Hxk2 and activates Glc7/Reg1 to trigger dephosphorylation of Snf1. Once active, Snf1-Snf4 binds to one of three β-subunits.

The Snf1-Snf4-Gal83 complex plays a major role in glucose derepression where it enters the nucleus and phosphorylates Mig1 and Cat8. This leads to the expression of genes involved in the use of alternative carbon sources, gluconeogenesis, and respiration. This diagram was adapted from a review by Conrad et al [29].

1.2 Hexokinases

In 1927, Nobel Prize winner Otto Meyerhof demonstrated the stimulatory effect of a yeast "activator" on glucose fermentation by muscle extracts. The word "hexokinase" was used for the first time to describe this "activator" [60]. Hexokinases and the related glucokinases (the latter of which are named for their altered substrate preferences relative to hexokinases) are enzymes that catalyze the conversion of glucose to glucose-6-phosphate and are found across every domain of life [61,62]. This includes a variety of species such as plants, yeast, and humans in addition to many other vertebrates and bacteria [61]. Though glucose is the preferred substrate of the hexokinases, they can also phosphorylate other hexose sugars to varying degrees such as fructose and mannose. In contrast, glucokinases get their namesake as they only have specificity for glucose. Once phosphorylated, glucose-6-phosphate can be metabolized through several pathways (see section 1.1) influenced by the metabolic demand of the cell or organism, thus underscoring the pivotal role of hexokinases in dictating the magnitude and direction of glucose metabolism. Aside from phosphorylating glucose, hexokinases possess non-canonical functions independent of their catalytic activity including, but not limited to, regulating pro-apoptotic signaling and redox homeostasis pathways, and transcription regulation [62]. They are also rather dynamic enzymes, localizing to different regions – including the outer mitochondrial membrane (OMM) [63], the nucleus [64–72], insulin-containing vesicles [73–75], and the endoplasmic reticulum [76] – of the

cell depending on nutrient conditions, environmental stressors, or signaling cues. These dynamic localization changes have led to the proposal that hexokinases may regulate more than just sugar metabolism, operating in 'moonlighting' functions at these other cellular locales. These alternative activities of hexokinases are considered in more depth in sections 1.2.2.2, 1.2.2.3, and 1.2.2.4. In the preceding sections, I focus on hexokinases of the budding yeast, *Saccharomyces cerevisiae,* and mammalian cells. Below, I discuss their structure, mechanism of catalysis, differential expression within each organism, physiological roles, disease implications, subcellular localization, and non-catalytic functions.

1.2.1 Structural overview

1.2.1.1 Hexokinase structure

Hexokinase proteins belong to the larger actin ATPase clan, whose constituents include sugar kinases, stress-70 proteins, and actin. Though these family members have strikingly disparate functions, they share common structural features; all family members have a conserved core that consists of two α/β subdomains with topology βββαβαβα [77,78]. The two subdomains are positioned on either side of a deep cleft that houses the ATP binding site (see Figure 3A) [78]. In the cleft, there is a central β-sheet surrounded by α-helices, with an identical topology of loop connections [78]. The phosphate tail of ATP is flanked and bound to residues on two β-hairpins, one on each of the subdomains [78]. Each family member has a unique pattern of insertions that occur at different locations within the conserved core domain, giving each hexokinase its unique biological function [77]. Hexokinases also have unique extensions at either the N- or C-terminus, or both [77].

The many crystal structures of hexokinases provide a comprehensive understanding of their structure [79–94]. All hexokinases are distinguished by a conserved α/β fold [77,78]. They generally fold into two distinct subdomains: a mostly α-helical large subdomain and a palm-shaped α/β small subdomain. The core of each is made up of a 5-stranded mixed β-sheet, where each β-sheet is flanked by α-helices. The active site is formed by a deep cleft between the two subdomains, where β-sheets from both subdomains form the active site pocket (see Figure 3) [79,80,83].

1.2.1.2 Substrate and allosteric binding sites

Crystal structures of hexokinases are often captured with glucose bound to the enzymatic cleft. Consistently, the glucose binding site is located underneath a β-hairpin structure within a polar region of the enzymatic cleft (Figure 3B) [79,83,86,89,94]. Here, glucose is bound to the active site through hydrogen bonding interactions between pocket lining residues and the glucose hydroxyl groups (Figure 3B) [79,83]. The adenine portion of ATP is sandwiched between two α-helices that form a defined pocket at the exterior portion of the enzymatic cleft (Figure 3B) [85,90,94,95]. The phosphate groups of ATP are buried in a hydrophilic tunnel and point toward the glucose molecule [85,87,94,95]. This positions ATP perfectly so that the γ-phosphate is positioned next to the C6 -OH group on glucose for catalysis. Mammalian hexokinases, except for GCK, are inhibited by physiological levels of G6P that binds a distinct allosteric site from the glucose binding in the enzymatic cleft [86,89,90,92,96]. This G6P binding site may compete with ATP binding, preventing further phosphorylation of glucose when G6P levels are high. Indeed, crystal structures demonstrate that the binding sites for ATP and G6P overlap; specifically, the 6-phosphate group of G6P occupies the same position as the ATP γ-phosphate [85,90,92]. Structural

evidence suggests that G6P stabilizes the closed conformation of hexokinases, thereby preventing glucose binding to the active site [89,92,96]. In addition to this regulation by G6P, mammalian HKI binds noncatalytic ADP/ATP at a site distinct from the enzymatic cleft [90,96]. Here, ADP/ATP is positioned in a surface cleft that is made up of a series of α-helices [90,96]. The adenine ring is buried at the very end of the cleft and held in place by stacking interactions, hydrogen bonds, and van der Waals forces with surface-facing residues on the α-helices [90,96]. This ADP/ATP binding site is positioned near an N-terminal helix responsible for anchoring HKI to the mitochondrial outer membrane through interactions with the phospholipid bilayer and porin [90,96]. Thus, it is suggested that ADP/ATP binding to this site may impact the conformation of this region; indeed, binding of triphosphates promotes dissociation of HKI from the mitochondrial membrane [86,90,91,97]. Kuettner, et al. captured an ATP analog bound to a similar region in Hxk1 of *Kluyveromyces lactis*, but in a different orientation [83]. However, they determined this to be an artifact due to the high concentration of the ATP analog present in the crystallization buffer.

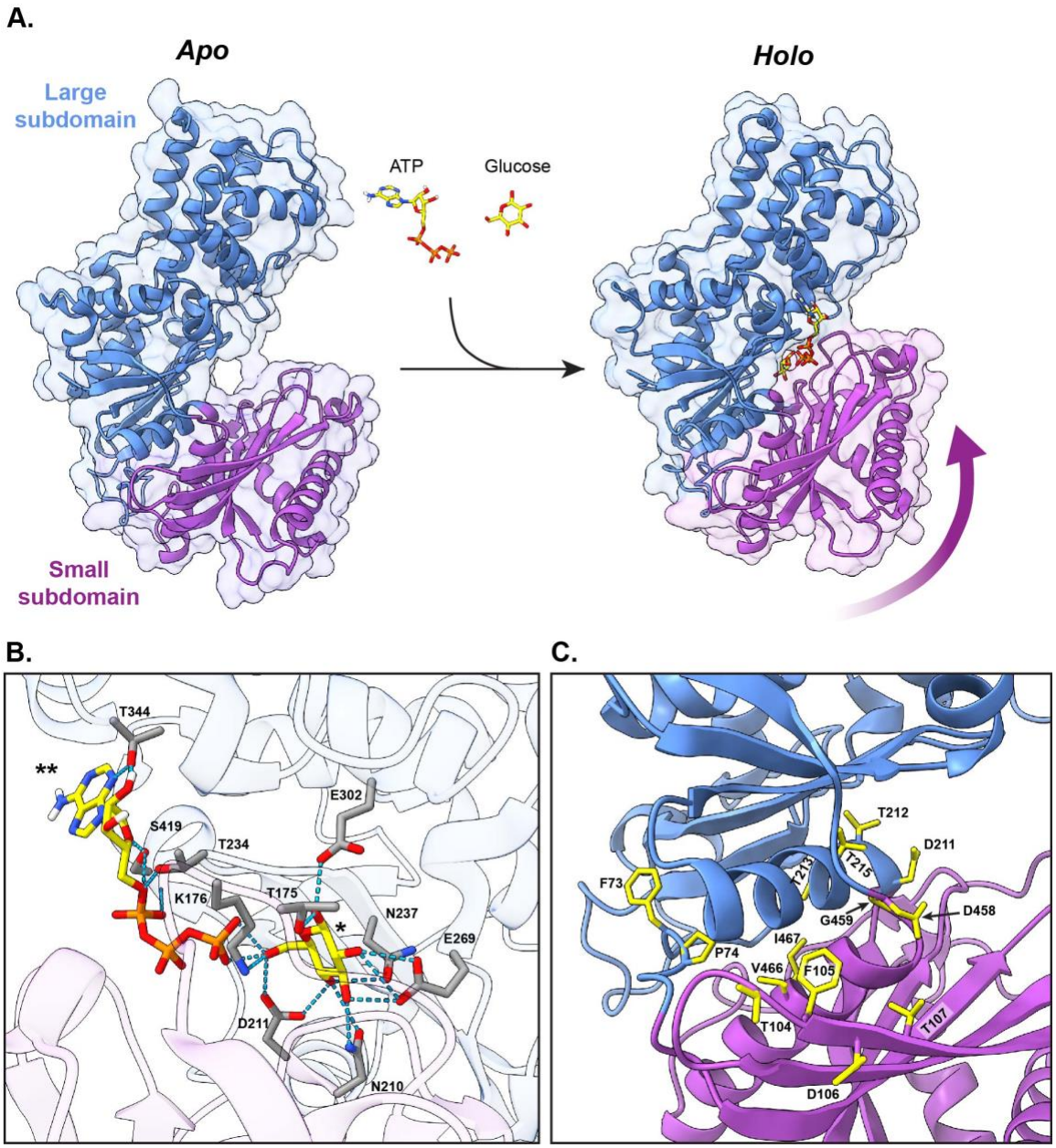

Figure 3. Yeast hexokinase structure and associated substrate-induced conformational change.

(A) Three-dimensional structures of yeast Hxk2 (apo, PDB 1IG8) and Hxk1 (holo, PDB 3B8A) in ribbon and surface representation. ATP and glucose are positioned in the enzymatic cleft (carbon atoms of both substrates are colored yellow). Blue and purple regions depict the large and small subdomains of each structure, respectively. The purple arrow depicts the approximate motion of domain closure. The glucose molecule was already captured in the *holo* crystal structure depicted. To indicate the location of the ATP binding site, we superimposed crystallographic ATP from a yeast Glk1 structure (PDB 6PDT). (B) Zoomed-in view of the hexokinase glucose (*) and ATP (**) binding

sites. The hexokinase backbone is depicted using ribbon representation. Sidechains of residues participating in hydrogen bonding interactions with glucose and/or ATP are depicted as gray rods. Blue, dashed lines indicate hydrogen bonds. (C) Zoomed-in image of Hxk2 focusing on the interface between the large (blue) and small (purple) subdomains.Yellow sidechains represent residues believed to be molecular hinge points.

1.2.1.3 Mode of substrate binding and catalytic mechanism

The induced fit mechanism theory of enzymatic action originally proposed by Koshland states that the active site of an enzyme changes shape to accommodate substrate binding [98]. Hexokinases are a classical example of this model, and their conformational changes are best studied in yeast (Figure 3A) [79–83,93,99,100]. They start in a state referred to as the 'open' conformation, which leaves the active site exposed to bulk solvent. Upon glucose binding to the active site, the large and small subdomains rotate relative to one another to bring the molecule to a 'closed' conformation. This rotation collapses the enzymatic cleft leading to the envelopment of the glucose molecule through an "embracing" mechanism [79,83,84,93,99,101]. In addition to the rigid-body closure, several loop regions in the small subdomain, namely residues 87-92, 115-124, 158-163, and 174-178 in yeast hexokinase, move forward to embrace the binding site and even interact with the glucose molecule directly (i.e., residues 175 and 176) [79,83]. ATP binding to the active site induces further conformational changes [81]. Several "hinge" points lie at the interface between the large and small subdomains, namely residues 73-74, 104-107, 211-215, 458-459, and 466-467 (Figure 3C) [79]. Residues 73-74 lie at the end of a longer 24-residue loop region present in all hexokinases called the connecting loop, which bridges together the large and small subdomains and is critical for ensuring proper domain closure in the presence of substrate [88,102]. Though initially controversial, it is now generally agreed that hexokinases show a random sequential mechanism where either ATP or glucose may bind first [103–107].

The sum of these conformational changes brings the ATP γ-phosphate directly next to the C6-OH group of glucose for transfer [94]. Next, an amino acid lining the active site acts as a catalytic base (usually an aspartic acid) by removing a hydrogen atom from the 6-oxygen of glucose. This enables nucleophilic attack on the ATP γ-phosphate, followed by transfer to the glucose 6-oxygen [87]. Electrostatic interactions between the resulting ADP and G6P drive the two products apart leading to their release from the enzymatic cleft.

1.2.2 Hexokinases in mammalian cells

1.2.2.1 Isoforms and differential expression

Five hexokinase isoforms are present in mammals: HK1, HK2, HK3, glucokinase (GCK), and hexokinase domain-containing protein-1 (HKDC1) [108,109]. HK1-3 and HKDC1 consist of two, 50 kDa N- and C-terminal lobes with high sequence similarity connected by a long, eight-turn linker helix (Figure 4A, B) [108,109]. These genes are likely to have evolved from the duplication and fusion of a gene encoding an ancestral 50 kDa hexokinase [110]. Catalytic activity is retained in both lobes of HK2, suggesting it is most closely related to the ancestral hexokinase produced from the gene duplication event (Figure 4B) [111–113]. In contrast, only the C-terminal lobes of HK1 and HK3 are active with the N-terminal lobe acting as a product inhibitory site for G6P (Figure 4B) [86,90,91,114,115]. It is likely that following gene duplication, HK1 and HK3 contained mutations that resulted in functional differentiation of the N-terminal lobes, allowing them to acquire these regulatory roles [110]. HK1-3 have relatively high enzymatic activity and are potently inhibited by physiological concentrations of the G6P product [110,114]. GCK has a single 50 kDa catalytic domain, a low affinity toward glucose, and is not product inhibited by G6P

[116]. HK1, HK2, and HKDC1 contain ~20-amino acid hydrophobic helices extending from the N-terminus that enable binding to the mitochondrial outer membrane [97,117,118].

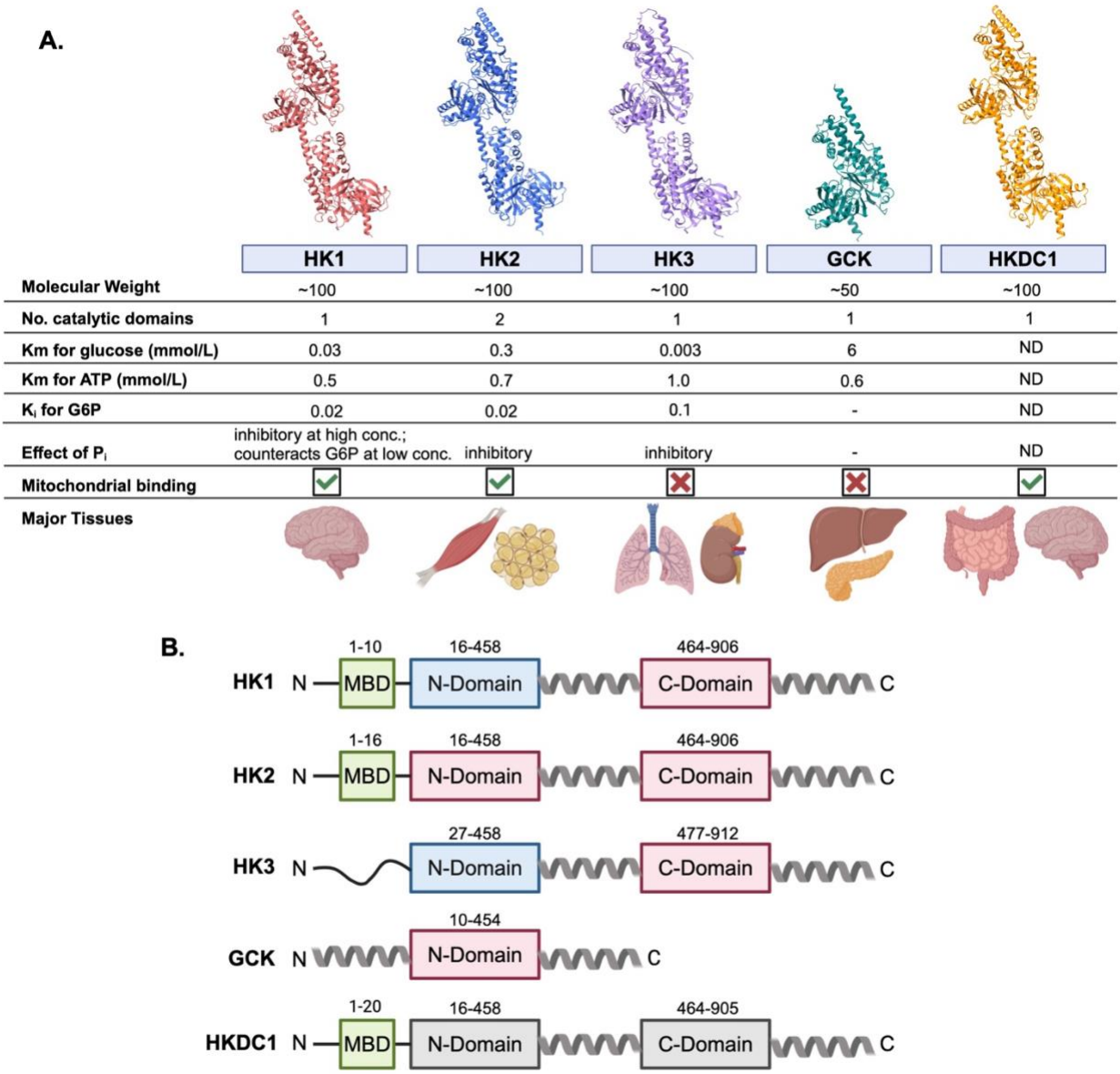

Figure 4. Hexokinase isozymes and their kinetic properties.

(A) Table summarizing the characteristics of each mammalian hexokinase isozyme. The structure of each isozyme, as predicted by AlphaFold (accession number from left to right: P19367, P52789, P52790, P35557, Q2TB90), is depicted

above its gene name. ND = No Data, - = no effect (B) Schematic of the functional domains of each hexokinase isozyme. The location of both hexokinase domains (if applicable) is depicted by rectangles. Blue rectangles depict inactive domains and red rectangles depict catalytically active domains. Though HKDC1 possesses hexokinase activity, it is unclear whether one or both of its domains are catalytically active. Therefore, both domains are colored gray. Mitochondrial binding domains (MBD) are depicted as green squares. Numbers above each domain represent the amino acids that make up the respective regions. Spirals represent α-helical domains and straight or curved lines depict unstructured domains. Portions of this figure were adapted from reviews published by Wilson, Farooq et al, and Guo et al [108–110].

Each hexokinase isoform has distinct tissue expression, subcellular localization, enzyme kinetics, and substrate specificities (Figure 4A). Engagement of multiple isoforms allows fine-tuning of glucose metabolism to meet the unique metabolic demands of specific cell and tissue types. For example, HK1 is the main isoform in the brain, but it is also ubiquitously and stably expressed across all tissue types and its gene is unaffected by most physiological conditions or stresses [108,110,119]. This ubiquitous and stable expression is due to the promoter of HK1, which has characteristics associated with those of "housekeeping enzymes" [120]. HK1 is inhibited by its product G6P but is activated by elevated levels of inorganic phosphate (P_i) in times of high energy use in the cell [86,112,115,121]. This suggests that HKI responds to cellular energy status and serves a primarily catabolic role by promoting glycolytic metabolism [108,110]. The ubiquitous expression of HK1 aligns with this view, considering the importance of glycolysis in all bodily tissues [110]. Consistent with a role in promoting glycolysis, HK1 is highly expressed in the brain, a tissue with high reliance on glycolytic flux to sustain high rates of energy production [122].

HK2 expression is more restrictive, limited to only insulin-sensitive tissues such as the heart, skeletal muscle, and adipose tissues [123]. G6P can inhibit HK2, but P_i adds to this inhibition

[111–113,115]. In muscle tissue, G6P and P_i levels elevate during exercise as glycogen breakdown and energy consumption increase. Inhibition of HK2 by these two metabolites limits glucose phosphorylation, uptake, and storage into glycogen in conditions when glycogenolysis (catabolic process) is the preferred means of energy production [124]. These features make HK2 well-suited for an anabolic role in recovering skeletal muscle to provide G6P for glycogen synthesis. Recent literature further proposes an anabolic role for HK2 where it generates G6P for NADPH production for lipid synthesis through PPP in the liver and mammary glands [125,126]. Importantly, HK2 induction is part of the anabolic program elicited by insulin in muscle cells, further supporting a role in promoting biosynthetic metabolism [127,128]. HK2 is the most well-studied hexokinase isozyme because of its role in the progression and maintenance of several cancers [70,129–139]. Indeed, a metabolic adaptation of cancer cells is a shift to aerobic glycolysis as a main source of ATP rather than oxidative phosphorylation, a phenomenon known as the Warburg effect [140]. HK2 overexpression, more so than other isoforms, is associated with this metabolic rewiring to support high glycolytic flux and tumor growth rates; HK2 inhibition suppresses cancer cell growth and metastasis [129,137,138,141,142]. Overexpressed or hyperactive HK2 is a negative prognostic marker in a variety of cancers, including breast cancer, liver cancer, pancreatic cancer, hepatocellular carcinoma, cervical, and glioblastoma multiforme [131,134,138,139,143–146].

GCK is primarily found in the liver, pancreas, intestine, and brain. GCK demonstrates sigmoidal enzyme kinetics and thus is not saturated by physiological glucose concentrations [147]. These properties allow GCK to act as a blood glucose sensor in pancreatic β-cells, ensuring that insulin secretion matches blood glucose levels [148]. In the liver, GCK expression increases in response to insulin where it removes glucose from the bloodstream when levels are high after a

meal (>5 mM) [149,150]. The resulting phosphorylated glucose is mostly stored as glycogen or used for fat synthesis [148]. Therefore, GCK serves as an important regulator of glucose homeostasis in the body. The importance of GCK in glucose balance is highlighted by the fact that metabolic diseases result from mutations in the GCK gene. Mutations in GCK are associated with diabetes and the severity correlates with the level of enzyme activity [149,151–154]. For example, a mild form of diabetes called maturity onset diabetes of the young type 2 (MODY2) is caused by heterozygous loss-of-function mutations in GCK [151,153,155,156] whereas homozygous loss-of-function mutations can cause more severe disease, specifically permanent neonatal diabetes mellitus (PNDM) [153]. Conversely, gain-of-function GCK mutations cause hyperinsulinemic hypoglycemia that is characterized by increased insulin secretion independent of blood glucose levels [151,153].

HK3 and HKDC1 are less characterized in comparison to the other isoforms. HK3 is expressed at low levels in the lung, kidney, and liver [157]. It is inhibited by glucose at high concentrations and is inhibited by G6P and P_i to a similar degree as HK2, supporting an anabolic role [108,110]. It also has the lowest affinity for ATP amongst the hexokinases, however, the physiological impact of this characteristic is unknown [110]. HKDC1 was only recently discovered (2007) and demonstrates a wide distribution of expression in human tissues including kidney, brain, small intestine, and thyroid amongst others [158]. Guo et al. confirmed that HKDC1 possesses hexokinase activity by expressing it in rat pancreatic β-cells and demonstrating increased hexokinase activity over a range of glucose concentrations [159]. HKDC1 has low catalytic activity, demonstrating a lower binding affinity than GCK and containing ~20% of the activity of HK1 when tested *in vitro* [117,159]. Recent studies suggest that HKDC1 may regulate

glucose tolerance during pregnancy and be associated with metabolic diseases including gestational diabetes mellitus and cancer [160–162].

1.2.2.2 Role in glucose homeostasis and sensing

Hexokinases are thought to have other, non-canonical roles outside of phosphorylating glucose. The best described of these, identified in a wide array of organisms, is the ability of hexokinases to sense glucose (see Rodriguez-Saavedra et al. 2021 [62] for a thorough review). For example, GCK plays a crucial role in preserving glucose balance by sensing glucose in bloodstream and controlling insulin secretion from mammalian pancreatic β-cells [148]. GCK is an excellent glucose sensor because it has sigmoidal enzyme kinetics due to positive cooperativity with glucose (Hill coefficient 1.6-1.8) with the steepest portion of the sigmoidal curve at about 4.0 mM, close to the threshold for inducing the secretion of insulin (~5 mM) [102,163–165]. GCK also has low affinity for glucose (Km = 8.0 mM) and so does not saturate at physiological concentrations (Vmax > 20 mM), which are kept in the tight window of 3.6-5.8 mM in the blood [147,148]. Importantly, GCK is not inhibited by G6P, unlike the other high affinity (HK1-3) hexokinase isozymes. These properties allow GCK to phosphorylate glucose at a rate proportionate to blood glucose concentrations and across a wide physiological range.

In pancreatic β-cells, GCK acts as a principal control for the secretion of insulin [166–168]. Briefly, glucose enters the β-cell cytoplasm through glucose transporters so that the intracellular and extracellular glucose concentrations rapidly equilibrate. As a result, GCK activity increases and drives higher rates of glycolysis and generation of reducing agents from the TCA cycle. This causes an increased flux of reducing agents into the mitochondria and the generation of ATP. Cytosolic pools of ATP increase followed by a decrease in cytosolic ADP. These changes

in ATP/ADP ratio inhibit ATP-sensitive K^+ ion channels, leading to membrane depolarization and opening of voltage-gated Ca^{2+} ion channels, calcium influx, and exocytosis of insulin granules [147–149]. GCK may similarly regulate the release of glucagon in pancreatic α-cells [169,170]. Increases in glucose phosphorylation by GCK, in-turn, increases the ATP/ADP ratio leading to closure of ATP-dependent K^+ channels and membrane depolarization. However, in α-cells, membrane depolarization inactivates voltage-gated Na+ channels involved in action potential firing which results in decreased activation of Ca^{2+} channels that promote Ca^{2+} entry. As a result, exocytosis of glucagon-containing granules, which would release glucagon into the circulation, is prevented [148].

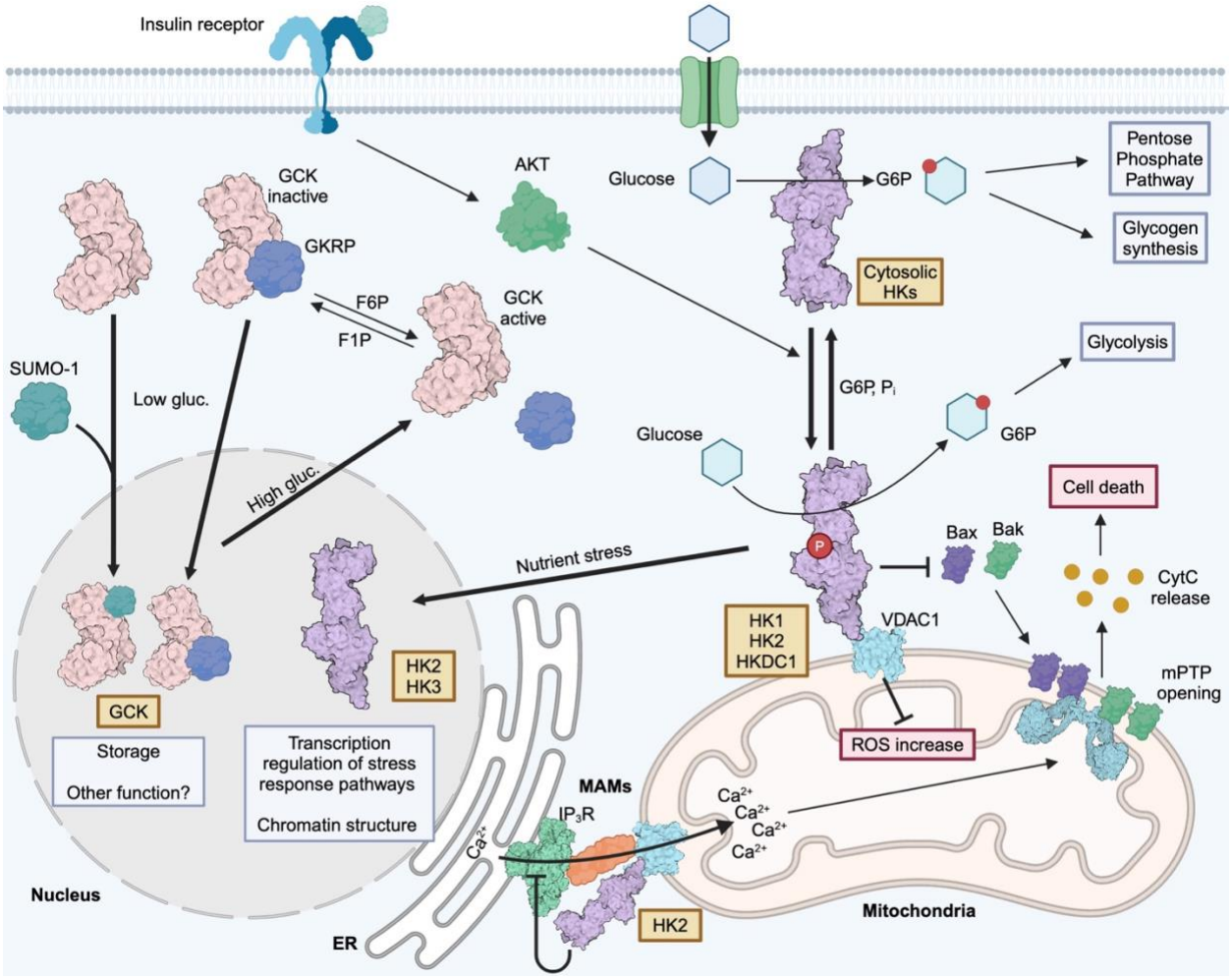

Figure 5. Mammalian hexokinase subcellular localization change and functions.

HK1, HK2, and HKDC1 can translocate from the cytosol and bind to the OMM through their interaction with VDAC. OMM binding of HK2 is stimulated through phosphorylation by AKT which becomes active in response to insulin signaling and other pro-growth signals. OMM binding propensity dictates the metabolic fate of glucose. When HK1 and HK2 are cytosolic, G6P is directed toward anabolic metabolism such as glycogen synthesis and PPP. When bound to the OMM, G6P is directed toward glycolysis and the production of ATP. Hexokinase binding to the OMM better couples ATP generation and G6P production which helps improve electron flow and alleviate ROS generation. Mitochondrial-localized HK1 and HK2 prevent the binding of Bcl2-family proteins and the subsequent opening of the mPTP. Mitochondrial HK2 associates with MAMs where it regulates flux of Ca2+ ions from the ER to the Mitochondria and prevents mPTP opening. In response to nutrient stress, HK2 and HK3 translocate to the nucleus. However, the functional significance of this not clear. HK2 may influence transcription of stress response genes by

interacting with transcription machinery and regulators of chromatin structure. Though HK3 may influence similar responses, it is unclear if this is by interacting directly with nuclear proteins. In the liver, GCK binds to GKRP, which acts as a competitive inhibitor of GCK in the absence of glucose. This complex is then imported into the nucleus where GCK is kept there for storage until glucose is re-introduced. In pancreatic β-cells, GCK enters the nucleus via a nuclear localization sequence and sumoylation induces nuclear translocation.

1.2.2.3 Localization at the mitochondria

Hexokinases are dynamic and change their subcellular localization in response to environmental stimuli (Figure 5). As early as the 1960s, it was demonstrated that a pool of HK1 and HK2, and more recently HKDC1, bind to the outer mitochondrial membrane [97,171]. Mitochondrial binding is driven by an N-terminal, hydrophobic helix that encodes a mitochondrial binding domain, embedding it within the lipid bilayer of the outer mitochondrial membrane [118,172]. At the mitochondrial surface, HK1, HK2, and HKDC1 bind to voltage-dependent anion channel 1 (VDAC1) (Figure 5) [117,173–175]. VDAC1 is a channel protein that exports ATP from the mitochondria into the cytosol. In this way, VDAC1 serves as a conduit for the flux of ions, metabolites, and various respiratory substrates across the OMM [176]. Binding to VDAC1 gives hexokinases preferential access to ATP, thereby maximizing their catalytic output and directing the flux of G6P.

What are the roles of mitochondrial hexokinases? Hexokinase binding to mitochondria may dictate the metabolic fate of glucose. HK1 binds more strongly to VDAC1 than HK2 and acts as a housekeeping enzyme, mainly committing glucose to glycolysis [177–180]. In contrast, HK2 is more dynamic and alternates between cytoplasmic and mitochondrial-bound states in response to metabolic stressors and glucose availability [177,178,181]. HK2 may have dual roles dictated by its cellular localization; cytosolic HK2 may channel G6P into glycogen and PPP pathways while

mitochondrial HK2 promotes G6P flux through glycolysis and oxidative phosphorylation [177,178,182,183]. Similarly, mitochondrial localized HK1 may have specific roles. A recent study of mitochondrial HK1 examined an HK1 lacking its N-terminal mitochondrial-binding domain (MBD). Mice expressing HK1-ΔMBD had decreased glucose flux in the latter stages of glycolysis and increased flux through the pentose phosphate pathway [180]. The block on glycolysis was mediated by cytosolic HK1 binding to and promoting iNOS-dependent nitrosylation and inhibition of GAPDH [180]. Therefore, the subcellular localization of HK1 dictates the metabolic fate of G6P between anabolic and catabolic metabolism. Mitochondrial HK1 prevents the inhibition of GAPDH thereby stimulating G6P catabolism through glycolysis. In contrast, cytosolic HK1 inhibits GAPDH and G6P is metabolized via anabolic PPP [180].

Mitochondrial HK2 protects the cell from apoptosis. In cardiomyocytes, AKT, an insulin-responsive kinase that elicits anabolic and anti-apoptotic signaling in cells [184], and prevents cell-death by promoting HK2 binding to the mitochondria [63]. HK2 mitochondrial binding is regulated by AKT, as AKT phosphorylates HK2 at T473 and induces its translocation to the OMM [181]. HK2 mitochondrial localization can be regulated by other kinases including DMPK and Src kinase that form a complex with HK2 at the OMM where it promotes antioxidant and pro-survival properties in rhabdomyosarcoma cells [185]. Furthermore, OMM-bound HK2 inhibits apoptosis by preventing the opening of the mitochondrial Permeability Transition Pore (mPTP) [186]. Mechanistically, HK2 binds to VDAC1 and prevents the assembly of pro-apoptotic Bcl2-family proteins, specifically Bad and Bax, at the OMM [187,188]. This hinders the formation and opening of the mPTP, thereby preventing the release of cytochrome C into the cytosol and inhibition of apoptosis [173,174,187]. Mitochondrial HK2 also inhibits mPTP opening by preventing Ca^{2+} overload and generation of reactive oxygen species (ROS), each of which normally induce mPTP

opening [76,174,182,183,185,189–191]. Indeed, mitochondrial HK2 couples glucose phosphorylation with ATP generation, thereby improving electron flow in the mitochondria and reducing mitochondrial ROS generation [189,192]. Mitochondrial HK2 can localize at Mitochondria-Associated Membranes (MAMs), which are inter-organelle contacts between the endoplasmic reticulum (ER) and the OMM [76]. MAMs are involved in Ca^{2+} transfer to mitochondria [193], which is required for mitochondrial enzyme function and cell survival as it suppresses apoptosis [194]. Displacement of HK2 from MAMs may be an effective mechanism to induce cell death in cancer cells as its dissociation leads to increased flux of Ca^{2+} into the mitochondria, triggering mPTP opening and apoptosis [76]. This highlights the impact of HK2 on preserving mitochondrial-ER Ca^{2+} fluxes and underscores the importance of regulating these fluxes in cancer cells.

Mitochondrial HK2 is beneficial to cancer cells as it provides a more efficient means to drive energy production from glucose phosphorylation for rapid growth. Additionally, mitochondrial HK2 prevents apoptotic signaling and thereby increases cancer cell survival. For example, AKT becomes constitutively active in several tumors [184] leading to the phosphorylation of HK2 and in turn, its localization to the OMM where it inhibits apoptosis [181,187]. Also, the ubiquitination of HK2 at K63 by the HectH9 E3 ligase drives its localization to the OMM by promoting HK2 binding to VDAC [145]. HK2 ubiquitination promotes proliferation, metabolic reprogramming, and chemoresistance in prostate cancer cells [145]. Finally, HK2 is sumoylated at K315 and K492 and this modification regulates mitochondrial binding in prostate cancer cells. De-sumoylation by the sumo-specific protease, SENP1, induces HK2 translocation to the mitochondria and enhances glucose consumption. In turn, this metabolic shift supports prostate cancer cell proliferation and provides chemoresistance [195]. These

observations underscore the potential of using AKT inhibitors [196] or targeting HectH9 and SENP1 as avenues to displace mitochondrial hexokinases and cause apoptosis in cancer cells.

Disruption of HK2 OMM binding can be detrimental to cancer cells and may be a therapeutic avenue against cancers. For example, a non-phosphorylatable mutant of HK2 (T473A) decreases tumorigenesis and metastasis in colon and breast cancer xenografts of mice [197]. Further highlighting its importance to cancer cell survival, loss of HK2 from the OMM stimulates mPTP opening and cell death [187,188,198]. Such observations offer an intriguing therapeutic strategy for triggering cancer cell death, prompting the development of small peptides that prevent HK2 binding to the OMM. The HK2pep, which mimics the N-terminal portion of HK2 necessary for mitochondrial delivery, competes with the anchoring of endogenous HK2 to the mitochondria, thus promoting cell death [76,174,185,187,199]. Reciprocally, VDAC1-based peptides also prevent HK2 binding to the OMM [199]. Introduction of peptides composed of the last eight C-terminal amino acids of HKDC1 also competes with its binding to VDAC1 and elicits cell death in T-cell lymphoma [200].

HKDC1 localizes to the OMM in liver and breast cancer cells [117,201]. Like HK2, HKDC1 binds to VDAC1 and increases mitochondrial membrane potential and glucose uptake, promoting cell survival and proliferation [160,200–202]. Knockdown of HKDC1 increases ROS generation, caspase-3 activity, and apoptosis, thereby similarly providing a means to induce cell death that could be leveraged in the fight against cancer and other diseases [201].

1.2.2.4 Nuclear localization and proposed roles

In addition to their cytosolic functions in glycolysis, all enzymes of the glycolysis pathway can accumulate in the nucleus. The purpose of nuclear-localized glycolytic enzymes remains poorly understood, but this whole-sale relocalization to the nucleus raises the hypothesis that

glycolysis may be occurring in this compartment [203]. Studies from the 1960s incubated isolated nuclei with glucose and found that ATP and lactate were produced, supporting the idea that the nucleus may perform glycolysis [204]. Nuclear glycolytic enzymes may serve to alter transcription factor function, associate with RNA polymerase III, interact with DNA, regulate nuclear ubiquitin ligases, stimulate DNA polymerase, and protect telomeres [205–209]. Though a variety of putative functional linkages have been assembled, compelling and detailed mechanistic insight remains to be provided. As an example, phosphofructokinase, which catalyzes the third step in glycolysis, accumulates in the nucleus in HeLa, colorectal carcinoma, and breast cancer cell lines where its product, fructose-2,6-bisphosphate, triggers signaling pathways that promote cell growth [210]. In another example, nuclear pyruvate kinase and pyruvate dehydrogenase (steps 10 and 11 in glycolysis) form a complex with histone acetyltransferases. This allows for local production of acetyl-CoA, which can be used to acetylate histones and regulate gene transcription [211,212]. Though many examples like these exist, much remains to be defined for the nuclear activities of glycolytic enzymes.

What induces accumulation of nuclear hexokinases? In plants and humans, nuclear accumulation often occurs in response to glucose depletion or other stress conditions [64,65,69,70,95]. In mammals, the HK2, HK3, and GCK hexokinases can all accumulate in the nucleus (Figure 5) [64–68,70,213]. The best-defined nuclear translocation for any mammalian hexokinase is that of GCK. In liver hepatocytes under fasting conditions, GCK binds to the glucokinase regulatory protein (GKRP), and this is needed for GCK nuclear translocation [69,213–215]. GKRP binds to the open conformation of GCK, acting as a competitive inhibitor of glucose binding [69,216]. GKRP then sequesters GCK into the nucleus through a “piggy-backing” mechanism where it is stored until blood glucose levels rise again [69,215]. Phosphorylated

carbohydrates regulate the assembly of the GCK-GKRP complex. Specifically, fructose-6-phosphate promotes complex formation, whereas fructose-1-phosphate disrupts complex formation following feeding [216–219]. It remains possible that that GCK nuclear shuttling is controlled via a nuclear localization signal (NLS). A putative nuclear localization sequence (NLS) has been identified in pancreatic GCK (L30-R36) that is also conserved in the liver isoform [215,220]. Mutation of lysine residues in this region decreased the nuclear accumulation of transfected GCK in mouse pancreatic β-cells [215,220]. GCK is sumoylated *in vitro* and in pancreatic β-cells at K12, K13, K15, and K346 and these modifications increase its catalytic activity and cellular stability [221]. Sumoylation may additionally regulate GCK nuclear shuttling (Figure 5) as its co-transfection with sumoylation machinery including the sumo-conjugating enzyme, Ubc9, promoted its nuclear localization in pancreatic β-cells [220]. Interestingly, one of the GCK sumoylation sites is adjacent to a predicted nuclear export sequence (NES) composed of E300-V310 [215]. It is feasible that sumoylation of this residue may mask the NES and prevent the nuclear export of GCK. The nuclear function of GCK in pancreatic β-cells is currently unknown. Whether sumoylation contributes to GCK nuclear shuttling in liver hepatocytes also remains an open question. Still, several studies have indicated that GCK nuclear accumulation is fully dependent on GKRP [69,213–215].

The nuclear roles of HK2 and HK3 are not well understood. In brief, HK2 remains bound to the mitochondria in glucose-replete conditions but then translocates to the nucleus under glucose-starvation conditions in cancer cells and hematopoietic stem cells [64–66,68,70]. HK2 nuclear shuttling is induced in response to metabolic stress, particularly after cancer cells are treated with 2DG or when starved for glucose [64–66]. In cancer cells, AKT regulates the nuclear-cytosolic shuttling of HK2 [65]. When active, AKT phosphorylates and promotes mitochondrial

localization of HK2 (see section 1.2.2.3). With AKT inactivated, HK2 likely becomes dephosphorylated and dissociates from the mitochondria. Mitochondrial dissociation is thought to drive nuclear accumulation of HK2, but a detailed mechanism for how this occurs is yet to be defined [65]. However, its nuclear localization may require additional inputs as the pharmacological detachment of HK2 from the mitochondria did not lead to its nuclear shuttling [65].

Several putative mono- (K41-K51, K144-K147, R190-R196, K424-K428, K487-K491) and bipartite (P420-R432, K424-V435, K762-R778) NLS sequences have been identified in HK2, suggesting regulation by nuclear import machinery [64,66,70]. Indeed, evidence of regulation by nuclear import machinery was demonstrated, as knockdown of the nuclear importin IPO5 in a leukemic cell line resulted in decreased levels of HK2 in the nucleus [66]. K to E mutations at two of the monopartite NLS sites (K41-K45 and K424-K428) attenuated HK2 nuclear shuttling in epithelial ovarian cancer cells in response to cisplatin treatment [70]. Follow-up will be required to assess the contributions of the other putative NLS sites.

HK2 nuclear shuttling is linked with several putative functions. Accumulation of nuclear HK2 pools may be associated with increased glucose uptake in cancer cells [65]. Moreover, HK2 interacts with nuclear proteins to modulate chromatin structure, transcription, and responses to DNA damage in both leukemic and normal hematopoietic stem cells [66]. Furthermore, nuclear HK2 increases leukemic stem cell properties by reducing differentiation and instances of double-strand breaks, while also imparting chemoresistance independently of HK2 enzymatic activity [66]. In glucose-deprived glioma cells, HK2 plays a role in regulating redox homeostasis by forming a complex and acting as a coactivator of erythroid 2-related factor 2 (Nrf2) to enhance the expression of xanthine reductase (XOR) [68]. Importantly, HK2 forms a complex with apoptosis-

inducing factor (AIF) at the OMM of ovarian cancer cells, where together they translocate to the nucleus, eliciting AIF-induced apoptosis after cisplatin treatment [70]. These data further support the idea that nuclear translocation of hexokinases can have important roles in regulating cell fate, and this ability to induce apoptosis would be useful as a strategy to impair cancer cell progression.

In support of this idea, HK3 accumulates in the nucleus of acute myeloid leukemia (AML) cell lines, however, its precise role in this compartment remains unclear [67]. Loss of HK3 leads to the accumulation of ROS and DNA damage, subsequently triggering cell death pathways, oxidative stress, and the DNA damage response [67]. However, more work is required to understand the regulatory roles of nuclear hexokinases. My work in the proceeding chapters advances our understanding of these points.

1.2.3 Hexokinases in *S. cerevisiae*

To understand the nuclear functions of hexokinases, my work uses the model organism *Saccharomyces cerevisiae*, or budding yeast. Yeast express three hexokinase isozymes, namely, Hxk1, Hxk2, and Glk1. Hxk1 and Hxk2, which are closely related paralogs with 77% identity and 89% similarity in their amino acid sequences, have broad substrate specificity and can phosphorylate glucose, fructose, and mannose [222,223]. In contrast, Glk1 is more specific to glucose and mannose [223]. Like mammalian GCK, all three yeast hexokinases possess one catalytic lobe. Each is sensitive to G6P inhibition, similarly to most of the mammalian isozymes [90,224,225]. A putative fourth hexokinase and paralog of Glk1, Emi2, was recently identified and shown to have hexokinase activity [226]. However, Emi2 activity is insufficient to support growth on glucose in *hxk1*Δ *hxk2*Δ *glk1*Δ cells [227,228]. Hxk2 is the major glucose kinases in yeast cells grown in abundant glucose [228,229]. Upon a shift of yeast cells to non-fermentable carbon

sources, the *HXK2* gene is repressed while *HXK1* and *GLK1* genes are expressed [230]. In this way, the cell transitions from using Hxk2 to Hxk1 and Glk1 in carbon sources alternative to glucose. In terms of conservation, the yeast isoforms are divergent from the mammalian hexokinases, though they still retain high sequence identity at functionally important residues (see Figure 6 for a sequence alignment and percentage identity between yeast and mammalian hexokinases).

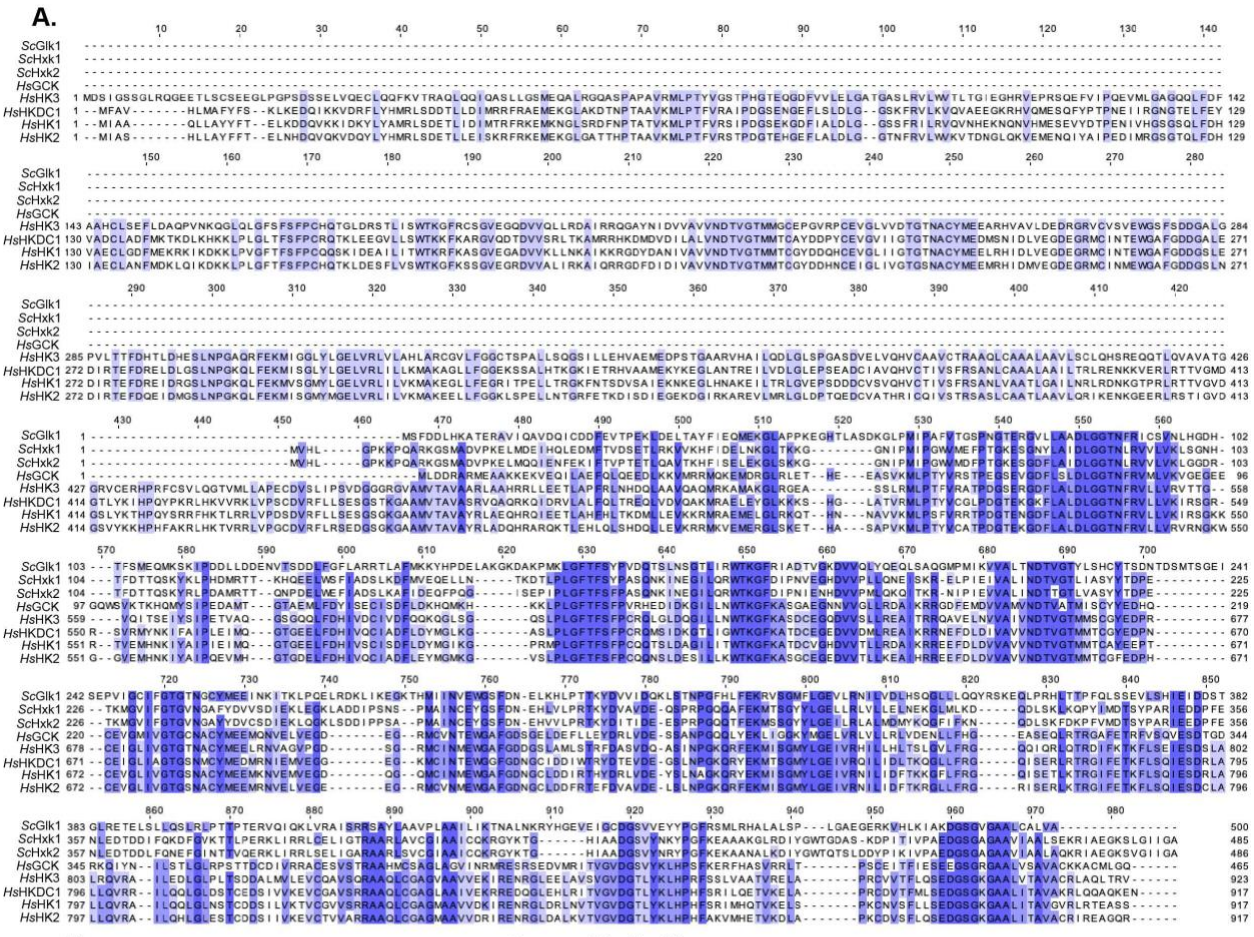

B.

Sequence identity (%)

	*Sc*Hxk1	*Sc*Hxk2	*Sc*Glk1	*Hs*HK1	*Hs*HK2	*Hs*HK3	*Hs*GCK
***Hs*HKDC1**	34.69	34.21	33.67	70.88	67.61	52.56	51.61
***Hs*GCK**	32.71	29.75	31.29	52.90	52.04	51.40	
***Hs*HK3**	33.06	32.12	34.19	52.23	55.16		
***Hs*HK2**	33.20	31.85	36.17	73.61			
***Hs*HK1**	33.94	34.62	32.73				
***Sc*Glk1**	38.05	37.38					
***Sc*Hxk2**	77.37						

Figure 6. Conservation of yeast and mammalian hexokinases.

(A) Amino acid sequence alignment of all mammalian and yeast hexokinase isoforms. Blue regions indicate residues that have high sequence identity. (B) Table summarizing the overall sequence identities (shown as percentages) between each hexokinase isoform.

1.2.3.1 Role in glucose repression and sensing

In yeast grown on glucose, the expression of genes that encode enzymes to breakdown alternative carbon sources (like sucrose and ethanol) are repressed. This phenomenon is known as glucose-repression of gene expression, and it has wide-ranging effects on gene expression, altering the transcription of >2000 genes [224,231,232]. In addition to their roles in phosphorylating glucose, hexokinases are thought to be key regulators of glucose repression of gene expression. Key for this transcriptional rewiring is the nuclear localization of the Mig1 transcriptional repressor complex. When in the nucleus, Mig1 binds to the promoters of glucose-repressed genes and prevents their expression [29,50]. However, under glucose starvation conditions or in the presence of alternative carbon sources, Mig1 becomes phosphorylated and this prevents its nuclear accumulation [50,54]. When in the cytosol, Mig1 can no longer repress gene expression, and this leads to activation of the glucose-repressed genes.

Thus, yeast hexokinases have been posited to have dual roles in the cell: 1) they phosphorylate glucose, and 2) they act as intracellular glucose sensors that maintain glucose repression of gene expression [233]. Interestingly, all three hexokinase isozymes can act as glucose sensors and initiate both phases of carbohydrate repression in yeast depending on the sugar used. Early studies showed that the activity of any of the yeast hexokinases is required to initiate glucose repression [228,234,235], and that Hxk2 specifically is required to sustain repression in adapted cells long-term [228,233–235]. In response to fructose, either Hxk1 or Hxk2 are required for long-term repression, but not Glk1 [228,234,235]. Building on these earlier reports, it was proposed that the yeast hexokinases play a role in the nuclear shuttling of Mig1, modulating its nuclear function [235]. While previous work posited a physical interaction between Hxk2 and Mig1, necessary for Mig1 nuclear import [236–238], our work in Chapter 2 puts this model into question as we detect

no interaction of Mig1 with Hxk2. Later work by the Hohmann lab instead showed that the initial nuclear import of Mig1 is promoted by the activity of any of the three hexokinases upon the addition of mannose or glucose, but Glk1 alone does not elicit Mig1 nuclear import on fructose [235]. For continuous import of Mig1 into the nucleus, Hxk2 activity is required in the presence of glucose or mannose and either Hxk1 or Hxk2 are required in the presence of fructose [235]. This would suggest that Mig1 nuclear shuttling may be regulated by two distinct mechanisms where the initial import of Mig1 is triggered by hexokinase activity, and continuous shuttling requires the Hxk2 and Hxk1 proteins through an unknown mechanism [235]. Elbing et al 2004 demonstrated that Mig1 only remains unphosphorylated under high glycolytic flux to sustain glucose repression [239]. It could be that Hxk1 and Hxk2 promote greater glycolytic flux to inhibit Mig1 phosphorylation as they have higher Vmax values against glucose than Glk1 [223,224]. Collectively, this work, combined with our observations in Chapter 2, suggest that Mig1 nuclear import is regulated by hexokinase activity through a mechanism yet to be elucidated, rather than via a "piggy-backing" mechanism with Hxk2.

Several mechanisms have been proposed describing how hexokinases regulate Mig1 localization. First, Hxk2 and Mig1 are posited to interact in the presence of glucose and move into the nucleus together [236,237,240]. However, these observations have not been confirmed by others, nor has an association between Mig1 and Hxk2 been reported in any of the high-content copurification studies in yeast [241–244]. Second, Hxk2 may act upstream of Snf1 and modulate its phosphorylation state and activation by promoting the activity of the PP1 phosphatase complex in glucose-rich conditions which dephosphorylates and deactivates Snf1 [49]. In line with this, cells lacking the *HXK2* gene or mutagenesis of the D211 catalytic residue leads to increased phosphorylation of Snf1 followed by phosphorylation of Mig1 and release of glucose repression

[224,245,246]. Finally, Hxk2 may physically shield Mig1 from phosphorylation at S211 by Snf1 [39,237]. The precise molecular mechanisms by which hexokinases control glucose repression and Mig1 nuclear translocation require more study.

In yeast grown on glucose, the expression of genes that encode enzymes to breakdown alternative carbon sources (like sucrose and ethanol) are repressed. This phenomenon is known as glucose-repression of gene expression, and it has wide-ranging effects on gene expression, altering the transcription of >2000 genes [224,231,232]. In addition to their roles in phosphorylating glucose, hexokinases were thought to be key regulators of glucose repression of gene expression. Key for this transcriptional rewiring is Mig1 nuclear localization. When in the nucleus, Mig1 binds to the promoters of glucose-repressed genes and prevents their expression [29,50]. However, under glucose starvation conditions or in the presence of alternative carbon sources, Mig1 becomes phosphorylated and this prevents its nuclear accumulation [50,54]. When in the cytosol, Mig1 can no longer repress gene expression, and this leads to transcriptional activation of the glucose-repressed genes.

1.2.3.2 Multimerization of yeast hexokinases

Yeast hexokinases exist in different oligomeric states depending on the energy status and carbon source supply in cells [94,247–251]. In cells, there is a monomer-dimer equilibrium for Hxk2 and the amount of glucose the cells are grown in drives this balance; glucose-starved cells have predominantly monomeric Hxk2 while cells grown in glucose-replete conditions have a balance of monomer and dimer [247,249–251]. Importantly, modification of Hxk2 by phosphorylation at S15 disrupts dimer formation [232,249,252,253]. This site is phosphorylated in glucose-starved cells, helping to stably separate dimeric Hxk2 into monomers [247,249].

S15 phosphorylation shifts the dimer-monomer equilibrium to promote greater emergence of the monomeric species. The upstream kinase regulating S15 phosphorylation was initially controversial [251,254]. One group proposed Snf1 (yeast AMPK) as the major kinase regulating S15 [254], while another group found that deleting *SNF1* had no effect of Hxk2 dimer propensity [251]. Later work by the Kriegel lab, demonstrated that Snf1 plays only a minor role in regulating phosphorylation at S15, as modestly less monomer was formed in *snf1*Δ cells [247]. Through single-gene deletion and other follow-up studies, it became clear that S15 phosphorylation status, and therefore dimerization of Hxk2, is regulated by glucose availability and by Tda1 (Figure 7) [247,249,250]. Tda1, a NUAK-family kinase and that itself is phosphorylated by Snf1, has only one other reported function so far in yeast [255]. In glucose starvation conditions, Tda1 expression and activity (due to Snf1-dependent phosphorylation) increases and under these conditions it phosphorylates histones (Figure 7) [232,255]. In high glucose conditions, Tda1 expression and activity is low and so its ability to phosphorylated Hxk2 is likely reduced, leaving Hxk2 as a dimer [247,249,255]. In low glucose conditions, Tda1 phosphorylates Hxk2 at S15 and promotes Hxk2 monomer formation (Figure 7) [247,249]. In cells lacking Tda1, Hxk2 remains as a dimer in glucose-replete and starvation conditions [247,249]. Though Tda1 phosphorylates Hxk2 S15 *in vitro,* other somewhat redundant kinases could also be involved *in vivo*. Indeed, Cmk1, Ypk1, Mck1, and Snf1 were identified in TAP-eluates with Tda1 [247]. Though their individual deletions did not impact Hxk2 dimer propensity *in vivo*, the authors concluded that Tda1 represents either the terminal Hxk2 kinase or an upstream regulatory kinase, therefore not ruling out a role for the other co-purifying kinases [247].

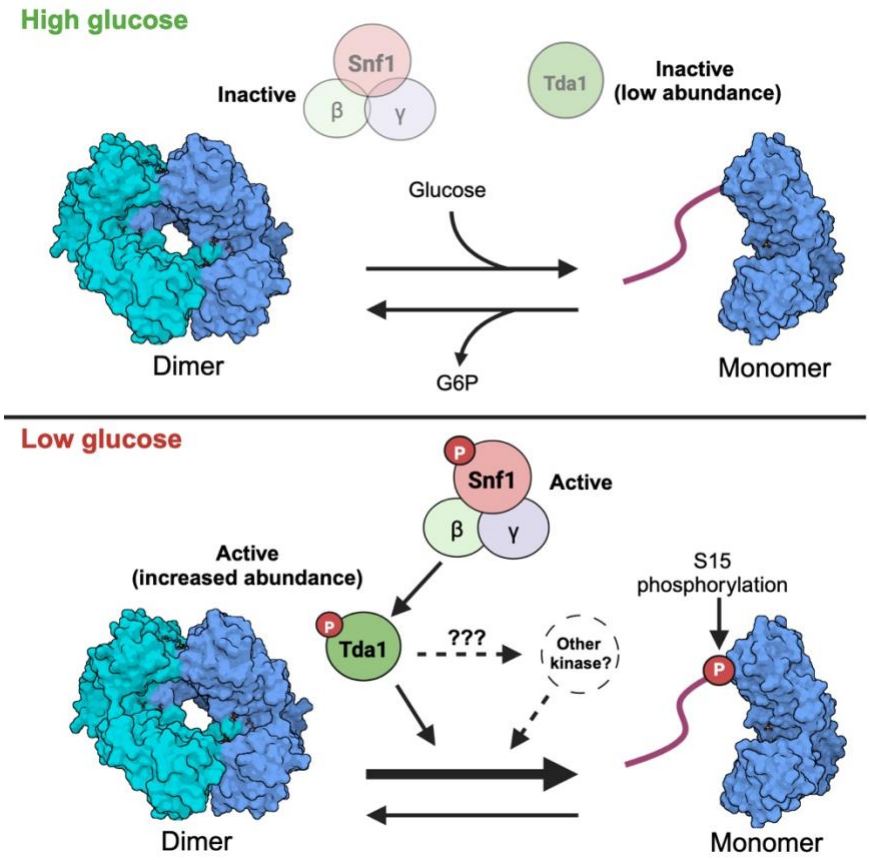

Figure 7. Regulation of Hxk2 dimer-monomer balance.

In high glucose conditions, Hxk2 exists in a dimer-monomer balance. Emergence of the monomeric species is regulated by the rate of glucose binding and subsequent catalytic cycles. In glucose-fed cells, Snf1 has low activity, and Tda1 is present in low abundance and remains inactive. In glucose-starved cells, Snf1 is phosphorylated and hyperactive in the cell. Tda1 abundance increases under these conditions and is phosphorylated and activated by Snf1. Tda1 subsequently phosphorylates Hxk2 at S15, thereby altering the dimer-monomer equilibrium and facilitating an increase in the abundance of the monomeric species. Recent studies suggest that Tda1 functions either as the terminal kinase responsible for phosphorylating Hxk2 at S15 or as an upstream kinase that activates other factors involved in Hxk2 phosphorylation.

The monomeric species of Hxk2 represents the form with the greatest glucose affinity, while the dimeric species has lower affinity [252,253]. Our computational modeling approaches discussed in Chapter 2, suggest that the N-terminal tail prevents stable glucose binding by

occupying space in the enzymatic cleft and that neither glucose nor the N-terminal tail can occupy the cleft at the same time, likely helping to explain why the dimeric species is less catalytically active [232].

Hxk1 also exists in a dimer-monomer equilibrium, however, its regulation is not as well-described as Hxk2 [232,248,249,256]. Hxk1 dimer-monomer balance is similarly regulated by Tda1-dependent phosphorylation at S15 [249]. Since Hxk1 and Hxk2 share remarkable sequence conservation, it is likely that Hxk1's dimer propensity is regulated similarly to Hxk2 where the dimeric species is favored in glucose-fed conditions and the monomeric species is preferred under glucose starvation.

As mentioned before, the hexokinase family belongs to the larger actin ATPase clan [78]. A common feature of these proteins is the ability to form polymers. Yeast Glk1 forms two-stranded, antiparallel filaments mediated by an elongated N-terminal helix that inserts into a hydrophobic pocket at the small subdomain of the next monomer [94]. These polymers form in cells upon addition of glucose and depolymerize and become diffuse in the absence of glucose [94]. Polymerization of Glk1 inhibits its catalytic activity by impairing the ability to transition between open and closed conformations [94]. Finally, Glk1 polymerization limits the rate of glucose phosphorylation and prevents toxic overactivity in response to glucose refeeding [94].

Structurally, the Hxk2 dimer is organized such that the small subdomain of one monomer interacts with the large subdomain of the other in a "head-to-tail" arrangement [83,232]. The dimer is held together by a series of electrostatic and hydrogen bonding interactions that occur along the interface between the two monomers [83,232]. Hxk2 possesses a disordered, 20-residue N-terminal tail that adopts an extended conformation and folds along the dimer interface into the catalytic cleft of the opposite monomer [83,232]. The N-terminal tail contributes several

electrostatic and hydrogen bonding interactions (see Chapter 2, Table 2) at the dimer interface, suggesting great importance in promoting dimer formation. Indeed, our experiments in Chapter 3, reveal the N-terminal tail is required for dimer formation [83,232].

1.2.3.3 Hxk2 nuclear shuttling and glucose repression

Decades of work from a single lab led to a model where Hxk2 was thought to have direct involvement in glucose repression of gene expression [230,236–238,254,257–261]. This 'moonlighting' function for Hxk2 involved Hxk2's nuclear translocation and interaction with Mig1, the transcriptional repressor that controls glucose repression [236–238,261]. Briefly, the model states that Hxk2 translocates into the nucleus in glucose-rich conditions in a manner dependent on the Kap60/Kap95 α/β importin proteins [260]. Nuclear translocation is then stimulated by 1) a nuclear localization sequence (NLS) in the N-terminal tail of Hxk2 that lies between K6 and K13 [260], 2) binding to Mig1, a transcription repressor involved in glucose repression, through the Hxk2 N-terminal tail [236], and 3) dephosphorylation of S15 in Hxk2 [254]. Once in the nucleus, Hxk2 was proposed to incorporate into a larger transcriptional repression complex with the Mig1 and Mig2 transcription repressors; Med8, a subunit of the Mediator complex; Reg1, a regulatory subunit of the Glc7 phosphatase; and the nuclear isoform of Snf1, which is composed of the Snf1 kinase and the Snf4 and Gal83, β and γ regulatory subunits, respectively [238]. Once assembled, this complex was thought to repress transcription of genes that promote respiration and metabolism of alternative carbon sources such as sucrose, maltose, and galactose [29,238]. Upon a shift to low glucose conditions, Hxk2 S15 was thought to be phosphorylated by Snf1, which promotes dissociation of the transcriptional repressor complex

[254]. Hxk2 was then posited to be shuttled out of the nucleus and into the cytosol by the Crm1 nuclear exportin protein, which recognized two distinct nuclear export sequences on Hxk2 [259].

However, multiple lines of evidence call nearly every aspect of this proposed model into question. First, in the initial model, Hxk2 is reported to translocate into the nucleus in glucose-rich conditions rather than in response to glucose-starvation; this is contradictory to observations in mammals and plants where hexokinase and glucokinase nuclear localization primarily occurs in response to stress and starvation [64–66,69,70,213]. Second, previous studies show that deletion of the N-terminal tail, proposed by the Moreno lab to interact directly with Mig1, is not required for Hxk2-mediated glucose repression of gene expression [222]. Third, the regions ascribed as nuclear export sequences that bind to Crm1 in this early model were later shown not to bind Crm1 and it was suggested that these sites were not nuclear export sequences [262]. Fourth, no aspect of this model was independently corroborated by another lab. Fifth, global protein-protein association studies, two-hybrid screens, and ChIP-Seq data fail to identify Hxk2 association with components of the proposed transcriptional repression complex or its association with the *SUC2* promoter region [241–244,263]. Sixth, in earlier imaging experiments assessing the localization of Hxk2, cells were incubated in glucose-free medium containing high concentrations of glycerol (80%) to allow for DAPI penetration into cells and nuclear staining [236,254,259,260]. Such conditions would most certainly induce starvation and stress-related responses that could confound interpretations of the imaging data and muddy studies of nuclear translocation. Finally, despite phosphorylation status of S15 being implicated in the proposed model of Hxk2 nuclear translocation, the authors fail to account for the existence of the different oligomeric forms of the enzyme, a shortcoming that has been openly criticized by experts in the field [264].

Chapter 3 of this dissertation highlights our work in reassessing the nuclear localization of Hxk2. We find that no aspect of the originally proposed model is correct. Therefore, we propose a new model that will form the basis of future studies to further evaluate the regulation and function of nuclear Hxk2.

1.3 2-Deoxyglucose

Entwined with my research on hexokinases were my studies focused on the molecular mechanisms of toxicity and resistance to a glucose analog, 2-deoxyglucose (2DG) (Figure 8). 2DG is a structural analog of glucose that differs from glucose as the hydroxyl group on the C2 carbon is lost. The toxic effects of 2DG have been recorded as early as the 1950s when Woodward and Cramer reported the inhibitory effect of 2DG on the proliferation of rat mammary carcinoma cells [265]. Since then, countless other studies have demonstrated the inhibitory effect of 2DG on cancer cell growth and on the growth of yeast cells (reviewed in [266]). 2DG has been an essential tool in yeast research, helping investigators discover genes that regulate glucose metabolic pathways. 2DG biochemically competes with glucose and is highly disruptive to glucose metabolic pathways. This has motivated studies testing 2DG's utility as an anti-cancer treatment due to the highly glycolytic metabolism demonstrated by some tumor types. Though 2DG and related analogs show promise as a viable cancer treatment, cells frequently gain resistance to the drug after prolonged exposure. Here, I focus on the role of hexokinases, examining select hexokinase mutants, in conferring resistance to 2DG (Figure 9). These studies have ramifications for the potential of 2DG as an anti-cancer treatment, and my work help defines the mechanisms by which cells gain resistance to 2DG (Figure 9 and Table 1).

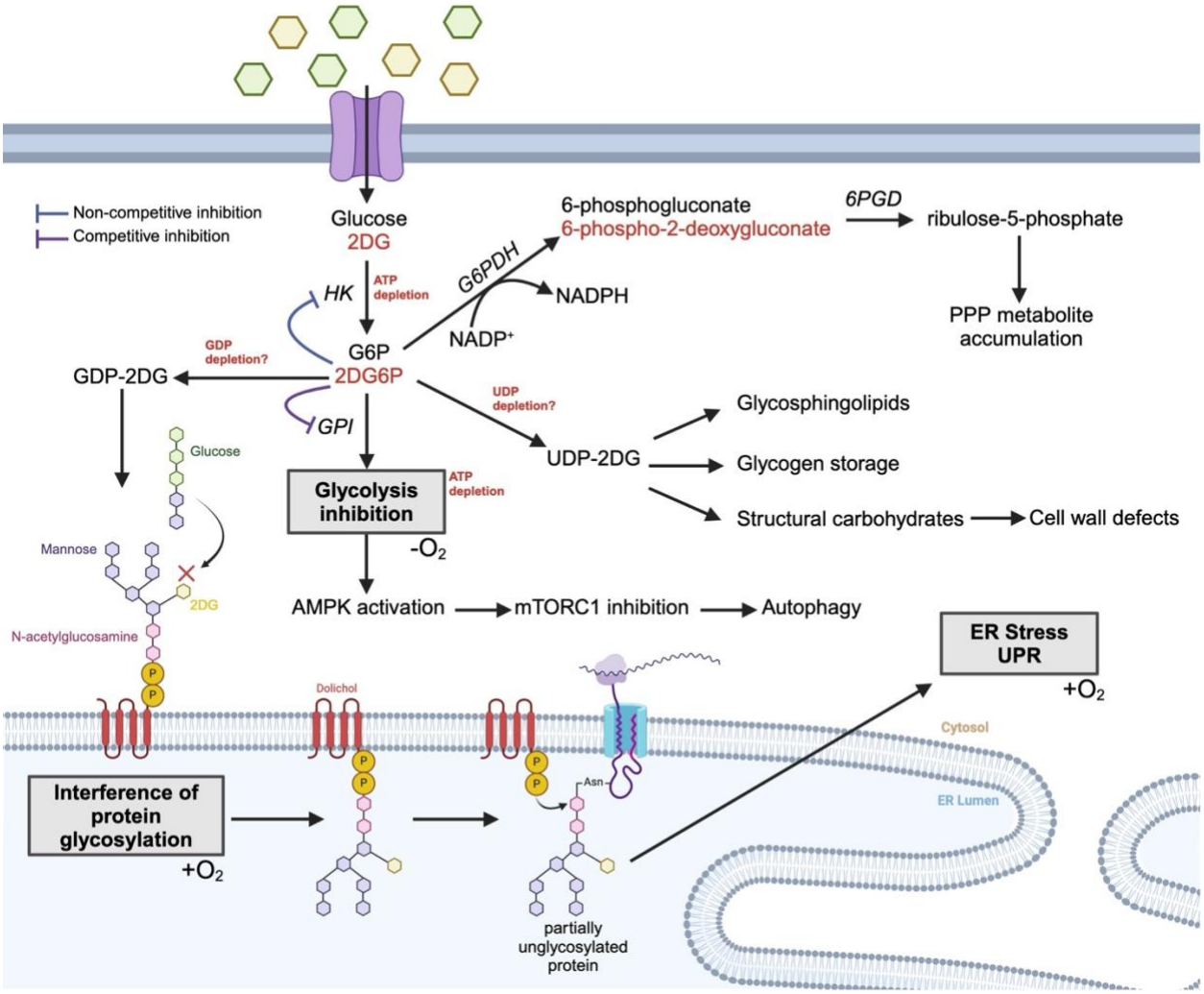

Figure 8. Mechanisms of 2DG toxicity.

2DG enters the cell through hexose transporters at the PM. 2DG is phosphorylated and converted to 2DG6P by hexokinases. Because it cannot be converted through glycolysis, 2DG6P accumulates in the cytosol where it acts as a non-competitive and competitive inhibitor of hexokinase and glucose-6-phosphate isomerase, respectively. 2DG6P consumes ATP and prevents ATP generation through glycolysis. This leads to a decrease in intracellular ATP pools. Decreased intracellular ATP levels activate AMPK. AMPK redirects cellular metabolism toward catabolic processes and inhibits mTORC1-dependent anabolic processes. A consequence of this is the induction of autophagy. GDP-2DG competes with GDP-mannose for incorporation into N-linked glycans used in protein glycosylation. The result is partially unglycosylated proteins that misfold and induce ER stress and activate the UPR. UDP-2DG has been identified in 2DG-treated cells where it is incorporated into glycogen stores, structural carbohydrates, and glycosphingolipids. Finally, 2DG6P is a substrate for the PPP and may redirect glucose flux toward this pathway

because of its inhibitory effect on glycolysis. 2DG treatment promotes the accumulation of PPP metabolites. Gray boxes represent the primary means of 2DG toxicity. Glycolysis inhibition is the primary mechanism of action in hypoxic cells, whereas 2DG mostly interferes with protein glycosylation in oxygenated cells.

1.3.1 2DG's impact on glycolysis

2DG competes with glucose for transport into the cell through glucose transporters in both yeast (called hexose transporters or HXTs in yeast) and mammalian cells (where the homologous glucose transporters are referred to as GLUTs) [267,268]. Upon entry into the cell, 2DG is phosphorylated by hexokinases into 2-deoxyglucose-6-phosphate (2DG6P) [265,269–272]. No evidence of free 2DG has been detected in cells suggesting that its rate of phosphorylation is faster than its transport [273]. Due to the missing hydroxyl group at the C2 carbon, 2DG6P cannot proceed to later steps of the glycolysis pathway and thus, ATP cannot be generated from its metabolism [269,274]. Therefore, 2DG consumes ATP, but cannot continue to the energy payoff phase of glycolysis (Figure 8).

2DG also prevents the phosphorylation of glucose. Indeed, 2DG is thought to block glycolysis at the hexokinase step [270]. 2DG acts as a non-competitive inhibitor of hexokinase and a competitive inhibitor of phosphoglucose isomerase [271,275]. Due to its inability to be metabolized, 2DG6P accumulates in cells [272,276]. Consequently, this impairs ATP-dependent processes and initiates starvation response pathways that halt cellular growth and proliferation [277]. However, inhibition of glycolysis is not the only means by which 2DG impairs growth of cells.

1.3.2 Effects of 2DG on cellular metabolic pathways

While 2DG6P is not a good substrate for glycolytic enzymes, this product can enter the PPP where it is converted to 6-phospho-2-deoxygluconate by glucose-6-phosphate dehydrogenase (G6PDH) [278]. This reaction provides a source of the reducing agent NADPH [279]. 2DG treatment can even be beneficial in glucose-starved cells by decreasing the level of ROS due to this conversion in the PPP [280]. After this step, 6-phospho-2-deoxygluconate does not progress further in the PPP because it is a poor substrate for 6-phosphogluconate dehydrogenase [281]. Because 2DG disrupts glycolytic flux at the hexokinase step, it may promote redirection of G6P flux toward the PPP. In yeast and fibroblasts treated with 2DG, increased levels of erythrose-4-phosphate, a PPP intermediate from the non-oxidative branch and competitive inhibitor of phosphoglucose isomerase, were detected [282]. In metabolomic studies of human endometrial carcinoma cell lines, 2DG treatment led to increased concentrations of PPP metabolites [283]. The contribution of the PPP to 2DG toxicity remains unclear as opposing effects on 2DG sensitivity were observed after deletion of the yeast G6PDH gene, *ZWF1* [245,282].

The existence of UDP-2DG and GDP-2DG in 2DG-treated yeast cells suggests that 2DG may interfere with processes such as synthesis of structural carbohydrates, glycogen, and glycosylated lipids [284–286]. In yeast, 2DG treatment causes fragile cell walls and activation of mitogen-activated protein kinase (MAPK) signaling pathways that specifically respond to cell wall damage [287]. Lysis of 2DG-treated yeast cells occurs at regions of β-glucan synthesis suggesting interference with cell wall formation that leads to this defect in cell integrity [288,289]. It could be that incorporation of 2DG-derivatives causes cell wall instability, but it may also be the case that 2DG leads to trapping of uridine- or guanosine-nucleotide pools and thereby competes with the normal pathways for synthesis [266]. Finally, the inhibitory effects of 2DG on cell growth

remains in yeast cells initially grown in 2DG-containing media then shifted to fresh media without 2DG, suggesting that a metabolic intermediate accumulates in 2DG-exposed cells that cannot be rapidly metabolized [245]. In line with this, 2DG can be incorporated into glycogen stores [286,290], suggesting it long-term presence in cells. 2DG also integrates into glycolipids, including glycosphingolipids, but it remains unclear whether 2DG alters the biochemical properties of these compounds [291,292]. It should be noted that glycolipids participate in a variety of important cellular processes such as signal transduction, endocytosis, protein trafficking, and autophagy [293]. Therefore, any interference with their synthesis or breakdown could lead to a variety of consequences.

2DG treatment induces ER stress, activating the unfolded protein response pathway by incorporating into protein N-glycosylation modifications [294–300]. 2DG is also known as 2-deoxymannose, as it is structurally like both glucose and mannose. As such, 2DG can enter mannose metabolic pathways. Specifically, GDP-2DG competes with GDP-mannose for incorporation into N-linked glycans [294,295]. Several lines of evidence in viruses, yeast, and mammalian cells show that 2DG treatment interferes with protein glycosylation [287,294,295,301,302]. Consequently, 2DG causes protein misfolding and initiates the unfolded protein response and ER stress [287,295,297,299,300]. The effect of 2DG on protein glycosylation and activation of these pathways is a key mechanism of toxicity in oxygenated cancer cells, as these cells are otherwise insensitive to 2DG since they can respire and better manage the decreased glycolytic flux [294,295,297]. This is an important facet of 2DG's biology as a cancer treatment; tumors are heterogenous with mixed populations of oxygenated, proliferating cells and hypoxic, slow-growing cells and 2DG can negatively impact both cell types [1]. The effects of 2DG on protein glycosylation can be rescued in yeast and cancer cells upon the addition of exogenous

mannose, further demonstrating the importance of protein glycosylation in 2DG toxicity [287,295,297].

1.3.3 Effects of 2DG on metabolic signaling pathways

Because of altered carbohydrate metabolism, 2DG triggers signaling pathways that respond to changes in nutrient availability and stress. A well-known effect of 2DG treatment on mammalian cells is the activation of the AMP-activated kinase (AMPK) [279,299,303–305]. 2DG likely activates AMPK by decreasing intracellular ATP levels [303]. Other cellular stresses caused by 2DG may also activate AMPK, as AMPK can be activated by 2DG-induced ER stress in pancreatic cancer cells [299]. Interestingly, AMPK activation helps cancer cells to adapt to the toxic effects of 2DG, a trend that is also true in yeast cells (discussed below) [224,245,272,306–308]. AMPK-dependent signaling pathways are also activated in response to 2DG treatment. In mouse embryonic fibroblasts 2DG treatment leads to phosphorylation and activation of the AMPK model substrate, acetyl-CoA carboxylase and phosphorylation of CREB (cAMP response element-binding protein) and activates its downstream signaling in breast cancer cells [306,309]. Therefore, 2DG treatment activates AMPK and AMPK-dependent signaling pathways to slow cell growth, an effect that also helps cells adapt to 2DG toxicity.

AMPK controls a wide variety of cellular processes that likely participate in 2DG toxicity. For example, it is well known that activated AMPK inhibits mTORC1 (mammalian target of rapamycin complex 1) [310]. mTORC1 is a central regulator of cell metabolism that counter acts AMPK, promoting anabolic metabolism, protein translation, and growth [19]. 2DG treatment promotes increased phosphorylation of Raptor, an mTORC1 component and AMPK substrate, but does not prevent phosphorylation S6K1, another mTORC1 substrate, suggesting that mTORC1 is

only partially inhibited by 2DG treatment [309]. In line with this, 2DG inactivation of mTORC1 is impaired in breast cancer cells lacking AMPK activity, providing evidence that 2DG inhibits mTORC1 through AMPK signaling [311]. Given mTORC1's role in inhibiting autophagy, 2DG may help induce autophagy, as has been shown in many cell lines, via this mTORC1 inhibition [312–315].

The impact of 2DG treatment on the yeast AMPK ortholog, Snf1, has been well studied. In glucose-grown cells treated with 2DG, Snf1 phosphorylation at its activation loop modestly increases, but this did not affect the phosphorylation of the Snf1 model substrate Mig1 [245,272]. When yeast cells are grown in medium lacking glucose, 2DG treatment causes dephosphorylation of Snf1, demonstrating that these cells perceive 2DG as glucose in these conditions [245]. The Snf1 target, Mig1, in this same context is also dephosphorylated in response to 2DG [245]. These studies suggest that 2DG could promote activation of the Glc7/Reg1 phosphatase complex, however, it remains unclear if 2DG or a downstream metabolite plays a role in regulating Glc7/Reg1. Interestingly, Snf1 is a critical modulator of 2DG sensitivity in yeast, as loss of Snf1 promotes hypersensitivity to 2DG treatment, whereas hyperactivation of Snf1 causes cells to be resistant to 2DG's toxic effects [224,245,307,316].

1.3.4 2DG's potential as a cancer therapeutic

Many cancers undergo a metabolic shift first characterized by Otto Warburg in 1927, termed the Warburg effect [317]. In general, this is characterized by increased glucose uptake and glycolytic metabolism even in the presence of sufficient oxygen [1]. Because of some cancer's total reliance on this shift to aerobic glycolysis, such as pancreatic ductal adenocarcinoma and glioblastoma multiforme (GBM) [318,319], there is great therapeutic potential in blocking early

steps of glucose uptake and glycolysis. Such cancers are highly susceptible to the toxic effects of 2DG [320,321].

Patients with islet-cell carcinoma, leukemia, bronchogenic carcinoma, and renal cell carcinoma were first treated with 2DG in 1958 [268]. After intravenous injection of 2DG, an increase in blood glucose levels was reported along with hypoglycemia-like symptoms such as sweating, drowsiness, and hypothermia, which dissipated after 90 minutes [268]. A single 2DG infusion did not impact disease progression in either case [268]. The reported side effects in this study prevented use of higher doses and further attempts were abandoned for several years [268]. A phase I dose escalation trial in 2010 tested the use of 2DG as a monotherapy to specifically target hypoxic cells [322]. The study recommended a phase II dose of 45 mg/kg [322]. Five of eight patients tested with FDG-PET scanning revealed that 2DG decreased ^{18}FDG uptake [322]. Since ^{18}FDG utilizes glucose transporters for uptake [323], these findings imply glucose import may be reduced, possibly due to the removal of glucose transporters from the surface. This contradicts the competition model for 2DG impairment of glucose uptake and instead suggests that 2DG prevents glucose uptake by affecting the availability of glucose transporters. Expression of the protein p62 in patient peripheral blood mononuclear cells decreased in five of six patients tested after 24 hours [322]. None of the patients with prostate cancer who completed the study showed a decrease in prostate-specific antigen [322]. Conflicting reports called into question 2DG's efficacy as a monotherapy [321,324–326]. This, combined with the fact that 2DG treatment alone activates pro-survival pathways in cancer cells [327], prompted examination of 2DG in combination therapies.

Tumors are often heterogenous populations of cells with the interior made up of hypoxic cells reliant on anaerobic glycolysis and generally less sensitive to chemotherapy and radiation

[1]. The exterior consists of cells that respire and are thus less sensitive to glycolysis inhibition [1]. This implied that 2DG could be used in combination with other drugs and radiation by selectively targeting the hypoxic population of cells. In fact, the use of 2DG has been shown to increase the toxic effects of various chemotherapies such as paclitaxel (microtubule depolymerization inhibitor), adriamycin (DNA topoisomerase II inhibitor), and etoposide (topoisomerase II inhibitor), as well as agents that induce apoptosis and Bcl2 agonists in murine models of a diverse set of cancers including lung cancer, osteosarcoma, retinoblastoma, prostate cancer, and T-cell lymphoma [324,328,329]. A phase I clinical trial investigated the combination of 2DG with docetaxel, a microtubule depolymerization inhibitor, in patients with advanced solid tumors [330]. Notable side-effects observed during treatment included elevated blood glucose levels, symptoms resembling hypoglycemia, and prolonged but asymptomatic QTc intervals [330]. Nevertheless, the combination therapy was generally well-tolerated, exhibiting no pharmacokinetic interactions [330]. Following 8 weeks of treatment approximately one-third of patients displayed stable disease [330]. Many other studies combining 2DG with other chemotherapies and radiation have been reported and show promise for improving these therapies [331]. Interestingly, the combination of 2DG with metformin has been extensively studied [315,332–335]. Metformin is commonly used to treat patients with type 2 diabetes and lowers blood glucose levels by impairing liver lipogenesis and gluconeogenesis and promotes insulin sensitivity [336]. Though its mechanism of action is still controversial, metformin is proposed to activate AMPK through mild inhibition of mitochondrial respiratory chain complex I leading to decreased cellular ATP levels, or by inducing its activation at the lysosome [336]. The combination of 2DG with metformin depletes cellular ATP levels and increases AMPK activation and autophagy in several cancer types [335]. The effect of 2DG and metformin on cancer cells may

seem promising, but as mentioned above, AMPK activation is important in helping cancer cells (and yeast, as we will discuss in the next section) adapt to 2DG toxicity [224,245,272,306–308]. Therefore, we posit that the use of AMPK inhibitors should be considered in treatments that utilize 2DG. Finally, two clinical trials showed that 2DG could be used in combination with radiation therapy in glioblastoma multiforme (GBM) patients [337,338]. Both studies showed that 2DG is tolerated at high concentrations (up to 250 mg/kg) and helped enhance survival [337,338].

The 2DG derivative, ^{18}FDG is commonly used in positron emission tomography-based imaging (PET) [339]. The idea is that poorly metabolized 2DG analogs should be transported across the cell membrane of highly glycolytic cells and accumulate in regions of increased glycolysis [339]. Therefore, ^{18}FDG is used as a traceable 2DG analog that helps detect metabolically active tumors [323]. This approach is also helpful in helping to monitor how various tumors react to treatment over time.

Other 2DG derivatives have been developed and compared to 2DG. The Lampidis lab developed glucose analogs with halogen-substituted C2 carbons (Fluoro/Chloro/Bromo-2-deoxyglucose) and tested their efficacy in inhibiting glycolysis compared to 2DG [340]. It was shown that FDG is more potent at inhibiting glycolysis compared to 2DG and was overall more efficient at killing hypoxic tumor cells [340]. This was demonstrated again in mouse model studies of retinoblastoma [341].

An acetylated pro-drug of 2DG, WP1122, is currently undergoing clinical trials as a treatment against GBM [342]. The chemical modifications to 2DG to generate WP1122 allows it to passively diffuse through the blood-brain barrier rather than requiring a glucose transporter for transit [331,342]. Once in cells, WP1122 undergoes deacetylation by esterases leaving behind 2DG that is phosphorylated and trapped in the cell [331,342]. WP1122 has an increased half-life

compared to 2DG and achieves greater accumulation of 2DG in plasma [342]. *In vitro* studies showed that WP1122 inhibits glycolysis and growth of GBM cell lines more potently than 2DG [342]. A mouse model study of GBM demonstrated real-time inhibition of glycolysis by comparing pyruvate to lactate conversion rates after oral administration of WP1122 using magnetic resonance spectroscopy [342]. Therefore, WP1122 represents an efficient, targeted delivery system of 2DG to glycolytic cancers residing in the brain.

1.3.5 Mechanisms of cellular resistance to 2DG in yeast

The potential for 2DG and derivatives as anti-cancer therapeutics has motivated researchers to understand how cells gain resistance to the drug. The budding yeast, *S. cerevisiae*, is a powerful model system to address this question as they, like cancer cells, are highly glycolytic, preferring glycolysis to OXPHOS even in sufficient oxygen [28]. As in mammalian cells, yeast acquire spontaneous resistance to 2DG at a high frequency [224,343].

Used since the 1970s, 2DG has been an effective tool in yeast genetic screens defining components of the glucose repression pathway [344–347]. 2DG treatment activates glucose repression and prevents the use of alternative carbon sources. Therefore, these early screens were centered around identifying mutants that alleviated glucose repression and promoted spontaneous growth on alternative carbon sources such as raffinose, sucrose, and galactose [344–347]. In one screen, the authors isolated mutants capable of growth on raffinose in the presence of 2DG and identified three complementation groups that we now know of as *HXK2*, *REG1*, and *GRR1* [344]. Another screen subjected cells to random mutagenesis and selected for growth on sucrose with 2DG. Here, mutations were identified in the *REG1*, *HXK2*, and *GLC7* genes [345]. Bailey and Woodward subjected yeast to random mutagenesis using ethylmethansulfonate and waited for

spontaneous mutants to grow on galactose with 2DG. Mutants in the *GRR1* gene were isolated [346]. A similar approach was used to first identify mutants in the *SNF1* gene which impacted the ability for yeast cells to grow on non-fermentable carbon sources [348]. Since these initial screens were performed, several follow-up studies ensued to further characterize these mutants that have shaped our current understanding of the yeast glucose repression pathway [29].

Recent studies by us and others have focused on understanding 2DG resistance mechanisms in yeast cells grown on glucose, which is more akin to cancer cells' environment cancer [224,227,245,282,287,307]. Resistant mutants were isolated in these screens by 1) plating wild-type cells on glucose medium containing 2DG and waiting for spontaneous resistant mutants to arise [224,287,307], 2) developing 2DG resistance in wild-type cells using lab evolution [227], or 3) screening the yeast knockout collection for resistance-conferring mutants [282]. These studies revealed key cellular mechanisms of 2DG resistance, which are summarized below (Figure 9 and Table 1).

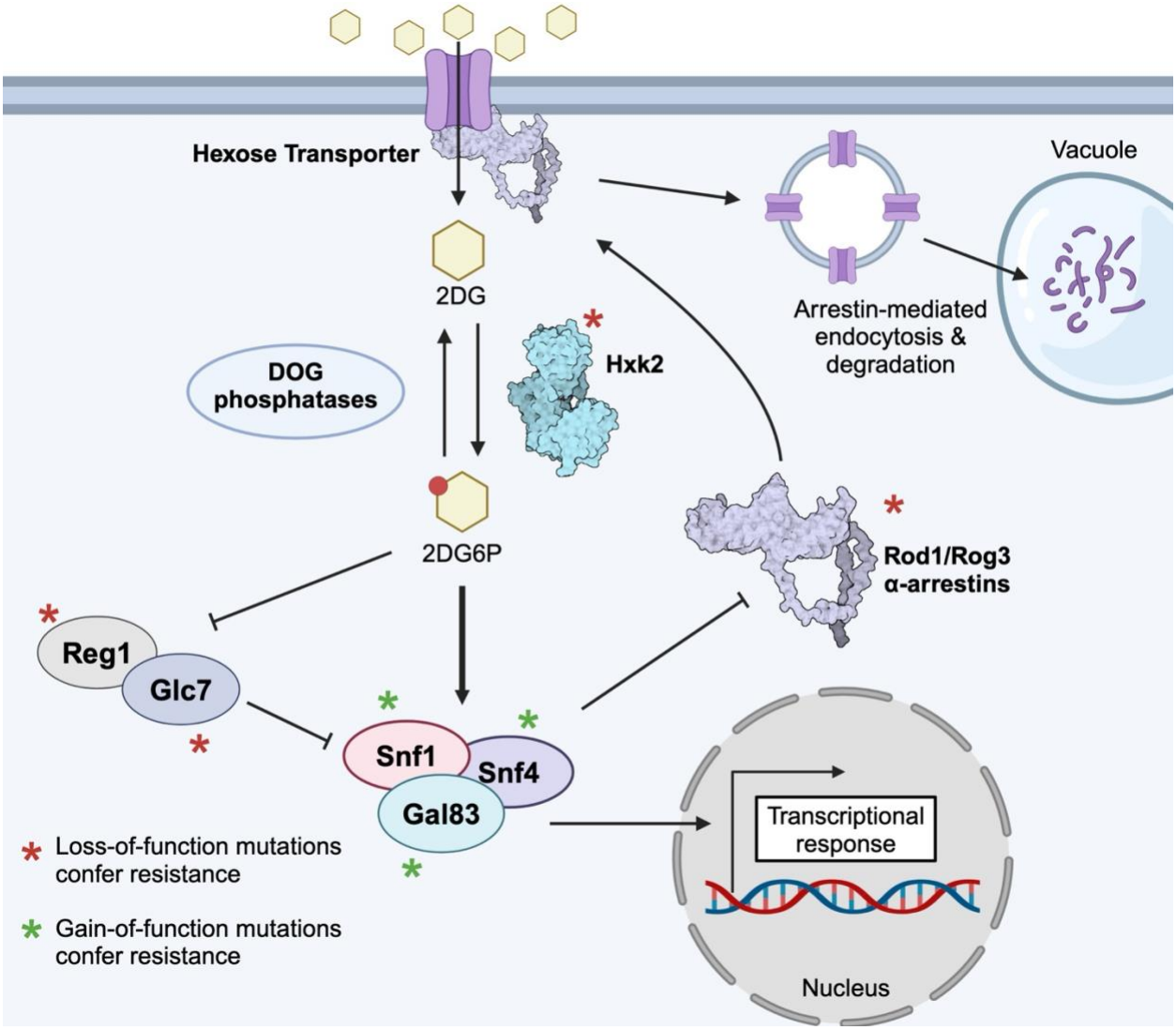

Figure 9. Summary of 2DG resistance mechanisms in yeast.

2DG enters the cells through hexose transporters and is phosphorylated by hexokinase into 2DG6P. 2DG6P accumulates in the cell and is toxic to the cell through a variety of mechanisms (see Figure 8). 2DG resistance requires the presence of the Snf1 kinase complex. Resistance to 2DG is achieved by hyperactivating Snf1 with dominant-acting mutations in genes encoding subunits of the kinase complex or through loss-of-function mutations in the *REG1* or *GLC7* genes, which encode the PP1 phosphatase subunits. Resistance is also obtained through loss-of-function mutations in Hxk2 or upregulation of the *DOG1* and *DOG2* phosphatases. Both result in decreased production of 2DG6P. Almost all resistance-conferring mutations result in decreased endocytosis and degradation of HXT transporters and their increased retention at the PM. This is regulated by the α-arrestins Rod1 and Rog3 and Snf1 in response to 2DG. Though Snf1 lifts glucose repression of some genes through Mig1 phosphorylation, there are likely

other transcriptional responses that modulate 2DG toxicity independently of Snf1. Portions of this figure are adapted from [266].

Table 1. Genetic adaptations that confer 2DG resistance in haploid and diploid yeast cells.

Dominant alleles are capitalized and recessive alleles are lowercase. Italicized triangles represent gene deletions that confer 2DG resistance.

	Genetic Adaptation	
Cellular Function or Complex	**Haploid**	**Diploid**
Hexokinase	*hxk2-G55V, hxk2-G418C, hxk2-D417G, hxk2-G238V, hxk2-R423T, hxk2-T212P, hxk2-Q299H, hxk2-K176T, hxk2-T75I/S345P, hxk2*Δ	-
DOG phosphatases	Chromosome 8 disomy	Chromosome 8 trisomy and tetrasomy
PP1 phosphatase	*glc7-Q48K, reg1-P231L, reg1*Δ	*REG1-Q332Stop, REG1-Y638Stop*, Chromosome 4 monosomy
AMPK/Snf1	*SNF1-G53R*	*SNF4-N177Y, GAL83-S224R*
Glucose Transporters	*hxt1-17*Δ	Duplication of HXT genes on Chromosome 4
Glucose Transporter endocytic adapters (α-arrestins)	*rod1*Δ, *rog3*Δ	-

1.3.5.1 Hexose transporters

2DG must be taken up by the cell through glucose transporters before it can be converted to 2DG6P. Indeed, deletion of all 17 yeast hexose transporters (*hxt1-17*Δ) results in resistance to 2DG and substitution of *HXT7* to this genetic background restores sensitivity [316,349]. However, retention of glucose transporters at the cell surface helps induces cellular resistant to 2DG when grown in the presence of glucose, which at first seems somewhat paradoxical given that this is the mechanism by which 2DG enters cells [224,272,316]. This likely reflects the cell reaching a crossroads where it needs to continue taking up glucose for normal metabolism to proceed, but the presence of glucose transporters allows 2DG to continue entering the cell, where it has toxic effects on downstream metabolic pathways. In one of our recent genetic screens, we showed that all but one 2DG resistant mutant increased retention of glucose transporters at the plasma membrane,

highlighting the importance of retaining the ability to internalize glucose to mitigate 2DG toxicity [224].

1.3.5.2 2DG phosphorylation and dephosphorylation

Once internalized through glucose transporters, 2DG is phosphorylated and converted to 2DG6P by hexokinase. In our and others' genetic screens looking for mutations that confer 2DG resistance, many loss-of-function mutations in the yeast *HXK2* gene were isolated [224,227,287]. Deletion of the *HXK2* gene also results in 2DG resistance [224,227,245,287]. This would suggest that one route to evading 2DG toxicity is by simply diminishing its phosphorylation. Interestingly, only mutations in Hxk2 have been isolated, yet yeast express two other hexokinase isoforms (see section 1.2.3). This could be explained if Hxk2 were the only isozyme capable of phosphorylating 2DG however, enzymatic assays revealed that Hxk1 has a greater affinity and Vmax for 2DG [223,224]. When Hxk2 is absent, Hxk1 expression increases and so it should be able to compensate and phosphorylate 2DG [230]. Also, Glk1 mRNA and protein abundance increase in response to 2DG treatment and Glk1 expression in a hexokinase triple mutant strain promotes 2DG sensitivity when growing on glycerol medium [224,287]. It is currently not clear why the other hexokinase isozymes do not contribute to the 2DG resistance pathway. Hxk2 has many activities in the cell (e.g., acts as glucose sensor, has an undefined nuclear role, and alters Snf1 activation; see sections 1.2.3.1 and 1.2.3.3). Commonly, *HXK2* mutations that confer 2DG resistance promote phosphorylation and activation of Snf1 kinase, which is itself, beneficial in decreasing 2DG toxicity [224,245]. Whether any of these functions contributes to Hxk2-mediated resistance is unknown and warrants further study.

Accumulation of 2DG6P can be relieved by the action of two 2DG6P phosphatases, Dog1 and Dog2. Overexpression of either of the DOG genes confers resistance to 2DG [287,350]. Both

genes belong to a superfamily of phosphohydrolases named halo-acid dehalogenase (HAD) family. This family of enzymes is found in all living organisms, and they mostly act on small compounds with specificity toward single substrates or can be broader [351]. Multiple stress response pathways induce expression of the DOG phosphatases including the Hog1 pathway, Snf1 pathway, the UPR pathway, and the cell wall integrity pathway [224,287]. Overexpression of a human HAD phosphatase in HeLa cells also increases their resistance to 2DG treatment [287]. Thus, preventing phosphorylation of 2DG can partially mitigate its toxic effects.

A recent genetic screen was performed to understand how diploid yeast gain resistance to 2DG [307]. It was revealed that diploid yeast can also obtain resistance to 2DG by inhibiting its conversion to 2DG6P [307]. This mechanism was exploited by overexpression of the DOG phosphatases resulting from aneuploidy specifically through trisomies and tetrasomies of chromosome 8 where the *DOG1* and *DOG2* genes are located [307]. Hxk2 mutations were not isolated from this screen, suggesting that dampening its activity is not sufficient to promote resistance in diploids [307].

1.3.5.3 AMPK signaling

2DG treatment elicits metabolic stress and impairs normal glucose metabolism [266]. The resulting reduced energy status activates the yeast AMPK, Snf1 [224,245,272]. In yeast, Snf1 has emerged as the key player in dictating sensitivity to 2DG treatment and its activation makes cells strongly resistant [224,245,287,316]. Indeed, cells lacking Snf1 are hypersensitive to 2DG [224,316]. In contrast, Snf1 hyperactivation through gain of function mutations in the *SNF1* gene, loss of function mutations in either the Glc7 or Reg1 subunits of the PP1 phosphatase complex (negative regulators of Snf1), and loss-of-function mutations in Hxk2 (decreasing glycolytic flux and activating Snf1), makes cells resistant to 2DG [40,224,287,307]. Snf1 is also hyperactivated

in resistant diploid yeast by dominant mutations in the Snf1/AMPK β and γ subunits, Snf1 and Gal83, respectively [307]. Second, dominant, nonsense mutations of the *REG1* gene confer 2DG resistance through haploinsufficiency [307]. Snf1-mediated resistance to 2DG occurs, in part, through its regulation of transcription and its control of α-arrestin-mediated turnover of glucose transporters [224,316,349]. Each of these mechanisms is discussed in detail below.

One mechanism of Snf1-mediated resistance is its regulation of the Mig1 transcription repressor and glucose-repressed gene expression. When Snf1 becomes active and phosphorylates Mig1, this transcriptional repressor is exported from the nucleus, lifting of glucose repression [50,54]. This leads to increased expression of a suite of genes [352]. Despite causing metabolic stress, 2DG treatment does not result in Snf1-dependent phosphorylation of Mig1, but it does induce Mig1 translocation out of the nucleus ([245,272] and Mitch Lesko unpublished observations). Nevertheless, the abundance of Mig1 decreases and a suite of Mig1-regulated genes is altered [224,245,349]. Interestingly, this includes increased expression of the *DOG* phosphatase genes, suggesting their contribution to the observed resistance [224,287]. This may suggest that resistant cells release glucose repression to promote alternative metabolic pathways. In addition to Mig1-regulated changes in gene expression, detailed analysis of 2DG-responsive transcriptome identified several other possible transcriptional regulators that may additionally contribute to 2DG resistance, which are further being explored in the O'Donnell lab.

Snf1 targets multiple downstream transcription regulators [29] and likely influences 2DG-responsive transcription through other factors in addition to Mig1. Indeed, Carbon source stress, either through glucose starvation or 2DG, elicits global-scale changes in the yeast transcriptome [224,353]. RNA sequencing experiments of wild-type yeast cells exposed to either of these conditions revealed that almost one-third of the yeast transcriptome (~2000 genes) exhibits at least

a 2-fold change in expression [224]. A striking transcriptional change in these cells was a ~10-fold reduction in the abundance of ribosomal protein mRNAs [224]. This may be reflective of a decreased growth rate in response to nutrient starvation and 2DG. In contrast, 2DG resistant cells showed a muted transcriptional change and the reduction of ribosomal protein mRNAs was significantly dampened [224]. In response to 2DG treatment, wild-type cells decreased the expression of hexose transporter genes as well as their abundance at the PM. 2DG-resistant cells did not show as dramatic a change in HXT gene expression [224]. Overall, this study showed that resistant cells have a more muted response to 2DG and perhaps evade toxicity by not overreacting to accumulating 2DG6P. On the other hand, wild-type cells demonstrate an exaggerated response by altering transcription in a way that reduces fermentation of glucose and increases starvation.

Another key mechanism of Snf1-mediated resistance is its regulation of glucose transporter endocytosis. Work from the Schmidt and O'Donnell labs revealed that 2DG treatment induces the endocytosis of glucose transporters, namely Hxt1 and Hxt3 [224,316]. 2DG-induced glucose transporter endocytosis requires two proteins of the α-arrestin family, namely Rod1 and Rog3, which are phosphorylated by Snf1 [316]. In cells lacking Snf1, cells are hypersensitive to 2DG, and the glucose transporters are endocytosed and degraded in the vacuole, leaving cells with a reduced capacity to take up glucose [316]. Overexpression of glucose transporters Hxt1 and Hxt3 suppresses the 2DG-sensitivity of *snf1*Δ cells [316]. The 2DG-induced endocytosis of Hxts is regulated by α-arrestins; deletion of Rod1 and Rog3 prevents internalization of the glucose transporters, confers 2DG resistance, and restores 2DG resistance of *snf1*Δ cells back to wild-type levels [224,272,316]. Thus, a primary role of Snf1 upon 2DG addition is to negatively regulate Rod1 and Rog3-dependent endocytosis of glucose transporters. In the absence of Snf1, Rod1 and Rog3 execute unregulated endocytosis of glucose transporters, leading to starvation of these cells

for glucose [316]. In terms of 2DG resistance mechanisms, hyperactive Snf1 prevents the endocytosis of glucose transporters and allows the internalization of glucose to promote normal metabolism [224]. In support of this, 2DG resistance-conferring mutations in *HXK2*, *REG1*, *GLC7*, and *SNF1* genes that promoted hyperactivity in Snf1 increased PM retention of the Hxt3 transporter [224]. Consistent with an important role in 2DG resistance, overexpression of glucose transporters (*HXT3*, *HXT6*, and *HXT7*) through chromosomal duplication helps diploid yeast become 2DG resistant [307]. From these studies it was proposed that 2DG stimulates α-arrestin-mediated endocytosis of glucose transporters, causing decreased glucose uptake and starvation even when glucose is abundant.

Though each of these mechanisms participates in Snf1-mediated resistance to 2DG, another unidentified Snf1-regulated pathway may also be contributing. A dominant allele of *SNF1* can promote 2DG resistance in cells lacking the *ROD1, ROG3, DOG1, DOG2,* and *HXK2* genes [224]. Therefore, the Snf1 signaling pathway must have a wider range of targets in response to 2DG that warrants further study.

1.3.6 Cellular resistance to 2DG in mammalian cells

The mechanisms of 2DG resistance in cancer cells are not completely understood, but some similarities to resistant yeast cells can be drawn. For example, in 1962, S. Barban isolated a 2DG-resistant HeLa cell line after prolonged exposure to the drug [354]. Notably, these cells had reduced hexokinase activity toward glucose and 2DG, with diminished cellular accumulation of 2DG6P [354]. These cells showed increased usage of pyruvate for growth and grew more slowly than the parental strain [354]. This indicates the isolated strain had greater dependence on respiration than glycolysis. Though specific mutations were not defined in these cells, these data

hint at the presence of loss-of-function mutations in hexokinase. Such mutations are routinely observed in 2DG-resistant yeast cells. In a separate study, a pig kidney cell line was isolated, which displayed a decreased rate of 2DG phosphorylation [355].

Countering hexokinase activity, a 2DG6P phosphatase is an important part of the 2DG resistance mechanisms in yeast. The same 2DG-resistant HeLa cells isolated by S. Barban, also demonstrated increased phosphatase activity which reacted with 2DG6P [354]. However, the phosphatase has never been identified from these studies. Recently, overexpression of a human HAD-like phosphatase (homolog of the yeast DOG phosphatases), HDHD1, in a HeLa cell line conferred resistance to 2DG [287]. Whether this phosphatase is responsible for the observed resistance in the earlier studies is unknown. Alkaline phosphatase treatment has been correlated with 2DG resistance in multiple cell lines [356,357]. Therefore, it seems that detoxification of 2DG6P by dephosphorylation could also be an important resistance mechanism in mammalian cells. Other mechanisms may be at play in mammalian cells. It has been shown that in hypoxic conditions, where 2DG toxicity should be greatest since respiration cannot be used, increases in glycolytic enzymes through a HIF1-dependent manner may prevent 2DG toxicity [358]. Also, 2DG activates pro-survival pathways in several cancer cell lines and this may also provide a way for cancer cells to avoid toxicity [327].

1.4 Goals and Discoveries

The goals of my dissertation project are two-fold. First, I investigate the regulatory mechanisms surrounding Hxk2 nuclear localization in response to carbon-source stress and propose potential roles of this subcellular localization change. Second, I investigate the

mechanisms of 2DG-resistance conferred by loss-of-function mutations in Hxk2. Here, we present evidence that Hxk2 translocates to the nucleus when the enzyme becomes unstable and discuss possible reasons. Finally, using quantitative fluorescent microscopy, we refute a long-standing model describing the regulatory mechanisms and function surround Hxk2 nuclear localization. We show that Hxk2 translocates to the nucleus in response to glucose starvation as consistently observed in mammalian cells. Cis- and trans-regulatory elements were identified that impact Hxk2 nuclear shuttling. Among these, Tda1 was identified as being indispensable for starvation-induced Hxk2 nuclear accumulation. Also, a lysine residue in the Hxk2 N-terminal tail was shown to be required for glucose-induced nuclear exclusion of Hxk2. We present the first atomic-resolution model using molecular dynamics (MD) simulations to describe how Hxk2 mutations confer 2DG resistance. 2DG resistance was evolved in yeast cells followed by identification of a novel resistance-conferring mutation in Hxk2, $Hxk2^{G238V}$, that does not line the enzymatic pocket or diminish protein stability. We present evidence that this mutation diminishes Hxk2 enzymatic activity by impacting dynamics of the catalytic cleft and large-scale conformational changes required for substrate binding. Next, we perform the first, comprehensive study to understand the causal relationship of all Hxk2 mutations and 2DG resistance. Most isolated mutants were shown to confer 2DG resistance when expressed as the only *HXK2* allele. We find that a subset of Hxk2 mutants, altering substrate binding residues, impact nuclear localization. One mutation, $Hxk2^{G55V}$, does not impact a substrate binding residue and lies far from the enzymatic cleft. Still, it promotes Hxk2 nuclear shuttling regardless of available glucose. We show that $Hxk2^{G55V}$ may encode an unstable enzyme. Using MD simulations, we show that $Hxk2^{G55V}$ impacts the stability and dynamics of a key “hinge-point” and affects enzyme conformational changes. This work opens the

door for future studies addressing the functional role of Hxk2 nuclear localization and highlights the contributions of hexokinase mutations to 2DG resistance.

2.0 Changing course: Glucose starvation drives nuclear accumulation of Hexokinase 2 in *S. cerevisiae*

Lesko MA, Chandrashekarappa DG, Jordahl EM, Oppenheimer KG, Bowman RW II, Shang C, Durrant JD, Schmidt MC, O'Donnell AF (2023) Changing course: Glucose starvation drives nuclear accumulation of Hexokinase 2 in *S. cerevisiae*. PLoS Genetics 19(5): e1010745. https://doi.org/10.1371/journal.pgen.1010745

Specific author contributions include:

- Lesko MA: Figures 10A-D, 11A-F, 12A-D, 13B-F, 14A-D, 15A-B, 19A-D, 20B-D, 21A-G, 22C-F, 23A-C, 24A-C, 25A-F, 27A-E, 28A-C, 29A-C, 32, Tables 3 & 4, writing, review & editing
- Chandrashekarappa DG: Figures 10E, 11G, 13A, 14E-F, 17B-G, 19E-F, 22G-H, 24D, 26, 27F, 30, 31
- Jordahl EM: Plasmid construction, review & editing
- Oppenheimer KG: Plasmid construction, review & editing
- Bowman RW: Guidance with NIS.*ai* quantification, review & editing
- Shang C: Guidance with FRAP experiments, review & editing
- Durrant JD: Figures 14G, 16, Table 2, 17A, 18A-F, 20A, 22A-B, writing, review & editing, project administration, resources, supervision
- Schmidt MC: Figures 30, 31, writing, review & editing, project administration, resources, supervision

- O’Donnell AF: writing, review & editing, project administration, resources, supervision

2.1 Introduction

The functional complexity of proteomes is extended by “moonlighting” proteins, a term describing proteins with “other jobs” in the cell [359]. Enzymes with roles in signal transduction, independent of their catalytic activities, are good examples. For instance, cytochrome c is part of the mitochondrial electron transport chain. However, when released from the mitochondria, cytochrome c becomes a messenger of apoptotic signaling [360]. Glycolytic enzymes in many species have moonlighting functions distinct from their catalytic potential [361]. We examine the yeast hexokinase 2 (Hxk2), the enzyme that catalyzes the first step of glycolysis. Like other glycolytic enzymes, Hxk2 can translocate to the nucleus, suggesting that it may carry out a ‘moonlighting’ nuclear function distinct from its glycolytic role. Here we assess Hxk2 nuclear translocation and its potential nuclear function as a transcription regulator.

The budding yeast Saccharomyces cerevisiae express three enzymes capable of phosphorylating glucose, any one of which can support growth on glucose [224]. Two of these enzymes, Hxk1 and Hxk2, are hexokinases with broad substrate specificity, including glucose and fructose [362]. The third enzyme, Glk1, is a glucokinase, named for its glucose specificity. Hxk1 and Hxk2 are closely related paralogs with 77% identity and 89% similarity in their amino acid sequences. Glk1 is less closely related to the hexokinases (37% identity and 53% similarity) but has a paralog, Emi2, whose function is uncertain. Recombinant Emi2 has detectable glucose

phosphorylating activity [226] but the presence of Emi2 is not sufficient to confer growth on glucose in *hxk1*Δ *hxk2*Δ *glk1*Δ cells, suggesting it may not function as a hexokinase *in vivo* [224].

Hxk2 is proposed to have a moonlighting function in the nucleus regulating gene expression [230,237,238,254,257–261,363]. The current model for Hxk2, proposed by the Moreno lab, states that Hxk2 translocates to the nucleus in glucose-rich conditions [261] in a manner dependent upon (1) binding to Mig1, a transcriptional repressor [236], (2) a nuclear localization signal (NLS) in the N-terminus of Hxk2 between lysine 6 and lysine 13 [260], and (3) dephosphorylation of Hxk2 at serine 15 [254]. Nuclear Hxk2 is proposed to be one subunit of a transcriptional repressor complex that includes the DNA binding proteins Mig1 and Mig2; the Tup1 repressor; Med8, a subunit of the Mediator complex; Reg1, a regulatory subunit of the PP1 phosphatase; and the nuclear isoform of yeast AMP-activated protein kinase (AMPK) composed of the Snf1, Snf4, and Gal83 proteins. In this model, this large complex is needed for glucose repression of gene expression [238].

While the studies that support this model are cited collectively >1000 times [29,62,225,266,364,365], there has been no independent corroboration for the model, and aspects have been questioned in published commentaries [264]. The idea that yeast Hxk2 is excluded from the nucleus in glucose-starvation conditions and found in the nucleus in glucose-replete conditions is counter to many models of hexokinase/glucokinase regulation in other organisms [64,95,213,366]. Mammalian hexokinase isoforms II and III and glucokinase (aka hexokinase IV) can each be nuclear [64,67,213]. Most data suggest that these enzymes are nuclear in response to glucose limitation or stress, which is the opposite of what has been reported for yeast Hxk2 [64,67,213].

Unfortunately, entwined with the model of Hxk2 nuclear-cytosolic shuttling is the idea that Hxk2's oligomeric state regulates nuclear partitioning. Rigorous *in vivo* biochemical analyses demonstrate that in glucose-grown cells, a balance of monomeric and dimeric Hxk2 exists [247]. In glucose-starved cells, Hxk2 is predominantly monomeric [247,251–253,367]. A key regulator of Hxk2 dimerization is serine 15, which is phosphorylated in glucose-starvation conditions to disrupt the dimer [247,251–253,367]. The Tda1 kinase is required for serine 15 phosphorylation, while Snf1 plays only a minor role [247]. In cells lacking Tda1, Hxk2 remains a dimer in both glucose replete and restricted conditions [247], suggesting that Tda1 controls Hxk2 monomer-dimer balance. Unlike the clear link between serine 15 phosphorylation and Hxk2 monomer-dimer balance, the proposition that serine 15 regulates Hxk2 nuclear translocation is poorly supported [264].

We use high-resolution quantitative fluorescent imaging, biochemical and genetic methods to study the nuclear localization, dimerization, and function of Hxk2. Our data contradict all aspects of the current Hxk2 nuclear localization model. We demonstrate that Hxk2 is excluded from the nucleus in glucose-replete conditions, the very time when it is proposed to operate in a glucose repression transcriptional complex. We find that yeast Hxk2 enters the nucleus, but only in glucose starvation conditions, which is in line with the starvation and stress induced nuclear translocation of mammalian hexokinases [64,213]. Our imaging studies differ from earlier work, [236,254,259,260] in that we maintain the appropriate glucose supply throughout live-cell imaging, ensuring representation of the cellular response in these conditions.

We further define cis and trans regulatory elements that control the starvation-induced nuclear accumulation of Hxk2. We identify Hxk2 lysine 13 as required for the glucose-regulated nuclear exclusion of Hxk2 and dimerization. In contrast to earlier studies, mutation of serine 15

did not alter glucose-regulated nuclear accumulation of Hxk2. In keeping with Kriegel lab studies, serine 15 mutants of Hxk2 altered the monomer-dimer balance in cells [251–253,367]. Thus, Hxk2 glucose-regulated nuclear translocation and dimerization can be uncoupled. The Tda1 kinase, and not Snf1 or Mig1, was needed for Hxk2 nuclear translocation in response to glucose starvation.

Finally, our RNAseq analyses showed that the expression of the most highly glucose-repressed genes was not affected by loss of the *HXK2* gene. Taken together, our data refute the idea that Hxk2 moonlights as a transcriptional repressor important for glucose repression. The function of nuclear Hxk2 in glucose-starved cells remains to be defined.

2.2 Results

2.2.1 Hxk2 nuclear shuttling

We examined the impact of glucose abundance on the nuclear propensity of the three hexokinases in S. cerevisiae: Hxk1, Hxk2, and Glk1. Earlier studies suggested that Hxk2 from *S. cerevisiae* and *C. albicans* is nuclear excluded in glucose starvation and partially nuclear localized in abundant glucose [236,254,259,260,368]. However, in these earlier studies, cells were incubated in glucose-free medium before imaging (glycerol-containing medium or PBS in the *S. cerevisiae* or *C. albicans* experiments, respectively), perhaps to allow for DAPI nuclear staining [236,254,259,260,368]. We generated functional GFP-tagged, plasmid-borne versions of these hexokinases and expressed them in cells lacking their respective endogenous genes. To examine the localization of these hexokinase-GFP fusions in glucose-replete conditions (2% glucose, “high” glucose) and after acute glucose starvation (0.05% glucose, “low” glucose), we used live-

cell confocal microscopy and a mScarlet-tagged nuclear marker to quantify nuclear co-localization. In contrast to past qualitative Hxk2 studies [236,254,259,260,368], Hxk2 was largely cytosolic in glucose-grown cells, and a portion of Hxk2 became nuclear upon glucose starvation (Figure 10A).

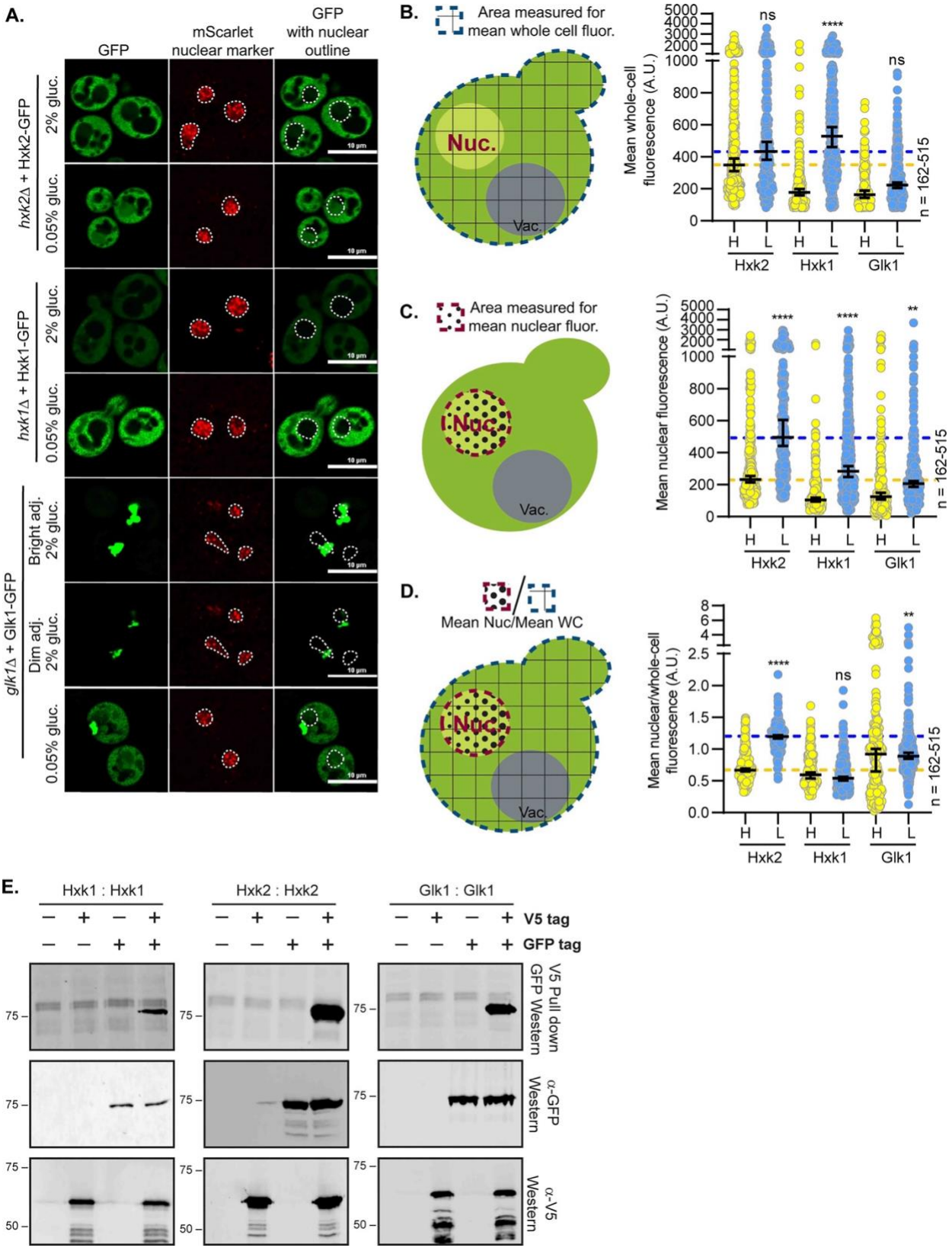

Figure 10. Hexokinases alter localization in response to glucose starvation and can form multimers.

(A) Confocal microscopy of GFP-tagged yeast hexokinases expressed from CEN plasmids under the control of their endogenous promoters. Each hexokinase is expressed in cells where the endogenous gene has been deleted. Co-localization with the nucleus is determined based on overlap with the Tpa1-mScarlet nuclear marker, and a dashed white line indicates the nucleus. (B-D) Automated quantification (using Nikon.*ai* and GA3 analyses) of the images shown in panel A where (B) shows the mean whole-cell fluorescence intensities, (C) shows the mean nuclear fluorescence, (D) shows the mean nuclear fluorescence over the whole-cell fluorescence for each hexokinase as XY-scatter plots. The regions measured for each of these analyses are shown to the left of each graph with (B and D) the area for whole-cell measurement shown as a blue-dashed line filled with grid lines and (C-D) the area for the nuclear measurement shown as a red-dashed line filled with black dots. Horizontal bars show the median, and error bars indicate the 95% confidence interval. Dashed yellow and blue lines represent the median value for Hxk2-GFP cells in high and low glucose, respectively. Kruskal–Wallis statistical analysis with Dunn's post hoc test was performed to compare the (B) mean whole-cell fluorescence, (C) mean nuclear fluorescence, or (D) mean nuclear/whole-cell fluorescence ratio between high and low glucose medium conditions for each hexokinase. (E) To assess multimerization, we prepared extracts from yeast cells grown in 2% glucose and expressing the indicated hexokinase proteins either untagged (-) or tagged (+) with V5 or GFP. Protein inputs were monitored by immunoblotting (bottom two panels). Association of tagged proteins was assessed by co-immunoprecipitation using anti-V5 beads followed by immunoblotting with anti-GFP (top panel).

We next quantified for each hexokinase: (1) the mean whole-cell fluorescence, (2) mean nuclear fluorescence, and (3) the mean nuclear to mean whole-cell fluorescence ratio to assess the relative contribution of the nuclear signal to that of total cellular fluorescence (Figure 10B–10D). This last measure is essential as it accounts for changes in gene expression or protein abundance/stability that accompany nutrient changes, as is evident for Hxk1 and Glk1 (Figure 10A–10D). In addition, higher whole-cell fluorescence can increase fluorescence in the nuclear compartment because background fluorescence increases. The ratio of the nuclear to whole cell fluorescence is thus the most useful measure to assess nuclear distribution. Manual and automated

image analyses were performed in four biological replicate experiments. Data from manual and automated quantification were consistent, validating the automated quantification pipeline (Figure 10C-D, 11A-B). In response to glucose starvation, the mean nuclear fluorescence of Hxk2-GFP increased 3-fold, and the ratio of nuclear-to-whole-cell Hxk2-GFP fluorescence more than doubled, demonstrating a shift in Hxk2 to the nucleus upon glucose restriction. We also observed a glucose-starvation-induced increase in nuclear fluorescence with chromosomally-integrated, mNeonGreen-tagged Hxk2 (Figure 11C-E).

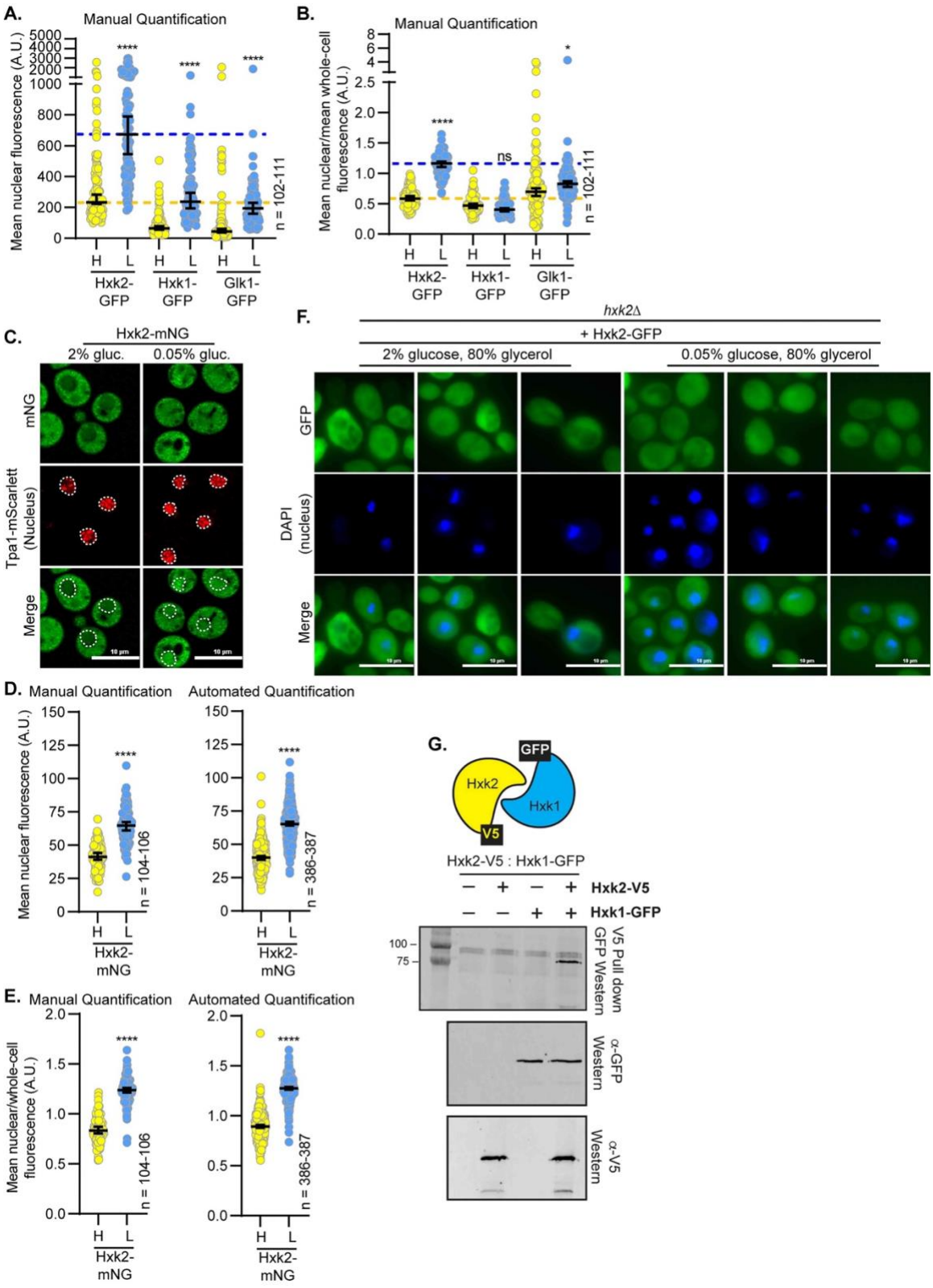

Figure 11. mNG-tagged Hxk2 localizes to the nucleus in response to glucose starvation, and pre-incubation of cells in glycerol before imaging makes interpretations of localization difficult.

(A-B) Manual quantification (using Image J) of the imaging data shown in Figure 10A and comparable to the automated approach used in Figure 10C–10D, to measure (A) mean nuclear fluorescence or (B) the ratio of the mean nuclear/whole-cell fluorescence. Horizontal black lines show the median, and error bars indicate the 95% confidence interval. Dashed yellow and blue lines represent the median value for Hxk2-GFP in high glucose and low glucose, respectively. Black asterisks represent statistical comparisons between low and high glucose for Hxk2-GFP. (C) Confocal microscopy of mNeonGreen-tagged Hxk2 expressed as a chromosomal integration. Co-localization with the nucleus is determined based on overlap with the Tpa1-mScarlet nuclear marker, and a dashed white line indicates the nucleus. (D-E) Manual quantification (using Image J) or automated quantification (using Nikon.*ai* and GA3) of the images shown in panel C to measure (D) mean nuclear fluorescence or (E) the ratio of the mean nuclear/whole-cell fluorescence. Horizontal black lines show the median, and error bars indicate the 95% confidence interval. Dashed yellow and blue lines represent the median value for Hxk2-mNG in high glucose and low glucose, respectively. Black asterisks represent statistical comparisons between low and high glucose for Hxk2-mNG. (F) Confocal microscopy of GFP-tagged Hxk2 expressed from a CEN plasmid under the control of the *HXK2* promoter in cells lacking *HXK2* alone. For this experiment, cells were grown in glucose (2% glucose) or shifted into 0.05% glucose (low glucose) for 2 h, but before imaging, these cells were incubated in 80% glycerol with DAPI to recreate the imaging conditions from earlier studies [9–13]. (G) To assess multimerization, we prepared extracts from yeast cells expressing the indicated hexokinase proteins either untagged (-) or tagged (+) with V5 or GFP. Protein inputs were monitored by immunoblotting (bottom two panels). The association of the tagged proteins was assessed by co-immunoprecipitation using anti-V5 beads followed by immunoblotting with anti-GFP (top panel).

These data run counter to earlier findings that suggested Hxk2-GFP was retained in the nucleus in glucose-grown cells and excluded from the nucleus upon glucose starvation [236,254,259,260,368]. Three factors may account for this discrepancy. First, earlier studies incubated cells in glycerol or PBS (i.e., lacking glucose) before imaging [236,254,259,260,368]. This pre-incubation could provoke the glucose starvation-induced nuclear translocation we observed. When we imaged S. cerevisiae after incubation in 80% glycerol, we found nuclear accumulations of Hxk2-GFP regardless of the medium in which cells were pre-grown (Figure

11F). Second, high-copy plasmids were used to express Hxk2-GFP in the earlier studies, so this overexpression might have made localization changes difficult to interpret. Third, our studies differ from earlier studies due to improvements in microscopy and the lack of quantification of earlier datasets [236,254,259,260,368].

2.2.2 Hxk1 and Glk1 nuclear shuttling

In contrast to Hxk2, we saw no nuclear accumulation of Hxk1 in glucose-grown or -starved cells (Figure 10A). Hxk1 transcription is upregulated upon glucose starvation, resulting in an ~2.5-fold change in Hxk1 whole-cell fluorescence (Figure 10B). Considering only mean nuclear fluorescence, Hxk1 appears to undergo modest nuclear accumulation in glucose starvation, likely due to increased total Hxk1-GFP expression (Figure 10C). When data were normalized to account for protein abundance changes using the ratio of mean nuclear to mean whole-cell fluorescence, we saw no change in the relative distribution of Hxk1 upon glucose restriction (Figure 10C-D). The abundance of Hxk1 was lower than that of Hxk2 in glucose-replete conditions, but in glucose starvation, Hxk1 levels rose higher than those of Hxk2 (Figure 10B). If there was a significant accumulation of Hxk1 in the nucleus, we should have been able to detect it in the glucose starvation conditions, and we did not (Figure 10A-C).

Consistent with recent reports [94], Glk1 formed cytosolic inclusions in high glucose (Figure 10A). These inclusions were diminished in low-glucose conditions, where Glk1 may be mobilized to help phosphorylate glucose [94]. Our Glk1 quantitative analyses were somewhat confounded by the large cytosolic inclusions often present near the nuclear marker; some cytosolic fluorescent signal was captured in the nucleus due to this overlap. Glk1 is transcriptionally upregulated in response to glucose starvation, causing a modest increase in its whole-cell

fluorescence intensity (Figure 10B) [229]. As with Hxk1, changes in mean nuclear fluorescence suggested Glk1 may modestly accumulate in the nucleus in glucose starvation, but when normalized to whole-cell-fluorescence intensity, we observed no change in the relative distribution of Glk1 upon glucose restriction (Figure 10C-D). These findings suggest that while Hxk2 undergoes a glucose starvation-induced nuclear translocation, Hxk1 and Glk1 do not.

2.2.3 Hexokinase multimerization

Hxk2 nuclear localization could be linked to its transition from a dimer to a monomer. In cells grown in glucose-replete conditions, Hxk2 exists in a balance between dimeric and monomeric species [247,251]. Upon glucose starvation of cells, this balance shifts toward the monomeric state [247,251]. Hxk2 phosphorylation at S15 by the Tda1 kinase is vital for the transition to the monomer [247]. The Moreno lab suggested that Hxk2 is both nuclear and cytosolic in rich glucose conditions, but in response to glucose starvation, Hxk2 reportedly becomes nuclear excluded [236,254,259,260]. Further, this same lab showed that the phosphomimetic S15D mutation produced a nuclear-excluded Hxk2. Since S15D also gives rise to monomeric Hxk2, they argued that monomeric Hxk2 might be nuclear excluded [254], an idea contested in the literature [264].

Given the uncertainty of the relationship between Hxk2 monomer-dimer regulation and nuclear propensity, we assessed *in vivo* Hxk2 multimerization, as well as multimerization of Hxk1 and Glk1. We performed co-purification assays from yeast cells expressing differentially tagged forms of either Hxk1, Hxk2, or Glk1. In all cases, the V5-purified versions co-purified with the GFP-tagged Hxk2, providing evidence for *in vivo* interaction (i.e., the formation of a dimer or higher-order multimer) (Figure 10E). We found evidence for heterodimer or multimer formation

between Hxk1 and Hxk2 (Figure 11G), which co-purify in high-content yeast studies [37]. Given that all three hexokinases can multimerize, yet Hxk1 and Glk1 do not undergo nuclear translocation, multimerization is unlikely to explain the differences in their nuclear propensities.

2.2.4 Dynamics of Hxk2 nuclear partitioning in response to glucose starvation

To ensure that Hxk2-GFP was functional, we assessed the ability of Hxk2-GFP and an untagged Hxk2 to support growth on glucose when present in *hxk1*Δ *hxk2*Δ *glk1*Δ cells and found that either of these forms supported robust growth (Figure 13A). We examined Hxk2-GFP nuclear partitioning in response to glucose starvation by performing a time-course image analysis. In low glucose, we observed increased nuclear Hxk2-GFP within 15 minutes, with nuclear accumulation further increasing at 4 and 8 hours before declining at the 24-hour mark (Figure 12A-C, 13B-D). In prolonged starvation, nuclear accumulation of Hxk2-GFP diminished, likely due to increased protein degradation as evidenced by the accumulation of free-GFP that begins at 8 h post starvation and increases after 24 h of starvation (Figure 13B-E). Note that there is almost no free-GFP at early timepoints in glucose starved cells (1–4 h) (Figure 13E).

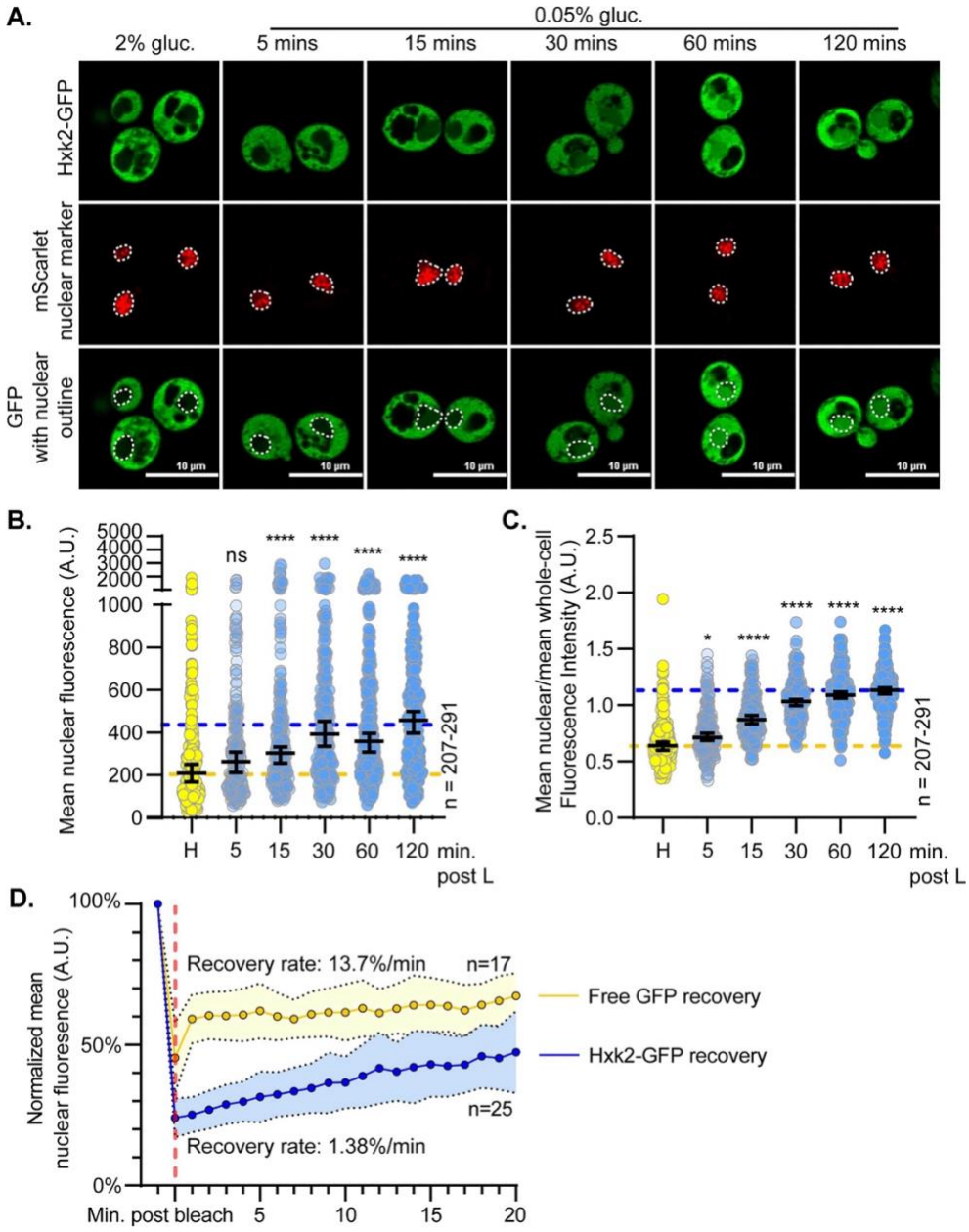

Figure 12. Hxk2 increases its nuclear propensity upon shift to glucose starvation conditions.

(A) Confocal microscopy of GFP-tagged Hxk2 expressed from a CEN plasmid under the control of its own promoter in *hxk2*Δ cells. Co-localization with the nucleus is determined based on overlap with the Tpa1-mScarlet nuclear marker, and a dashed white line indicates the nucleus. (B-C) Automated quantification of images shown in panel A to measure (B) mean nuclear fluorescence or (C) the ratio of the mean nuclear/whole-cell fluorescence. Horizontal black lines show the median, and error bars indicate the 95% confidence interval. Dashed yellow and blue lines represent the median value for Hxk2-GFP in high and low glucose, respectively. Kruskal-Wallis statistical analysis with Dunn's

post hoc test was performed to determine if the values obtained post low-glucose shift were statistically different from those obtained in high-glucose conditions. (D) Quantification of FRAP experiments done with cells expressing GFP-tagged Hxk2 from CEN plasmids under the control of its own promoter, and free GFP from CEN plasmids under the control of the TEF1 promoter. The post-bleaching recovery rate was calculated by measuring the slope of the linear portion of each graph. Blue and gold dots represent the percentage of nuclear fluorescence recovered for Hxk2-GFP and free GFP, respectively. The vertical, red dashed line represents the time point at which nuclear ROI bleaching occurred.

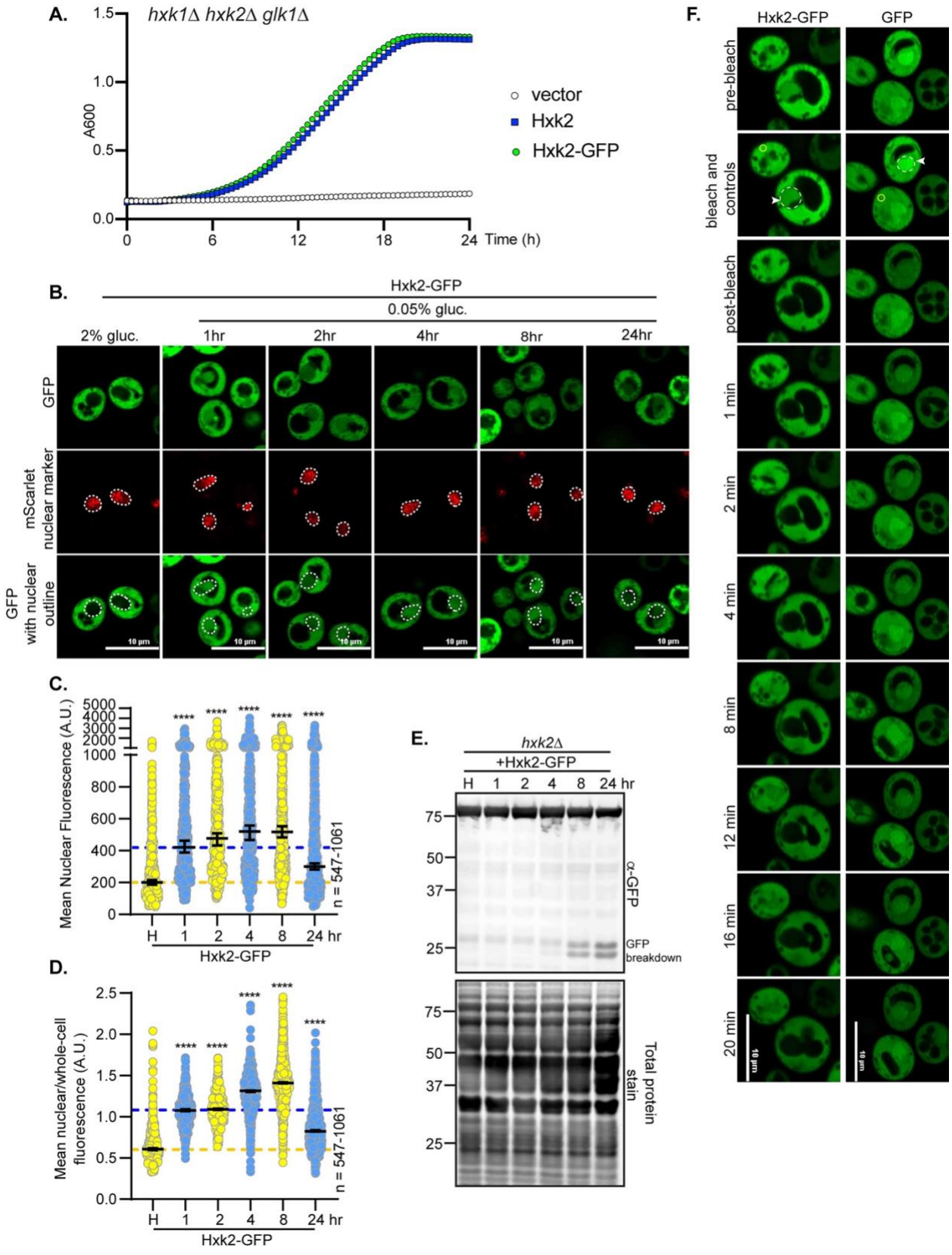

Figure 13. Assessing nuclear dynamics of Hxk2-GFP in response to glucose starvation.

(A) Cells lacking all three hexokinase genes (*hxk1*Δ *hxk2*Δ *glk1*Δ) were transformed with empty vector or plasmids expressing wild-type, untagged Hxk2, or Hxk2-GFP. Cell growth (A_{600}) in media containing glucose as the carbon source was monitored for 24 hours. (B) Confocal microscopy of GFP-tagged Hxk2 expressed from a CEN plasmid under the control of the *HXK2* promoter in cells lacking *HXK2*. Co-localization with the nucleus is determined based on overlap with the Tpa1-mScarlet nuclear marker, and a dashed white line indicates the nucleus. Cells were imaged at the indicated time points post-shift to glucose-depleted media for up to 24 hours. (C-D) Automated quantification of the images shown in panel B to measure (C) mean nuclear fluorescence or (D) the ratio of the mean nuclear/whole-cell fluorescence. Horizontal black lines show the median, and error bars indicate the 95% confidence interval. Dashed yellow and blue lines represent the median value for Hxk2-GFP in high and 1 hour in low glucose, respectively. Black asterisks represent statistical comparisons between high glucose and low glucose time points. (E) Immunoblot analyses of Hxk2-GFP in whole-cell protein extracts made from cells grown in high glucose or shifted to low glucose for the indicated times. (F) Still frames from FRAP time-lapse images, corresponding to quantified data in Figure 12D, showing pre- and post-bleached cells at selected time points. In the left-hand column, images from *hxk2*Δ cells expressing Hxk2-GFP from a CEN plasmid under the control of the endogenous *HXK2* promoter are shown. In the right-hand column, images from BY4742 cells expressing free GFP from CEN plasmids under the control of the TEF1 promoter are shown as a control for rapid nuclear recovery after photobleaching. White-dashed circles and arrowheads indicate the location of the nucleus. Yellow circles represent portions of the cytosol in an adjacent cell that was measured and used as a control for the rate of photobleaching due to repeated rounds of imaging over time.

To determine the exchange rate between nuclear and cytosolic Hxk2, we performed fluorescence recovery after photobleaching (FRAP). We bleached the nuclear Hxk2-GFP in glucose-starved cells and monitored recovery of nuclear signal. In the 20 min post-bleaching, there was modest recovery of nuclear signal (~15% of its initial Hxk2-GFP nuclear signal), suggesting a slow exchange between nuclear and cytosolic Hxk2 (Figure 13D, 13F). Nuclear Hxk2-GFP recovered only 1.4% of its fluorescence per minute (Figure 12D).

As a control, we monitored nuclear recovery in cells expressing free-GFP. Free-GFP transitioned between the nucleus and cytosol [369], recovering nuclear fluorescence at a rate of ~14%/minute and plateauing at 60% of original nuclear signal (Figure 12D and 13F). Unlike GFP, which freely diffuses into the nucleus, Hxk2-GFP has a slow, regulated nuclear translocation.

2.2.5 Modification of Hxk2 at serine 15 does not alter nuclear partitioning but does prevent dimerization

Hxk2 phosphorylation at S15 regulates the dimer-to-monomer transition [251–253]. This site is sometimes called S14 because proteolytic processing removes the Hxk2 N-terminal methionine [370]. Others have reported that in glucose-starvation, phosphorylation at S15 results in nuclear-excluded Hxk2 [254]. We found that Hxk2 with S15 mutated to alanine or the phospho-mimetic aspartic acid ($Hxk2^{S15A}$ and $Hxk2^{S15D}$, respectively) had equivalent nuclear fluorescence to wild-type Hxk2 in glucose-replete and -starvation conditions (Figure 14A-B). Regulation of $Hxk2^{S15A}$ and $Hxk2^{S15D}$ nuclear translocation appeared the same as wild-type Hxk2, occurring upon glucose restriction (Fig 14A-C). These results suggest that Hxk2 nuclear propensity does not depend on S15, contradicting earlier studies [254].

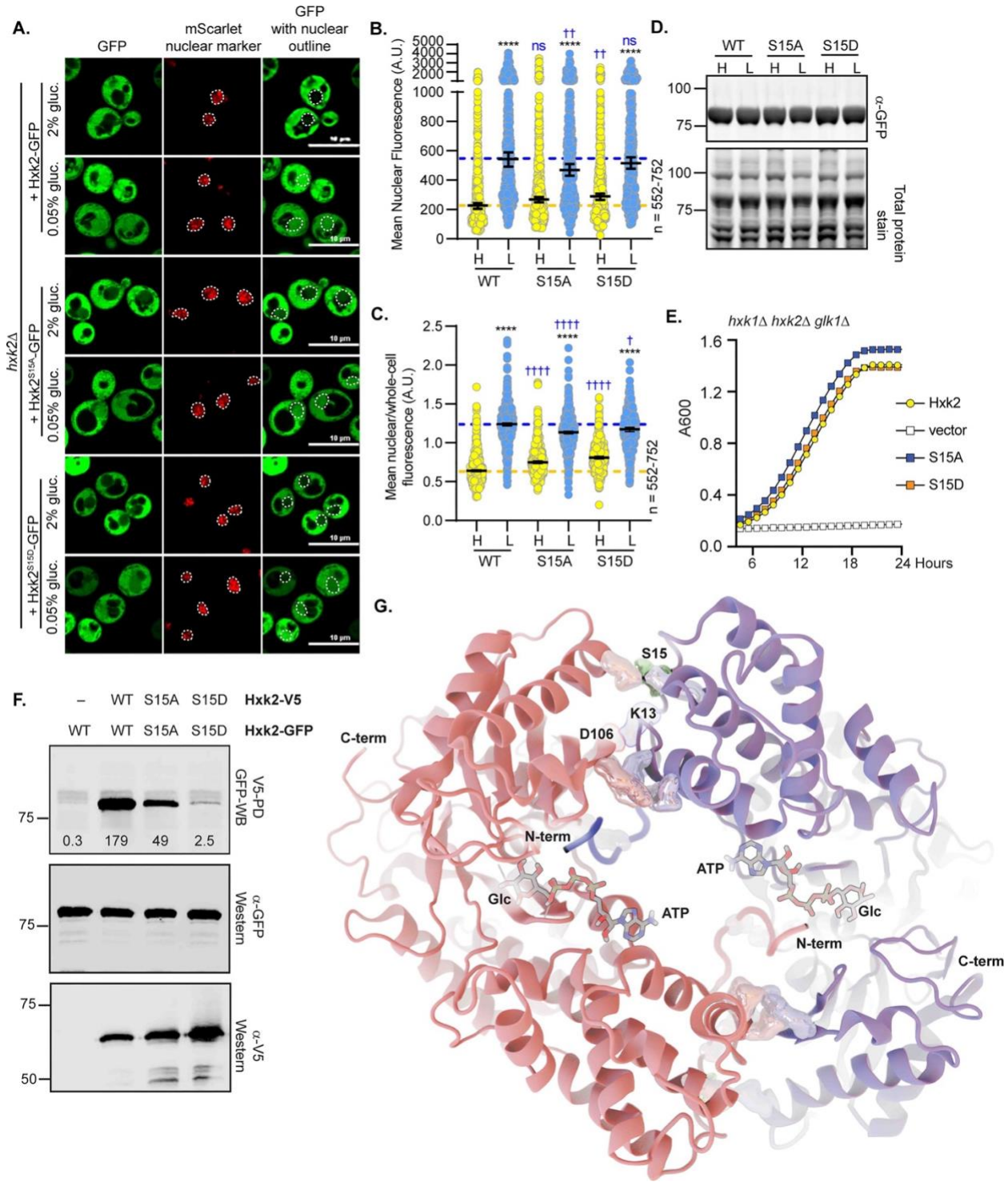

Figure 14. Mutation of Hxk2 at S15 does not alter the regulation of its nuclear translocation but does change its ability to form multimers.

(A) Confocal microscopy of GFP-tagged Hxk2 or mutant forms, expressed from a CEN plasmid under the control of the *HXK2* promoter in *hxk2*Δ cells. Co-localization with the nucleus is determined based on overlap with the Tpa1-

mScarlet nuclear marker, and a dashed white line indicates the nucleus. (B-C) Automated quantification of the images shown in panel A to measure (B) mean nuclear fluorescence or (C) the ratio of the mean nuclear/whole-cell fluorescence. Horizontal black lines show the median, and error bars indicate the 95% confidence interval. Dashed yellow and blue lines represent the median value for Hxk2-GFP in high and low glucose, respectively. Black asterisks represent statistical comparisons between low and high glucose for a specific *HXK2* allele, and blue daggers represent statistical comparisons between mutant alleles and the corresponding WT Hxk2 in the same medium condition. (D) Immunoblot analyses of Hxk2-GFP from whole cell protein extracts made from cells grown in high glucose or shifted to low glucose for 2 hours. REVERT total protein stain serves as a loading control. (E) Cells lacking all three hexokinase genes (*hxk1*Δ *hxk2*Δ *glk1*Δ) were transformed with empty vector or plasmids expressing wild-type Hxk2, $Hxk2^{S15A}$, or $Hxk2^{S15D}$. Cell growth (A_{600}) in media containing glucose as the carbon source was monitored for 24 hours. (F) Extracts were prepared from yeast cells expressing the Hxk2 tagged with either V5 or GFP. Hxk2 proteins contained wild-type (WT) S15 or the S15A or S15D mutations. Protein expression was monitored by immunoblotting (bottom two panels). The association of the tagged proteins was assessed by co-immunoprecipitation using anti-V5 beads followed by western blotting with anti-GFP (top panel). Quantitation of the signal in the top panel is shown. (G) The Hxk2-dimer model, with the two monomers shown as pink and blue ribbons, respectively. The glucose molecule and ATP molecules are shown as sticks. The N- and C-terminal tails are marked with "N-term" and "C-term," respectively. All residues predicted to participate in intermonomer electrostatic interactions are shown as pink and blue metallic surfaces per the associated monomer (see Table 1 for residue numbers). Residue S15 is shown as a metallic green surface.

We considered the possibility that the role of S15 in Hxk2 localization could be strain specific. Our studies used BY4741-derived yeast, related to the S288C background [371], but earlier studies used W303-derived yeast [236,254,259,260]. We repeated our experiments in W303-derived cells and observed similar Hxk2 nuclear regulation to what we found in BY4741 (Figure 15A-B). Based on these data, S15 does not alter Hxk2 nuclear regulation.

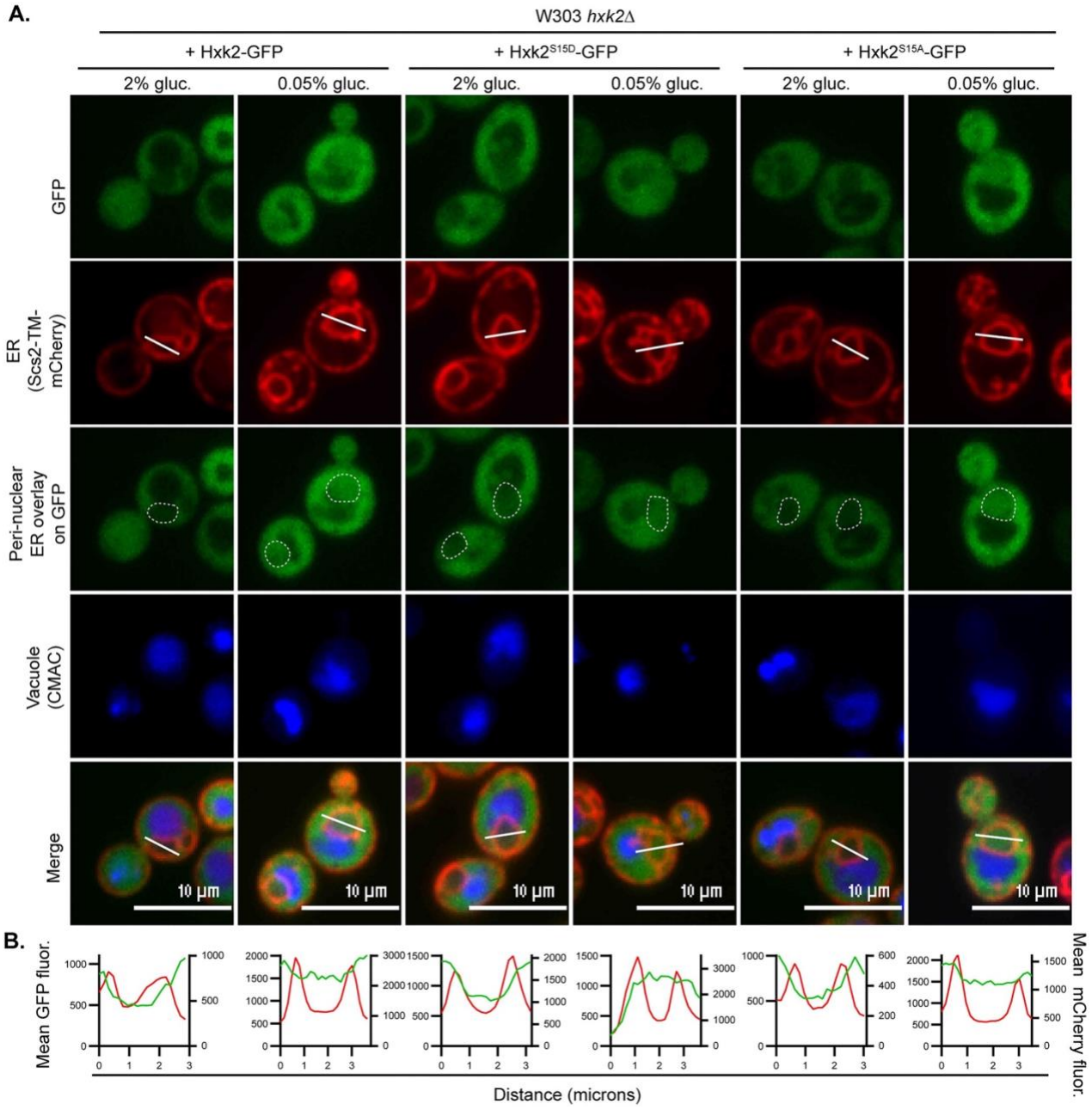

Figure 15. Hxk2 nuclear localization in response to glucose starvation is also observed in the W303 genetic background.

(A) Confocal microscopy of GFP-tagged Hxk2 or select mutant alleles expressed from a CEN plasmid under the control of the *HXK2* promoter in *hxk2*Δ cells derived from a W303 genetic background. Nuclear localization was determined based on the peri-nuclear ER localization of the mCherry-tagged Scs2-TM construct [14]. This marker was used to generate the white-dashed line that represents the peri-nuclear ER overlay in row 3. (B) A line scan of the region shown as a white line in row 2 of (A) is provided. The fluorescence intensities for GFP (green line) are graphed

based on the left Y-axis values, which in each case measures the mean GFP fluorescence intensity (a.u.) along the line. The fluorescence intensities for the mCherry-tagged peri-nuclear ER (red line) are graphed based on the right Y-axis values, which measure the mean mCherry fluorescence intensity (a.u.) along the line. All fluorescence measures are graphed vs. the distance along the line (microns) from panel A.

Hxk2-S15 mutant protein abundances and ability to support growth on glucose in *hxk1*Δ *hxk2*Δ *glk1*Δ cells were indistinguishable from wild-type Hxk2, demonstrating that they encode stable and active hexokinases (Figure 14D-E). When we assessed *in vivo* multimerization, we found that Hxk2^{S15D} failed to multimerize and Hxk2^{S15A} reduced multimerization, suggesting that each mutant diminished Hxk2 dimer abundance (Figure 14F). Hxk2^{S15D} disrupts Hxk2 dimerization *in vivo* and *in vitro*, while Hxk2^{S15A} has a more modest impact on dimerization *in vitro* [247,251–253]. Consistent with our observations (Figure 14E), Hxk2^{S15D} and Hxk2^{S15A} have identical catalytic activities *in vitro* [251–253]. These data confirm that S15 is critical for Hxk2 multimerization, but changes to S15 did not alter Hxk2 nuclear propensity in wild-type cells. Nuclear translocation was still regulated by glucose starvation.

2.2.6 Hxk2 homology model provides insight into the molecular mechanisms of dimerization

To understand the mechanisms that govern Hxk2 dimerization and nuclear translocation, we generated a homology model of dimeric *S. cerevisiae* Hxk2 (referred as *Sc*Hxk2) based on a crystal structure of the *K. lactis* Hxk1 dimer (PDB 3O1W; referred to as *Kl*Hxk1) [83]. In *K. lactis*, the sole Hxk1 ortholog corresponds to both *Sc*Hxk1 and *Sc*Hxk2. *Sc*Hxk1 and *Sc*Hxk2 are paralogs that arose from a whole genome duplication in *S. cerevisiae*, which did not occur in *K. lactis*

[372,373]. *Kl*Hxk1 is like both *Sc*Hxk1 (70% identity) and *Sc*Hxk2 (73% identity) (Figure 16A), but it is slightly more similar to *Sc*Hxk2, as is evident when structures of these three enzymes are superimposed (Figure 16B-D) [83]. The similarity between *Kl*Hxk1 and *Sc*Hxk2 (Figure 16C) makes *Kl*Hxk1 ideal for modeling dimeric *Sc*Hxk2. Crystal structures of many proteins lack N-terminal tails, which are often disordered, but the 3O1W [83] structure covers almost all the *Kl*Hxk1 sequence without gaps, including the two N-terminal tails. Each 3O1W N-terminus extends into the enzymatic cleft of the opposite *Kl*Hxk1 monomer, which may lock it into a stable position that can be crystallographically resolved. Our *Sc*Hxk2 homology model is similarly complete, including the cleft-bound N-terminal tails (Figure 14G).

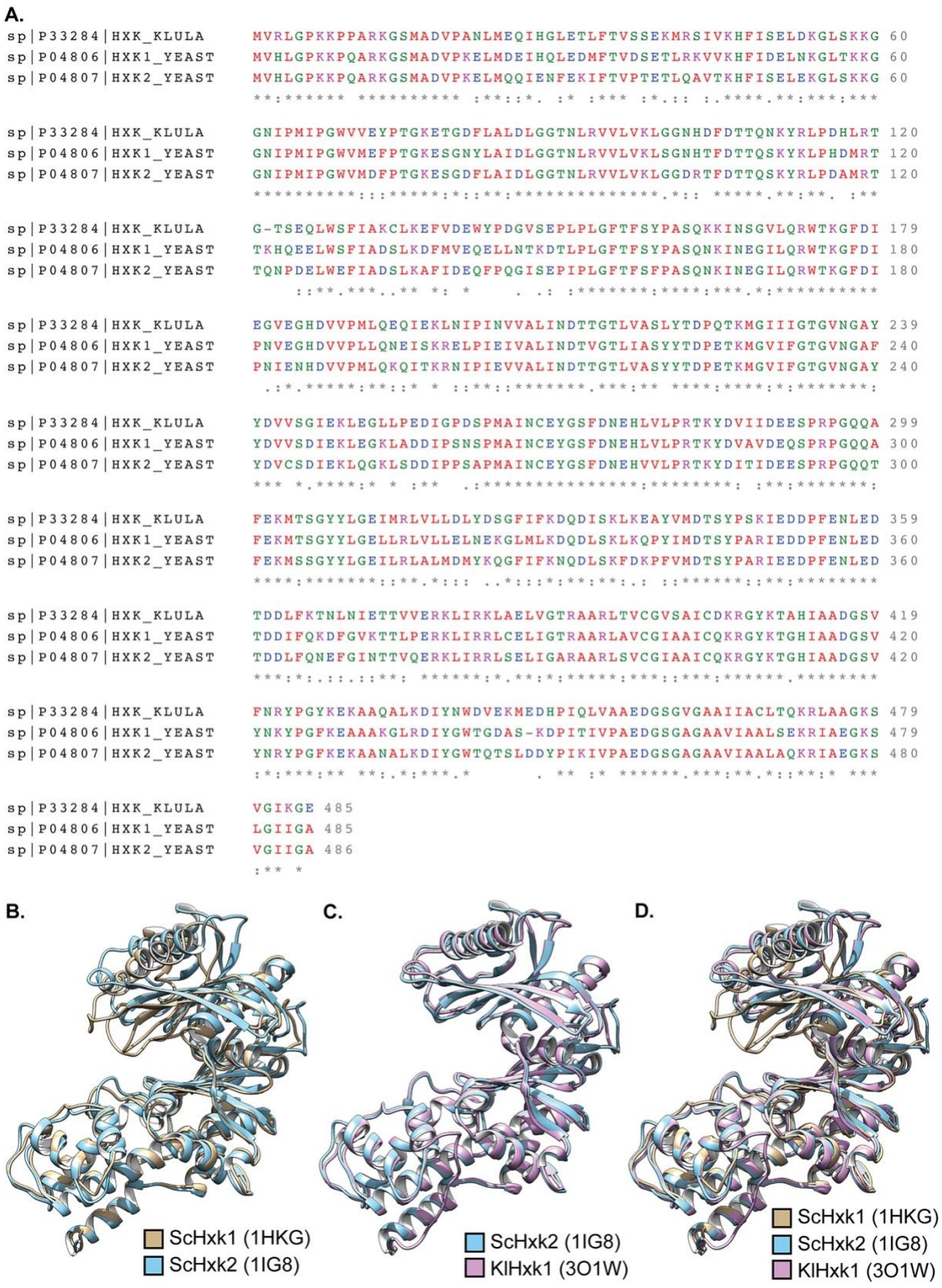

Figure 16. Comparison of the amino acid sequences and structures for *Sc*Hxk1, *Sc*Hxk2, *Kl*Hxk1.

(A) Clustal Omega amino-acid sequence alignment of *Sc*Hxk1, *Sc*Hxk2, and *Kl*Hxk1. Identical amino acids, conserved residues, and non-conserved residues are shown in the consensus motif as asterisks, colons, or spaces, respectively. Colors represent the amino-acid side-chain functional groups, with red representing alkyl side chains, blue representing acidic side chains, purple representing basic side chains, and green representing neutral side chains. (B-D) Crystal structures of *Sc*Hxk1, *Sc*Hxk2, and *Kl*Hxk1 (PDB IDs 1HKG, 1IG8, and 3O1W) superimposed using UCSF Chimera. The structures are all highly similar, but *Sc*Hxk2 and *Kl*Hxk1 have the greatest similarity.

To identify molecular interactions responsible for dimerization, we used BINANA [44,45] to find inter-chain interactions in the modeled dimer (Table 2 and highlighted in Figure 14G). This analysis identified two primary regions. The first is the N-terminal tail itself. Several charged tail residues participate in salt bridges with the opposite monomer (V2-D417*, K7-E457*, K13-D106*, where an asterisk denotes a residue belonging to the opposite monomer). The Q10 sidechain also forms hydrogen bonds with T107* and F105*. The second region of inter-chain interactions is at the interface between the two distal lobes, where the two monomers meet. Here K111 forms salt bridges with two residues (E359* and D360*), as does R113 (E359* and D363*). E141 forms a single salt bridge with K379*, and the Q109 and K111 backbones form hydrogen bonds with E356* and N357*, respectively.

Table 2. Summary of residues at the Hxk2 dimer interface per the homology model of the *Sc*Hxk2 dimer.

Monomer 1	Monomer 2	Interaction type
VAL 2	ASP 417	Salt bridge
LYS 7	GLU 457	Salt bridge
GLN 10	PHE 105	Hydrogen bond
GLN 10	THR 107	Hydrogen bond
LYS 13	ASP 106	Salt bridge
GLN 109	GLU 356	Hydrogen bond
LYS 111	ASN 357	Hydrogen bond
LYS 111	GLU 359	Salt bridge
LYS 111	ASP 360	Salt bridge
ARG 113	GLU 359	Salt bridge
ARG 113	ASP 363	Salt bridge
GLU 141	LYS 379	Salt bridge

Based on our analyses of the *Sc*Hxk2 dimer model, it is not surprising that the two S15 mutants impact dimerization, as S15 is close to two inter-chain salt bridges (E141-K379* and K13-D106*) (Table 2 and Figure 14G). S15 phosphorylation (-2 e charge) would change the regional electrostatics, possibly disrupting dimer-promoting interactions. Mutation of this site to Ala would preclude phosphorylation and preserve the interactions, leaving the dimer intact (Table 2 and Figure 14G).

The cleft-bound N-terminal tails appear to play an important role in promoting *Sc*Hxk2 dimerization (Figure 14G, 17A). Given the crystallographic positions of bound glucose and ATP observed in other structures (e.g., 6PDT [94]), there do not appear to be substantial steric clashes between these bound substrates and the N-terminal tail, even if all three were to occupy the same cleft. We posit that the bound tail might instead be incompatible with catalytic-cleft closure, as required for glucose phosphorylation. Indeed, our homology model and published crystal structures [83] suggest that hexokinase dimerization generally—and perhaps N-terminal-tail binding specifically—maintains the catalytic cleft in an open conformation. In high glucose concentrations, bound glucose might disrupt N-terminal-tail binding within the catalytic pocket to destabilize the dimer (Figure 17A), and this could help form the monomer-dimer balance of Hxk2

observed in glucose-grown cells [247]. Alternatively, N-terminal-tail binding may prevent glucose binding in low glucose concentrations, encouraging dimerization. However, *in vivo* the Tda1 kinase phosphorylates Hxk2, which helps preserve it as a monomer even in glucose starvation conditions. When the Tda1 kinase is lost, along with its accompanying Hxk2 posttranslational modifications, Hxk2 is retained as a dimer in low glucose conditions [247], as would be predicted from our model.

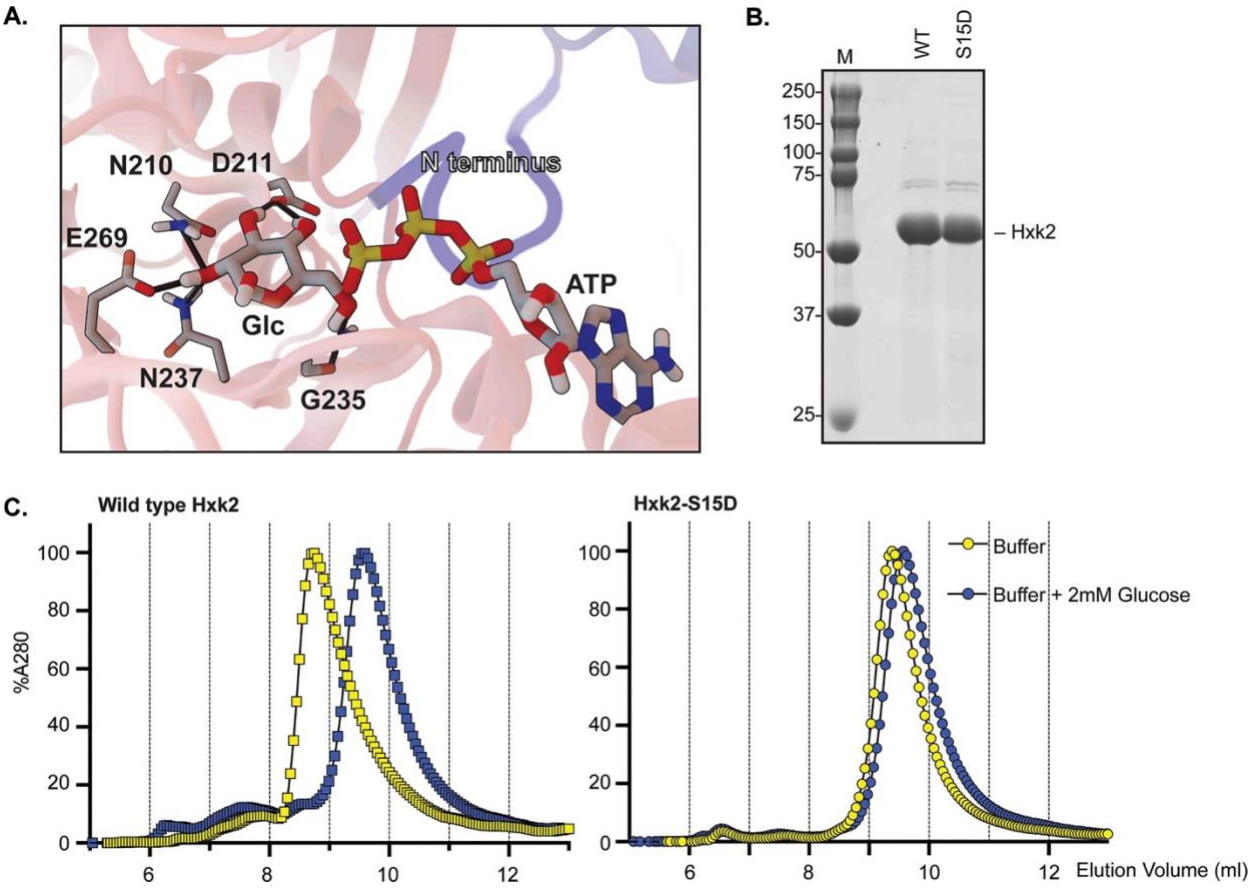

Figure 17. Glucose binding prevents Hxk2 dimer formation.

(A) A close-up view of the enzymatic clefts of the Hxk2 dimer model (shown in Figure 14G). The N-terminus from one monomer (in blue) binds in the catalytic pocket of the opposing monomer (in pink). Positioned glucose and ATP molecules are shown in sticks representation. Hydrogen bonds are shown as solid black lines. (B) Yeast Hxk2 proteins (wild type and Hxk2-S15D) were expressed in and purified from E. coli. Each protein (5 μg) was resolved by SDS gel

electrophoresis and stained with Coomassie blue. (C) Purified, recombinant Hxk2 proteins (WT, square symbols; Hxk2-S15D, round symbols) were resolved by size exclusion chromatography using a buffer with (blue) and without (yellow) glucose.

We tested this model using molecular dynamics simulations. We found evidence that a glucose molecule and the N-terminal tail may not simultaneously occupy the catalytic pocket of the dimer (see Figure 18A-F). However, in simulations of the dimer where glucose was omitted, the N-terminal tail remained stably associated throughout the simulation (see Figure 18A-F). This finding is consistent with the idea that the N-terminal tail and its modification are key in regulating the dimer-to-monomer transition.

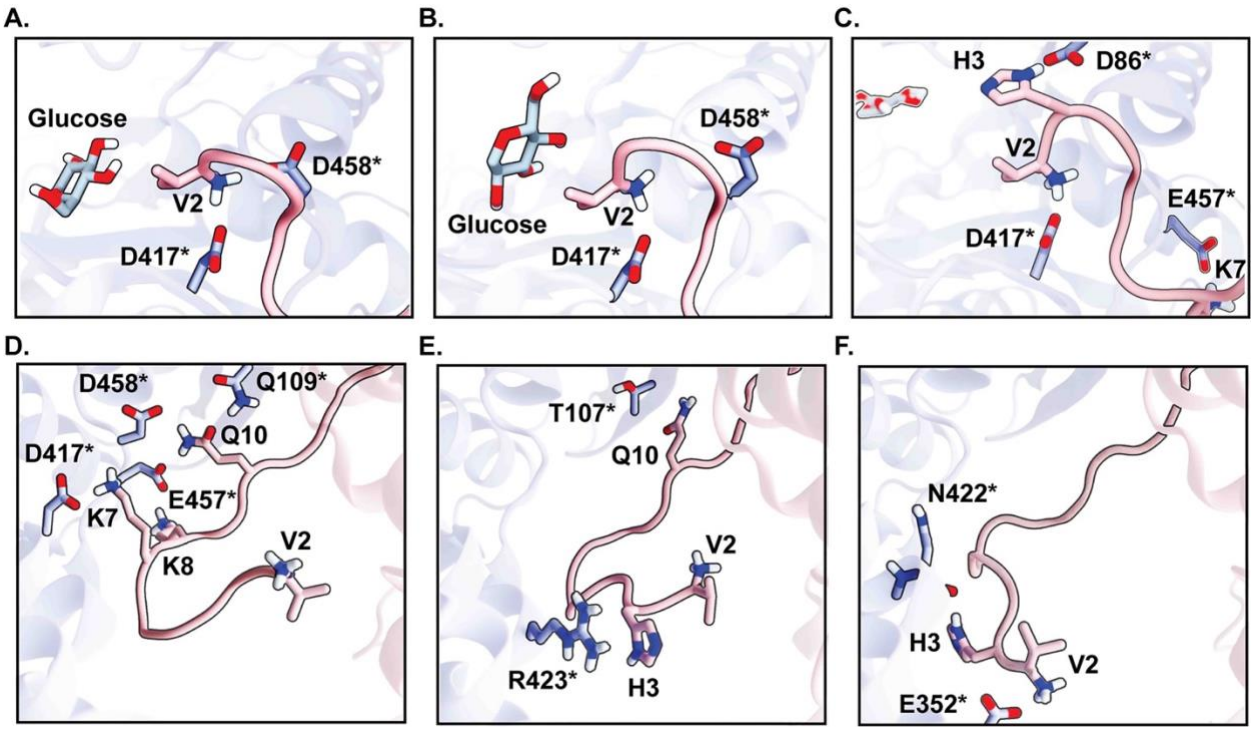

Figure 18. Molecular dynamics simulations demonstrating a possible mechanism of N-terminal-tail dissociation from the enzymatic pocket upon glucose binding.

(A) Early in the simulation, the positively charged V2 terminal amine slides between D417* and D458*, forming salt bridges with both. (B) The bound glucose molecule briefly forms hydrophobic contacts with the V2 side chain. (C) Glucose moves to a different location within the enzymatic cleft, and the V2-D458* salt bridge brakes. At roughly the same time, a hydrogen bond forms between H3 and D86*. (D) The tail beings to dissociate from the opposite-monomer cleft. K7, which previously formed a salt bridge with E457*, now forms a salt bridge with D417* instead. K8, which did not previously interact with the opposite monomer, forms a salt bridge with E457*. (E) Tail dissociation is stabilized by a cation-π interaction between H3 and R423*, and Q10 shifts to form a hydrogen bond with T107*. (F) Finally, the V2 terminal amine forms a salt bridge with E352*, and H3 forms a hydrogen bond with the backbone carbonyl oxygen of N422*.

To verify that glucose promotes dimer dissociation independently of S15 phosphorylation, we used chromatography to biochemically examine multimerization of purified Hxk2 and Hxk2^{S15D}. Using nickel affinity columns, we obtained highly purified Hxk2 and Hxk2^{S15D} from E. coli (Figure 17B). As a control, we confirmed that Hxk2^{S15D} promotes monomerization in the absence of glucose. In size exclusion chromatography, wild-type Hxk2 eluted as a single peak with an ~8.8 mL elution volume. Hxk2^{S15D} took longer to elute from the column (elution volume of ~9.5 mL), consistent with a smaller size than wild-type Hxk2 (Figure 17C, compare yellow curves). This change in elution profile is consistent with wild-type Hxk2 forming a larger, dimeric complex than the Hxk2^{S15D} mutant in the absence of glucose. In contrast, Hxk2^{S15D} cannot dimerize unless much higher enzyme concentrations are used [252] and represents monomeric Hxk2 [252,253].

We next preincubated Hxk2 with glucose in the absence of ATP, locking the enzyme in a glucose-bound state before performing size exclusion chromatography. In the presence of glucose, Hxk2 migrated slowly and eluted as a single peak at ~9.5 mL, the same elution profile observed with monomeric Hxk2^{S15D} (Figure 17C, compare blue curve for WT Hxk2 to yellow Hxk2^{S15D}

curve). Unlike wild-type Hxk2, the elution profile of the monomeric Hxk2^{S15D} did not change upon adding glucose, as expected since it was already monomeric (Figure 17C, compare yellow and blue curves for Hxk2^{S15D}). Since these assays were done without ATP, unphosphorylated glucose remained in the binding pocket. They are thus comparable to the simulations, which similarly omitted ATP.

These results confirm that glucose binding disrupts dimer formation. They support earlier biochemical studies demonstrating that glucose binding (1) promotes Hxk2 monomer formation and (2) greatly decreases the dimerization association constant. The Hxk2 dimer had a K_a of 1.2 x 10^7/M when glucose was absent versus 4.5 x 10^4/M in the presence of glucose. A similar mutant to the one used here, Hxk2^{S15E}, had a dimer K_a of 1.3 x 10^4/M without glucose present, nearly 1000-fold lower than wild-type Hxk2 in the same conditions [252]. We propose a model that incorporates our MD simulations and biochemical findings with the earlier work from the Kriegel lab: (1) Glucose and N-terminal tail binding in the Hxk2 catalytic cleft are incompatible. (2) N-terminal tail docking into the catalytic cleft of the opposing monomer stabilizes Hxk2 dimerization. (3) Modification of S15 disrupts the dimer interface by occluding the N-tail/catalytic-pocket association between opposing monomers.

2.2.7 The Hxk2 N-terminal tail, thought initially to contain an NLS, is required for Hxk2 dimer formation and nuclear exclusion

To assess the role of the N-terminal tail, we made a mutant Hxk2 lacking amino acids 7–16 (referred to as Hxk2$^{\Delta 7-16}$). The Moreno group has studied this same mutation. They referred to it as either Hxk2ΔK^7M^{16}, described as having lost its nuclear localization sequence [261], or the "without regulatory function" (WRF or Hxk2^{WRF}) mutation, described as having lost its ability to

regulate glucose-repression of the *SUC2* gene [236,258]. Studies from the same lab suggest that Hxk2$^{\Delta 7–16}$ retains full catalytic function but fails to bind Mig1 and does not localize to the nucleus, leading to their claim that amino acids in this region constitute an Hxk2 NLS [236,258].

We demonstrated that the Hxk2$^{\Delta 7–16}$ mutant retains only partial catalytic activity (~50% that of WT Hxk2) and maintains glucose repression of the *SUC2* gene [224], refuting earlier claims [236,258]. Since this stretch of amino acids was reported as an NLS [261], we were surprised to find that Hxk2$^{\Delta 7–16}$ localized to the nucleus in both glucose-replete and glucose-starvation conditions (Figure 19A-C). In contrast to the reports that this region serves as an NLS [261], the Hxk2 N-terminus seems critical for maintaining glucose-regulated nuclear exclusion of Hxk2.

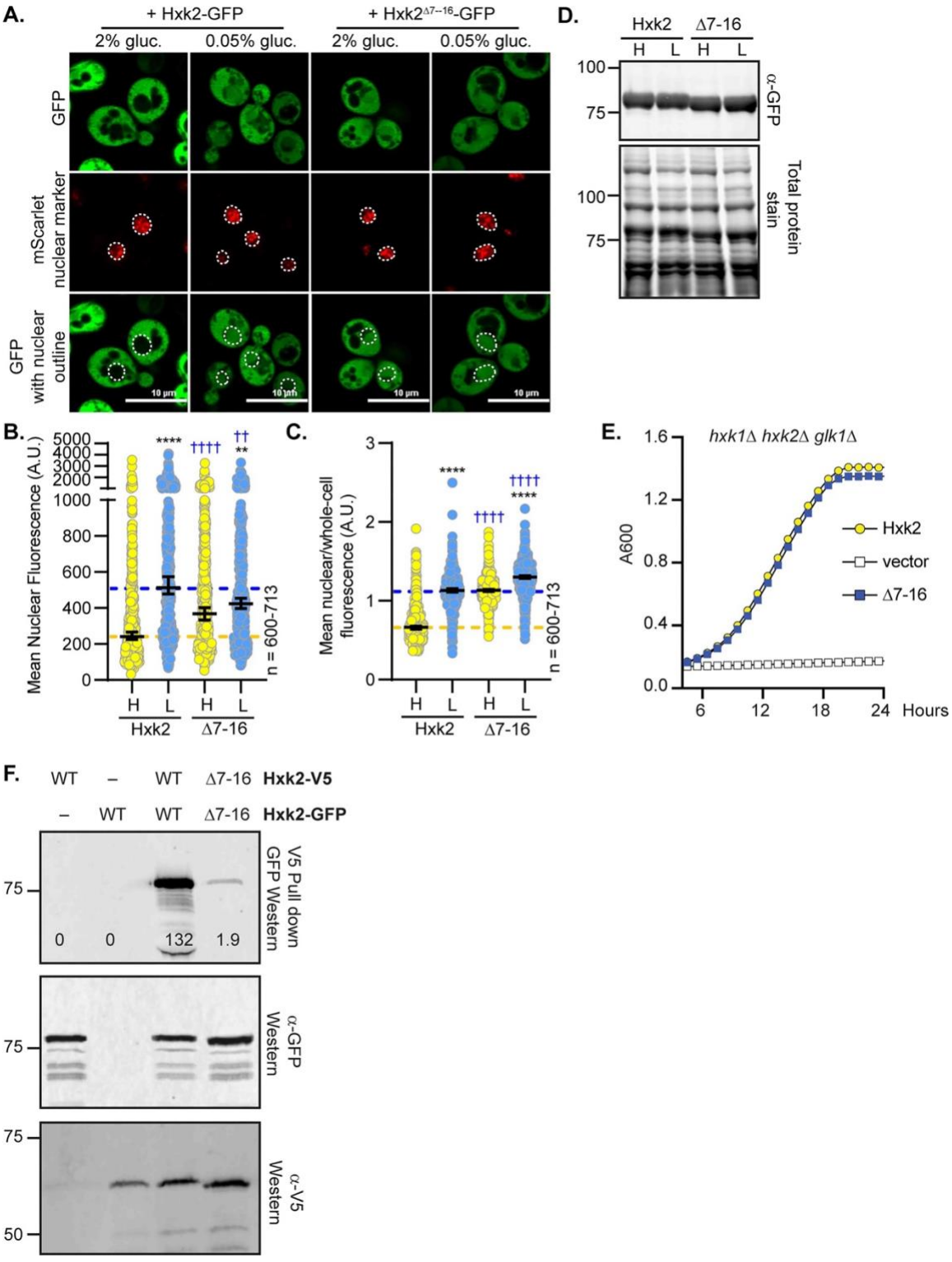

Figure 19. Deleting the N-terminal amino acids 7-16 results in a pool of constitutively nuclear localized Hxk2, prevents Hxk2 dimerization but maintains catalytic function.

(A) Confocal microscopy of GFP-tagged Hxk2 or Hxk2$^{\Delta 7–16}$ expressed from a CEN plasmid under the control of the *HXK2* promoter in *hxk2*Δ cells. Co-localization with the nucleus is determined based on overlap with the Tpa1-mScarlet nuclear marker, and a dashed white line indicates the nucleus. (B-C) Automated quantification of the images shown in panel A to measure (B) mean nuclear fluorescence or (C) the ratio of the mean nuclear/whole-cell fluorescence. Horizontal black lines show the median, and error bars indicate the 95% confidence interval. Dashed yellow and blue lines represent the median value for Hxk2-GFP in high and low glucose, respectively. Black asterisks represent statistical comparisons between low and high glucose for a specific *HXK2* allele, and blue daggers represent statistical comparisons between mutant alleles and the corresponding WT Hxk2 in the same medium condition. (D) Immunoblot analyses of Hxk2-GFP in whole-cell protein extracts made from cells grown in high glucose or shifted to low glucose for 2 hours. REVERT total protein stain of the membrane serves as a loading control. (E) Cells lacking all three hexokinase genes (*hxk1*Δ *hxk2*Δ *glk1*Δ) were transformed with plasmid vector or plasmids expressing wild-type Hxk2 or Hxk2-Δ7–16, as indicated. Cell growth (A_{600}) in media containing glucose as the carbon source was monitored for 24 hours. (F) To assess multimerization, we prepared extracts from yeast cells expressing the untagged Hxk2 or Hxk2 tagged with either V5 or GFP. Hxk2 proteins contained either the wild-type (WT) N-terminus or the Δ7–16 deletion. Protein expression was monitored by western blotting (bottom two panels). The association of the tagged proteins was assessed by co-immunoprecipitation using anti-V5 beads followed by western blotting with anti-GFP (top panel).

The Hxk2$^{\Delta 7–16}$ protein was stable and functional, as confirmed by immunoblotting and its ability to support robust growth on glucose for cells lacking endogenous hexokinase (Figure 19D-E). However, the Hxk2$^{\Delta 7–16}$ mutant did not copurify a differentially tagged version of Hxk2$^{\Delta 7–16}$, suggesting it cannot multimerize (Figure 19F). This result is not surprising considering our modeling and simulations, in which the Hxk2 N-terminal tail is necessary for dimerization (Figure 14G and Table 2).

Since residues 7–16 are not a bona fide NLS, we mapped surface-exposed lysines and arginines (Figure 20A) and used several NLS prediction tools [46–50] to try to identify the

sequence responsible for Hxk2 nuclear translocation. Two of these tools identified a string of lysines at K54, K58, and K59 as a putative NLS. When we mutated these residues to alanine, the nuclear partitioning of Hxk2 in response to glucose fluctuations was unchanged (Figure 20B-D). Hxk2 does not contain an easily definable, canonical K/R-rich NLS.

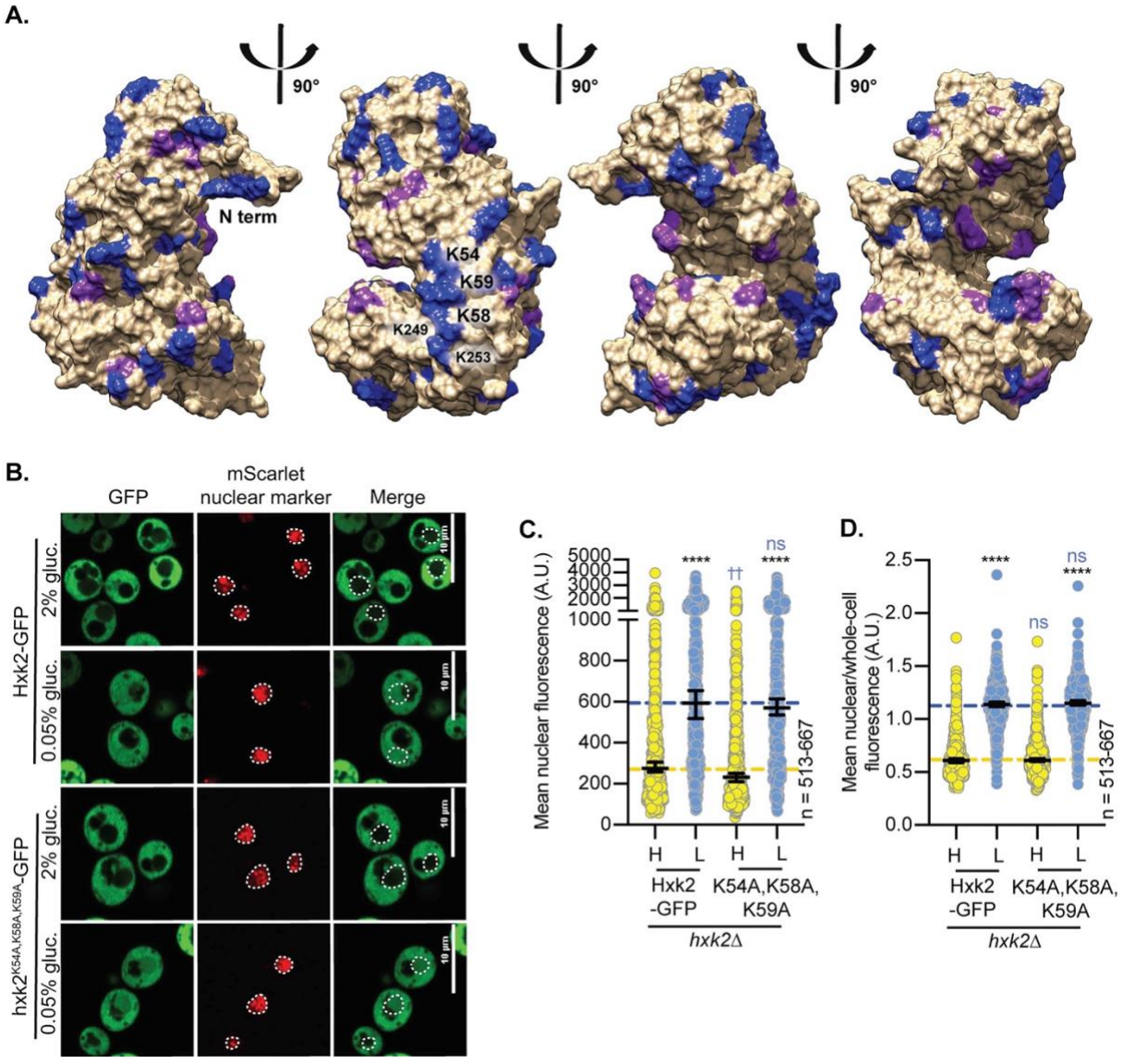

Figure 20. A second K/R-rich, putative nuclear localization sequence in Hxk2 does not impact its nuclear partitioning in response to changing glucose conditions.

(A) One monomer of the full-length *Sc*Hxk2 homology model is shown in surface representation. Surface-exposed lysine residues are shown in blue, and arginine residues are shown in purple. Labeled amino acids indicate the location of a basic, lysine-rich patch and predicted NLS at residues K54, K59, and K59, as identified by SeqNLS and NLStradamus [15,16]. Note that per PSORTII, Predict NLS, and cNLS Mapper, there are no predicted NLSs in Hxk2 [17–19]. (B) Confocal microscopy of GFP-tagged Hxk2 and K54A, K58A, and K58A mutant expressed from a CEN plasmid under the control of the *HXK2* promoter in cells lacking *HXK2* alone. Co-localization with the nucleus is determined based on overlap with the Tpa1-mScarlet nuclear marker, and a dashed white line indicates the nucleus. (C-D) Automated quantification of the images shown in panel B to measure (C) the mean nuclear fluorescence or (D) the mean nuclear/whole-cell fluorescence ratio. Horizontal black lines show the median, and error bars indicate the 95% confidence interval. Dashed yellow and blue lines represent the median value for Hxk2-GFP in high and low glucose, respectively. Black asterisks represent statistical comparisons between low and high glucose for a specific *HXK2* allele. Blue daggers represent statistical comparisons between mutant alleles and the corresponding WT Hxk2 in the same medium condition.

2.2.8 K13 in the Hxk2 N-terminal tail is required for Hxk2 dimer formation and glucose regulation of nuclear localization

There are three lysines among amino acids 7–16, and lysines are often critical for NLS function [374]. We made site-directed mutants at lysines 7, 8, and 13, converting these residues to alanine (referred to as $Hxk2^{K7,8,13A}$). This triple mutant recapitulated the high glucose nuclear localization observed for $Hxk2^{\Delta 7–16}$ (Figure 21A-C). Rather than forming an NLS, this region helps maintain glucose-induced nuclear exclusion of Hxk2.

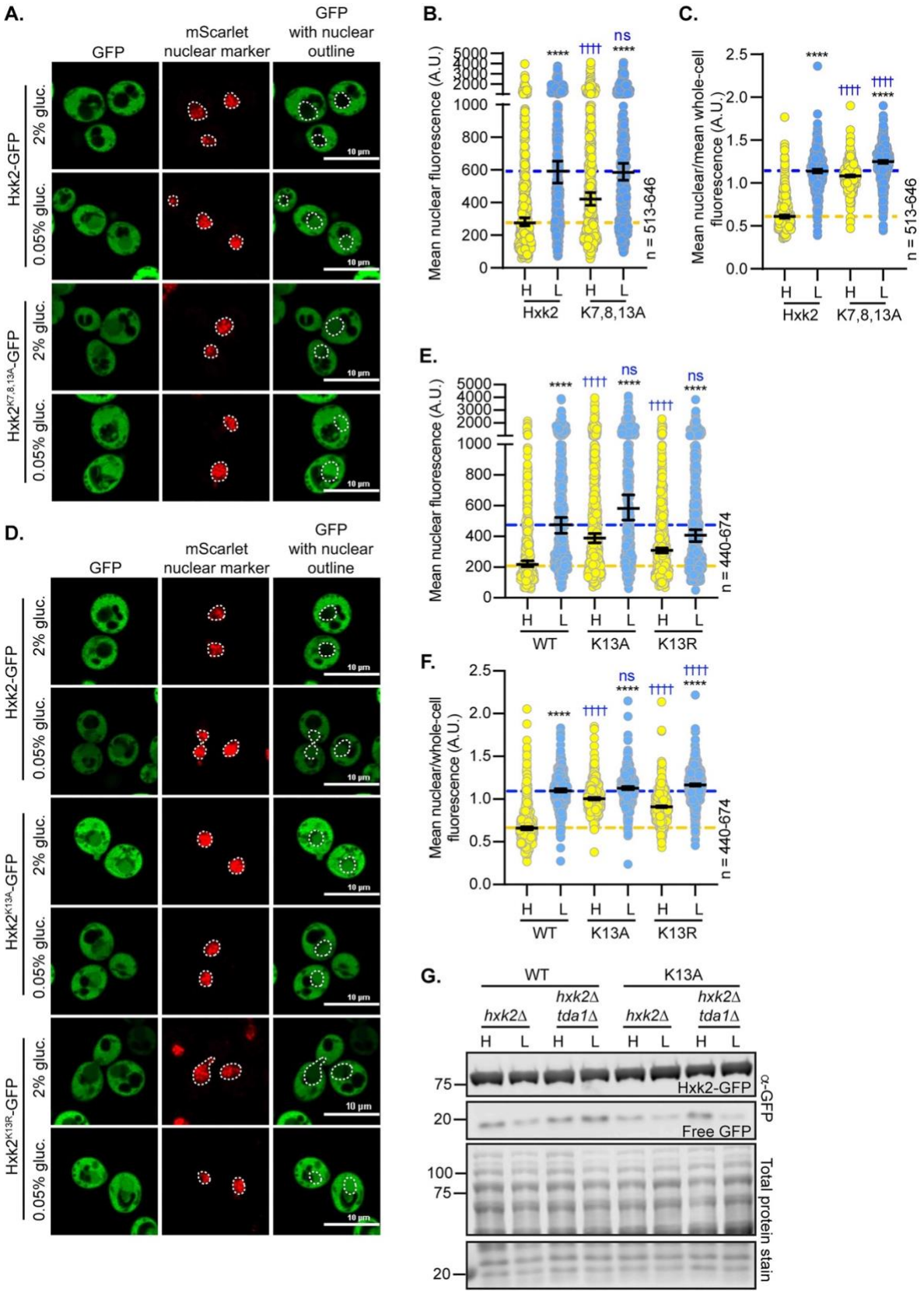

Figure 21. Mutational analyses of lysine-rich putative nuclear localization sequences in Hxk2.

(A) Confocal microscopy of GFP-tagged Hxk2 and K7A, K8A, and K13A mutant expressed from a CEN plasmid under the control of the *HXK2* promoter in cells lacking *HXK2* alone. Co-localization with the nucleus is determined based on overlap with the Tpa1-mScarlet nuclear marker, and a dashed white line indicates the nucleus. (B-C) Automated quantification of the images shown in panel A to measure (B) the mean nuclear fluorescence or (C) the mean nuclear/whole-cell fluorescence ratio. Horizontal black lines show the median, and error bars indicate the 95% confidence interval. Dashed yellow and blue lines represent the median value for Hxk2-GFP in high and low glucose, respectively. Black asterisks represent statistical comparisons between low and high glucose for a specific *HXK2* allele. Blue daggers represent statistical comparisons between mutant alleles and the corresponding WT Hxk2 in the same medium condition. (D) Confocal microscopy of GFP-tagged Hxk2, K13A, or K13R mutants expressed from a CEN plasmid under the control of the *HXK2* promoter in cells lacking *HXK2* alone. Co-localization with the nucleus is determined based on overlap with the Tpa1-mScarlet nuclear marker, and a dashed white line indicates the nucleus. (E-F) Automated quantification of the images shown in panel D to measure € the mean nuclear fluorescence or (F) the mean nuclear/whole-cell fluorescence ratio. Horizontal black lines show the median, and error bars indicate the 95% confidence interval. Dashed yellow and blue lines represent the median value for Hxk2-GFP in high and low glucose, respectively. Black asterisks represent statistical comparisons between low and high glucose for a specific *HXK2* allele. Blue daggers represent statistical comparisons between mutant alleles and the corresponding WT Hxk2 in the same medium condition. (G) Immunoblot analyses of Hxk2-GFP or the K13A mutant from whole-cell protein extracts of WT or *tda1*Δ cells that were grown in high glucose or shifted to low glucose for 2 h. The full-length Hxk2-GFP and the free GFP breakdown products are shown for each and are equally adjusted so that their abundances can be compared. Total protein stain is shown as a loading control. Note that there is no increase in the free-GFP signal in response to low glucose shift, nor is there increased free GFP from the K13A mutant protein.

We found that the Hxk2$^{\Delta 7–16}$ and Hxk2^{K7,8,13A} mutants prevented dimerization and circumvented glucose-regulated nuclear translocation, giving rise to a pool of constitutively nuclear Hxk2. However, disrupting dimerization is not sufficient to drive nuclear localization of Hxk2 because Hxk2^{S15D}, which prevents dimerization, retains glucose-regulated nuclear exclusion (Figure 14A-G, 15A-B). Amino acids 7–16 in Hxk2 are conserved in Hxk1, yet Hxk1 does not

accumulate in the nucleus in glucose starvation (Figure 22A and Figure 10A-D), and analogous mutations in Hxk1 to those under study for Hxk2 did not result in accumulation of nuclear Hxk1 (Figure 23A-C).

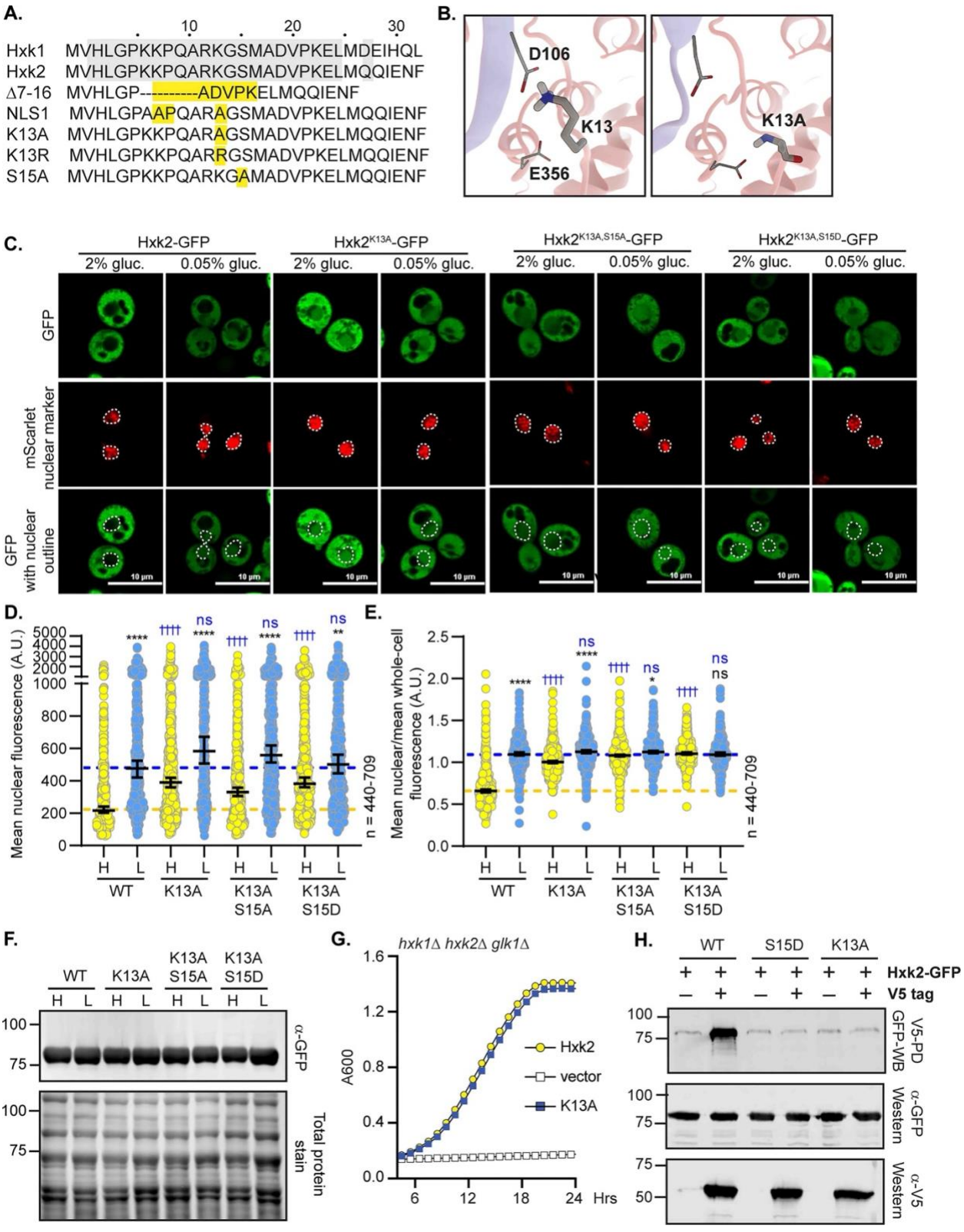

Figure 22. Mutation of K13 to alanine in the Hxk2 N-terminal tail results in a pool of nuclear localized Hxk2 in both high and low glucose and prevents Hxk2 dimerization but maintains catalytic function.

(A) Sequence alignment of the Hxk2 N-terminal tail with Hxk1, highlighting key mutated residues. The first 30 residues of Hxk1 and Hxk2 are shown with identical residues shaded. Select mutations in this region are shown in yellow. (B) Modeled K13 interactions. The two Hxk2 monomers are shown as pink and blue ribbons. In the first panel, a close-up view of K13 interactions with E356 (same monomer) and D106 (opposing monomer). In the second panel, an alanine substitution at K13 cannot form the same electrostatic interactions. (C) Confocal microscopy of GFP-tagged Hxk2 or the mutant alleles expressed from a CEN plasmid under the control of the *HXK2* promoter in *hxk2*Δ cells. Co-localization with the nucleus is determined based on overlap with the Tpa1-mScarlet nuclear marker, and a dashed white line indicates the nucleus. (D-E) Automated quantification of imaging shown in (C) to measure (D) mean nuclear fluorescence or (E) the ratio of the mean nuclear/whole-cell fluorescence. Horizontal black lines show the median, and error bars indicate the 95% confidence interval. Dashed yellow and blue lines represent the median value for Hxk2-GFP in high and low glucose, respectively. Black asterisks represent statistical comparisons between low and high glucose for a specific *HXK2* allele, and blue daggers represent statistical comparisons between mutant alleles and the corresponding WT Hxk2 in the same medium condition. (F) Immunoblot analyses of Hxk2-GFP in whole-cell protein extracts made from cells grown in high glucose or shifted to low glucose for 2 hours. (G) Cells lacking all three hexokinase genes (*hxk1*Δ *hxk2*Δ *glk1*Δ) were transformed with plasmid vector or plasmids expressing wild-type Hxk2 or Hxk2^{K13A}, as indicated. Cell growth (A_{600}) in media containing glucose as the carbon source was monitored for 24 hours. (H) Extracts were prepared from yeast cells expressing Hxk2-GFP and Hxk2 with or without the V5 as indicated. Hxk2 proteins contained either the wild-type (WT) sequence or the S15D or K13A mutations. Protein expression was monitored by western blotting (bottom two panels). The association of the tagged proteins was assessed by co-immunoprecipitation using anti-V5 beads followed by western blotting with anti-GFP (top panel). Quantitation of the signal in the top panel is shown.

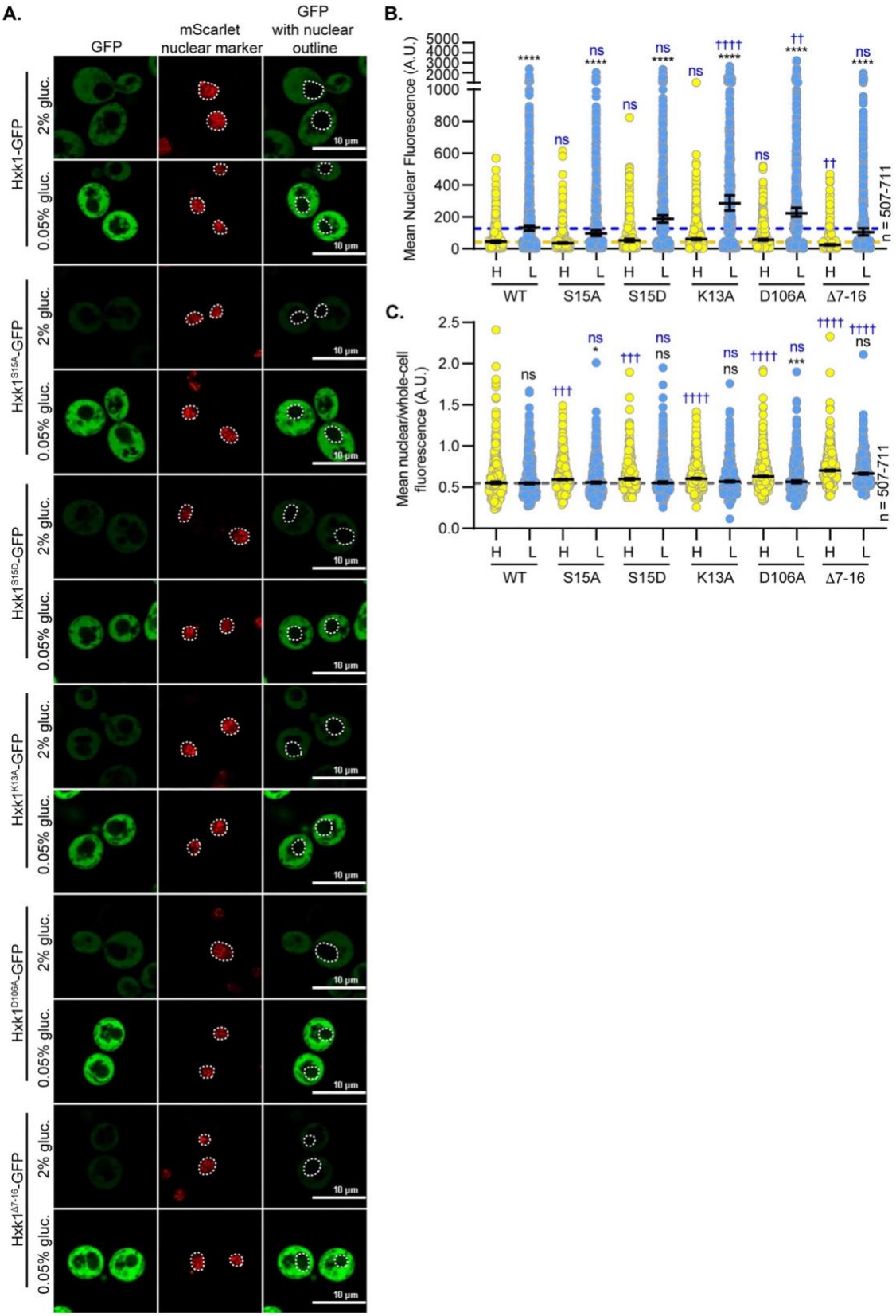

Figure 23. N-terminal mutations in Hxk1 do not alter Hxk1 nuclear propensity.

(A) Confocal microscopy of GFP-tagged Hxk1 and the indicated mutant alleles expressed from CEN plasmids under the control of the *HXK1* promoter in cells lacking *HXK1*. Co-localization with the nucleus is determined based on overlap with the Tpa1-mScarlet nuclear marker, and a dashed white line indicates the nucleus in the GFP with a nuclear outline row. (B-C) Automated quantification of the images shown in panel A to measure (B) the mean nuclear fluorescence or (C) the mean nuclear/whole-cell fluorescence ratio. Horizontal black lines show the median, and error bars indicate the 95% confidence interval. Dashed yellow and blue lines represent the median value for Hxk1-GFP in high and low glucose, respectively. The dashed gray line represents the median value for Hxk1 in high/low glucose media simultaneously for panel C since these values are not distinguishable. Black asterisks represent statistical comparisons between low and high glucose for a specific *HXK1* allele. Blue daggers represent statistical comparisons between mutant alleles and the corresponding WT Hxk1 in the same medium condition.

To refine the region responsible for glucose-regulated nuclear localization, we considered our *Sc*Hxk2 dimer homology model, which suggests the N-terminal-tail residues K7 and K13 form important salt bridge interactions that may stabilize the dimer (Figure 14G and 22B). Of these two sites, K13 may be dimethylated or sumoylated in Hxk2 [375,376] (Figure 22B) but ubiquitinated in Hxk1 [377]; this putative differential regulation could account for the distinct Hxk1 and Hxk2 nuclear localizations. We assessed the localization of GFP-tagged $Hxk2^{K13A}$, a mutation likely to disrupt the K13-D106 electrostatic interaction observed in the ScHxk2 model (Figure 22B, center panel). Like $Hxk2^{\Delta 7–16}$ and $Hxk2^{K7,8,13A}$, $Hxk2^{K13A}$ was nuclear localized in both glucose-replete and glucose-starved conditions (Figure 22C-E). In glucose-grown cell, it had elevated nuclear fluorescence and a nuclear to whole-cell fluorescence ratio that was indistinguishable from wild-type Hxk2 under glucose-starvation conditions. Further, there was little change in the mean nuclear to whole-cell fluorescence ratio of $Hxk2^{K13A}$ between glucose-grown or -starved cells (Figure 22E), demonstrating that this mutant bypasses glucose-inhibition of nuclear localization. A mutation of K13 to arginine, which would disrupt sumoylation and likely disrupt methylation

(arginine's can be methylated but use differing enzymes than lysine methylation) but could leave Hxk2 dimerization intact, similarly prevented nuclear exclusion of Hxk2 in high glucose conditions (Figure 21D-E). These data suggest that loss of sumoylation and/or methylation at K13 may be an important determinant for glucose restriction of Hxk2's nuclear translocation. The analogous Hxk1^{K13A} mutant did nothing to change the distribution of Hxk1, which remained cytosolic in all conditions (Figure 23A-C).

Hxk2^{K13A} encodes a stable and functional protein, has catalytic activity, and permits robust growth on glucose when expressed as the only hexokinase in cells (Figure 22F-G). There was no increase in the free-GFP breakdown product for K13A relative to the WT control, so the elevated nuclear fluorescence is not due to increased free-GFP (Figure 21G). The K13A mutation disrupted multimer formation as effectively as Hxk2^{S15D} (Figure 14G and 22H); V5-tagged Hxk2^{K13A} from yeast extracts could not copurify GFP-tagged Hxk2^{K13A} (Figure 22H).

It should be noted that the K13A mutation and dimer disruption allow access to the S15 phosphorylation site, which others have suggested might control nuclear translocation [254]. To determine if S15 phosphorylation influenced the misregulated localization of the K13A mutant, we combined K13A with S15A or S15D, which prevent phosphorylation or mimic phosphorylation, respectively. Neither of these new double mutants–Hxk2^{K13A,S15A} nor Hxk2^{K13A,S15D} –showed any difference in nuclear localization compared to Hxk2^{K13A} (Figure 22C-E). We propose that S15 phosphorylation is dispensable for nuclear translocation and/or retention of Hxk2^{K13A}.

We mutated D106, the residue that pairs with K13 to form a salt bridge at the Hxk2 dimer interface (Figure 14G). Interestingly, the Hxk2^{D106A} mutant, which would presumably break the interaction with K13 and allow it to be accessible for modification and/or binding, maintained

normal Hxk2 cytosol-nuclear partitioning in both glucose-replete and -starvation conditions (Figure 24A-C). However, as anticipated, the D106A mutant could not form multimers *in vivo* (Figure 24D), supporting the idea that K13 should be accessible in this mutant. These data demonstrate that generating the Hxk2 monomer is not sufficient to drive nuclear localization of Hxk2. In addition, access to K13, as would be expected to occur in any mutant that breaks the dimer, is not enough to stimulate nuclear localization, supporting a model where post-translational modification or some aspect specific to the lysine at this position is required for glucose regulation of Hxk2's nuclear propensity.

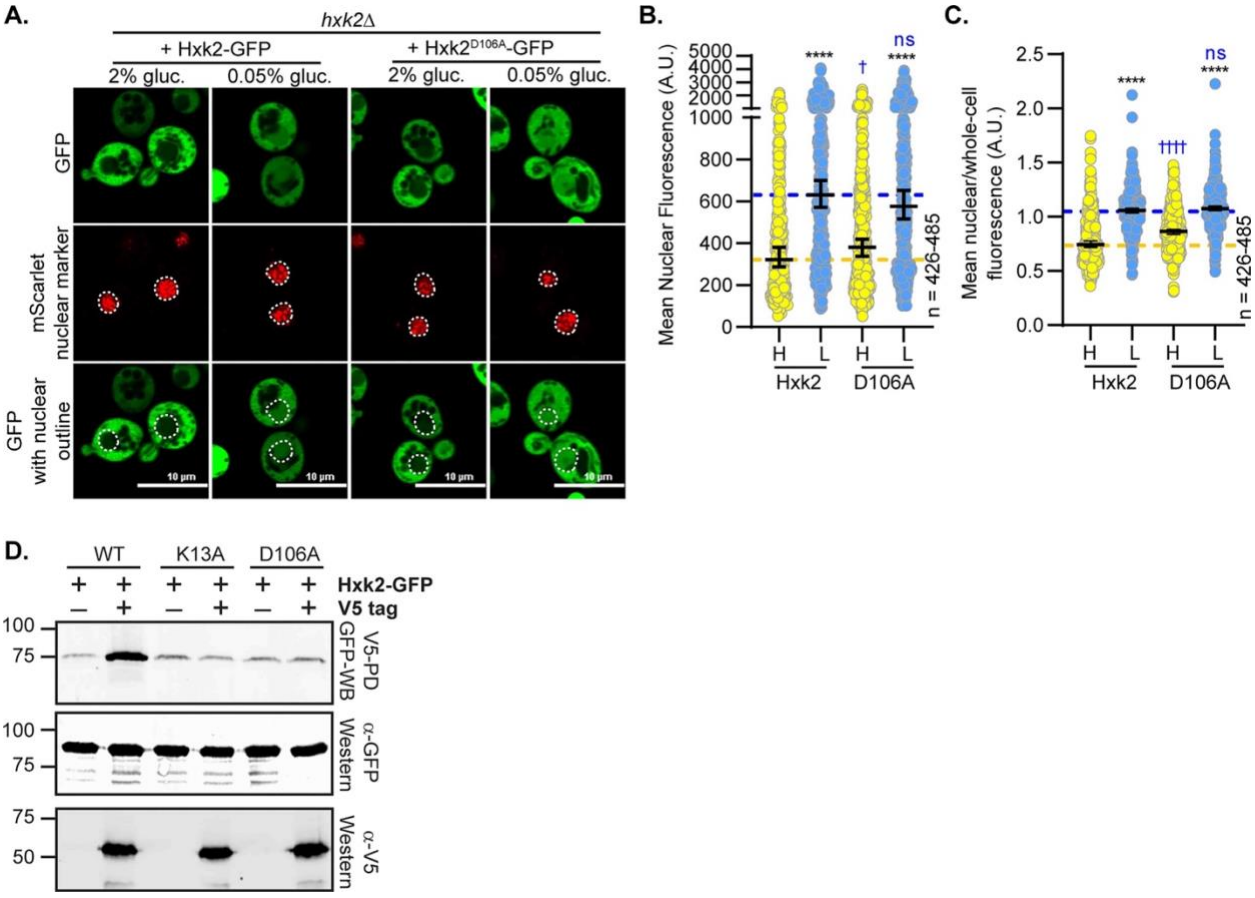

Figure 24. Mutation of D106, which interacts with K13, does not alter Hxk2 nuclear localization but does prevent Hxk2 dimerization.

(A) Confocal microscopy of GFP-tagged Hxk2 or the mutant alleles expressed from a CEN plasmid under the control of the *HXK2* promoter in *hxk2*Δ cells. Co-localization with the nucleus is determined based on overlap with the Tpa1-mScarlet nuclear marker, and a dashed white line indicates the nucleus. (B-C) Automated quantification of imaging shown in (A) to measure (B) mean nuclear fluorescence or (C) the ratio of the mean nuclear/whole-cell fluorescence. Horizontal black lines show the median, and error bars indicate the 95% confidence interval. Dashed yellow and blue lines represent the median value for Hxk2-GFP in high and low glucose, respectively. Black asterisks represent statistical comparisons between low and high glucose for a specific *HXK2* allele, and blue daggers represent statistical comparisons between mutant alleles and the corresponding WT Hxk2 in the same medium condition. (D) Extracts were prepared from yeast cells expressing Hxk2-GFP and Hxk2 with or without the V5 as indicated. Hxk2 proteins contained either the wild-type (WT) sequence or the K13A or D106A mutations. Protein expression was monitored by western blotting (bottom two panels). The association of the tagged proteins was assessed by co-immunoprecipitation using anti-V5 beads followed by western blotting with anti-GFP (top panel). Quantitation of the signal in the top panel is shown.

2.2.9 Tda1, but not Snf1, or Mig1, is required for Hxk2 nuclear accumulation

Many studies have identified Hxk2 S15 phosphorylation [367,378–383]. This site is conserved perfectly in Hxk1, where it is also phosphorylated [367,378–383]. Multiple kinases are linked to Hxk2 S15 phosphorylation, including PKA, Snf1, and Tda1 [247,254,367]. The Snf1 kinase, its substrate Mig1, and Reg1 (an activator of the PP1 protein phosphatase Glc7 that controls Snf1 activity) are thought to interact with Hxk2 to facilitate its nuclear translocation, where they form a large complex that controls Hxk2's alleged moonlighting function as a transcriptional regulator [236–238,254,257].

We examined the impact of Snf1 and Mig1 on Hxk2 nuclear propensity. In the absence of Snf1 or Mig1, there was little change in Hxk2 nuclear localization in glucose-replete or -starvation conditions (Figure 25A-C). Upon glucose starvation, *snf1*Δ and *mig1*Δ cells had slightly reduced

or elevated mean nuclear fluorescence, respectively, compared to WT cells, but these changes were either not significant or just past the significance threshold (Figure 25A-B). When the nuclear to whole-cell fluorescence ratio was considered, *mig1*Δ cells were not different than WT under any condition, while *snf1*Δ cells had increased Hxk2 nuclear balance in high glucose conditions (Figure 25C). These results counter earlier findings, which suggested Mig1 is required for Hxk2 nuclear translocation [236].

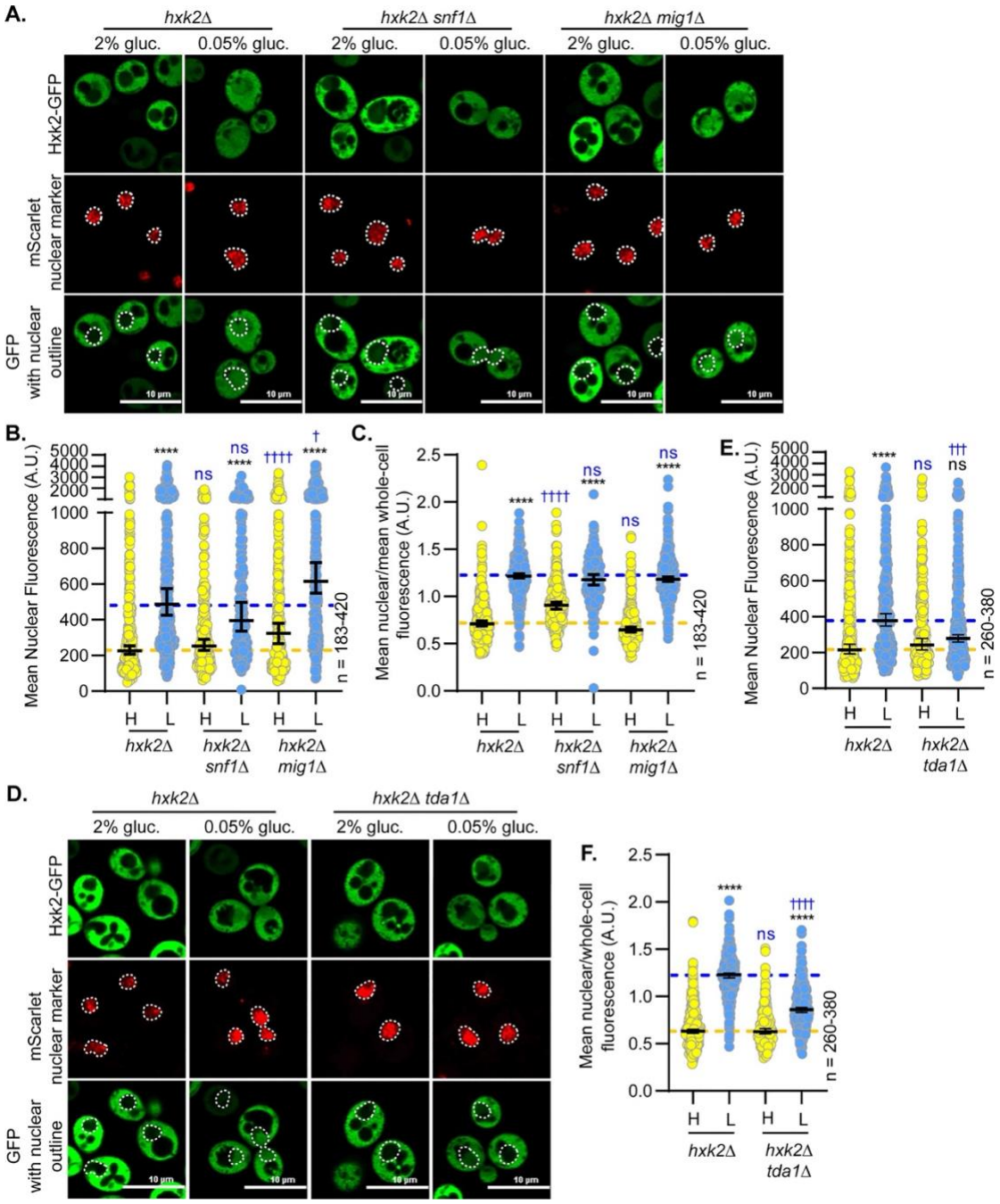

Figure 25. Hxk2 nuclear localization is not regulated by Snf1 or Mig1 but is controlled by the Tda1 kinase.

(A and D) Confocal microscopy of GFP-tagged Hxk2 expressed from a CEN plasmid under the control of the *HXK2* promoter in cells lacking *HXK2* alone or further missing (A) *SNF1* or *MIG1* or (D) *TDA1*. Co-localization with the nucleus is determined based on overlap with the Tpa1-mScarlet nuclear marker, and a dashed white line indicates the nucleus. (B-C; E-F) Automated quantification of the images shown in panels A or D to measure (B or E, respectively) mean nuclear fluorescence or (C or F, respectively) the ratio of the mean nuclear/whole-cell fluorescence. Horizontal

black lines show the median, and error bars indicate the 95% confidence interval. Dashed yellow and blue lines represent the median value for Hxk2-GFP in high and low glucose, respectively. Black asterisks represent statistical comparisons between low and high glucose for a specific *HXK2* allele, and blue daggers represent statistical comparisons between mutant alleles and the corresponding WT Hxk2 in the same medium condition.

We attempted to recapitulate the reported co-purification of Hxk2 with Mig1. However, we could not capture any HA-tagged Mig1 above the weak background signal of bead binding using a Hxk2-V5 pulldown (Figure 26A). Although negative data, they are consistent with our other observations suggesting *mig1*Δ does not impact Hxk2 nuclear translocation.

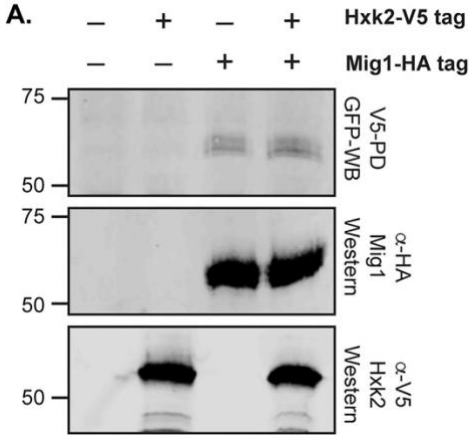

Figure 26. Mig1 does not co-purify with Hxk2.

(A) Mig1 does not associate with Hxk2. Extracts were prepared from yeast cells expressing the untagged Hxk2 or Hxk2 tagged with either V5 and Mig1 untagged or tagged with HA as indicated. Protein expression was monitored by western blotting (bottom two panels). The association of Mig1 with Hxk2 was assessed by co-immunoprecipitation using anti-V5 beads, followed by western blotting with anti-HA (top panel).

The Tda1 kinase is important for phosphorylating Hxk2 S15, thereby preventing Hxk2 dimerization [249,250,264]. Consistent with a role for Tda1 in Hxk2 regulation, glucose-starvation-induced Hxk2 nuclear accumulation was severely dampened in *tda1*Δ cells (Figure

25D-F). Recent biochemical fractionation studies found that Tda1 becomes nuclear in glucose-starved cells [255]. In our experiments, the mNeonGreen-tagged Tda1 signal was low in glucose-replete conditions, with a 3-fold increase in the mean nuclear and whole-cell fluorescence upon glucose starvation (Figure 27A-C). However, the nuclear-to-whole-cell fluorescence ratio was only modestly different in glucose-grown versus -starved cells demonstrating that the nuclear-cytosolic balance of Tda1 was maintained in these two conditions (Figure 27D). Immunoblot analyses showed a significant increase in Tda1-mNG abundance in response to glucose starvation (Figure 27E).

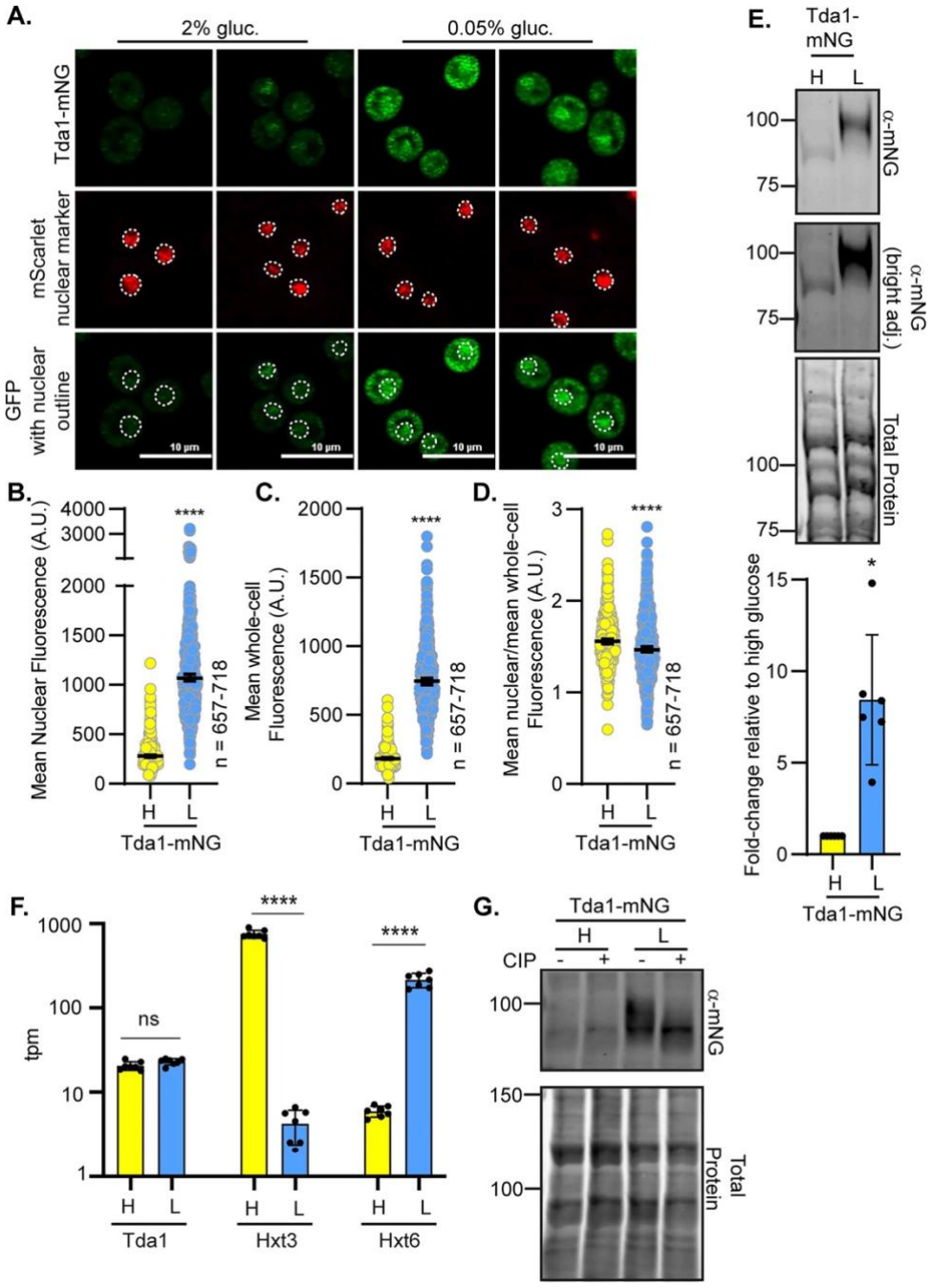

Figure 27. Tda1 protein abundance and phosphorylation are increased in response to glucose starvation.

(A) Confocal microscopy of chromosomally integrated Tda1-mNG. Co-localization with the nucleus is determined based on overlap with the Tpa1-mScarlet nuclear marker, and a dashed white line indicates the nucleus. (B-D) Automated quantification of the images shown in panel A to measure (B) mean nuclear fluorescence, (C) mean whole-cell fluorescence, or (D) the ratio of the mean nuclear/whole-cell fluorescence. Horizontal black lines show the median, and error bars indicate the 95% confidence interval. A Student's t-test was used to assess significance (****

= p-value < 0.0001). (E) Immunoblot analyses of Tda1-mNG in whole-cell protein extracts made from cells grown in high glucose or shifted to low glucose for 2 hours. REVERT total protein stain of the membrane serves as a loading control. One representative blot from 6 biological replicates is shown. Quantification of Tda1-mNG abundance is presented as a fold-change in Tda1 levels after a 2 h shift to low glucose in comparison to glucose-grown cells (high glucose). (F) Yeast mRNA abundance (transcripts per million mapped reads; tpm) was measured by RNAseq in cells grown in high glucose (H) or two hours after shifting to low glucose, L. The mean tpm values (±SD) of multiple replicates for each condition are plotted for three genes: *TDA1*, *HXT3*, and *HXT6*. Statistical differences between the values in high and low glucose are indicated. (G) Whole-cell extracts were made from strains expressing Tda1-mNG and grown in either 2% glucose, H, or shifted for 2 h into low glucose, L (0.05% glucose). Extracts were either treated with calf intestinal alkaline phosphatase (CIP) or incubated in the same conditions without enzyme (mock), resolved by SDS-PAGE, and immuno-blotted with anti-mNG antibody. REVERT total protein stain is shown as a loading control. Molecular weights are shown on the left side in kDa.

Increased Tda1 levels were not driven by elevated transcription, as RNAseq analyses showed no change in TDA1 transcript abundance for cells grown in 2% or 0.05% glucose (Figure 27F), unlike the glucose-responsive transcripts of hexose transporters 3 and 6 (*HXT3* and *HXT6*, respectively) shown as controls. As expected [384,385], *HXT3* transcripts were reduced upon glucose starvation, and *HXT6* transcripts increased (Figure 27F). The increased Tda1 could be due to altered translation or a change in protein stability/regulation.

Consistent with altered regulation, immunoblots showed a sizeable shift to a slower-mobility Tda1 in low-glucose conditions (Figure 27E). This mobility change was due to phosphorylation, as incubation with phosphatase generated a single band that migrated like Tda1 in glucose-grown cells (Figure 27G). Recent studies identified several Snf1-dependent phosphorylation sites in Tda1, so perhaps the increased phosphorylation of Tda1 under glucose starvation conditions is partially regulated by Snf1 [386]. We propose that Tda1 is required for

Hxk2 nuclear accumulation in glucose-starved cells. Tda1 is a glucose-regulated kinase, and glucose starvation increases its protein abundance and phosphorylation. Elevated Tda1 levels likely reflect post-transcriptional regulation since Tda1 transcript abundance is unchanged in glucose-starved cells.

We next examined the impact of Hxk2 mutations on Tda1-dependent Hxk2 nuclear translocation. As before, Hxk2 accumulation in the nucleus was blunted in glucose-starved tda1Δ cells (Figure 25D-F and 28A-C). However, the S15D mutation restored glucose-starvation-induced Hxk2 nuclear localization in *tda1*Δ cells (Figure 28A-C). The balance of $Hxk2^{S15D}$ or $Hxk2^{S15A}$ nuclear-to-whole-cell fluorescence ratios in *tda1*Δ cells was similar to those of Hxk2 in wild-type cells but shifted higher in $Hxk2^{S15D}$ *tda1*Δ or $Hxk2^{S15D}$ *tda1*Δ cells in high glucose conditions. Unlike $Hxk2^{S15D}$ or $Hxk2^{S15A}$, the $Hxk2^{K13A}$ mutation bypassed both Tda1 and glucose-starvation regulation. $Hxk2^{K13A}$ was nuclear in glucose-grown *tda1*Δ cells, though its overall nuclear abundance was somewhat reduced compared to glucose starvation (Figure 28B), and $Hxk2^{K13A}$ retained a larger nuclear pool than WT Hxk2 in both glucose-grown and -starved cells (Figure 28A-C). There were no changes in the free-GFP breakdown product at 2 h post low glucose shift in the *tda1*Δ cells containing K13A (Figure 21G).

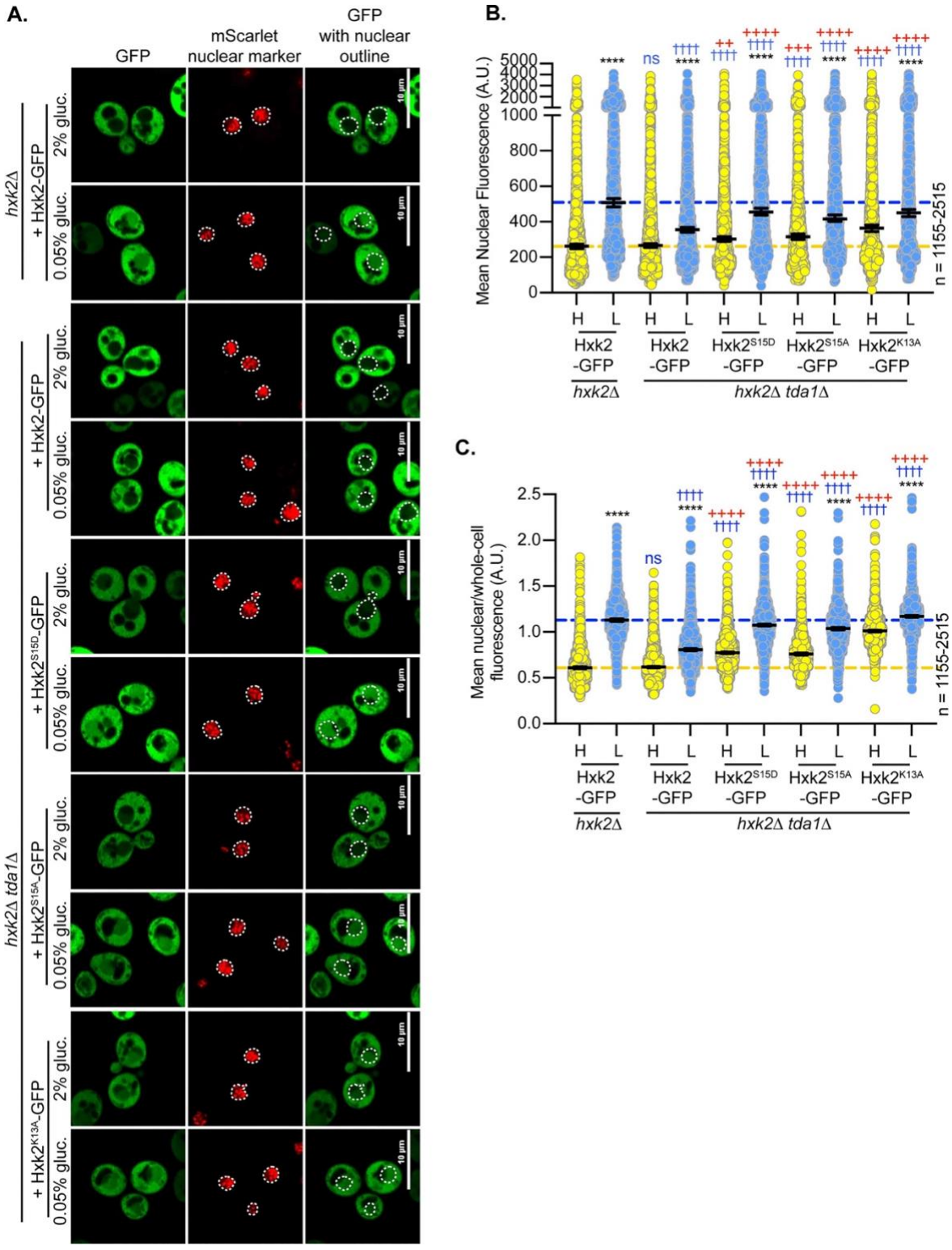

Figure 28. Mutating Hxk2 S15 to aspartic acid rescues the impaired nuclear localization caused by a *tda1*Δ.

(A) Confocal microscopy of GFP-tagged Hxk2 and S15D mutant expressed from a CEN plasmid under the control of the *HXK2* promoter in cells lacking *HXK2* alone or with the additional deletion of *TDA1*. Co-localization with the

nucleus is determined based on overlap with the Tpa1-mScarlet nuclear marker, and a dashed white line indicates the nucleus. (B-C) Automated quantification of the images shown in panel A to measure (B) mean nuclear fluorescence or (C) the ratio of the mean nuclear/whole-cell fluorescence. Horizontal black lines show the median, and error bars indicate the 95% confidence interval. Dashed yellow and blue lines represent the median value for Hxk2-GFP in high and low glucose, respectively. Black asterisks represent statistical comparisons between low and high glucose for a specific *HXK2* allele. Blue daggers represent statistical comparisons between mutant alleles and the corresponding WT Hxk2 in the same medium condition. Red crosses represent statistical comparisons between WT Hxk2 and mutants in the *hxk2*Δ *tda1*Δ background in the same media condition.

Although the Hxk2^{S15D} mutation restored nuclear localization in glucose-starved *tda1*Δ cells, this mutation had a different effect in *snf1*Δ cells (Figure 29A-C). We observed a higher nuclear-to-whole-cell ratio in glucose-grown *snf1*Δ cells expressing Hxk2^{S15D} than wild-type Hxk2 (Figure 29C). Interestingly, this increase in nuclear-to-whole-cell fluorescence was not driven by higher mean nuclear fluorescence, which is the same for Hxk2^{S15D} and Hxk2 in *snf1*Δ or wild-type cells (Figure 29B). These findings suggest the S15D mutation bypasses Tda1 regulation, restoring glucose-regulated Hxk2 nuclear accumulation. However, unlike the Hxk2^{K13A} mutant, the Hxk2^{S15D} mutation does not alter Hxk2 localization in glucose-grown cells.

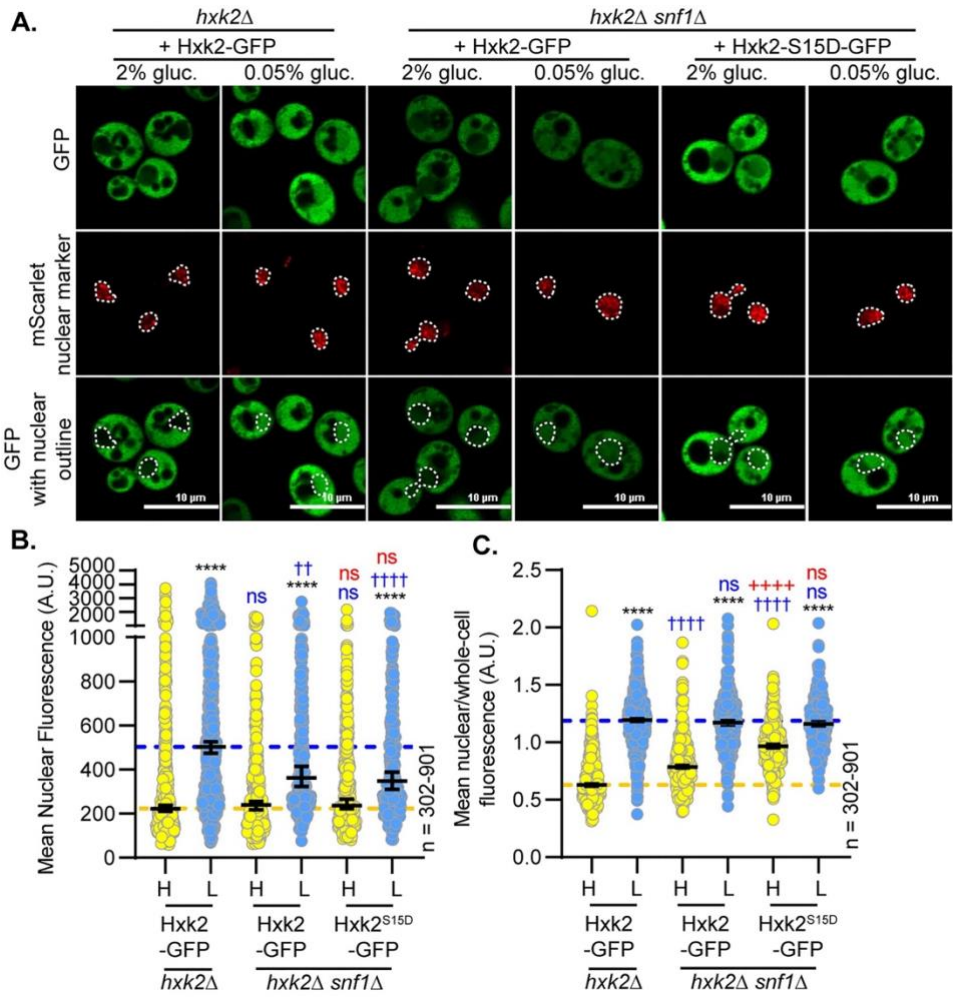

Figure 29. Hxk2 nuclear translocation is still regulated in a *snf1*Δ background, independent of S15 phosphorylation status.

(A) Confocal microscopy of GFP-tagged Hxk2 and S15D mutant expressed from a CEN plasmid under the control of the *HXK2* promoter in cells lacking *HXK2* alone or with the additional deletion of *SNF1*. Co-localization with the nucleus is determined based on overlap with the Tpa1-mScarlet nuclear marker, and a dashed white line indicates the nucleus. (B-C) Automated quantification of the images shown in panel A to measure (B) the mean nuclear fluorescence or (C) the mean nuclear/whole-cell fluorescence ratio. Horizontal black lines show the median, and error bars indicate the 95% confidence interval. Dashed yellow and blue lines represent the median value for Hxk2-GFP in high and low glucose, respectively. Black asterisks represent statistical comparisons between low and high glucose for a specific *HXK2* allele. Blue daggers represent statistical comparisons between mutant alleles and the

corresponding WT Hxk2 in the same medium condition. Red crosses represent statistical comparisons between WT Hxk2 and Hxk2^{S15D} in the *hxk2*Δ *snf1*Δ background in the same media condition.

Since Hxk2^{S15D}, Hxk2^{D106A}, and Hxk2^{K13A} all disrupt Hxk2 dimerization *in vivo*, yet only Hxk2^{K13A} prevents glucose-regulated nuclear exclusion, Hxk2 monomer-dimer balance cannot the only thing controlling Hxk2 nuclear partitioning. Hxk2^{S15D}, which is monomeric, does not change Hxk2 nuclear partitioning in glucose-grown cells. Instead, it is only important for glucose-starvation-induced Hxk2 nuclear localization in the *tda1*Δ. In contrast, Hxk2^{K13A}, which is also monomeric, bypasses the glucose regulation of Hxk2 nuclear partitioning and this is not altered by modification at S15.

2.2.10 Role of Hxk2 in regulating glucose-repression of gene expression

Earlier studies proposed that Hxk2 is a subunit of a DNA-bound repressor complex that regulates glucose repression of gene expression [238,261]. We performed RNA-seq analyses of the yeast transcriptome in wild type and *hxk2*Δ cells grown in high glucose or shifted to glucose-limiting conditions (0.05% glucose) for two hours. RNA samples were prepared in triplicate, and the log2+1 ratios (low glucose/high glucose) for the mean abundance of each mRNA were plotted (Figure 30A-D). As reported previously [224,231], the yeast transcriptome undergoes large-scale changes in transcript levels in response to glucose limitation, with >15% of the transcripts showing a 4-fold or higher change in abundance (Figure 30A). Notably, large changes (both increases and decreases) in the abundance of the hexose transporter (HXT) mRNAs were observed, as well as a decrease in the abundance of ribosomal protein mRNAs. A comparable pattern, scale, and scope of mRNA abundance changes were observed in the RNA samples generated from *hxk2*Δ cells

(Figure 30B), demonstrating that the Hxk2 protein is not required for the global transcriptional response to changes in glucose abundance. Replotting these values to show the ratio of mRNA abundance (*hxk2*Δ/wild type) in high glucose (Figure 30C) and low glucose (Figure 30D) further demonstrated that *HXK2* deletion impacts very few mRNAs. Previous studies have suggested that Hxk2 is involved in glucose repression based on changes in a small number of genes (*SUC2*, *HXT1*, *HXK1*, *CYC1*, etc.) [230,261,384]. We also see similar expression changes in our RNAseq data with *hxk2*Δ to those previously reported (Figure 31A). However, we find that glucose repression is largely unaffected by *hxk2*Δ, suggesting that the small number of genes whose transcription changes in *hxk2*Δ cells are not representative of a global loss of glucose repression. A violin plot of the log2+1 ratios from this experiment demonstrated the large and similar response to glucose limitation in both wild-type and *hxk2*Δ cells (Figure 30E). By comparison, the difference between wild-type and *hxk2*Δ cells under these conditions was modest, with nearly no 2-fold or greater changes in transcript abundances (Figure 30E). Next, we plotted the mean mRNA abundance of the top 20 glucose-repressed genes in high and low glucose in wild type and *hxk2*Δ cells (Figure 30F). Glucose repression and derepression of these mRNAs were not affected by deletion of *HXK2*, even for the genes whose promoters are bound by the Mig1 protein [263]. When we analyzed Mig1-regulated genes [263] with a 2-fold or greater change in transcript abundance in response to low glucose, we found no evidence that any of these were altered in *hxk2*Δ cells (Figure 31B). These data support a model where Hxk2 is not a transcriptional regulator, and does not regulate glucose repression.

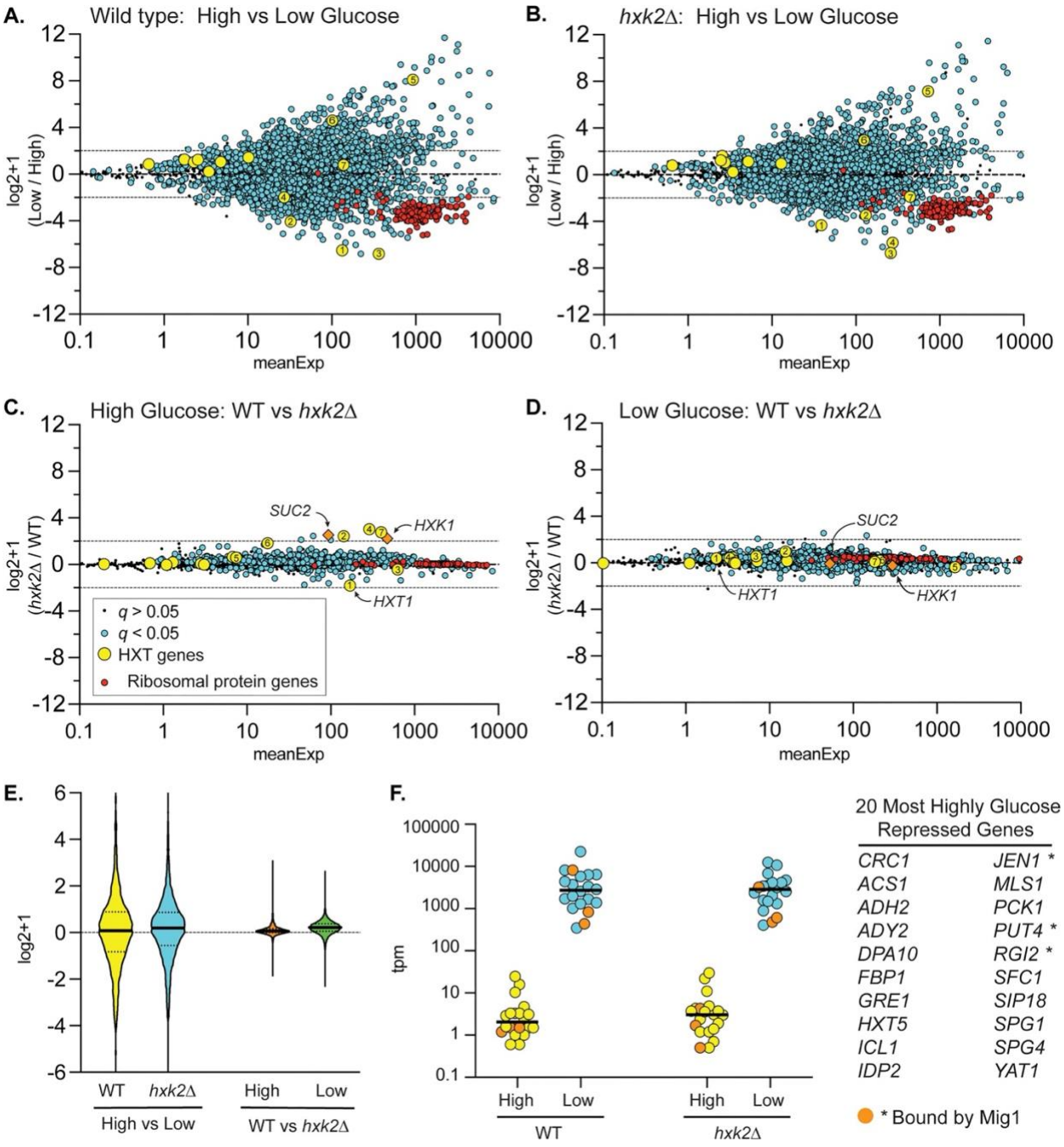

Figure 30. Effect of Hxk2 on the transcriptional response to glucose limitation.

Total RNA was collected from 3 independent cultures of wild-type cells or *hxk2*Δ cells grown to mid-log phase in high glucose or two hours after shifting to low glucose. mRNA abundance (tpm) for all genes was determined by RNAseq and is plotted as the mean expression level (x-axis) versus the log2+1 value of the ratio of the mean value in low glucose divided by the mean value in high glucose (A and B) in wild type (A) or *hxk2*Δ cells (B). The same data are replotted, showing the log2+1 ratio of hxk2 and wild-type cells in high (C) and low glucose (D) conditions. In

each plot, statistical significance was defined as a false discovery rate (q) less than 0.05. Log2+1 values deemed significant were plotted as blue circles, while those failing to meet this threshold were plotted as smaller black dots (see key). *HXT* gene mRNAs were plotted as yellow circles with the number referring to the specific *HXT* gene. Ribosomal mRNA genes were plotted as red circles. The known Hxk2-regulated genes, *SUC2* and *HXK1*, were plotted as orange diamonds. (E) Violin plot of these data showing the relative magnitude of glucose limitation (high vs. low) and hxk2 deletion (WT vs. *hxk2*Δ). (F) The top 20 glucose-repressed genes (listed at right) are plotted based on their TPMs from both high glucose (yellow) and low glucose (blue) conditions. Three of these genes (indicated by * in the table at right and shown as orange-filled circles on the plot) are reported to have Mig1 bound in their promoters based on ChIP-Seq.

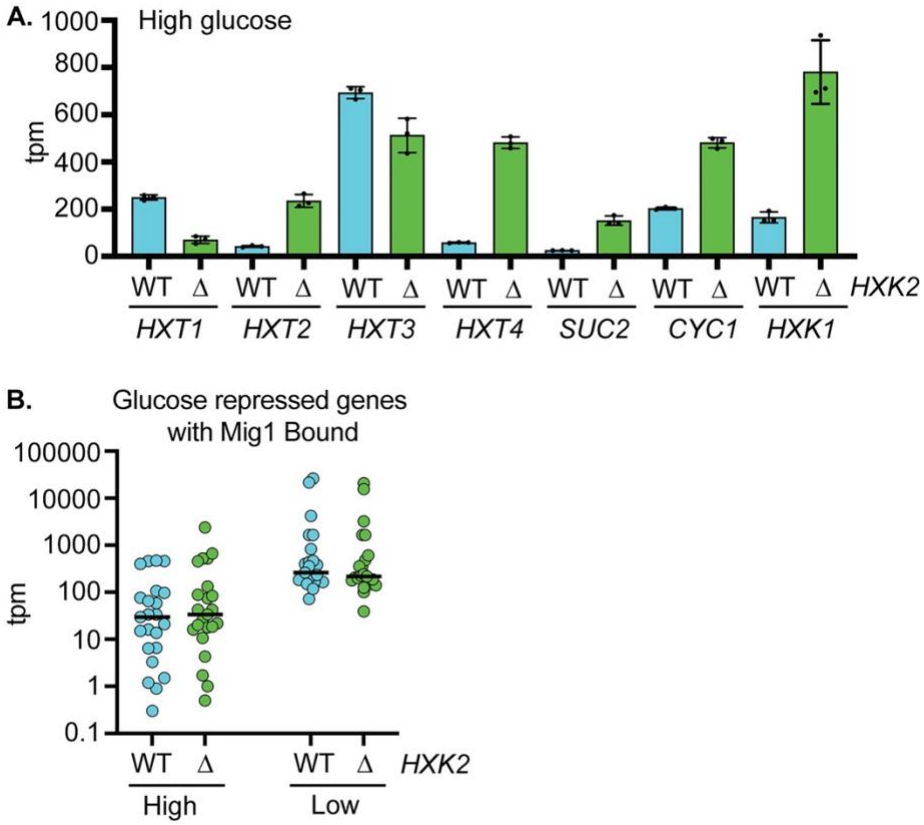

Figure 31. Loss of Hxk2 modestly alters the expression of some glucose-regulated genes, but it does not alter Mig1-induced transcription in response to low glucose.

(A) Analysis of transcript abundances (tpm) for the genes indicated in either WT cells or those lacking *HXK2* in high glucose. The genes indicated are selected as they have previously been shown to have some altered expression in

*hxk2*Δ cells. We suggest that these modest changes are not due to defective glucose repression but instead are secondary compensation mechanisms for the loss of hexokinase. (B) We took the high-confidence set of genes identified as regulated by Mig1 [266] and then determined which had increased expression (>2-fold) in response to low glucose. We plotted the average tpm values for these genes from WT or *hxk2*Δ cells grown in high glucose or shifted into low glucose. We find little to no difference in the Mig1-regulation of glucose repression in *hxk2*Δ cells compared to WT cells.

2.3 Discussion

Glucokinases and hexokinases are central metabolic regulators that convert glucose to G6P, the first step in glycolysis. In addition to cytosolic functions in glycolysis, each enzyme of this pathway can accumulate in the nucleus. For mammalian and plant hexokinases, nuclear accumulation typically occurs in glucose starvation or other stress conditions [64,65,69,70,213]. What is the nuclear function of glycolytic enzymes? Perhaps they act together in nuclear glycolysis to regulate a nuclear pool of ATP or NADH [203,249]. Alternatively, could they have a nuclear role in regulating gene expression or other facets of nuclear biology? The nuclear function of many glycolytic enzymes remains unclear [203]. For a handful of examples, there is evidence for diverse roles that involve altering transcription factor function, associating with RNA polymerase III, interacting with DNA, regulating nuclear ubiquitin ligases, stimulating DNA polymerase, and protecting telomeres [205–209]. In some instances, the metabolic products generated by glycolytic enzymes may be the active nuclear component rather than the proteins [210]. Much remains to be discovered about the "moonlighting" nuclear activities of glycolytic enzymes.

In studies of hexokinase localization, *S. cerevisiae* and *C. albicans* hexokinase 2 have been outliers. Their nuclear accumulation reportedly occurs in glucose-replete rather than starvation

conditions [236,254,259,260,368]. However, the methodologies used in early imaging studies involved cells pre-incubated in a way that would induce glucose starvation. This confounds the interpretation of these studies, especially if the incubation time in the glucose-starvation medium was not regimented [236,254,259,260,368].

2.3.1 Contrasts between our findings and the existing model for Hxk2 nuclear regulation

Here we report high-resolution, live-cell, confocal microscopy of fluorescently tagged Hxk2 performed in high (2% glucose) and low (0.05% glucose) glucose medium. Our findings support a new model for Hxk2 nuclear translocation and suggest that in yeast, Hxk2 accumulates in the nucleus under glucose-starvation conditions, not in glucose-replete conditions. This is consistent with a conserved model for glucose-regulated hexokinase nuclear localization spanning the ~1 billion years of evolution that separate yeasts and humans [387,388].

In contrast to earlier models, we find that: (1) Mig1 is not required for Hxk2 nuclear translocation; (2) the previously reported NLS/Mig1 binding site (amino acids 7–16) is not required for Hxk2 nuclear translocation but instead maintains a glucose-regulated, nuclear-excluded pool of Hxk2; (3) Snf1 is not required for glucose-regulated nuclear localization of Hxk2; (4) phosphorylation of S15, though a key regulator of the Hxk2 monomer-dimer balance, is not required for glucose-regulated Hxk2 nuclear accumulation; and (5) except for modest changes in a handful of transcripts, Hxk2 is not required to maintain glucose-repression of transcription.

The past model for Hxk2 nuclear shutting was based on studies from a single lab that others have not corroborated. For example, large-scale protein-protein association studies using TAP-purification and mass spectrometry [241,242] or global two-hybrid screens [243,244] have not detected Hxk2 association with the components of the proposed Hxk2 nuclear complex. Targeted

studies from other labs have not provided secondary confirmation of this Hxk2-containing complex or the glucose-stimulated nuclear translocation of Hxk2. Comprehensive ChIP-Seq data fail to identify this complex at the *SUC2* promoter [263], a gene regulated by glucose repression whose transcription is reportedly controlled by Hxk2 [238,261,389,390]. The role of S15 phosphorylation in regulating Hxk2 nuclear translocation has been openly questioned [264]. Our data, together with these observations, suggest that the previous model of Hxk2 nuclear accumulation in yeast is not correct.

2.3.2 A new model for regulation of Hxk2 nuclear translocation

Based on our studies, we propose a new model for glucose-regulated Hxk2 nuclear accumulation (Figure 32). In a glucose-replete environment (Figure 32A), the Glc7-Reg1 phosphatase is active, maintaining inactive Snf1 [47,49]. The Tda1 kinase, though transcribed, is in low abundance in cells grown in 2% glucose, suggesting it is either not translated or is an unstable protein. Under these conditions, Hxk2 S15 is not phosphorylated, and Hxk2 exists in cells as a balance between monomer and dimer species [252,253].

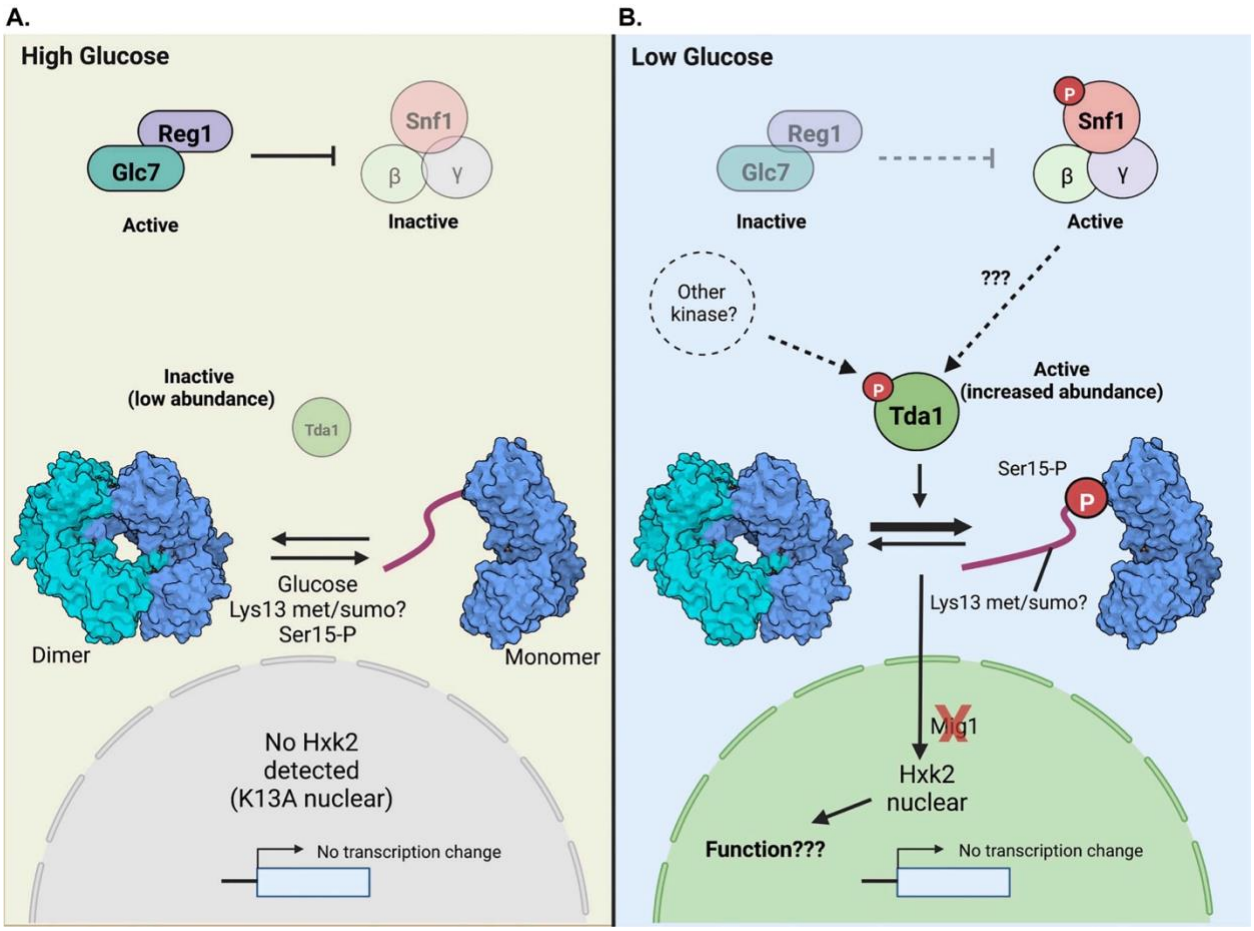

Figure 32. Model for glucose-regulation of Hxk2 nuclear accumulation and dimerization.

(A) A schematic of key regulatory factors and their function when cells are grown in glucose replete (referred to as high glucose) conditions. For cells grown in glucose, the Reg1-Glc7 protein phosphatase complex is active, and this dephosphorylates Snf1 to keep it inactive. The impact of this regulation on Tda1 is currently unclear. The Tda1 kinase is present in cells at very low levels and is an inactive kinase. Glucose binding to the Hxk2 dimer (the two Hxk2 monomers are shown in light and dark blue, respectively) stimulates monomer formation, as does mutation of the enzyme at S15, K13 and D106. Under these conditions, no nuclear Hxk2 is detected unless the K13A mutant is present, which somehow inactivates the glucose-induced block to Hxk2 nuclear accumulation. From the RNA-seq analyses, Hxk2 does not regulate glucose-repressed gene expression. (B) A schematic of key regulatory factors and their function when cells are glucose starved (referred to as low glucose). Under these conditions, Reg1-Glc7 is inactivated. However, we find that Reg1 is needed for Hxk2 nuclear translocation in this condition, but the mechanism underlying this requirement is unclear. Snf1 kinase is phosphorylated and activated. It is unclear if Snf1 is responsible for phosphorylating Tda1 to activate it kinase. While loss of Snf1 did not alter Hxk2 nuclear accumulation in low glucose,

prior work demonstrates that Snf1 controls Tda1 phosphorylation in alternative carbon sources and that loss of Snf1 reduces the amount of Hxk2 monomer in cells. If Snf1 is involved in this pathway, its function may be redundant with other kinases that operate in this pathway. In glucose starvation conditions, the abundance of Tda1 increases dramatically, and Tda1 is phosphorylated and activated. Phosphorylation of Hxk2 by Tda1 at S15 regulates the Hxk2 dimer to monomer transition. Tda1 is required for Hxk2 nuclear translocation, but Mig1 and Snf1 are not needed. Hxk2 phosphorylation at S15 reduces the capability of Hxk2 to dimerize by more than 1000-fold [253]. This stabilization of the monomeric species could allow for additional modifications at the Hxk2 N-terminus. Notably, K13 is reportedly dimethylated or sumoylated [375,376]. However, the K13R mutant, which would block sumoylation at this site, also promotes nuclear localization of Hxk2 in high glucose conditions. Thus, sumoylation cannot be required for the nuclear translocation but could be important for preventing Hxk2 nuclear localization in high glucose. Methylation can occur on either K or R residues, thus the K13R mutation does not necessarily prevent this modification. Once in the nucleus, Hxk2 does not significantly impact transcription regulation. Based on our RNA-seq analyses, there is little difference between the expression profiles of WT vs. *hxk2*Δ cells glucose starvation conditions. The function of nuclear Hxk2 remains to be determined.

We find that Hxk2 shifts to a monomer when glucose binds, confirming earlier studies that demonstrate a dramatic decrease in the association constant of Hxk2 dimers when glucose is present [252]. Molecular dynamics simulations provide insight into why glucose might favor Hxk2 monomer formation (Figure 18). In our simulations, bound glucose impacts multiple electrostatic interactions between the opposite monomer's N-terminal tail and the catalytic pocket, which may promote Hxk2 dimer dissociation. Our experimental evidence confirms that the N-terminal tail is critical for dimerization. Deleting amino acids 7–16 or mutating K13 to alanine both give rise to monomeric Hxk2. Disrupting the K13-D106 salt bridge at the dimer interface by alanine substitution at D106 also breaks the dimer but does not stimulate the nuclear accumulation of Hxk2 in glucose-replete conditions.

Hxk2 monomer-dimer balance is likely an important facet of Hxk2 regulation, but it is not responsible for Hxk2 nuclear translocation. Mutations that induce monomer formation do not all stimulate Hxk2 nuclear accumulation. For example, Hxk2^{S15D} and Hxk2^{D106A} both fail to dimerize but retain glucose-regulated nuclear translocation. On the other hand, Hxk2^{K13A} and Hxk2$^{\Delta 7–16}$, which also fail to dimerize, lose glucose-regulated Hxk2 nuclear exclusion. The K13R mutation gives rise to a nuclear pool of Hxk2 in high glucose conditions. These experiments identify the Hxk2 N-terminal region as key in regulating Hxk2 nuclear localization, but via a completely different mechanism than that proposed in earlier studies [236,258]. In the absence of Hxk2, glucose repression of transcription is intact; only a few transcripts show minimal changes compared to wild-type cells (Figure 32).

In response to glucose starvation (Figure 32B), the Glc7-Reg1 phosphatase is inactive, and the Snf1 kinase is activated by phosphorylation [47,49]. However, the loss of Snf1 or its substrate Mig1 does not alter the formation of the nuclear Hxk2 pool. Similarly, the Tda1 kinase is required for starvation-induced Hxk2 nuclear accumulation. When glucose is limiting, Tda1 protein levels rise, not because of altered transcription but due to increased protein stability or elevated translation. Tda1 is phosphorylated in these conditions, which activates the kinase towards histone substrates [255]. In cells starved for glucose, Tda1 phosphorylates Hxk2 at S15 and this modification disrupts the dimer in favor of monomeric Hxk2 [247,249]. The primary role of Tda1 in glucose-starved Hxk2 regulation may be to promote Hxk2 monomer formation, as both the S15A and S15D mutants, which each disrupt the dimer, were able to restore nuclear partitioning in *tda1*Δ cells.

A second layer of glucose-induced regulation must exist for Hxk2 because Hxk2^{S15D} and Hxk2^{S15A}, unlike Hxk2^{K13A}, remain nuclear excluded in glucose-grown cells. In contrast, deleting

the N-terminal amino acids 7–16 or changing K13 to alanine bypasses this glucose regulation. Nuclear Hxk2 accumulation in glucose-starvation conditions is not needed for transcriptional changes, as there were little to no differences in gene expression between wild-type and *hxk2*Δ cells. Given that Hxk2 does not substantially impact global gene expression, future studies must determine its nuclear function in *S. cerevisiae*.

2.3.3 Comparison of *Sc*Hxk1 and *Sc*Hxk2

The first 20 amino acids that seem important for regulating Hxk2 nuclear exclusion in high glucose are perfectly conserved in Hxk1 (Figure 22A). Hxk1 and Hxk2 are paralogs, arising from the whole-genome duplication and sharing a high degree of conservation (Figure 16A-B). What then drives this nuclear partitioning for Hxk2, which does not seem to occur for Hxk1? Perhaps the answer lies in posttranslational modifications of these two enzymes. For the conserved K13 residue in Hxk1 and Hxk2, there is a differential modification with K13 being ubiquitinated in Hxk1 while this residue is sumoylated or dimethylated in Hxk2 [375–377]. However, if ubiquitination at K13 was required for Hxk1 nuclear exclusion, the K13A mutation we generated should have prevented this modification and permitted nuclear accumulation. However, this was not the case. The K13A mutation in Hxk2 breaks the dimer and would also prevent sumoylation and dimethylation. Since this mutant always has a nuclear-localized pool, irrespective of glucose quantity, perhaps modification at this site is needed to maintain the nuclear exclusion of Hxk2. With the K13R mutation, glucose has lost its ability to restrict the nuclear accumulation of Hxk2. This mutation likely maintains the monomer-dimer balance but would prevent sumoylation and have a somewhat unclear impact on methylation (i.e., arginine residues can be methylated, but arginine methylation uses different enzymes than lysine methylation and so it seems unlikely that

this would be the case). If sumoylation or methylation at K13 in Hxk2 is needed for its glucose-induced nuclear restriction, then loss of these modifications may explain why K13A and K13R accumulate in the nucleus.

2.3.4 Regulation of hexokinase nuclear localization in mammals

Most isoforms of hexo- and glucokinase in mammals and plants translocate to the nucleus. However, in many instances, the nuclear function is poorly understood [203]. Glucokinase (GCK) regulation by glucokinase regulatory protein (GKRP) is one interesting example of nuclear regulation in mammals [216]. GCK is an important regulator of glucose balance that controls glucose metabolism in the liver and pancreas and regulates insulin secretion from β-islet cells [156,216,391]. In response to glucose starvation, GCK in the liver binds to GKRP, which competitively inhibits glucose binding [392]. When bound to GKRP, GCK translocates into the nucleus, where it serves as a reservoir of inactive GCK that can be rapidly remobilized to the cytosol when glucose becomes available [216,392].

No yeast equivalent of GKRP has been identified, and it is unclear if Hxk2 nuclear accumulation could act as a reservoir for Hxk2 function. It seems unlikely that nuclear Hxk2 would follow this “nuclear storage model” because after prolonged starvation there is still a lot of Hxk2 the cytoplasm (Figure 13B). In addition, Hxk1 and Glk1 are both expressed in response to glucose starvation and so they can phosphorylate glucose in these conditions, negating the need for a return of Hxk2 to the cytosol.

Human HKII, the isoform with the highest sequence homology to Hxk1 and Hxk2, localizes to the mitochondria in glucose-replete conditions but then translocates to the nucleus in some cancer cells [64,65,68,70]. In one case, this HKII nuclear translocation is associated with the

apoptosis-inducing factor (AIF) and phosphorylated p53, a tumor suppressor [70,174]. HKII moves with these factors from the mitochondria to the nucleus to trigger apoptosis. In yeast, Aif1 is the yeast ortholog of mammalian AIF, and loss of Hxk2 is suggested to induce apoptosis via an Aif1-dependent mechanism [393,394]. It is unclear if, like the mammalian model, Hxk2 is involved in the nuclear transition of Aif1 in yeast.

Others have found ~10% of Hxk2 activity is mitochondrially associated in yeast [395]. Mass spectroscopy aimed at identifying the mitochondrial proteome under glucose-replete conditions and in alternative carbon sources further supports the presence of a mitochondrial pool of Hxk1 and Hxk2 [396]. We did not observe a distinct mitochondrial pool of Hxk2, but the bright cytosolic Hxk2 could have masked it. Perhaps a preexisting mitochondrial Hxk2 gives rise to nuclear Hxk2 in glucose-starvation conditions, as can be the case for mammalian HKII [393,394].

2.4 Materials & Methods

2.4.1 Yeast strains and growth conditions

Yeast strains are summarized in Table 3 and are typically derived from the BY4742 background of *S. cerevisiae*. Where indicated, yeast were grown in synthetic complete (SC) medium lacking the appropriate amino acid for plasmid selection [397] with ammonium sulfate as a nitrogen source, or in yeast peptone dextrose (YPD). Plasmids were introduced into yeast using lithium acetate transformation [398]. Unless indicated, yeast cells were grown at 30°C. For experiments where cells were shifted into low glucose medium, yeast cells were first grown to mid-log phase in SC medium with 2% glucose (high glucose medium). Next, cells were washed

into 0.05% glucose medium (low glucose medium), resuspended low glucose medium and incubated for 2 hours at 30°C unless otherwise indicated.

To assess whether Hxk2 mutants were enzymatically active in cells, we performed growth assays in cells lacking chromosomal *HXK1*, *HXK2*, and *GLK1* genes. Cells lacking these hexokinases fail to grow on a glucose-containing medium because they cannot phosphorylate glucose, which is required for glycolysis [228]. These *hxk1*Δ *hxk2*Δ *glk1*Δ cells were grown in SC media containing 2% (w/v) galactose as a carbon source. Cells were transformed with plasmids expressing the genes encoding hexokinase proteins (wild type or mutant) or an empty vector. To assay hexokinase function, we grew cells in 96-well plates with media containing galactose and then inoculated them into SC media with glucose. Absorbance at 600 nm was determined using a Synergy 2 plate reader (BioTek).

Table 3. Yeast strains used in this study

Strain	Genotype	Source
BY4742	*MAT* α *his3Δ1 leu2Δ0 lys2Δ0 ura3Δ0*	[399]
MSY1212	*MAT* **a** *ura3-52 leu2Δ1 his3Δ200*	[245]
AFO3935	*MAT* α *ura3Δ0 leu2Δ0 his3Δ1 hxk2Δ::KANMX4 TPA1-mScarlet::HYGRO*	This study. Using the Tpa1-mScarlet strain from the mScarlet C-SWAT collection [400], we PCR amplified the mScarlet::HYGRO cassette using primers with homology to the C-terminal and downstream regions of the Tpa1 coding sequence. We transformed the Tpa1-mScarlet::HYGRO cassette into MSY1254 [224]. We then validated that the mScarlet::HYGRO cassette was integrated next to Tpa1 using a PCR-based approach.
AFO4345	*MAT* α *ura3Δ0 leu2Δ0 his3Δ1 hxk2Δ::KANMX4 tda1Δ::NAT TPA1-mScarlet::HYGRO*	This study. Using the Tpa1-mScarlet strain from the mScarlet C-SWAT collection [400] we PCR amplified the mScarlet::HYGRO cassette using primers with homology to the regions upstream and downstream of the Tpa1 coding sequence. Using pBB1 as a template, we PCR amplified the NAT cassette using primers with homology to the regions upstream and downstream of

		the Tda1 coding sequence. We transformed the Tpa1-mScarlet::HYGRO cassette into MSY1254 [224]. We then validated that the mScarlet::HYGRO cassette was integrated next to Tpa1 and the NAT drug resistance marker replaced the endogenous *TDA1* gene using a PCR-based approach.
AFO4354	*MAT α ura3Δ0 leu2Δ0 his3Δ1 met15Δ0 hxk1Δ::KAN TPA1-mScarlet::HYGRO*	This study. Using the Tpa1-mScarlet strain from the mScarlet C-SWAT collection [400], we PCR amplified the mScarlet::HYGRO cassette using primers with homology to the C-terminal and downstream regions of the Tpa1 coding sequence. We transformed the Tpa1-mScarlet::HYGRO cassette into RG5867 [224]. We then validated that the mScarlet::HYGRO cassette was integrated next to Tpa1 using a PCR-based approach.
AFO4547	*MAT α ura3Δ0 leu2Δ0 his3Δ1 glk1Δ::KAN TPA1-mScarlet::HYGRO*	This study. Using the Tpa1-mScarlet strain from the mScarlet C-SWAT collection [400], we PCR amplified the mScarlet::HYGRO cassette using primers with homology to the C-terminal and downstream regions of the Tpa1 coding sequence. We transformed the Tpa1-mScarlet::HYGRO cassette into MSY1471 [224]. We then validated that the mScarlet::HYGRO cassette was integrated next to Tpa1 using a PCR-based approach.
MSY1475	*MAT α ura3Δ0 leu2Δ0 his3Δ1 met15Δ0 hxk1Δ::KAN hxk2Δ::KAN glk1Δ::KAN*	[224]
AFO3936	*MAT α ura3Δ0 leu2Δ0 his3Δ1 met15Δ0 hxk1Δ::KAN hxk2Δ::KAN glk1Δ::KAN TPA1-mScarlet::HYGRO*	This study. Using the Tpa1-mScarlet strain from the mScarlet C-SWAT collection [400], we PCR amplified the mScarlet::HYGRO cassette using primers with homology to the C-terminal and downstream regions of the Tpa1 coding sequence. We transformed the Tpa1-mScarlet::HYGRO cassette into MSY1475 [224]. We then validated that the mScarlet::HYGRO cassette was integrated next to Tpa1 using a PCR-based approach.
AFO4705	*MAT α ura3Δ0 leu2Δ0 his3Δ1 lys2Δ0 hxk2Δ::KAN snf1Δ10 TPA1-mScarlet::HYGRO*	This study. Using the Tpa1-mScarlet strain from the mScarlet C-SWAT collection [400], we PCR amplified the mScarlet::HYGRO cassette using primers with homology to the C-terminal and downstream regions of the Tpa1 coding sequence. We transformed the Tpa1-mScarlet::HYGRO cassette into MSY1261 (this study). We then validated that the mScarlet::HYGRO

		cassette was integrated next to Tpa1 using a PCR-based approach.
AFO4707	*MAT α ura3Δ0 leu2Δ0 his3Δ1 hxk2Δ::KAN mig1Δ::KAN TPA1-mScarlet::HYGRO*	This study. Using the Tpa1-mScarlet strain from the mScarlet C-SWAT collection [400], we PCR amplified the mScarlet::HYGRO cassette using primers with homology to the C-terminal and downstream regions of the Tpa1 coding sequence. We transformed the Tpa1-mScarlet::HYGRO cassette into MSY1590 (this study). We then validated that the mScarlet::HYGRO cassette was integrated next to Tpa1 using a PCR-based approach.
AFO4748	*MAT α ura3-52 leu2Δ1 his3Δ200 reg1Δ::HIS3 TPA1-mScarlet::HYGRO*	This study. Using the Tpa1-mScarlet strain from the mScarlet C-SWAT collection [400], we PCR amplified the mScarlet::HYGRO cassette using primers with homology to the C-terminal and downstream regions of the Tpa1 coding sequence. We transformed the Tpa1-mScarlet::HYGRO cassette into MSY1226 (this study). We then validated that the mScarlet::HYGRO cassette was integrated next to Tpa1 using a PCR-based approach.
Tda1-mNG strain	*MAT a his3Δ1 leu2Δ0 met15Δ0 ura3Δ0 Tda1-mNeonGreen*	[400]
AFO4545	*MAT a his3Δ1 leu2Δ0 met15Δ0 ura3Δ0 Tda1-mNeonGreen Tpa1-mScarlet::HYGRO*	This study. Using the Tpa1-mScarlet strain from the mScarlet C-SWAT collection [400], we PCR amplified the mScarlet::HYGRO cassette using primers with homology to the C-terminal and downstream regions of the Tpa1 coding sequence. We transformed the Tpa1-mScarlet::HYGRO cassette into the Tda1-mNG strain. We then validated that the mScarlet::HYGRO cassette was integrated next to Tpa1 using a PCR-based approach.
YSH202 (W303 background)	*MAT**a** ura3-1 leu2-3/112 trp1-1 his3-11/15 ade2-1 can1-100*	[235]

Table 4. Plasmids used in this study

Name	Description	Source
pRS315	CEN *LEU2*	[401]
pRS315-Hxk2-GFP	Genomic clone of *HXK2* with 592 bp upstream of ATG and 373 bp downstream of the stop and a C-terminal fusion to EGFP; CEN *LEU2*	[227]
pRS315-Hxk1-GFP	Genomic clone of *HXK1* with 820 bp upstream of ATG and 704 bp downstream of the stop and a C-terminal fusion to EGFP. CEN *LEU2*	This study.
pRS315-Glk1-GFP	Genomic clone of *GLK1* with 939 bp upstream of ATG and 780 bp downstream of the stop and a C-terminal fusion to EGFP; CEN *LEU2*	This study.

pRS315-Hxk2^{S15A}-GFP	The pRS315-Hxk2-GFP plasmid listed above had the S15A mutation introduced by site-directed mutagenesis with primers (Fwd: GAAAGGGTGCAATGGCCGATGTGCCAAAGG; Rev: TCGGCCATTGCACCCTTTCTGGCTTGTGGT). CEN *LEU2*	This study.
pRS315-Hxk2^{S15D}-GFP	The pRS315-Hxk2-GFP plasmid listed above had the S15D mutation introduced by site-directed mutagenesis with primers (Fwd: GAAAGGGTGATATGGCCGATGTGCCAAAGG Rev: TCGGCCATATCACCCTTTCTGGCTTGTGGT). CEN *LEU2*	This study.
pRS315-Hxk2^{K13A}-GFP	The pRS315-Hxk2-GFP plasmid listed above had the K13A mutation introduced by site-directed mutagenesis with primers (Fwd: TTAGGTCCAAAAAAACCACAAGCCAGAGCAGGTTCCATGGCCGAT; Rev: CAATTCCTTTGGCACATCGGCCATGGAACCTGCTCTGGCTTGTGG). CEN *LEU2*	This study.
pRS315-Hxk2^{K13A,S15A}-GFP	The pRS315-Hxk2-S15A-GFP plasmid listed above had the K13A mutation introduced by site-directed mutagenesis with primers (Fwd: TTAGGTCCAAAAAAACCACAAGCCAGAGCAGGTGCAATGGCCGAT; Rev: CAATTCCTTTGGCACATCGGCCATTGCACCTGCTCTGGCTTGTGG). CEN *LEU2*	This study.
pRS315-Hxk2^{K13A,S15D}-GFP	The pRS315-Hxk2-S15D-GFP plasmid listed above had the K13A mutation introduced by site-directed mutagenesis with primers (Fwd: TTAGGTCCAAAAAAACCACAAGCCAGAGCAGGTGACATGGCCGAT; Rev: CAATTCCTTTGGCACATCGGCCATGTCACCTGCTCTGGCTTGTGG). CEN *LEU2*	This study.
pRS315-Hxk2$^{\Delta 6\text{-}17}$-GFP	We truncated pRS315-Hxk2-GFP residues 6-17 by PCR using primers (Fwd: TTTAGGTCCAGCCGATGTGCCAAAGGAA Rev: CACATCGGCTGGACCTAAATGAACCATTTTATTTAAT). CEN *LEU2*	This study.
pRS315-Hxk2-3V5	Genomic clone of *HXK2* with 592 bp upstream of ATG and 373 bp downstream of the stop and a C-terminal fusion to 3V5; CEN *LEU2*	[224]
pRS315-Hxk2^{S15A}-3V5	The pRS315-Hxk2-3V5 plasmid listed above had the S15A mutation introduced by site-directed mutagenesis with primers (Fwd: GAAAGGGTGCAATGGCCGATGTGCCAAAGG; Rev: TCGGCCATTGCACCCTTTCTGGCTTGTGGT). CEN *LEU2*	This study.
pRS315-Hxk2^{S15D}-3V5	The pRS315-Hxk2-3V5 plasmid listed above had the S15D mutation introduced by site-directed mutagenesis with primers (Fwd: GAAAGGGTGATATGGCCGATGTGCCAAAGG Rev: TCGGCCATATCACCCTTTCTGGCTTGTGGT). CEN *LEU2*	This study.
pRS315-Glk1-3V5	Genomic clone of *GLK1* with 939 bp upstream of ATG and 780 bp downstream of the stop and a C-terminal fusion to 3V5; CEN *LEU2*	This study.
pRS315-Hxk1-3V5	Genomic clone of *HXK1* with 820 bp upstream of ATG and 704 bp downstream of the stop and a C-terminal fusion to 3V5; CEN *LEU2*	This study.
pRS315-Hxk2$^{\Delta 6\text{-}17}$-3V5	We truncated pRS315-Hxk2-3V5 residues 6-17 by PCR using primers (Fwd: TTTAGGTCCAGCCGATGTGCCAAAGGAA Rev: CACATCGGCTGGACCTAAATGAACCATTTTATTTAAT). CEN *LEU2*	This study.
pRS315-Hxk2^{K7,K8,K13A}-GFP	The pRS315-Hxk2-GFP plasmid listed above had the K7A, K8A, and K13A mutations introduced by site-directed mutagenesis with primers (Fwd: AAATGGTTCATTTAGGTCCAGCAGCACCACAAGCCAGAGCGGGTTCCATG; Rev: CTTTGGCACATCGGCCATGGAACCCGCTCTGGCTTGTGGTGCTGCTGGAC). CEN *LEU2*	This study.
pRS315-Hxk2^{D106A}-GFP	The pRS315-Hxk2-GFP plasmid listed above had the D106A mutation introduced by site-directed mutagenesis with primers (Fwd: CCATACCTTTGCCACCACTCAATCCAAGTAT; Rev: GATTGAGTGGTGGCAAAGGTATGGTTA). CEN *LEU2*	This study.

pSM3203-*TDH3pr*-Scs2-TM-mCherry	*TDH3* promoter- mCherry-Scs2-TM CEN *HIS3* AMP	[402]
pRS315-Hxk1^{S15A}-GFP	The pRS315-Hxk1-GFP plasmid listed above had the S15A mutation introduced by site-directed mutagenesis with primers (Fwd: GGTCCAAAGAAACCACAGGCTAGAAAGGGTGCCATGGCTGATGTG; Rev: CAATTCCTTGGGCACATCAGCCATGGCACCCTTTCTAGCCTGTGG). CEN *LEU2*	This study.
pRS315-Hxk1^{S15D}-GFP	The pRS315-Hxk1-GFP plasmid listed above had the S15D mutation introduced by site-directed mutagenesis with primers (Fwd: GGTCCAAAGAAACCACAGGCTAGAAAGGGTGACATGGCTGATGTG; Rev: CAATTCCTTGGGCACATCAGCCATGTCACCCTTTCTAGCCTGTGG). CEN *LEU2*	This study.
pRS315-Hxk1^{K13A}-GFP	The pRS315-Hxk1-GFP plasmid listed above had the K13A mutation introduced by site-directed mutagenesis with primers (Fwd: TTAGGTCCAAAGAAACCACAGGCTAGAGCAGGTTCCATGGCTGAT; Rev: CAATTCCTTGGGCACATCAGCCATGGAACCTGCTCTAGCCTGTGG). CEN *LEU2*	This study.
pRS315-Hxk1^{K7,K8,K13A}-GFP	The pRS315-Hxk1-GFP plasmid listed above had the K7A, K8A, and K13A mutations introduced by site-directed mutagenesis with primers (Fwd: AGATGGTTCATTTAGGTCCAGCGGCACCACAGGCTAGAGCGGGTTCCATG; Rev: CTTGGGCACATCAGCCATGGAACCCGCTCTAGCCTGTGGTGCCGCTGGAC). CEN *LEU2*	This study.
pRS315-Hxk1^{D106A}-GFP	The pRS315-Hxk1-GFP plasmid listed above had the D106A mutation introduced by site-directed mutagenesis with primers (Fwd: CCATACCTTTGCCACCACTCAATCCAAGTAT; Rev: GATTGAGTGGTGGCAAAGGTATGGTTA). CEN *LEU2*	This study.
pRS315-Hxk1$^{\Delta 6\text{-}17}$-GFP	We made an internal deletion of pRS315-Hxk1-GFP so that residues 6-17 were lost using PCR with the primers (Fwd: GTTCATTTAGGTCCAGCTGATGTGCCCAAGGAATTGATGGATG; Rev: CCTTGGGCACATCAGCTGGACCTAAATGAACCATCTTATTTTTTC). CEN *LEU2*	This study.

2.4.2 Yeast protein extraction, CIP treatments, and immunoblot analyses

Whole-cell protein extracts were generated using the trichloroacetic acid (TCA) method [403]. An equal density of mid-log phase cells (typically ~ $5x10^7$ cells) was harvested by centrifugation, washed in water, and then resuspended in water with 0.25 M sodium hydroxide and 72 mM β-mercaptoethanol. Samples were incubated on ice, and proteins precipitated by adding 50% TCA. After further incubation on ice, proteins were collected by centrifugation, the supernatant was removed, and the proteins were solubilized in 50 µL of TCA sample buffer (40

mM Tris-Cl [pH 8.0], 0.1 mM EDTA, 8 M Urea, 5% SDS, 1% β-mercaptoethanol, and 0.01% bromophenol blue). Samples were heated to 37°C for 15 min, and the insoluble material removed by centrifugation before resolving by SDS-PAGE. For Figure 27G, 15 µL of cell lysate was further treated for 1 h at 37°C with 40 units of Quick calf intestinal alkaline phosphatase (CIP, New England Biolabs, Ipswich, MA, USA) per the manufacturer's recommendations, or mock-treated in CIP buffer without enzyme. These samples were then precipitated using 50% TCA and solubilized in SDS/Urea sample buffer as above, before analysis via SDS-PAGE. Proteins were identified by immunoblotting with a mouse anti-GFP antibody (Santa Cruz Biotechnology, Santa Cruz, CA, USA) to detect green fluorescent protein (GFP) fused to Hxk2, or mouse anti-mNeon Green (mNG) nanobody (ChromoTek, Planegg-Martinsried, Germany) to detect mNG fused to Tda1. Primary antibodies were detected using anti-mouse or anti-rabbit secondary antibodies conjugated to IRDye-800 or IRDye-680 (Li-Cor Biosciences). Revert (Li-Cor Biosciences, Lincoln, NE, USA) total protein stain was used as a loading and membrane-transfer control. Secondary antibodies or Revert staining were detected on an Odyssey CLx infrared imaging system (Li-Cor Biosciences).

2.4.3 Co-immunoprecipitation assays

Hexokinase proteins were C-terminally tagged with either three copies of the V5 epitope [404] or the GFP protein and expressed from CEN plasmids under the control of their respective promoters. Cells were grown in 2% glucose to mid-log phase and harvested for protein extraction. Protein expression was monitored by immunoblotting with a 1:1000 dilution of Anti V5 Antibody (Fisher Scientific Catalog # R960-25) or a 1:1000 dilution of Anti-GFP polyclonal Antibody (Product # PA1-980A). Hxk2-3V5 and associated proteins were immunoprecipitated from glass

bead extracts (250 μg total protein) using 20 μL of agarose conjugated anti-V5 antibody (Sigma; A7345). The extract and beads were incubated at 4°C overnight, then washed three times in 1 mL of hexokinase buffer with protease inhibitors and eluted in 15 μL SDS sample buffer.

2.4.4 Recombinant protein purification and size exclusion chromatography

Hxk2 was cloned into the bacterial expression plasmid pET14b (Novagen) such that the C-terminus contained a 6-histidine tag. Hxk2 expression was induced with 1 mM IPTG at 25°C for 2 hours. Recombinant proteins were purified on Ni-NTA columns (1 ml Ni-NTA Agarose; Qiagen Cat # 30210), washed with 20 ml hexokinase buffer (20 mM HEPES, 5 mM Mg Acetate, 100 mM NaCl, 0.5 mM EDTA, 0.5 mM DTT) with 100 mM imidazole before elution in hexokinase buffer with 500 mM imidazole. Proteins were dialyzed into hexokinase buffer with 5% glycerol and stored at -80°C.

Purified proteins were analyzed by size exclusion chromatography using a TOSOH G2000 SW_{XL} column on a Shimadzu HPLC system. Samples (40 μg protein in 50 μl of buffer) were resolved in hexokinase buffer with or without 2 mM glucose at a 1 mL/min flow rate.

2.4.5 Fluorescence microscopy

Unless otherwise indicated, imaging was performed using a live-cell microscopy protocol, maintaining yeast in the same medium they were grown in throughout the imaging process. Fluorescent protein localization was performed by growing cells in SC medium with 2% glucose overnight, re-inoculating at an optical density $(OD)_{600}$ of 0.3 into fresh SC medium with 2% glucose, and growing cells until they reached mid-logarithmic phase (an additional 4–5 h) at 30°C

with aeration. For low glucose treatments (SC with 0.05% glucose), cells were washed and incubated as described above in the "Yeast Strains and Growth Conditions" section. For imaging, cells were plated on a 35 mm glass bottom microwell dish coated with 15 μL (0.2 mg/mL) of concanavalin A (MatTek Corporation, Ashland, MA). They were imaged using a Nikon Eclipse Ti2 A1R inverted confocal microscope (Nikon, Chiyoda, Tokyo, Japan) outfitted with a 100 x oil immersion objective (NA 1.49). Images were captured using GaAsP or multi-alkali photomultiplier tube detectors, and the acquisition was controlled using NIS-Elements software (Nikon). All images within an experiment were acquired using identical settings, and images were adjusted evenly and cropped using NIS-Elements.

For Figure 11F, cells were grown as described [254]. 25 μL of cells were loaded onto ConA-coated glass slides. Then the remaining suspension was aspirated off the slide. DAPI (1 μL of 2.5 μg/mL dissolved in 80% glycerol) was added to the cells. Cells were covered with a glass coverslip [254] and then imaged as described above, this time using a Nikon Eclipse Ti2-E inverted microscope (Nikon, Chiyoda, Tokyo, Japan) equipped with an Apo100X objective (NA 1.45) and captured with an Orca Flash 4.0 cMOS (Hamamatsu, Bridgewater, NJ) camera and NIS-elements software (Nikon). These conditions mirror those used in earlier publications of Hxk2-GFP localization [236,254,258–260].

Fluorescence recovery after photobleaching (FRAP) experiments (see Figures 12F and 13) were performed by adding 25 μL of low-glucose incubated cells to ConA-coated Matek dishes. The experiment was conducted using the confocal microscope described above. First, images were captured before the nuclei were bleached. Next, a region of interest (ROI) for bleaching (see Figure 13F) was defined in the nucelus, using the mScarlet marker reference. A 1 sec pulse of the 488 nm

laser (10% power) bleached the nuclei. An image of the bleached cells was captured immediately after and then every minute for 20 mins to monitor nuclear fluorescence recovery.

2.4.6 Image quantification and statistical analyses

Quantification of nuclear fluorescence and whole-cell fluorescence intensity was done using Nikon General Analysis 3 software (Nikon, Chiyoda, Tokyo, Japan) with the segmentation from NIS-Elements.ai (Artificial Intelligence) software (Nikon, Chiyoda, Tokyo, Japan) unless otherwise described. For quantification of whole-cell fluorescence, the NIS.ai software was trained on a ground truth set of samples where cells had been manually segmented using the DIC channel images. Next, the NIS.ai software was iteratively trained until it achieved a training loss threshold of <0.02, indicating a high degree of agreement between the initial ground truth and the output generated by the software. To measure the mean nuclear fluorescence, we trained the NIS.ai software to identify the nucleus using the chromosomally integrated Tpa1-mScarlet nuclear marker (see Table 4). The NIS.ai software was trained using a manually defined ground truth set of nuclear segmentations. Using the General Analysis 3 software, fields of images captured through confocal microscopy were processed so that individual whole-cell and nuclear objects in a field of view were segmented using the DIC and 561 nm (mScarlet) channels. A parent-child relationship was applied to individual nuclear objects (child) within the same cell (parent) to aggregate them as single objects and pair them to the appropriate whole cell. Any partial cells at the edges of the image were removed along with their child objects. Then the mean fluorescence intensity of each parent or child object was defined in the appropriate channel. All imaging quantification graphs, except for manual quantification data in Figure 11A, 11B, 11D and 11E, were derived using this method.

Manual quantification to measure mean nuclear or whole-cell fluorescence (Figure 10A, 10B, 10D and 10E) was performed using ImageJ software (National Institutes of Health, Bethesda, MD). A 2-pixel wide line was hand drawn around the nuclei using images of the Tpa1-mScarlet nuclear marker to create a mask that was then overlaid on the GFP images, and the mean GFP signal was measured. The same was done to measure whole-cell fluorescence, except lines were drawn around the perimeter of each cell using the GFP or mNG signal since Hxk2 has a diffuse cytosolic distribution. Mean background fluorescence intensity was measured for each image and subtracted from the mean fluorescence measurements to calculate mean nuclear and whole-cell intensities.

Statistical analyses of fluorescence quantification were done using Prism (GraphPad Software, San Diego, CA). Unless otherwise indicated, we performed Kruskal-Wallis statistical tests with Dunn's post hoc correction for multiple comparisons. In all cases, significant p-values from these tests are represented as * p-value<0.1; ** p-value<0.01; *** p-value<0.001; **** p-value<0.0001; not significant (ns) = p-value>0.1. In some instances where multiple comparisons are made, the † or + symbols may be used in place of * to indicate the same p-values but relative to a different reference sample (see the figure legends).

FRAP data were analyzed first by measuring the mean nuclear fluorescence of a nuclear ROI both before and after bleaching. In some cases, nuclei shifted positions at different time points along the lateral plane. In these cases, we manually re-positioned the ROI and re-measured to ensure we did not erroneously measure the cytosolic pool. To account for non-specific photobleaching that occurred due to repeated rounds of imaging, an ROI reference was used in an adjacent cell when no targeted laser bleaching was performed. The mean cytosolic GFP

fluorescence in the ROI of the control cell was also measured at each time point. Then the data were normalized using the following equation [405]:

$$Norm(t) = \frac{Ref_{pre-bleach}}{ref(t)} \times \frac{FRAP_t}{FRAP_{pre-bleach}}$$

The normalized data were plotted over time, and the recovery rates were calculated by measuring the slope of the linear portion of each recovery plot.

2.4.7 RNA-seq sample preparation and analyses

RNA samples were prepared from multiple independent yeast cultures grown on synthetic complete medium using the RNeasy Mini Kit (Qiagen). Sequencing libraries were prepared using the TruSeq Stranded mRNA library method (Illumina). RNA sequences were mapped to *S. cerevisiae* mRNA using the kallisto software package [406]. Each RNA sample yielded 40–50 million reads. mRNA abundance was expressed in transcripts per million mapped reads (tpm). To compare mRNA expression under different conditions, we used a Student's t-test to calculate p values with a false discovery rate threshold of 0.01%. All RNA-seq data have been deposited in the SRA database under accession number PRJNA885127.

2.4.8 Homology models of the *Sc*Hxk2 dimer

We generated a homology model of the *Sc*Hxk2 dimer using SWISS-MODEL [407–411]. A *Kl*Hxk1 crystallographic dimer (PDB ID 3O1W [83]) served as the template. We removed all alternate locations from the 3O1W PDB file so that each amino acid had only one sidechain conformation. We then copied the two chains, A and B, into two separate files, each containing

the respective *Kl*Hxk1 monomer. We separately uploaded these two monomers to the SWISS-MODEL server, together with the full-length sequence of *Sc*Hxk2.

Since the 3O1W template structure covers *Kl*Hxk1 almost entirely—including the critical N-terminal tails—the homology models of each monomer included all *Sc*Hxk2 amino acids except the initial methionine and the terminal alanine. The initial methionine (M1) is cleaved *in vivo* [370,412], so we used UCSF Chimera [413] to add only the C-terminal alanine. To merge the two monomers into a single dimer model, we used multiseq [414], as implemented in VMD [415], to align each monomer to its respective chain in the original 3O1W dimeric structure. Finally, we processed the dimer model with PDB2PQR [416,417], which added hydrogen atoms per the PROPKA algorithm (pH 7.00) [418] and optimized the hydrogen-bond network.

To generate a final model of the *apo* (ligand-free) *Sc*Hxk2 dimer, we subjected the dimer homology model to one round of minimization in Schrödinger Maestro.

To generate a final model of the holo (glucose-bound) *Sc*Hxk2 dimer, we aligned a glucose-bound *Kl*Hxk2 dimer (PDB ID 3O5B [83]) to our *Sc*Hxk2 dimer model and copied the aligned glucose molecules. We then added hydrogen atoms to the glucose molecules using Schrödinger Maestro. To resolve minor steric clashes and optimize interactions between the receptor and glucose ligands, we minimized the *Sc*Hxk2/glucose complex using a stepwise protocol. First, we used Schrödinger Maestro to subject all binding-site atoms (excluding the ligand) to one round of minimization. Second, we subjected all protein atoms to two rounds of minimization. Third, we subjected all protein and glucose hydrogen atoms to one round of minimization. Finally, we minimized all the atoms of the complex.

To generate a model of the *holo* (glucose-bound) *Sc*Hxk2 monomer, we simply deleted one of the monomers of our *holo Sc*Hxk2 dimer model. We note that the ATP depicted in Figure 14G

and 17A was not part of the model itself (i.e., it was not included in the minimization procedure). We positioned ATP in the active site for visualization by aligning a crystal structure of a homologous protein (6PDT [94]) to each monomer of our *Sc*Hxk2 dimer model.

2.4.9 Molecular dynamics simulations

We performed molecular dynamics (MD) simulations of the *apo* dimer, *holo* dimer, and *holo* monomer systems. In each case, we used *tleap* (Ambertools18 [2]) to add a water box extending 10 Å beyond the protein along all dimensions. We also added Na+ counter ions sufficient to achieve electrical neutrality and then additional Na+ and Cl- counter ions to approximate a 150 mM solution. The protein, counter ions, water molecules, and glucose molecules were parameterized per the Amber ff14SB [419], TIP3P [420], and GLYCAM_06j-1 [421] force fields, respectively.

We applied four rounds of minimization using the Amber MD engine [422,423]. First, we minimized all hydrogen atoms for 5,000 steps. Second, we minimized all hydrogen atoms and water molecules for 5,000 steps. Third, we minimized all hydrogen atoms, water molecules, and protein side chains for 5,000 steps. Finally, we minimized all atoms for 10,000 steps.

After minimization, we equilibrated each system using three rounds of simulation. First, we subjected each system to a short simulation in the canonical ensemble (NVT, 0.02 ns total), with a 1.0 kcal/mol/$Å^2$ restraining force applied to the backbone atoms. Using the same backbone restraints, we continued the simulation in the isothermal–isobaric ensemble (NPT, 1 atm, 1.0 ns total). Finally, we finished the equilibration (NPT, 1 atm, 1.0 ns total) without restraints. In all cases, we used a 2-fs timestep and a 310 K temperature setting.

After minimization and equilibration, we ran three isothermal-isobaric (NPT, 310 K, 1 atm) productive simulations of the *Sc*Hxk2 *apo* dimer (550 ns, 262 ns, 266 ns), the *Sc*Hxk2 *holo* dimer (1000 ns, 261 ns, 262 ns), and the *Sc*Hxk2 *holo* monomer (530 ns, 253 ns, 260 ns). We used a different random seed for each simulation.

2.4.10 RMS and pairwise distance analyses

To calculate how far a bound glucose molecule deviated from its initial position, we used VMD [7] to align the associated *Sc*Hxk2 monomer by its alpha carbons. We then calculated the heavy-atom root mean square distances (RMSDs) between the starting glucose pose and the pose of each frame.

To monitor the hydrogen bond between K13 and Q142*, we used VMD to calculate the distance between the K13 terminal nitrogen atom and the Q142* sidechain carbonyl oxygen atom. We assumed a hydrogen bond had formed when this distance was less than 4.0 Å. To monitor the salt bridge between K13 and D106*, we calculated the distance between the K13 terminal nitrogen atom and the D106* terminal-most carbon atom. We assumed a salt bridge had formed when this distance was less than 4.0 Å.

2.4.11 Molecular visualization

Images were generated using VMD [415] and BlendMol [424].

2.5 Acknowledgements

We acknowledge the support of the Dietrich School of Arts and Sciences Microscopy and Imaging Suite (RRID: SCR_022084). We gratefully acknowledge the support of Dr. Patrick Thibodeau for help with our size-exclusion chromatography assays. We kindly acknowledge the feedback provided by Dr. Jeff Brodsky, his research team, and the Pittsburgh Area Yeast Meeting members before submission. We further acknowledge the support and feedback from members of the O'Donnell lab team.

3.0 Novel mutation in hexokinase 2 confers resistance to 2-deoxyglucose by altering protein dynamics

Hellemann E*, Walker JL*, Lesko MA*, Chandrashekarappa DG, Schmidt MC, O'Donnell AF, Durrant JD. (2022) Novel mutation in hexokinase 2 confers resistance to 2-deoxyglucose by altering protein dynamics. PLOS Computational Biology 18(3): e1009929. https://doi.org/10.1371/journal.pcbi.1009929. *equal contribution.

Specific author contributions include:

- Lesko MA: Figures 34A-B, 36B-C, 37B-E, Tables 5, 8, 9, writing, review & editing
- Hellemann E: Conducted MD simulations, Figures 41, 42C, 43, 44, 45, 47, Tables 7 & 10, writing, review & editing
- Walker JL: Conducted lab evolution experiments and MD simulations
- Chandrashekarappa DG: Figures 36A, 37A, F, 38, 39, Table 6
- Schmidt MC: Figure 35, writing, review & editing, project administration, resources, supervision
- O'Donnell AF: writing, review & editing, project administration, resources, supervision
- Durrant JD: Figures 33, 40, 42A-B, 46, writing, review & editing, project administration, resources, supervision

3.1 Introduction

Eukaryotic cells sense and respond to their nutrient environment, modulating their metabolic processes to grow and survive in a changing nutritional landscape. The available carbohydrate source dictates these metabolic shifts. Glucose, a six-carbon sugar critical for many biological processes, is the preferred carbon source for most eukaryotic cells. Glucose is first taken up from the environment by glucose transporters (e.g., the HXT hexose transporters in S. cerevisiae or the homologous GLUT glucose transporters in mammals). Catabolism then begins with the activity of a hexokinase, which transfers the γ phosphate of ATP to the C6 carbon of glucose, producing glucose-6-phosphate (Glc-6P) [425]. Through a series of enzymatic conversions, glycolysis ultimately converts Glc-6P into two pyruvate molecules, which are further catabolized via anaerobic fermentation and aerobic oxidative phosphorylation (OXPHOS) to produce the energy needed for cellular function [426]. Glucose-dependent reductive biosynthesis occurs in parallel, primarily through the pentose-phosphate pathway. The same hexokinase-generated Glc-6P molecules serve as initial building blocks to generate compounds such as NADPH and ribose 5-phosphate, which are in turn the precursors for many biosynthetic processes (e.g., nucleic-acid and fatty-acid synthesis) [427,428]. Because Glc-6P feeds into several glucose pathways, hexokinase enzymes are critical regulatory checkpoints [429].

The conformational changes that hexokinases undergo as they engage with substrate have been extensively studied [79–81,87,101,430–432]. Hexokinases generally adopt a palm-shaped α/β fold with at least two subdomains: a mostly helical large subdomain and an α/β small subdomain (Figure 33). The enzyme starts in an open conformation, such that the central inter-domain crevice (i.e., the enzymatic cleft) is accessible to bulk solvent and substrate [79,80]. Glucose binding to the cleft causes the two subdomains to rotate relative to each other [431,432].

This rotation collapses the solvent-accessible crevice, leading it to envelop the glucose molecule [80,430] via a so-called "embracing" mechanism [101]. ATP binding induces further conformational changes [81,430] that allow an amino acid acting as a catalytic base (D211 in yeast Hxk2) to abstract a hydrogen atom from the glucose 6-oxygen, enabling nucleophilic attack on the ATP γ phosphorus [87]. Electrostatic interactions between the resulting Glc-6P and ADP drive the two products apart, leading to the release of Glc-6P.

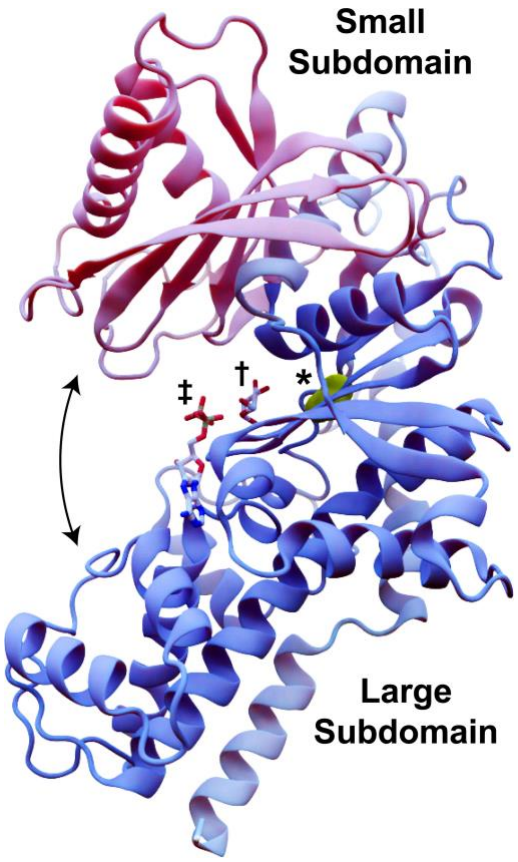

Figure 33. *Sc*Hxk2 structure and global dynamics.

The mostly helical large subdomain and the α/β small subdomain are shown in blue and pink, respectively (PDB 1IG8). The curved arrows indicate the approximate motion of domain closure. The location of residue 238 is shown in yellow and marked with an asterisk. To indicate the location of the glucose- and ATP-binding pockets, we superimposed crystallographic glucose (dagger) and ADP (double dagger) molecules from structures of *Hs*Hk1 (human, PDB 4FPB) and *Os*Hxk6 (rice, PDB 6JJ8), respectively.

While the mechanics of glucose binding and catalysis have been extensively studied in several species (e.g., *H. sapiens* [89], *K. lactis* [83], and *S. cerevisiae* [80]), it remains to be determined how glucose analogs impact those mechanisms. We focus on 2-deoxyglucose (2DG), a toxic glucose analog studied as an anti-cancer agent in clinical trials. 2DG is an excellent chemical probe for studying glucose metabolism, hexokinase enzymology, and resistance mechanisms. It is identical to glucose, except a hydrogen atom is present at the C2 carbon rather than a hydroxyl group. Because of these chemical similarities, studying the impact of 2DG on cellular function can reveal insights into wild-type (WT) glucose metabolic mechanisms.

After 2DG enters the cell via glucose transporters, it too is phosphorylated by hexokinases, producing 2-deoxyglucose-6-phosphate (2DG-6P) [331]. Unlike Glc-6P, 2DG-6P cannot advance through the glycolytic pathway [245,433] and even inhibits some glycolytic enzymes (e.g., hexokinase [275] and glucose-6-phosphate isomerase [271]). Aside from blocking glycolysis, 2DG also acts via several other toxic mechanisms. For example, it may deplete cellular ATP reserves because 2DG phosphorylation consumes ATP, but 2DG-6P cannot be recycled or used for energy production [434]. 2DG also incorporates into glycolipids, endogenous molecules that play critical roles in many cellular pathways [292]. Resulting downstream metabolites (e.g., GDP-2DG and UDP-2DG) also impact glycogen metabolism [286] and protein glycosylation [295]. The latter results in protein misfolding and endoplasmic reticulum stress, which can trigger the unfolded protein response and apoptosis [296,298]. In yeast, 2DG also compromises cell-wall integrity; altered protein glycosylation impacts mannan biosynthesis [435], and 2DG incorporates into cell-wall β-glucan polymers [435]. Additional mechanisms of toxicity are also likely

[316,436,437], and much remains uncertain [245,282]. See Laussel et al. [266] for a thorough review.

Yeast is an excellent organism for studying 2DG biology and resistance mechanisms. As early as the 1960s, researchers noted that when *S. cerevisiae* is grown in media containing 0.2% 2DG, it exhibits a glucose-starvation phenotype even when 2% glucose is present [288,438]. Yeast cells exposed to 2DG also acquire resistance, and the organism's well-characterized, small, and optionally haploid genome enables the rapid evolution and identification of resistance-conferring mutations [439]. For example, two recent genetic screens [224,287] identified several critical contributors to 2DG resistance, including glucose-transporter trafficking, altered signaling through the AMP-activated kinase (AMPK in mammals, Snf1 in yeast), and changes in the unfolded protein response or cell integrity pathways. Mutations that dampen the catalytic activity of hexokinase-2 (ScHxk2), the predominant glucose kinase in high-glucose conditions [238], can also confer 2DG resistance [224]. Indeed, Hxk2 is the only one of three hexokinase isozymes in yeast (Hxk1, Hxk2, and Glk1) implicated in 2DG resistance, even though Hxk1 (and possibly Glk1) can also phosphorylate 2DG [224]. However, the data to date do not provide any atomic-resolution models for how Hxk2 mutations promote 2DG resistance.

In the present work, we use *in vivo* evolution and whole genome sequence analysis as an unbiased approach to identify spontaneous 2DG-resistance mutations in *S. cerevisiae*. We identify a novel resistance-conferring mutation in the hexokinase-2 gene (*HXK2*). Curiously, the mutation alters an amino acid that does not immediately line the enzymatic cleft, nor does it disrupt the stability of the enzyme. We use molecular, biochemical, and genetic experiments coupled with atomic-resolution molecular dynamics (MD) simulations to provide evidence that this novel mutation diminishes Hxk2 catalytic activity by indirectly impacting (1) local cleft dynamics and

(2) the larger conformational changes required to envelop hexose substrates (e.g., glucose, 2DG). Our study illustrates how intra-protein allosteric communication can substantially impact overall activity and dynamics. Further, our findings provide generalizable insights into hexokinase resistance mechanisms that may be relevant to cancer biology.

3.2 Results

3.2.1 Directed evolution evolves resistance to 2DG

To identify novel resistance mechanisms, we used the uniquely sensitive ABC16-monster *S. cerevisiae* strain (also known as ΔABC16), which lacks 16 distinct ABC transporters [439–442]. Because cells from this background are less able to evade cytotoxic chemicals by simple export, resistance is more likely to occur through compensatory mutations, often in the very protein(s) to which a cytotoxic compound binds. In five independent lab-evolution experiments, we exposed ABC16-monster cells to escalating 2DG concentrations via serial passaging to select for cells that evolved 2DG resistance (referred to hereafter as 2DG-resistant strains 1–5; see Materials and Methods for details).

To verify 2DG resistance, we compared the growth of cells from the 2DG-resistant strains and two control strains: the parental ABC16-monster strain and an ABC16-monster strain that was passaged in parallel but without 2DG (referred to hereafter as naïve ABC16-monster; Figure 34). All strains grew robustly on YPD medium lacking 2DG, indicating that none of the mutations in the 2DG-resistant strains conferred a growth disadvantage in glucose (Figure 34A). In medium with 2DG, cells from the parental or naïve ABC16-monster strains grew poorly or failed to grow,

depending on the 2DG concentration (Figure 34A). In contrast, cells from 2DG-resistant strains 1–5 grew at all 2DG concentrations tested (Figure 34A). Growth curve analyses of cells from the control strains (parental and naïve ABC-monster) and 2DG-resistant strains over 24 hours in liquid media showed similar trends (Figure 34B).

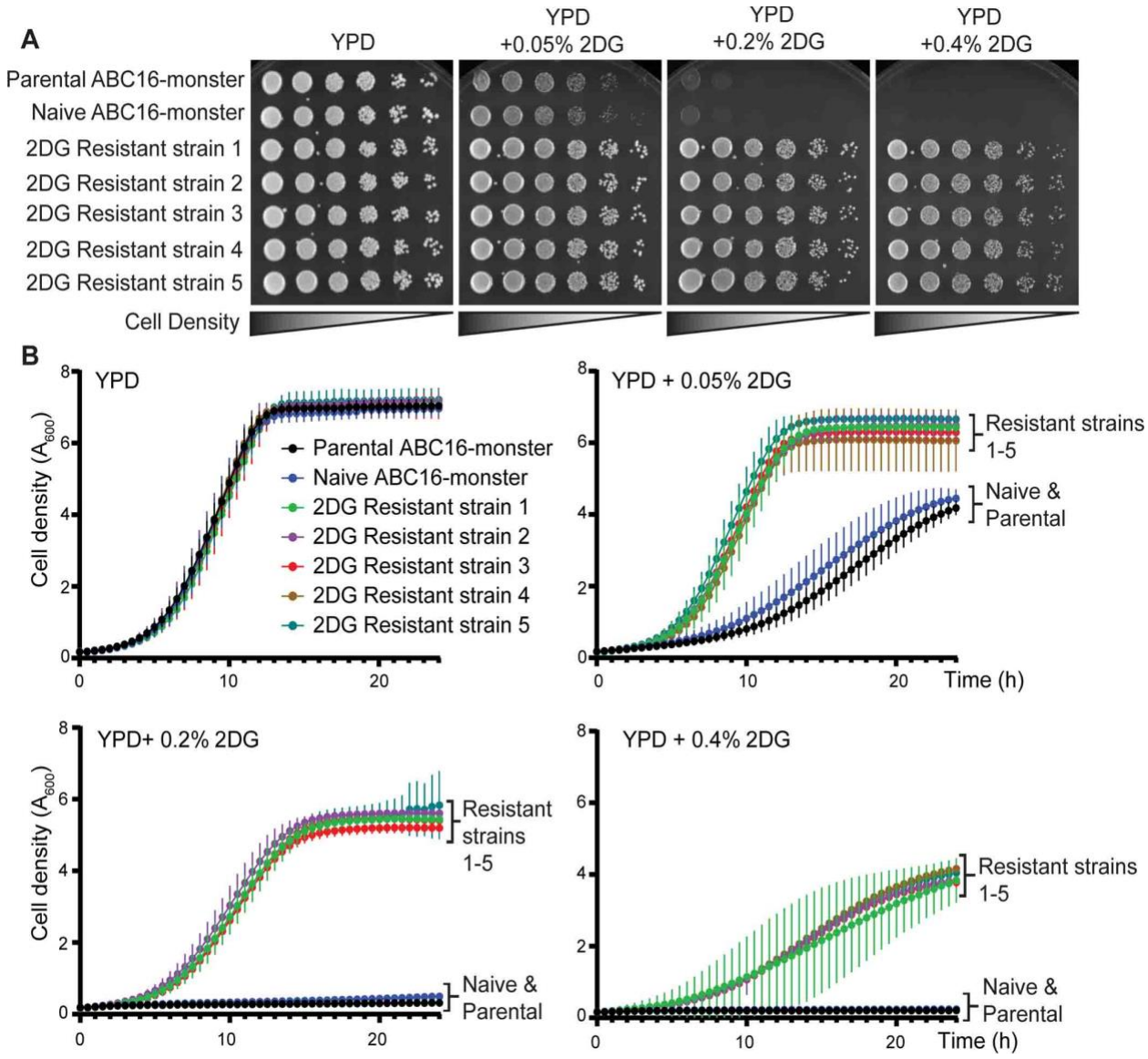

Figure 34. Cells from 2DG-resistant strains 1-5 are resistant to 2DG, but the parental control and naïve control cells are not.

(A) Images of serial dilution growth assays on YPD (2% glucose as carbon source) or YPD with increasing concentrations of 2DG (0.05%, 0.2%, and 0.4%) after two days of growth at 30°C. (B) Graphs showing the change in cell density over time for cells grown in YPD or YPD with increasing 2DG concentrations, each of which have 2% glucose as a carbon source. Data are plotted as the A600 measured every 30 minutes during a 24-hour time course. Curves represent the average A600 of three experimental replicates, and vertical lines emerging from each data point represent standard deviations.

These assays reveal that the 2DG-resistant strains exhibit similar growth kinetics to the parental and naïve ABC16-monster controls on YPD (Figure 34B and Table 5). However, in the presence of 2DG, 2DG-resistant strains 1–5 had much shorter doubling times than the control strains (Figure 34B and Table 5). At the higher concentrations of 2DG (0.2% or 0.4%), it was impossible to calculate doubling times for the parental or naïve ABC16-monster strains because the cells did not grow at all (Figure 34B and Table 5). In contrast, for the 2DG resistant strains the doubling times, while longer than at lower 2DG concentrations, were possible to assess. Strikingly, the 2DG growth profiles for 2DG-resistant strains 1–5 were similar across all concentrations of 2DG tested (Figure 34B and Table 5). These findings confirm that our lab-evolution protocol successfully generated 2DG-resistant yeast cells.

Table 5. Doubling times calculated from growth curves shown in Figure 2B (hours).

	Parental ABC16-Monster	**Naïve ABC16-Monster**	**2DG-resistant strain 1**	**2DG-resistant strain 2**	**2DG-resistant strain 3**	**2DG-resistant strain 4**	**2DG-resistant strain 5**
YPD	2.58±0.19 (ns)	2.48±0.31 (ns)	2.35±0.14	2.60±0.32 (ns)	2.47±0.29 (ns)	2.39±0.22 (ns)	2.51±0.20 (ns)
YPD + 0.05% 2DG	5.34±0.43 (***)	5.61±0.20 (***)	2.85±0.22	2.86±0.03 (ns)	2.75±0.06 (ns)	2.65±0.09 (ns)	2.84±0.07 (ns)
YPD + 0.2% 2DG	ND	ND	3.18±0.21	3.28±0.05 (ns)	3.20±0.06 (ns)	3.19±0.1 (ns)	3.25±0.09 (ns)
YPD + 0.4% 2DG	ND	ND	5.09±0.61	4.6±0.42 (ns)	4.59±0.16 (ns)	5.2±0.33 (ns)	4.91±0.27 (ns)

3.2.2 A novel 2DG-resistance mutation in *HXK2*

To determine the genetic cause of this resistance, we used whole genome sequencing to identify any altered protein-encoding genes in 2DG-resistant strains 1–5 and to assess the ploidy of these strains (Figure 35). Interestingly, all five evolved strains contained a missense mutation that substitutes valine for the glycine at Hxk2 amino acid 238 (i.e., Hxk2^{G238V}) and bore no changes in ploidy, which can also be associated with 2DG resistance [307]. Although other hypomorphic *HXK2* alleles have been associated with 2DG resistance [224,245,287,316], none have been identified in the ABC16-monster variant.

To confirm that the *hxk2*^{G238V} allele confers 2DG resistance, we introduced *hxk2*^{G238V} into cells lacking *HXK2* (*hxk2*Δ), which are themselves resistant to 2DG. The cells employed in these confirmatory assays had the ABC transporters intact (i.e., they were not isogenic to the ABC16-monster). As expected, the presence of a WT *HXK2* restored sensitivity to 2DG (negative control, Figure 36A). However, adding vector, *hxk2*^{G238V}, or the catalytically dead *hxk2*^{D211A} allele to *hxk2*Δ cells did not disrupt the 2DG resistance (Figure 36A).

While the *hxk2*^{G238V} allele is sufficient to cause 2DG resistance, each of the 2DG-resistant strains had other mutations that might also contribute to resistance [443]. To determine the extent of these contributions, we transformed WT *HXK2* on a plasmid into 2DG-resistant strains 1–5 and spotted the cells as serial dilutions. We found that 2DG sensitivity was completely restored in all five cases (Figure 36B), and growth kinetics in the presence of 2DG were comparable to the parental ABC16-monster strain (Figure 36C). This experiment suggests that the *hxk2*^{G238V} allele is primarily responsible for the observed 2DG resistance.

Because cells lacking *HXK2* entirely (*hxk2*Δ) are also resistant to 2DG, a trivial explanation for resistance is that the *hxk2*^{G238V} allele encodes an unstable protein product. We found that the steady-state protein abundance of Hxk2^{G238V} was comparable to that of two controls: WT Hxk2 and WT Hxk1 (Figure 37A). There was no statistically significant difference in Hxk2 or Hxk2^{G238V} abundance when cells were grown in high or low glucose conditions or in the presence of 2DG (Figure 37B-C), suggesting that the Hxk2^{G238V} variant is stable under all these conditions.

As further evidence of stability, we found that the *hxk2*^{G238V} allele supports growth on glucose in cells lacking all three hexokinases (*hxk2*Δ *hxk1*Δ *glk1*Δ), demonstrating that it is sufficiently folded and functional to convert enough glucose to Glc-6P to sustain life (Figure 37D, top panel). Indeed, even at elevated temperatures that unfold/destabilize metastable proteins encoded by some missense alleles [444,445], Hxk2^{G238V} permitted growth on glucose while the vector control did not (Figure 37D). At high temperatures, Hxk2^{G238V} also continued to confer 2DG resistance and was as stable as WT Hxk2 (Figure 37D-E). These results show that the *hxk2*^{G238V} allele alone is sufficient to confer 2DG resistance and that it encodes a stable, functional hexokinase.

In addition to its enzymatic role, Hxk2 regulates gene expression as part of the glucose repression system. Specifically, Hxk2 is required for glucose repression of the *SUC2* gene, which encodes the sucrose hydrolyzing enzyme invertase. Invertase activity thus serves as a valuable proxy for Hxk2-mediated regulatory activity [238]. Not all *HXK2* 2DG-resistance alleles alter Hxk2-mediated repression of *SUC2* expression and activity; while some are associated with aberrant *SUC2* expression, others have WT-like repression of invertase function [224]. In our assays, we found that cells with WT *HXK2* (control) fully repressed invertase activity; in contrast,

cells with the *hxk2*^{G238V} allele were unable to fully repress activity, though they repressed it better than cells with (1) vector alone or (2) the 2DG-resistance *hxk2*^{G55V} allele (Figure 37F).

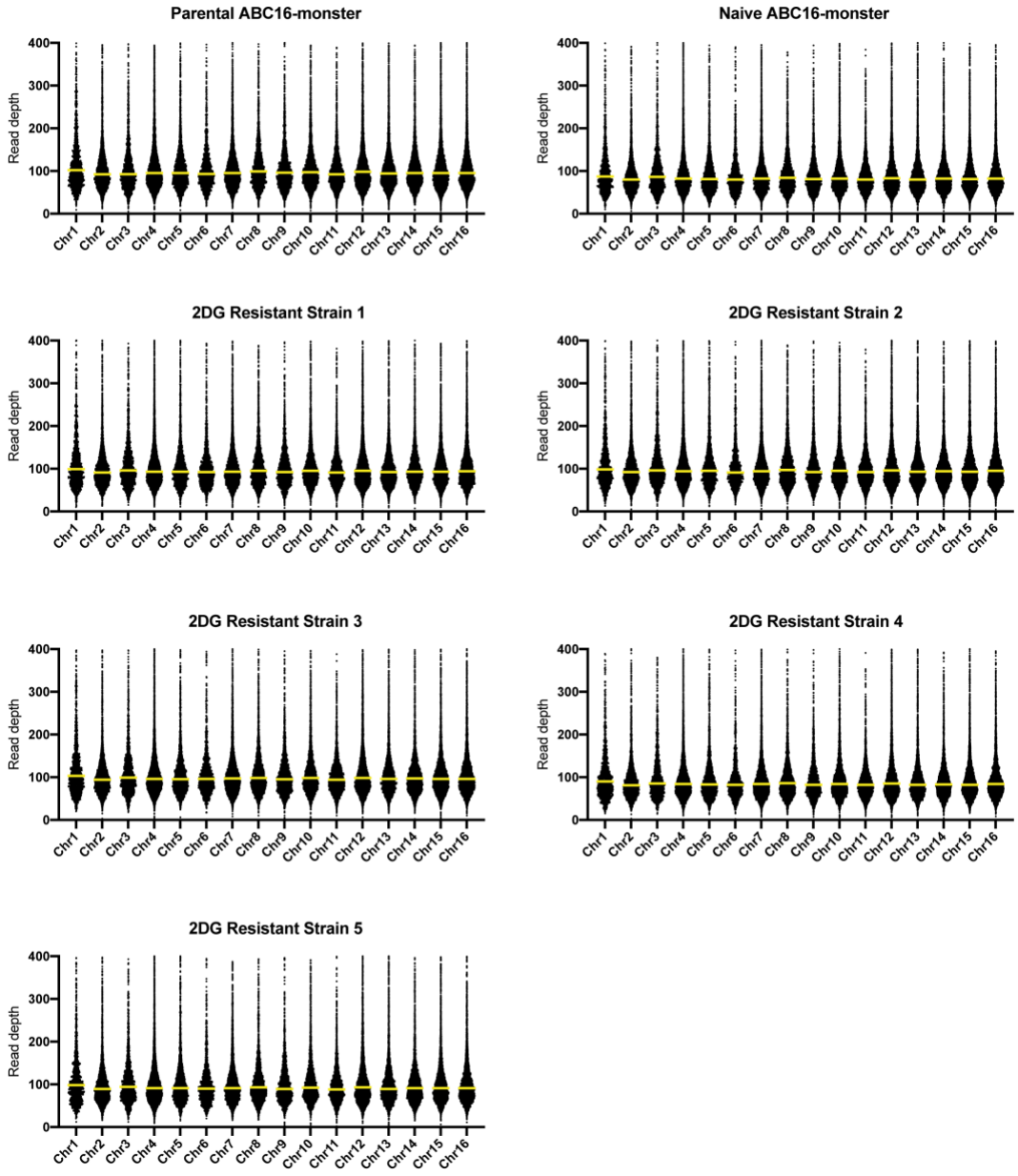

Figure 35. DNA sequence read depth across all sixteen chromosomes.

Data was plotted for the parental ABC16-monster, naïve ABC16-monster, and 2DG-resistant strains. The median value for each chromosome is shown as a yellow bar.

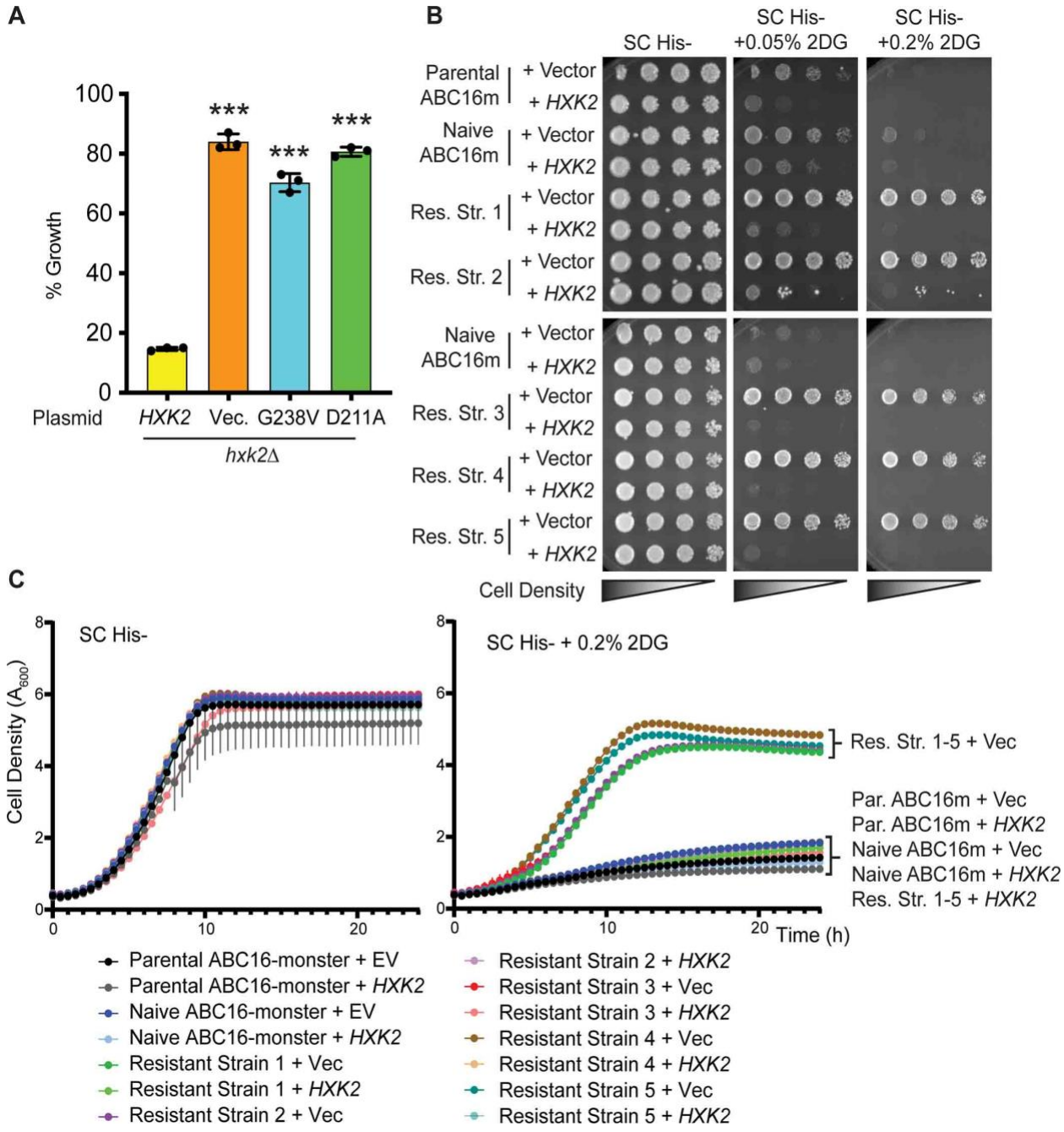

Figure 36. The *hxk2*^{G238V} mutation is sufficient to cause 2DG resistance.

(A) 2DG-resistance assay of *hxk2Δ* cells with CEN plasmids expressing either WT *HXK2*, *hxk2*^{G238V}, *hxk2*^{D211A}, or pRS313 vector. Three independent cultures were grown in medium with 2% glucose and either with or without 0.1% 2DG. Percent growth for each replicate is plotted relative to growth in the absence of 2DG, and the error bars represent +/- SD. A Student's t-test was used to compare *hxk2Δ* with the *HXK2*-expressing plasmids (*** indicates a p-value < 0.001). (B) Images of serial dilution growth plates containing cells from the parental or naïve ABC16-monster strain

as well as 2DG-resistant strains 1–5, each transformed with pRS313 empty vector or a plasmid expressing WT HXK2, after two days of growth at 30°C. All media contains 2% glucose as carbon source and the indicated added 2DG. (C) Graphs showing the change in cell density over time for cells grown in SC-His- or SC-His- with increasing 2DG concentrations (as described in B). Data are plotted as the A_{600} measured every 30 minutes, correcting for a 1 cm path length. Curves represent the average A_{600} of three technical replicates, and vertical lines from each data point represent +/-SD. In many cases, the SD was so small it did not expand beyond the data point itself.

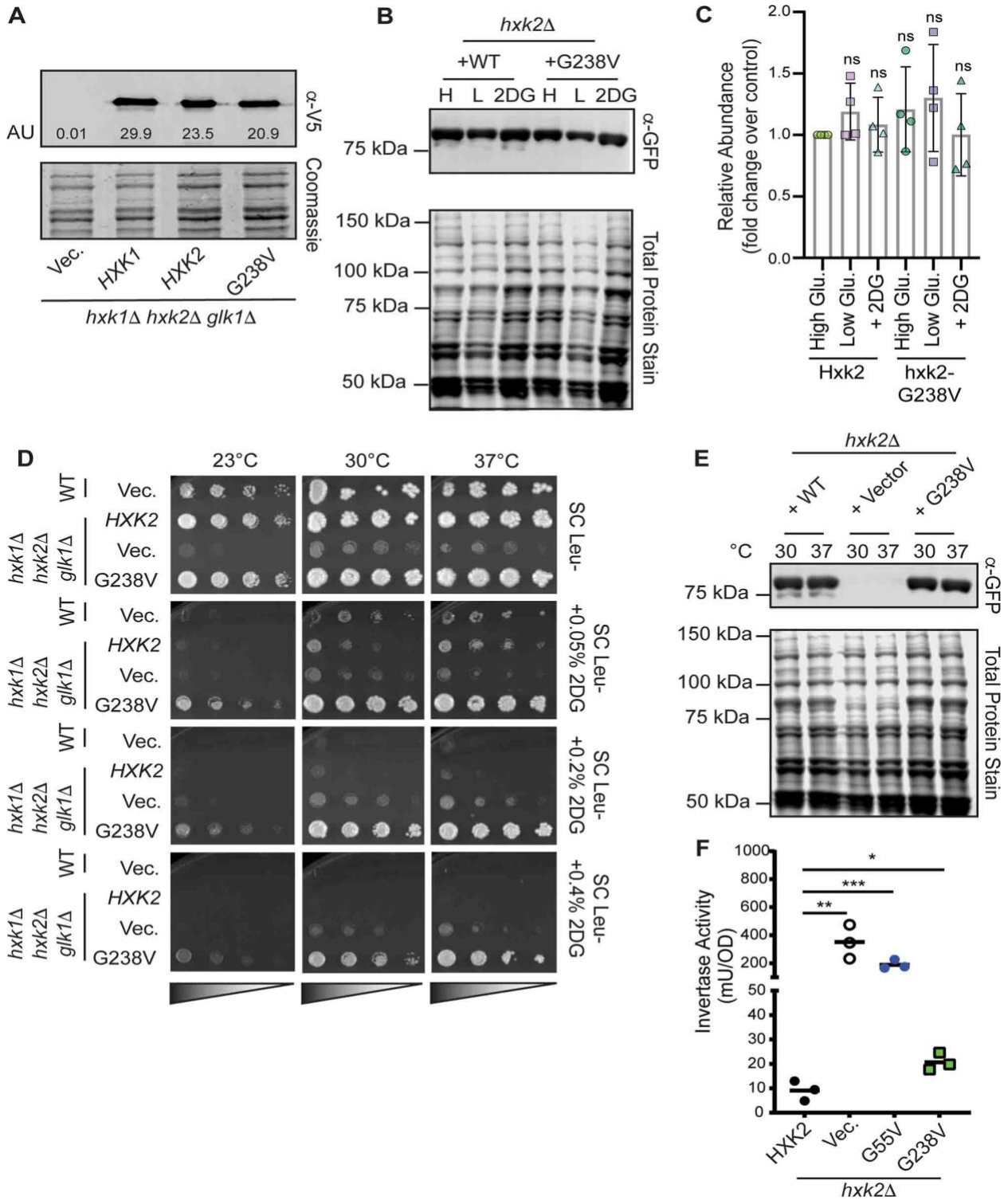

Figure 37. Hxk2^{G238V} is a stable protein that allows for growth on glucose in cells that otherwise lack hexokinase activity.

(A) Western blot of V5-epitope-tagged *HXK1*, *HXK2*, and *hxk2*^{G238V} expressed in *hxk1*Δ *hxk2*Δ *glk1*Δ cells. Quantification of the Hxk2 western signal is depicted in arbitrary units (AU) on the blot. (B) Western blot showing GFP-tagged Hxk2 protein levels from whole-cell extracts prepared from hxk2Δ cells grown in synthetic complete media with 2% glucose (H for high glucose) or 0.05% glucose (L for low glucose) alone, or with 2% glucose and the addition of 0.2% 2DG for two hours (2DG for medium containing this drug). REVERT total protein stain was used as a protein loading control. (C) Quantification of western signal as shown in panel B for four experimental replicates. The abundance of Hxk2 in high glucose conditions was normalized to 1 in each experiment, and all other values are shown as a relative fold change. A Student's t-test was performed to determine if any samples were different from the Hxk2 abundance in high glucose; none differed significantly from this standard. (D) Serial dilution spot assays of *hxk1*Δ *hxk2*Δ *glk1*Δ transformed with an empty vector control plasmid or one expressing Hxk2 or Hxk2^{G238V}. Cells were grown on the indicated medium, each of which contained 2% glucose as a carbon source and either no 2DG or 0.05–0.4% 2DG. The results pictured show cells after two days of growth at 23°C, 30°C, or 37°C. (E) Western blot showing GFP-tagged Hxk2 protein abundance in whole-cell extracts prepared from hxk2Δ cells expressing WT Hxk2 and Hxk2^{G238V}, from the same plasmids used in panel D. Cells were grown to mid-log phase in media containing 2% glucose before exposure to the indicated temperature for two hours. Proteins were then extracted. REVERT total protein stain was used as a protein loading control. (F) Invertase activity measured in three independent transformants of *hxk2*Δ cells grown in media with 2% glucose. A Student's t-test was used to assess the statistical difference between experimental groups and the Hxk2-expressing control.

3.2.3 Hxk2^{G238V} dampens catalytic activity

To assess the impact of Hxk2^{G238V} on glucose phosphorylation, we assayed the enzymatic function of Hxk2^{G238V} and WT Hxk2 by adding a precisely defined concentration of glucose to yeast total protein extracts made from *hxk1*Δ *hxk2*Δ *glk1*Δ cells containing only plasmid-borne Hxk2^{G238V} or Hxk2. We then compared the average production of NADPH, which is a proxy for measuring glucose phosphorylation (see Materials and Methods). Such coupled enzyme assays are well established and validated; this particular hexokinase assay was first developed in the 1950's

[446] and has subsequently been cited over 450 times. These experiments revealed that Hxk2^{G238V} was a significantly less effective enzyme and had a lower affinity for glucose and ATP (Figure 38A and Table 6). The specific activity (Vmax/au) of WT Hxk2 for glucose is substantially higher than that of Hxk2^{G238V}, while the Km is substantially lower (Table 6, Figure 39A-B). The same trend holds for the Km and specific activity of ATP (Table 6, Figure 39C-D). Yeast extract lacking all hexokinases (prepared using *hxk1*Δ *hxk2*Δ *glk1*Δ plus an empty vector) showed a very low background of Glc-6P conversion, serving as a negative control (Figure 38A). This low background confirms that other enzymes in the lysate that might similarly use ATP to reduce NADP to NADPH (e.g., galactokinase) are not active in our experiments due to the absence of their respective substrates (e.g., galactose).

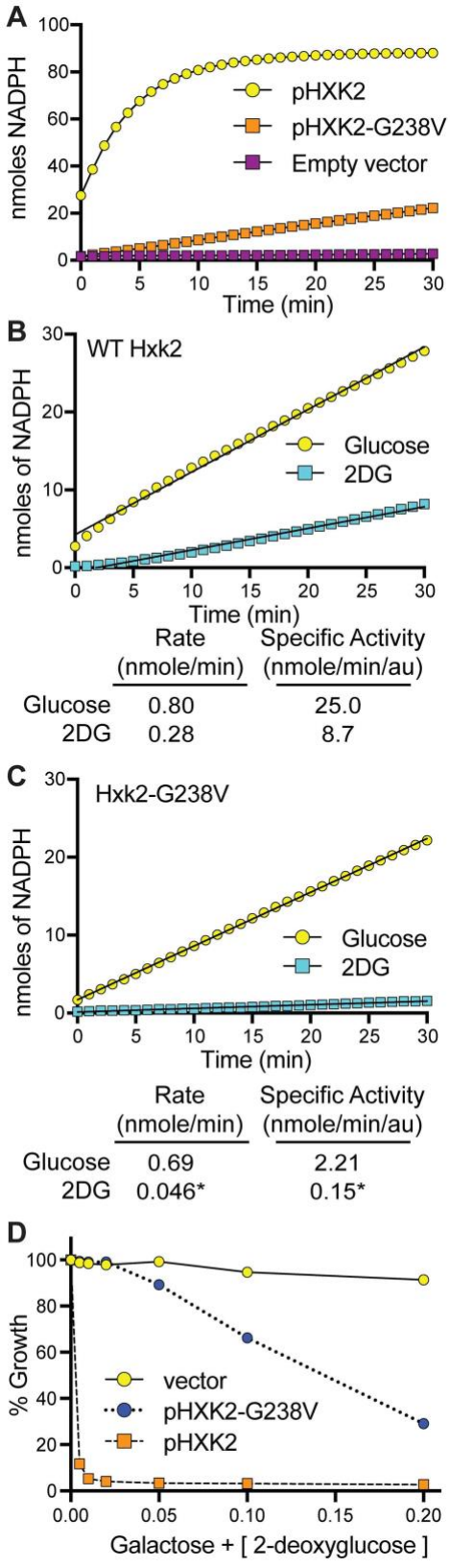

Figure 38. Hxk2^{G238V} has diminished enzymatic activity against glucose and 2DG.

(A) Measure of NADPH production (a proxy for hexose phosphorylation) over time using 5 μg of yeast total protein extracts made from *hxk1*Δ *hxk2*Δ *glk1*Δ cells containing the plasmids indicated. Use of the empty vector serves as a negative control and demonstrates the specificity of this approach for the activity of the plasmid-borne Hxk2. (B-C) Rate of NADPH production in cells expressing WT Hxk2 (B) or Hxk2^{G238V} (C) when total protein extracts were incubated with glucose (yellow) or 2DG (blue). In panel B, 0.68 μg of yeast extract was used (0.032 au per reaction). In panel C, 5.2 μg of yeast extract was used (0.31 au per reaction) to allow the reduced activity of Hxk2^{G238V} to be detectable in our assays. Even with the elevated amount of enzyme used, the rate of NADPH production in Hxk2^{G238V} expressing extracts incubated with 2DG was too low to be accurately measured; the values provided are marked with * to indicate that they are not reliable measures above background. (D) Cells lacking endogenous hexokinase activity (*hxk1*Δ *hxk2*Δ *glk1*Δ) but containing an empty vector or plasmid expressing Hxk2 or Hxk2^{G238V} were grown in galactose and varying concentrations of 2DG. Hxk2^{G238V}-expressing cells are more sensitive to 2DG than those lacking any Hxk2 activity at all, suggesting that Hxk2^{G238V} can phosphorylate 2DG *in vivo*.

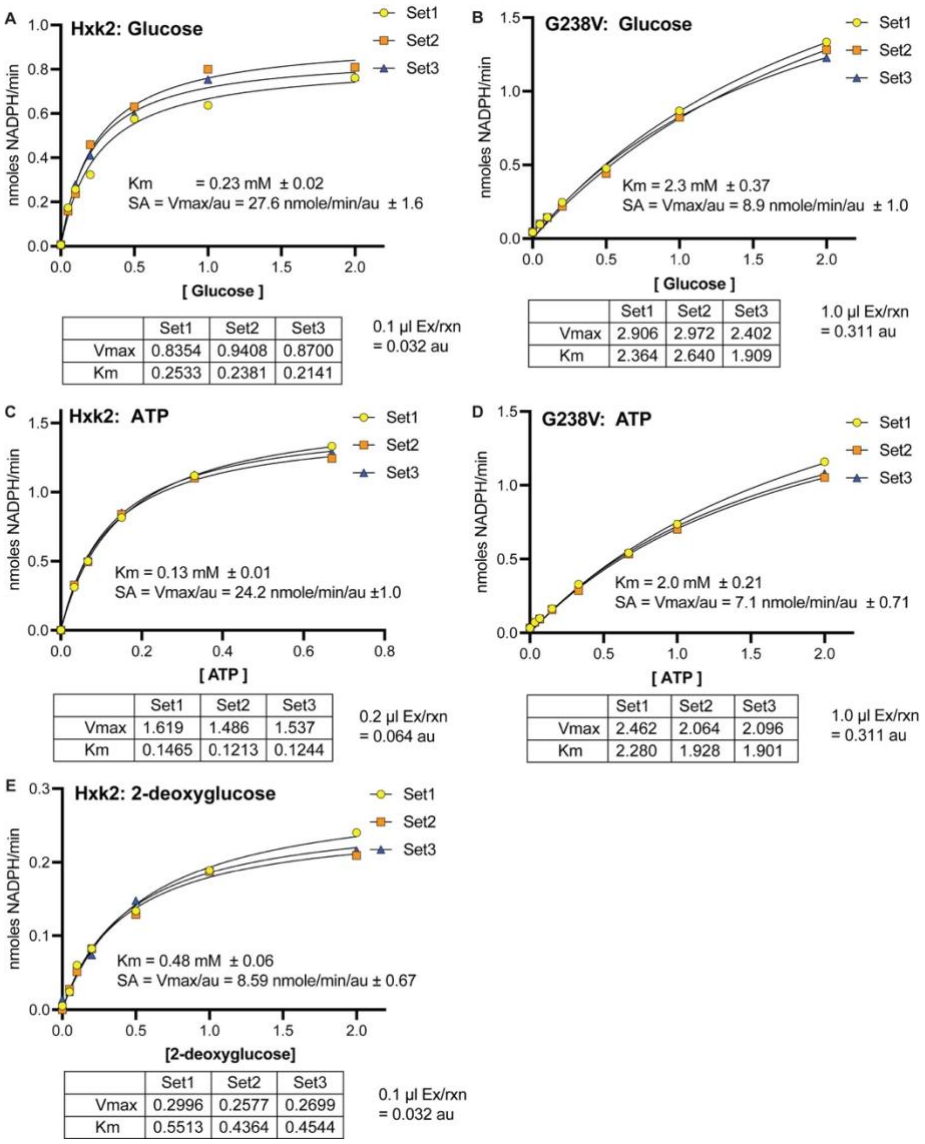

Figure 39. Glucose and ATP binding kinetics.

The data in these graphs support the enzymatic activity reported in Table 6. Three replicate experiments for each assay were preformed, and the results of each individual assay are presented here. In each case, total protein extracts were made from *hxk1Δ hxk2Δ glk1Δ* cells containing either WT Hxk2 (panels A, C and E) or Hxk2-G238V (panels D and B) and used in enzymatic assays where NADPH production is a readout for Hxk2 enzymatic function, as described in the Materials and Methods. (A) WT Hxk2 enzyme kinetics of glucose turnover were measured using 0.1 µl of yeast protein extract, which corresponds to 0.032 au of enzyme. (B) Hxk2-G238V enzyme kinetics of glucose turnover were measured using 1.0 µl of yeast protein extract, which corresponds to 0.311 au of enzyme. (C) WT Hxk2 enzyme kinetics of ATP turnover were measured using 0.2 µl of yeast protein extract, which corresponds to 0.064 au of

enzyme. (D) Hxk2-G238V enzyme kinetics of ATP turnover were measured using 1.0 µl of yeast protein extract, which corresponds to 0.064 au of enzyme. (E) WT Hxk2 kinetics of 2DG turnover were measured using 0.1 µl of yeast protein extract, which corresponds to 0.032 au of enzyme. A similar assay with Hxk2-G238V and 2DG did not yield values above the lower limits of detection for this assay.

Table 6. Enzyme kinetics for Hxk2 and Hxk2^{G238V}.

Each value is the mean of three experimental replicates ± standard deviation. The raw data to support these measurements is presented in Figure 39. Statistical analyses using a Student's t-test to compare WT Hxk2 values to those of Hxk2^{G238V} are provided in parenthesis, where a p-value of ns = not significant, * < 0.05, ** < 0.005, *** < 0.0005. The enzymatic activity of Hxk2^{G238V} against 2DG was not easily detectable above the background levels, so measurements were not determined (ND). However, Hxk2^{G238V} can clearly catalyze the conversion of 2DG because this allele elevates the sensitivity of galactose-grown cells to 2DG (see Figure 38D). K_m represents the Michaelis-Menten constant, and SA represents the specific activity (V_{max} normalized by the enzyme level).

	K_m Glucose (mM)	**SA Glucose (nmole/min/au)**	**K_m 2DG (mM)**	**SA 2DG (nmole/min/au)**	**K_m ATP (mM)**	**SA ATP (nmole/min/au)**
WT Hxk2	0.23±0.02	27.6±1.6	0.48±0.06	8.59±0.67	0.13±0.01	24.2±1.0
Hxk2^{G238V}	2.3±0.37 (***)	8.9±1.0 (***)	ND	ND	2.0±0.21 (***)	7.1±0.71 (**)

Using a similar approach, we next examined the ability of Hxk2 and Hxk2^{G238V} to phosphorylate 2DG using protein extracts again made from yeast cells lacking all three hexokinases and expressing only Hxk2 or Hxk2^{G238V}. We found that WT Hxk2 converted 2DG to 2DG-6P less effectively than it converted glucose to Glc-6P, as evidenced by a 2.5-fold reduction in the enzymatic rate and a 3-fold drop in specific activity with 2DG (Figure 36B and Table 6). Hxk2^{G238V} showed a similar trend, but Hxk2^{G238V} was less effective than WT Hxk2 at phosphorylating both glucose and 2DG (Figure 38C). The rate of Hxk2^{G238V} glucose phosphorylation was reduced to 0.69 nmole/min, consistent with what is reported in Table 6.

Hxk2^{G238V} 2DG phosphorylation was so low that we were unable to reliably calculate the rate, specific activity, Km, or Vmax (see notes in Figure 38B and Table 6).

To verify that Hxk2^{G238V} can still phosphorylate 2DG *in vivo*, we examined the physiological consequences of the allele in galactose-grown cells. We grew cells lacking the endogenous hexokinases (*hxk1*Δ *hxk2*Δ *glk1*Δ) and containing only plasmid-borne Hxk2 or Hxk2^{G238V} in galactose medium with increasing 2DG concentrations. We found that the cells with Hxk2^{G238V} were far more sensitive to 2DG than the vector control (Figure 38D). Because hexokinase activity is not needed for cell survival in galactose, this approach allowed us to selectively examine the impact of 2DG phosphorylation in the absence of glucose phosphorylation. These data support a model whereby Hxk2^{G238V} can phosphorylate both glucose and 2DG *in vivo*, but Hxk2^{G238V} is substantially less efficient than its WT Hxk2 counterpart.

3.2.4 Hxk2^{G238V} is unlikely to interfere directly with substrate binding

To characterize the molecular underpinnings of *Sc*Hxk2^{G238V}-mediated 2DG resistance and attenuated glucose phosphorylation, we first considered the possibility that the amino-acid change at position 238 directly interferes with substrate (e.g., 2DG or glucose) binding. A crystal structure of *Sc*Hxk2 in the open conformation (PDB 1IG8 [80]) reveals that G238 lies on a beta sheet (β10) near the glucose/2DG-binding site, but it does not line the site and so is unlikely to impede hexose association directly. We positioned a glucose molecule within the site by aligning a glucose-bound *Sc*Hxk1 structure (yeast, PDB 3B8A [79]) to 1IG8 [80]. The G238 residue is ~5.0 Å from the glucose substrate, and it participates in no apparent hydrogen-bond, electrostatic, or hydrophobic interactions with the sugar. The G238 side chain points away from the glucose molecule, so the larger V238 side chain in Hxk2^{G238V} is also unlikely to interact with the bound glucose.

To examine whether the amino acid at position 238 interacts with bound glucose when hexokinase is in the closed conformation—perhaps directly impeding the transfer of the γ phosphate from ATP—we examined a closed-state, glucose-bound structure of K. lactis Hxk1 (PDB 3O8M [83]). We chose this structure because there are no structures of glucose-bound *S. cerevisiae* Hxk2 in the Protein Data Bank [447,448]. Fortunately, *Kl*Hxk1 is a good model for *Sc*Hxk2 [83] because the two proteins are highly homologous (73.4% amino-acid identity per Clustal Omega [449,450], Figure 40), have similar oligomerization [83], and are similarly phosphorylated at regulatory residue S15 [83]. In the closed-state 3O8M *Kl*Hxk1 structure, the bound glucose molecule is 5.8 Å from the G238-equivalent residue (also a glycine). Furthermore, G238 forms no interactions with the key catalytic residue D211, nor with residues known to interact with the bound glucose (S158, K176, E269, and E302) [80]. We therefore conclude that the G238V mutation is unlikely to impair phosphorylation by altering any of the direct interactions between *Sc*Hxk2^{G238V} and 2DG or glucose.

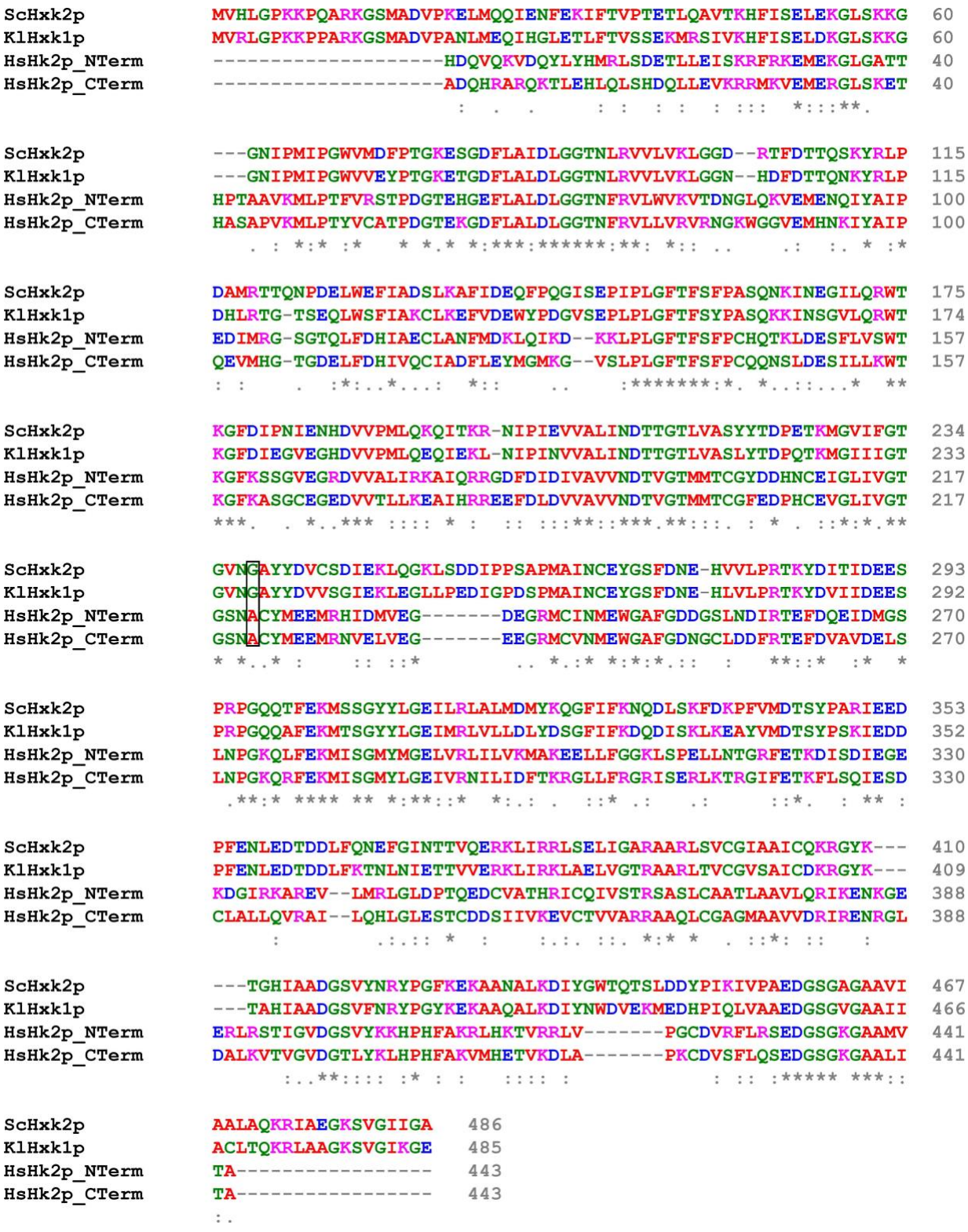

Figure 40. An alignment of *Sc*Hxk2, *Kl*Hxk1, and the two domains of *Hs*Hk2 reveals their high sequence similarity.

We used Clustal Omega to align the amino acid sequences of *Sc*Hxk2, *Kl*Hxk1, and the two domains of *Hs*Hk2.The position of residue 238 is marked with a box.

3.2.5 *Sc*Hxk2^{G238V} may interfere with glucose binding by altering protein dynamics

To determine whether changes in protein dynamics might explain the attenuated enzymatic activity and 2DG resistance, we performed twelve molecular dynamics (MD) simulations of four *Sc*Hxk2 systems: WT Hxk2 *apo* (ligand-absent), Hxk2^{G238V} *apo*, WT Hxk2 *holo* (glucose-bound), and Hxk2^{G238V} *holo*. For each of the four systems, we performed three simulations of ~250 ns, ~250 ns, and ~500 ns each (~1 μS for each system, ~4 μS total). Unless otherwise noted, we treat the three simulations associated with each system as one. All simulations started from the same open conformation (PDB 1IG8 [80]); those that include bound glucose thus capture the initial dynamics associated with glucose association, including the large-scale conformational change ("domain closure," Figure 33) required for catalysis.

3.2.6 Hxk2^{G238V} impacts local pocket dynamics

The simulations suggest that Hxk2^{G238V} influences three binding-cleft regions (Figure 41 and 42A): the β9/β10 β-hairpin (I231-V236), the catalytic residue D211, and the α11' helix (D417-P425). Specifically, Hxk2^{G238V} increases the *apo*-state flexibility of all three (Figure 41A, in blue ribbon) while stabilizing the holo-state β-hairpin (Figure 41B, in red ribbon). As detailed in the Discussion section, these changes in dynamics may impede glucose binding and phosphorylation, explaining the delayed Hxk2^{G238V} glucose catalysis we observed biochemically (Table 6 and Figure 38 and 39).

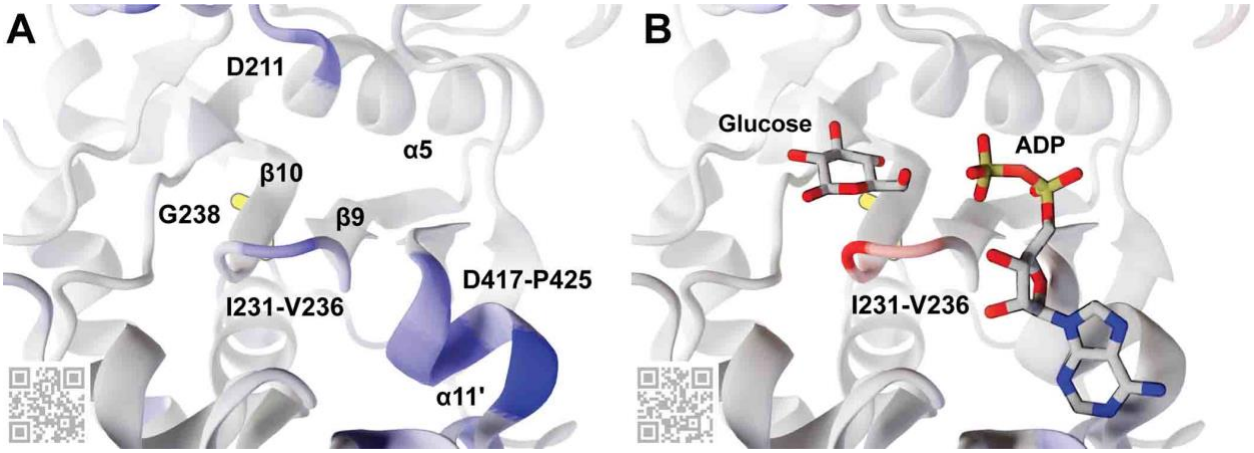

Figure 41. An Hxk2 pocket conformation taken from the MD simulations.

G238, though largely obscured by the β10 strand, is shown in yellow sticks. Other key amino acids, molecules, and secondary-structure elements are labeled. The Hxk2 protein (ribbon) is colored according to the calculated ΔRMSF values, where blue indicates that the G238V simulation was more flexible (ΔRMSF > = 0.85 Å), and red indicates that the WT simulation was more flexible (ΔRMSF < = -0.85 Å). (A) The ΔRMSF values for the apo (ligand-absent) simulations. (B) The ΔRMSF values for the holo (glucose-bound) simulations. Glucose and ADP crystallographic poses are superimposed only for reference, to indicate the locations of the glucose and ATP-binding pockets. They were taken from structures of *Hs*HK1 (human, PDB 4FPB) and *Os*HXK6 (rice, PDB 6JJ8), respectively. QR codes encode ProteinVR URLs for visualization in stereoscopic 3D (virtual reality).

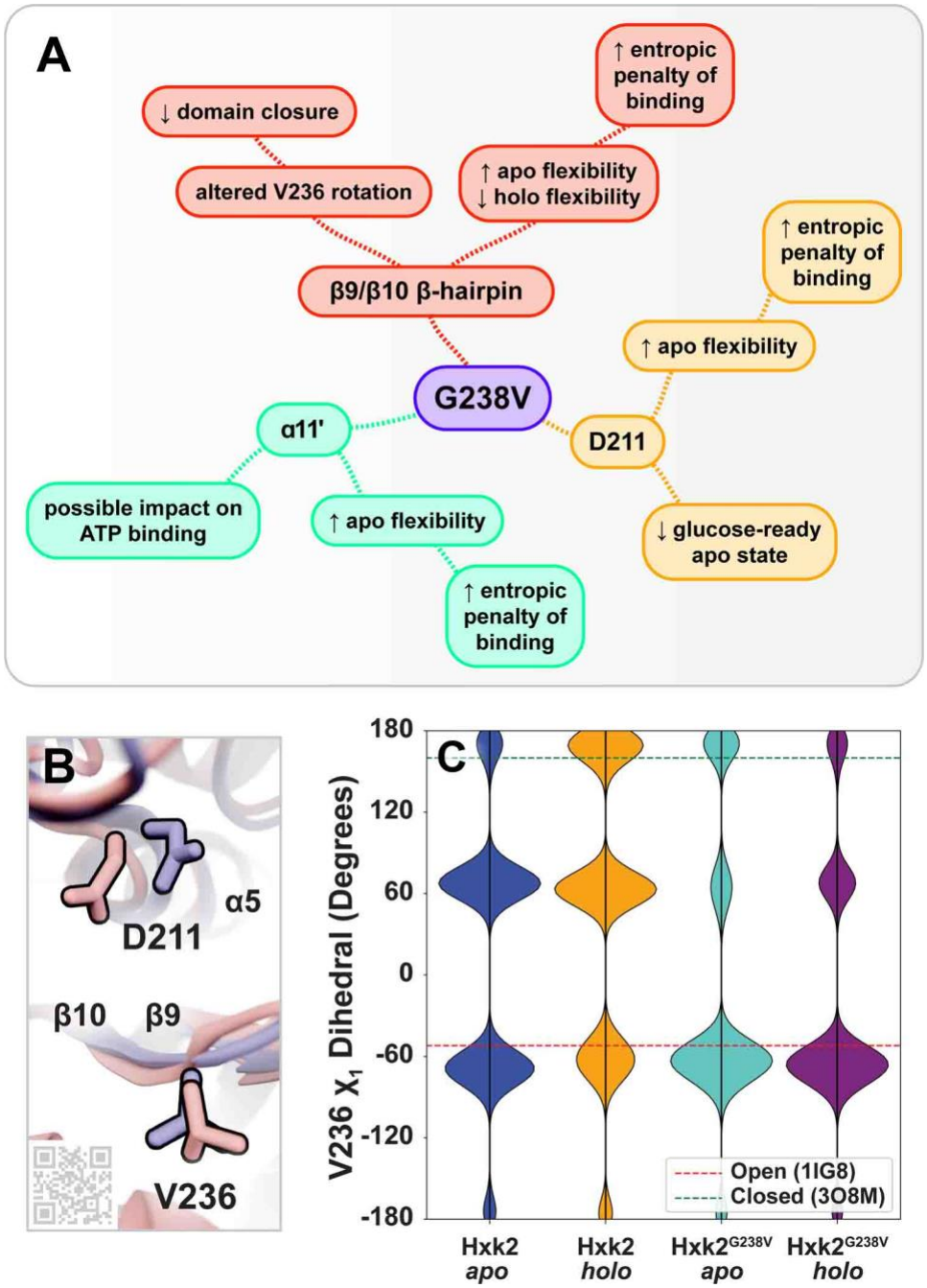

Figure 42. Hypothesized impacts of *Sc*Hxk2^{G238V} on the catalytic mechanism.

(A) The G238V mutation alters the dynamics of the β9/β10 β-hairpin, the catalytic D211 residue, and the α11' helix. The implications of these changes on enzyme function are summarized. (B) Two conformations taken from the *Sc*Hxk2^{G238V} apo simulations highlight the movements of V236 (loop residue) and D211 (catalytic residue). In blue, V236 is shown in an open-like conformation, and D211 is shown in a glucose-ready conformation. In pink, V236 is shown in a closed-like conformation, and D211 is shown in a displaced conformation. Key secondary-structure

elements are labeled with text, and the substrate-adjacent loop is labeled by its residues (I231-V236). The QR code provides a link to an online ProteinVR scene for virtual-reality visualization. (C) The distributions of the V236 χ1 dihedral angle. For reference, the red and green dashed lines show the corresponding values of the 1IG8 (*Sc*Hxk2, open) and 3O8M (*Kl*Hxk1, closed) crystal structures, respectively.

3.2.6.1 β9/β10 β-hairpin (I231-V236)

Hxk2^{G238V} substantially impacts the dynamics of a β-hairpin loop that bridges the β9 and β10 strands (I231 to V236) [80]. This loop resides at the center of the enzymatic cleft near the glucose and ATP binding sites (Figure 41), so its dynamics likely influence the catalytic mechanism. To assess the flexibility of the β-hairpin loop residues, we calculated per-residue root-mean-square fluctuation (RMSF) and B-factor values (Table 7, Suppl. Table). To visualize the impact of the mutation, we mapped RMSF differences (ΔRMSF, $RMSF_{WT}$—$RMSF_{G238V}$) onto the protein structure (Figure 41). These ΔRMSF calculations suggest that in the *apo* (ligand-absent) state, the G238V mutation enhances the flexibility of the β-hairpin loop over WT; in contrast, in the *holo* (glucose-bound) state, the mutation reduces β-hairpin flexibility over WT (Table 7, Suppl. Table).

Hxk2^{G238V} also impacts the extent to which β-hairpin and residue-238 motions are correlated. We used dynamic cross correlation (DCC) to compare the motions of G238/V238 to those of the other Hxk2 residues. Table 7 and Suppl. Table presents per-residue differences in correlation coefficients (ΔDCC, DCC_{WT}—DCC_{G238V}). The motions of key β-hairpin residues and residue 238 are more correlated in Hxk2^{G238V} than in WT Hxk2 (Table 7, Suppl. Table), suggesting an allosteric influence that is stronger in Hxk2^{G238V}. Indeed, multiple β-hairpin residues have ΔDCC values more than two standard deviations from the mean ΔDCC across all residues (G235

and V236 in the *apo* simulations, and T234 and G235 in the *holo* simulations; Table 7, Suppl. Table).

Hxk2^{G238V} also impacts the dynamics of β-hairpin-residue V236, which may influence the domain closure required for catalysis (see Discussion). We monitored the V236 χ1 dihedral angle (CG2-CB-CA-C) throughout the simulations. In the WT Hxk2 *apo* simulation, V236 heavily sampled the gauche conformation typical of the open state (~-51°), but in the WT Hxk2 *holo* simulation, it shifted more to the anti-conformation typical of the closed state (~160°, Figure 42B-C) [451]. Interestingly, the same shift was not observed in the Hxk2^{G238V} simulations, suggesting the mutation at position 238 might impede V236 rotation.

3.2.6.2 D211: catalytic residue

Hxk2^{G238V} also impacts the dynamics of D211, a residue that plays a critical role in catalysis (Figure 41 and 42B). In the glucose-bound state, our ΔRMSF calculations suggest that Hxk2^{G238V} has little impact on D211 flexibility. In contrast, in the unbound state, Hxk2^{G238V} enhances D211 flexibility over WT Hxk2 (Table 7, Suppl. Table). The Hxk2^{G238V} D211 samples much of the expected "glucose-ready" conformation (Figure 42B, in blue), but it also flips away from the ATP binding pocket as the α5 helix to which it belongs unfolds slightly (Figure 42B, in pink). This added D211 conformational flexibility could also contribute to reduced catalysis.

3.2.6.3 α11' helix

Hxk2^{G238V} impacts the local dynamics of a critical alpha helix (α11') that lines the ATP-binding site (Figure 41) [80]. The ΔRMSF analysis suggests that in the unbound state, the Hxk2^{G238V} enhances the flexibility of this helix over WT Hxk2 (e.g., S419, V420, Y421, and

R423). In contrast, in the glucose-bound state, the mutation has little impact on the flexibility of these residues (Table 7, Suppl. Table).

Table 7. The impact of Hxk2^{G238V} on the dynamics of the β9/β10 B-hairpin, D211 catalytic, and α11' residues. The differences in RMSF and DCC values (ΔRMSF and ΔDCC, respectively), followed by the corresponding raw WT and Hxk2^{G238V} values in parentheses. Negative and positive ΔRMSF values suggest Hxk2^{G238V} has increased or decreased the flexibility of the corresponding residue, respectively. Similarly, negative and positive ΔDCC values suggest that Hxk2^{G238V} has increased or decreased the degree of correlation between the motions of G/V238 and the corresponding residue, respectively. For convenience, we also show the differences in calculated B-factors, derived from the RMSF values using the equation $\boldsymbol{B_i = (8\pi^2/3)RMSF_i^2}$ (see reference [452]). In all cases, values that deviate from the respective means by more than two standard deviations are shown in bold. All values are rounded to the nearest hundredth.

Location	**Residue**	***apo* ΔRMSF**	***holo* ΔRMSF**	***apo* ΔDCC**	***holo* ΔDCC**
β9/β10 β-hairpin	I231	-0.13 (0.68-0.82)	0.00 (0.57-0.57)	-0.04 (0.65-0.69)	-0.04 (0.64-0.68)
	F232	-0.33 (0.73-1.06)	-0.07 (0.65-0.72)	-0.05 (0.50-0.55)	0.07 (0.58-0.51)
	G233	-0.25 (1.26-1.50)	0.00 (0.87-0.87)	-0.03 (0.28-0.31)	-0.11 (0.21-0.32)
	T234	-0.59 (1.06-1.66)	**0.49 (1.44-0.95)**	-0.14 (0.18-0.32)	**-0.30 (0.04-0.33)**
	G235	-0.22 (1.04-1.26)	**0.86 (1.81-0.95)**	**-0.28 (0.10-0.38)**	**-0.28 (0.08-0.36)**
	V236	0.12 (0.92-0.80)	0.41 (1.19-0.78)	**-0.41 (0.21-0.62)**	-0.21 (0.35-0.56)
D211 (catalytic)	D211	-0.66 (0.67-1.33)	0.00 (0.57-0.57)	-0.02 (0.23-0.25)	-0.20 (0.34-0.54)
α11' helix	D417	-0.09 (0.67-0.77)	0.00 (0.61-0.61)	-0.08 (0.47-0.55)	-0.07 (0.47-0.54)
	G418	-0.14 (0.82-0.96)	0.05 (0.71-0.66)	0.03 (0.41-0.37)	-0.03 (0.41-0.44)
	S419	-0.55 (1.03-1.58)	0.11 (0.92-0.81)	0.05 (0.29-0.24)	-0.08 (0.21-0.29)
	V420	-0.64 (0.89-1.53)	0.03 (0.83-0.80)	0.04 (0.27-0.24)	-0.09 (0.28-0.37)
	Y421	-0.67 (0.80-1.47)	-0.01 (0.81-0.82)	0.13 (0.29-0.16)	-0.10 (0.30-0.40)
	N422	-0.39 (0.96-1.35)	0.06 (0.98-0.92)	0.17 (0.25-0.07)	-0.09 (0.23-0.32)
	R423	**-0.97 (1.03-1.99)**	0.05 (0.98-0.93)	0.10 (0.19-0.10)	-0.12 (0.18-0.29)
	Y424	-0.24 (0.87-1.11)	-0.17 (1.04-1.22)	-0.04 (0.17-0.21)	-0.19 (0.17-0.36)
	P425	-0.05 (1.00-1.05)	-0.47 (1.60-2.06)	-0.06 (0.04-0.10)	-0.23 (0.12-0.35)
Location	**Residue**	***apo* ΔB-factor**		***holo* ΔB-factor**	
β9/β10 β-hairpin	I231	-5.53 (12.17 - 17.70)		0.00 (8.55 - 8.55)	
	F232	-15.54 (14.03 - 29.57)		-2.52 (11.12 - 13.64)	
	G233	-17.44 (41.78 - 59.22)		0.00 (19.92 - 19.92)	
	T234	-42.95 (29.57 - 72.52)		**30.82 (54.57 - 23.75)**	
	G235	-13.31 (28.47 - 41.78)		**62.47 (86.22 - 23.75)**	
	V236	5.44 (22.28 - 16.84)		21.26 (37.27 - 16.01)	
D211 (catalytic)	D211	-34.75 (11.81 - 46.56)		0.00 (8.55 - 8.55)	
α11' helix	D417	-3.79 (11.81 - 15.60)		0.00 (9.79 - 9.79)	
	G418	-6.56 (17.70 - 24.26)		1.81 (13.27 - 11.46)	
	S419	-37.78 (27.92 - 65.7)		5.01 (22.28 - 17.27)	

	V420	-40.76 (20.85 - 61.61)	1.29 (18.13 - 16.84)
	Y421	-40.03 (16.84 - 56.87)	-0.43 (17.27 - 17.70)
	N422	-23.71 (24.26 - 47.97)	3.00 (25.28 - 22.28)
	R423	**-76.31 (27.92 - 104.23)**	2.52 (25.28 - 22.76)
	Y424	-12.51 (19.92 - 32.43)	-10.70 (28.47 - 39.17)
	P425	-2.70 (26.32 - 29.02)	-44.31 (67.38 - 111.69)

3.2.7 *Sc*Hxk2^{G238V} affects global protein dynamics

Having examined the impact of *Sc*Hxk2^{G238V} on the local dynamics of the enzymatic cleft, we next examined its effect on the global domain-closure dynamics associated with glucose binding and catalysis. Our simulations ran long enough to sample both open (*apo*, unbound) and closed (*holo*, glucose bound) conformations. For example, included among the many conformations sampled throughout the WT *Sc*Hxk2 and *Sc*Hxk2^{G238V} *apo* simulations were those that differed from the open 1IG8 *Sc*Hxk2 crystallographic conformation [80] by only 0.78 and 0.75 Å, respectively, per heavy-atom backbone root-mean-square deviation (RMSD; Figure 43). Similarly, included among the conformations of the WT *Sc*Hxk2 and *Sc*Hxk2^{G238V} glucose-bound simulations were those that differed from the closed 3O8M *Kl*Hxk1 conformation [83] by only 1.13 and 1.18 Å, respectively (Figure 41). Because the simulations capture both open and closed conformations, they can reasonably inform a study of the transition between these two states.

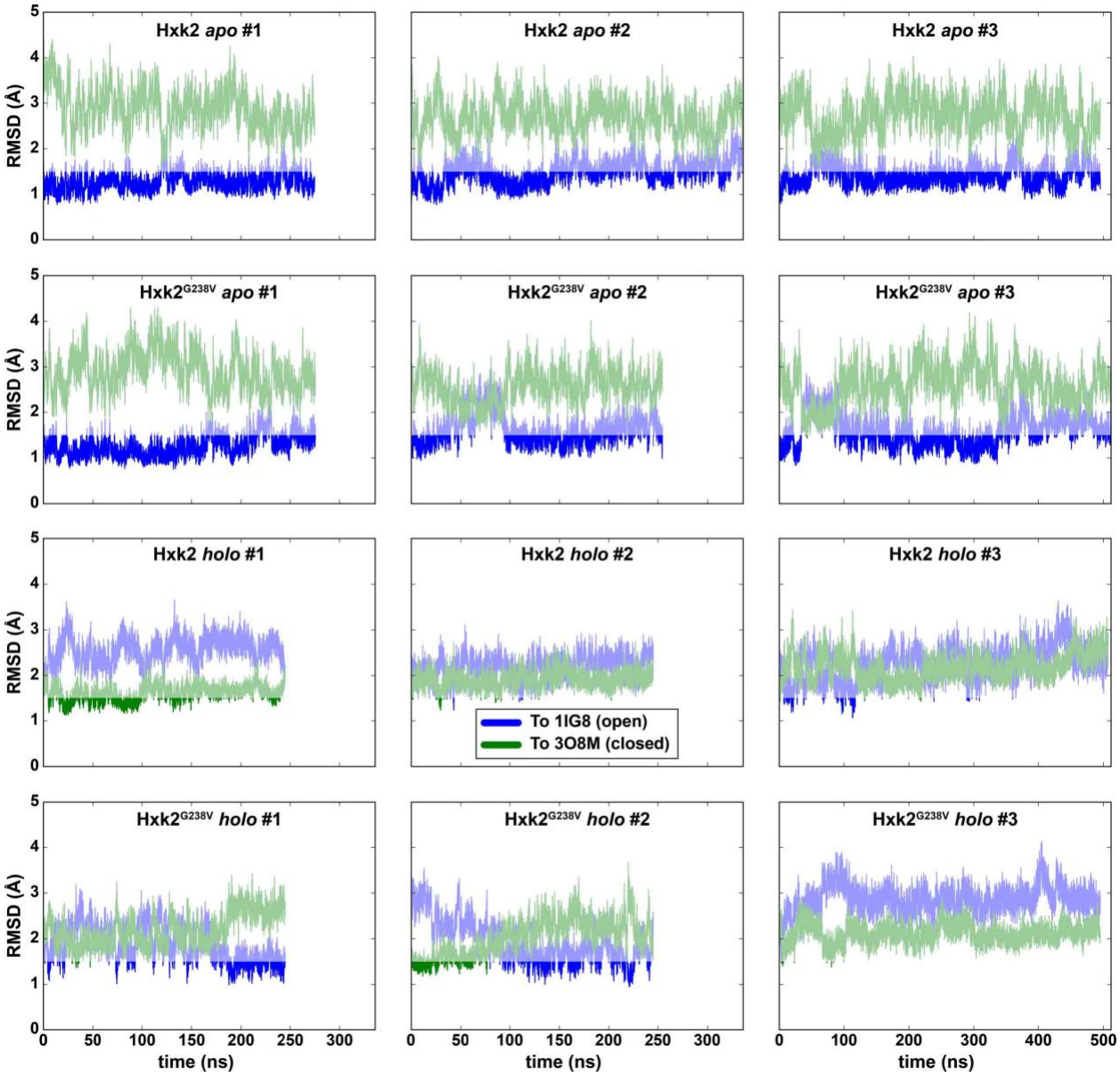

Figure 43. The simulations collectively sample both open and closed conformations.

The RMS distance between simulated conformations and the open (*Sc*Hxk2, PDB ID: 1IG8 [80]) and closed (*Kl*HXK1, PDB ID: 3O8M [83]) conformation, are shown in blue and green, respectively. The three simulations associated with the Hxk2 *apo*, Hxk2^{G238V} *apo*, Hxk2 *holo*, and Hxk2^{G238V} *holo* systems are shown on the first, second, third, and fourth row, respectively. RMSD values less than 1.5 Å are shown in bold to highlight simulated conformations that are notably close to the open (bolded blue) or closed (bolded green) states.

3.2.7.1 Hxk2^{G238V} alters large-scale opening and closing motions

Before glucose binding, Hxk2 exists predominantly in an open state (i.e., the helical large subdomain and the α/β small subdomain are positioned such that the enzymatic cleft is accessible [79,80]). Once the glucose binds, these two domains adopt a closed conformation by rotating relative to each other, thus collapsing the cleft and enveloping the glucose molecule [80,430] (Figure 33). Hxk2^{G238V} notably impacts these global motions, which substantially affect the entire protein structure.

To quantify this impact, we calculated the protein radius of gyration (RoG) throughout the four simulations (Figure 44). A larger RoG indicates that Hxk2 is in the open conformation (Figure 44, red dotted line), and a lower RoG indicates the closed conformation (Figure 44, green dotted line). Given that the RoG distributions are not all normally distributed, we performed a non-parametric statistical analysis called the Kruskal-Wallis test [453] to assess differences in means. This analysis led us to reject the hypothesis that there is no difference in the mean RoG values of the Hxk2 *apo*, Hxk2 *holo*, Hxk2^{G238V} *apo*, and Hxk2^{G238V} *holo* simulations (F-statistic: 2.6 x 106; p-value < 0.001). A subsequent Conover post hoc analysis [454] revealed that the four simulations are all different in terms of the RoG values sampled (adjusted p-value < 0.001 in all cases).

We found that the Hxk2^{G238V} RoG was generally lower than that of WT Hxk2 (Figure 44), suggesting that Hxk2^{G238V} is less prone to adopt a fully open conformation (Cohen's d values of 0.551 and 0.516 for the *apo* and *holo* states, respectively, corresponding to medium effect sizes for both). The standard deviations associated with the Hxk2^{G238V} simulations (both *apo* and *holo*) were also greater than those associated with the WT Hxk2 simulations, suggesting that glucose binding to Hxk2^{G238V} is less prone to induce the closed state required for catalysis, perhaps explaining why the Hxk2^{G238V} Km for glucose is ten times higher than that of WT Hxk2 (Table 6).

To further verify the impact of Hxk2^{G238V} on large-scale open-to-closed motions, we used the POVME2 algorithm [455,456] to measure the volume of the enzymatic cleft over the course of the simulations. The means and standard deviations of the binding-cleft volume showed similar trends (Figure 45), corroborating the observed differences in large-scale motions and suggesting that those differences directly impact the shape of the enzymatic cleft.

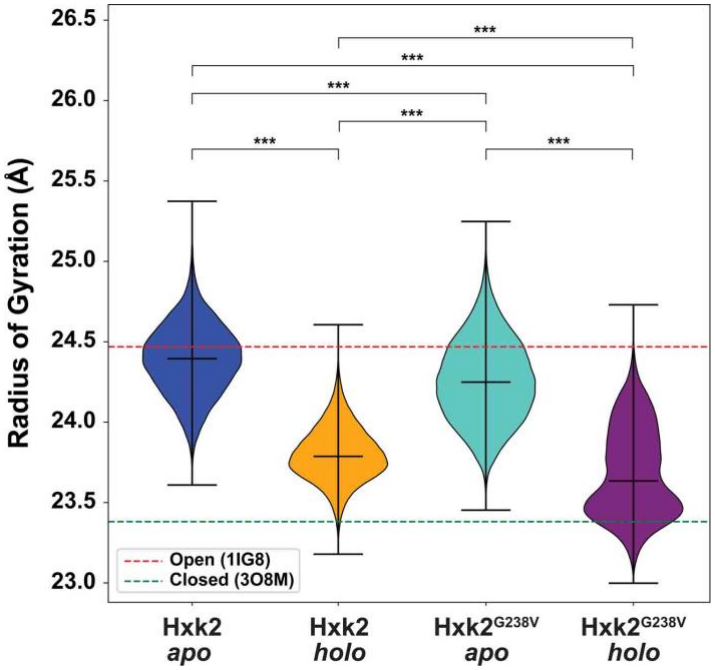

Figure 44. Distributions of the radii of gyration.

For reference, the red and green dashed lines show the corresponding values of the 1IG8 (*Sc*Hxk2, open) and 3O8M (*Kl*Hxk1, closed) crystal structures, respectively. The middle horizontal lines correspond to the median values associated with each simulation. The mean of each simulation differs statistically from the means of all others (Kruskal–Wallis, p-value < 0.001; Conover post hoc analysis, adjusted p-value < 0.001 in all cases, indicated by ***).

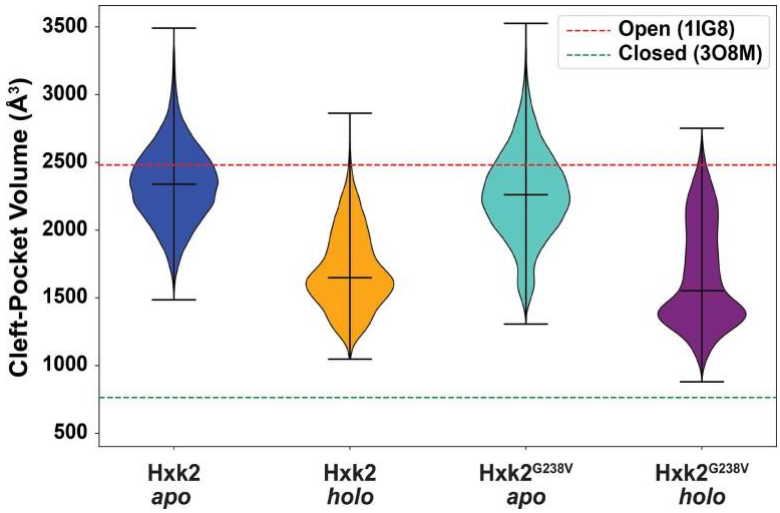

Figure 45. Distributions of the enzymatic-cleft volumes.

For reference, the red and green dashed lines show the corresponding values of the 1IG8 (*Sc*Hxk2, open) and 3O8M (*Kl*Hxk1, closed) crystal structures, respectively. The middle horizontal lines correspond to the median values associated with each simulation.

3.2.7.2 Hxk2^{G238V} alters the centrality of cleft-lining amino acids

Hxk2^{G238V} appears to modify how the impact of glucose binding propagates to distant protein regions (e.g., along pathways of adjacent residues whose motions influence one another), possibly explaining why glucose binding is less likely to induce domain closure. To assess potential shifts in these residue-residue communication pathways, we calculated each residue's betweenness centrality (BC), which measures the extent to which that residue participates in these many pathways. Said another way, BC indicates how essential a given amino acid is for intra-protein communication (e.g., signal propagation; see the Materials and Methods for a more formal description).

Ensemble-average, per-residue betweenness centrality (BC) calculations [457] revealed that residues of the WT Hxk2 enzymatic cleft have a substantial influence on intra-protein communication. The β9/β10 β-hairpin residues are present in 14.19% and 15.87% of the shortest

paths calculated from the WT Hxk2 *apo* and *holo* simulations, respectively, but comprise only 1.28% of the residues in the simulation (I231 to V236, 6/469); D211 is present in 4.96% and 3.70% of the *apo* and *holo* paths, respectively, but comprises only 0.21% of all residues (1/469); and α11' residues are present in 12.28% and 11.70% of the *apo* and *holo* paths, respectively, but comprise only 1.92% of all residues (D417 to P425, 9/469) (Suppl. Table).

These same BC calculations applied to Hxk2^{G238V} reveal substantial changes in the influence of cleft-lining residues. The BC of V238 increases, suggesting it has a greater influence on inter-protein communication (large effect size in both the *apo* and *holo* states; Cohen's d values of -2.45 and -2.22, respectively, more than for any other residue). In contrast, the BC of D211 decreases, suggesting reduced influence (medium effect size in *apo* state, Cohen's d value of 0.67, third largest decrease; negligible effect size in the *holo* state, Cohen's d value of 0.11). The impact on the BC of the β9/β10 β-hairpin and α11' residues is also profound, though more varied. Hxk2^{G238V} increases the BC of some residues while decreasing others (Suppl. Table).

These results suggest that in WT Hxk2, the enzymatic cleft is a nexus through which much intra-protein communication ("information") flows. The impact of glucose binding at the cleft can, in theory, readily propagate throughout the protein, inducing domain closure and catalysis. But Hxk2^{G238V} alters the betweenness centrality of the cleft-lining residues, in part by shifting centrality to V238, a residue that does not directly interact with bound glucose. These changes may alter how the glucose-binding signal propagates throughout the protein, impeding domain closure and catalysis.

3.3 Discussion

In this work, we exposed a drug-sensitive yeast strain to 2DG, a toxic glucose analog. Whole genome sequencing revealed a novel mutation in hexokinase 2 ($Hxk2^{G238V}$) that confers 2DG resistance. We demonstrate that this mutation is sufficient to confer 2DG-resistance and that the *hxk2*^{G238V} allele encodes a stable but hypomorphic protein. This enzyme has reduced catalytic activity toward both glucose and 2DG but appears capable of phosphorylating these molecules *in vivo*, as evidenced by our phenotypic analyses (Figures 34, 36, and 38). The altered residue does not appear to interact directly with glucose or ATP, but $Hxk2^{G238V}$ has higher Km values and reduced specific activity for both substrates. This finding is significant because, to the best of our knowledge, only one other 2DG-resistance Hxk2 mutation has been discovered that does not directly impact the enzymatic cleft ($Hxk2^{G55V}$) [224]. All others alter amino acids that line the glucose-binding (e.g., $Hxk2^{T212P}$, $Hxk2^{K176T}$, and $Hxk2^{Q299H}$ [287]) or ATP-binding (e.g., $Hxk2^{D417G}$, $Hxk2^{R423T}$, $Hxk2^{D211A}$ [224], $Hxk2^{G418C}$, and $Hxk2^{T75I/S345P}$ [287]) pockets.

3.3.1 Allosteric influences on local and global dynamics

The $Hxk2^{G238V}$ variant substitutes a glycine for a valine, two residues that differ only by an isopropyl group. Yet, the presence of those three additional heavy atoms indirectly influences multiple components of the catalytic mechanism (Figure 42A) via allosteric effects on local dynamics that shift the global conformational ensemble. Indeed, our work provides a dramatic example of how even small changes to protein structure can drastically alter protein function—in this case, catalysis—via allosteric mechanisms. Though V238 does not line the enzymatic cleft, it impinges on the motions of neighboring residues, which in turn impinge on their neighbors, etc.,

thus (1) propagating a signal to pocket-lining Hxk2^{G238V} residues, (2) perturbing local and global protein dynamics, and (3) ultimately reducing Hxk2^{G238V} catalytic activity.

Our work suggests this allosteric influence alters the flexibility of the enzymatic cleft, possibly increasing the entropic penalty of binding. Hxk2^{G238V} increases the flexibility of the *apo* (ligand-absent) binding cleft (Figure 41A, in blue ribbon; Suppl. Table and Table 7), which likely increases the number of sampled microstates. In contrast, Hxk2^{G238V} decreases the flexibility of the *holo* (glucose-bound) cleft (Figure 41B, in red ribbon). The entropic penalty of glucose binding may therefore be greater for Hxk2^{G238V} than for WT Hxk2, though other factors also impact entropy (e.g., the order imposed on ligand and water-molecule movements). Experimental methods such as isothermal titration calorimetry could be used to further assess the impact of the mutation on the entropic and enthalpic contributions to glucose and 2DG binding.

Hxk2^{G238V} may also impede glucose and 2DG phosphorylation by allosterically impacting the dynamics of β-hairpin residue V236. We hypothesize that the domain closure associated with catalysis requires V236 to rotate from a gauche conformation (prominent in our more open WT *apo* simulation as well as the open-state 1IG8 [80], 3O80, 3O1W, 3O4W, 4JAX, 3O6W, and 3O5B [83] structures) to an anti-conformation (prominent in our more closed WT *holo* simulation as well as the closed-state 3O8M structure [83]; Figure 42B-C, and 44). But in the Hxk2^{G238V} simulations, V236 was overwhelmingly in the gauche conformation typical of the open state, even in the more closed *holo* (glucose-bound) simulation (Figure 42B-C, and 44). By limiting V236 rotation, Hxk2^{G238V} makes V236 less likely to adopt the anti-conformation more typical of the close state. Mutagenesis experiments could further clarify the role of the V236 residue and its flexibility. We hypothesize that if larger amino acids (e.g., isoleucine, tryptophan) were substituted at this

position, residue 236 would be less prone to rotate, thus impeding domain closure. In contrast, a glycine substitution at position 236 may have the opposite effect.

Hxk2^{G238V} also alters the dynamics of the catalytic residue D211, perhaps further contributing to the reduced glucose and 2DG phosphorylation we observed. In the Hxk2^{G238V} *apo* (ligand-absent) simulation, D211 is less often in the conformation required to optimally engage a bound glucose. D211 at times even flips away from the ATP binding pocket into a displaced conformation (Figure 42B, in pink) that may directly impede glucose binding via steric hindrance.

These allosteric changes in local dynamics correspond to changes in large-scale dynamics. Our simulations suggest that Hxk2^{G238V} substantially interferes with domain closure (Figure 44), rendering the *holo* protein less able to embrace a bound glucose molecule. Indeed, the two ~250 ns Hxk2^{G238V} *holo* simulations both adopted an open conformation despite the presence of a bound glucose molecule; only the longer ~500 ns Hxk2^{G238V} *holo* simulation remained mostly closed (Figure 44). Changes in intra-protein, residue-residue communication pathways may explain the impaired domain closure. Hxk2^{G238V} shifts the betweenness centrality (i.e., importance for intra-protein communication, see Materials and Methods) [457] of some cleft-lining residues (e.g., D211) to residues that do not interact with the bound glucose (e.g., G238). These changes and others to β-hairpin and α11' residues may impair propagation of the glucose-binding signal throughout the protein, such that it cannot adequately induce domain closure. Experiments such as double electron-electron resonance (DEER) electron paramagnetic resonance (EPR) spectroscopy applied to doubly spin labeled Hxk2 could verify the impact of Hxk2^{G238V} on the average distance between the small and large domain.

In summary, this work is significant because it reaffirms two crucial insights into allosteric mechanisms. First, many nonfibrous ordered proteins are allosteric (i.e., subject to conformational

shifts due to point mutations, ligand binding, or changes in external conditions) [458]. Second, allosteric effects are often mediated via subtle changes in residue-residue pathways of correlated motions, not large-scale conformational changes [459].

3.3.2 Cancer relevance

This work is also significant because human hexokinases are potential cancer drug targets, and *Sc*Hxk2 is an excellent model hexokinase. Hexokinase II (*Hs*Hk2) is arguably the most studied of the four mammalian hexokinase isoforms. *Sc*Hxk2 and *Hs*Hk2 share notable sequence similarity, including ~33% sequence identity per Clustal Omega (Figure 38) [449,450]. The glucose- and ATP-binding sites are even more conserved (Figure 46), suggesting the two proteins have similar mechanisms of action. Phosphorylation of both *Sc*Hxk2 and *Hs*Hk2 increases catalytic activity while simultaneously promoting homodimer dissociation [460].

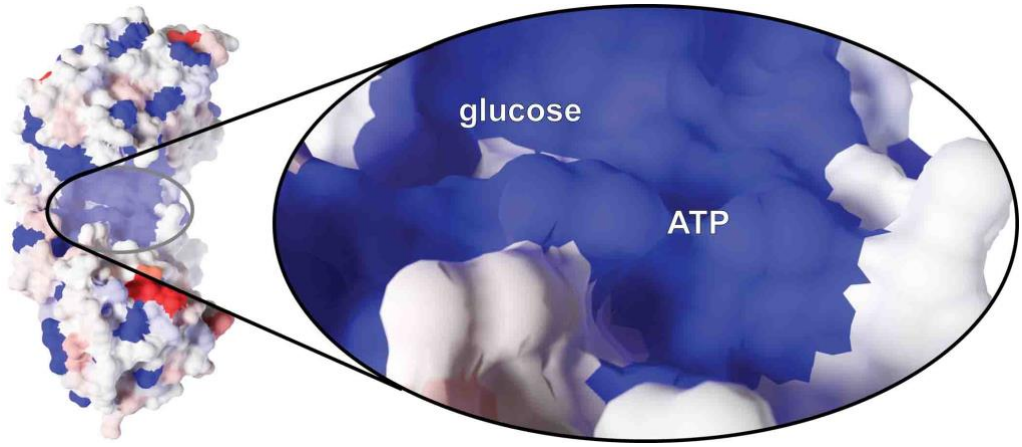

Figure 46. Residue similarity between *Sc*Hxk2 (yeast) and *Hs*Hk2 (human).

Similarity is projected onto a structure of ScHxk2 (PDB 1IG8) and colored per the BLOSUM30 scoring matrix. Highly similar amino acids are shown in blue, and dissimilar amino acids are shown in red.

3.3.2.1 Uncovering 2DG resistance mechanisms

*Hs*Hk2 is often upregulated in cancer [140,427,461]. Some cancer cells rely on glycolysis and lactic acid fermentation for ATP production, even in the presence of adequate oxygen. This tendency towards aerobic glycolysis over the more efficient OXPHOS is known as the Warburg effect [4,462–465]. *Hs*Hk2 upregulation is critical in such circumstances because it allows cancer cells to drastically increase glycolytic flux so they can maintain ATP levels via glycolysis/fermentation alone [428]. 2DG also binds *Hs*Hk2 and so has anti-cancer properties, both when used alone and in combination with other therapies [266,331]. Despite this promising therapeutic mechanism, spontaneous resistance to 2DG [327,354,355,358] and other hexokinase inhibitors [328,466–470] has complicated their use as anti-cancer agents.

To date, extensive genetic screens performed in yeast have revealed the 2DG responsive cellular network [224,266,287,316,471]. While analogous mapping of the same network in mammalian cells remains to be performed, all the components of the system defined in yeast are conserved in mammals and so can be informative. For example, overexpression of the DOG phosphatases, which dephosphorylate 2DG-6P to counter the activity of Hxk2 in yeast, provide resistance to 2DG in both yeast and HeLa cells [287]. As a second example, we note that the activation of AMPK (the mammalian ortholog of Snf1) after 2DG addition triggers α-arrestin-regulated endocytosis of the Glut1 glucose transporter [308,471], a pathway that is perfectly conserved in yeast [316,471]. These facets of the 2DG responsive network surround the activities of hexokinase and in some cases, such as the DOG phosphatases, directly counter its enzymatic function [349].

Given this high degree of pathway conservation, we expect that mutations in mammalian hexokinases (e.g., *Hs*Hk2) will influence 2DG responsiveness just as mutations in yeast Hxk2 do.

The existing literature provides some support for this hypothesis. For example, S. Barban developed a 2DG-resistant HeLa cell line that had reduced hexokinase activity for 2DG and glucose, reminiscent of our *Sc*Hxk2^{G238V} variant [354]. Bailey et al. also developed a 2DG-resistant pig kidney cell line with an altered rate of 2DG phosphorylation, hinting at the possibility of a 2DG-resistance mutation in hexokinase [355].

Understanding the hexokinase catalytic mechanism and anticipating potential resistance-conferring mutations is critical, given 2DG's potential as an anti-cancer therapeutic. The present work in *Sc*Hxk2 thus provides insights into the roles that *Hs*Hk2 plays in cancer biology and chemotherapy resistance, insights that will be a driving feature of our future research.

3.3.2.2 Is reduced Hxk2 activity oncogenic in some circumstances?

Given that cancer is generally associated with increased *Hs*Hk2 activity, we were surprised to discover that the COSMIC database [472] reports three *Sc*Hxk2^{G238V}-equivalent mutations in HK2 (A236S, A236T, and A684V) that are associated with various carcinomas. These mutations arise independent of 2DG resistance, but given their location it seems likely that they act analogously to *Sc*Hxk2^{G238V} by decreasing *Hs*Hk2 catalytic activity. Hk2 has two catalytically active hexokinase domains [89], so there are two G238V-equivalent positions. Two mutations at the N-terminus position, A236S (COSM4849004) and A236T (COSM3000068), are associated with cervical squamous cell carcinoma and stomach adenocarcinoma, respectively. A mutation at the C-terminus position, A684V (COSM6158814), is associated with lung adenocarcinoma. Although all three Hk2 mutations were also judged pathogenic per the FATHMM algorithm [473], the molecular connection between these mutations and cancer progression remains undefined.

Do these Hk2 mutations promote or impede cancer progression, given that they presumably impair glucose phosphorylation just as *Sc*Hxk2^{G238V} does? There is no data on this point; however,

we note that not all cancer cells are subject to the Warburg effect, so elevated Hk2 function may not always be beneficial to cancer cells. For example, although increased Hk2 expression is associated with a more aggressive phenotype in testicular germ cell tumors, overall Hk2 expression is reduced in such tumors relative to paired normal testicular tissues [474]. Per the GEPIA web server [475], the same may be true of lymphoid neoplasm diffuse large B-cell lymphoma, ovarian serous cystadenocarcinoma, acute myeloid leukemia, and thymoma.

While not yet defined molecularly, it is formally possible that reduced Hk2 activity may be advantageous in cancers that have not yet transitioned to a high-glycolytic state. Whether this benefit derives from changes in Glc-6P production or some other Hk2 function (e.g., the protein's role in apoptosis [187]) is uncertain. Much work remains to better understand the complex and varied roles hexokinases play in normal and disease states.

3.4 Materials & Methods

3.4.1 Yeast strains, plasmids, and growth conditions

Yeast strains employed in this study are listed in Table 8. The strains were grown on YPD (2% peptone, 1% yeast extract, 2% glucose) or synthetic complete medium (per O'Donnell et al. [476]) lacking the amino acids needed for maintaining plasmids. Plasmid information is provided in Table 9. Plasmids were introduced into yeast strains using the lithium acetate transformation method [398]. Where indicated, SC or YPD containing 2% glucose were supplemented with 2DG to a final concentration (presented as % w/v). We generated a 2% 2DG (Sigma-Aldrich, St. Louis

MO) stock by dissolving two grams of 2DG in 100 mL of water and then filter sterilizing. Unless otherwise indicated, cells were grown at 30°C.

Table 8. Yeast strains used in this study.

Strain	Genotype	Source
BY4742	*MATα* his3Δ1 leu2Δ0 lys2Δ0 ura3Δ0	[477]
Parental ABC16-monster (RY0568)	***MAT-α*** *adp1Δ snq2Δ ycf1Δ pdr15Δ yor1Δ, vmr1Δ pdr11Δ, nft1Δ bpt1Δ ybt1Δ ynr070wΔ yol075cΔ aus1Δ pdr5Δ pdr10Δ pdr12Δ can1Δ::GMToolkit-α* [CMVpr-rtTA NATMX4 STE3pr-LEU2] *his3Δ1 leu2Δ0 ura3Δ0 met15Δ0*	[442]
Naïve ABC16-monster	***MAT-α*** *adp1Δ snq2Δ ycf1Δ pdr15Δ yor1Δ, vmr1Δ pdr11Δ, nft1Δ bpt1Δ ybt1Δ ynr070wΔ yol075cΔ aus1Δ pdr5Δ pdr10Δ pdr12Δ can1Δ::GMToolkit-α* [CMVpr-rtTA NATMX4 STE3pr-LEU2] *his3Δ1 leu2Δ0 ura3Δ0 met15Δ0*	[442]
2DG Resistant Strain 1 (ABC16-monster)	***MAT-α*** *adp1Δ snq2Δ ycf1Δ pdr15Δ yor1Δ, vmr1Δ pdr11Δ, nft1Δ bpt1Δ ybt1Δ ynr070wΔ yol075cΔ aus1Δ pdr5Δ pdr10Δ pdr12Δ can1Δ::GMToolkit-α* [CMVpr-rtTA NATMX4 STE3pr-LEU2] *his3Δ1 leu2Δ0 ura3Δ0 met15Δ0, hxk2^{G238V}*	This study.
2DG Resistant Strain 2 (ABC16-monster)	***MAT-α*** *adp1Δ snq2Δ ycf1Δ pdr15Δ yor1Δ, vmr1Δ pdr11Δ, nft1Δ bpt1Δ ybt1Δ ynr070wΔ yol075cΔ aus1Δ pdr5Δ pdr10Δ pdr12Δ can1Δ::GMToolkit-α* [CMVpr-rtTA NATMX4 STE3pr-LEU2] *his3Δ1 leu2Δ0 ura3Δ0 met15Δ0, hxk2^{G238V}*	This study.
2DG Resistant Strain 3 (ABC16-monster)	***MAT-α*** *adp1Δ snq2Δ ycf1Δ pdr15Δ yor1Δ, vmr1Δ pdr11Δ, nft1Δ bpt1Δ ybt1Δ ynr070wΔ yol075cΔ aus1Δ pdr5Δ pdr10Δ pdr12Δ can1Δ::GMToolkit-α* [CMVpr-rtTA NATMX4 STE3pr-LEU2] *his3Δ1 leu2Δ0 ura3Δ0 met15Δ0, hxk2^{G238V}*	This study.
2DG Resistant Strain 4 (ABC16-monster)	***MAT-α*** *adp1Δ snq2Δ ycf1Δ pdr15Δ yor1Δ, vmr1Δ pdr11Δ, nft1Δ bpt1Δ ybt1Δ ynr070wΔ yol075cΔ aus1Δ pdr5Δ pdr10Δ pdr12Δ can1Δ::GMToolkit-α* [CMVpr-rtTA NATMX4 STE3pr-LEU2] *his3Δ1 leu2Δ0 ura3Δ0 met15Δ0, hxk2^{G238V}*	This study.
2DG Resistant Strain 5 (ABC16-monster)	***MAT-α*** *adp1Δ snq2Δ ycf1Δ pdr15Δ yor1Δ, vmr1Δ pdr11Δ, nft1Δ bpt1Δ ybt1Δ ynr070wΔ yol075cΔ aus1Δ pdr5Δ pdr10Δ pdr12Δ can1Δ::GMToolkit-α* [CMVpr-rtTA NATMX4 STE3pr-LEU2] *his3Δ1 leu2Δ0 ura3Δ0 met15Δ0, hxk2^{G238V}*	This study.
MSY1254	***MAT-α*** *ura3Δ0 leu2Δ0 his3Δ1 hxk2Δ::KANMX4*	[224]
MSY1475	***MAT-α*** *ura3Δ0 leu2Δ0 his3Δ1 met15Δ0 hxk1Δ::KANMX4 hxk2Δ::KANMX4 glk1Δ::KANMX4*	[224]

Table 9. Plasmid DNA used in this study.

Name	Description	Source
pRS313	CEN *HIS3*	[401]
pHxk2-3V5-313	Genomic clone of *HXK2* with 592 bp upstream of ATG and 373 bp downstream of the stop and a C-terminal fusion to 3V5; CEN *HIS3*	This study.
pRS315	CEN *LEU2*	[401]
pRS315-Hxk2-GFP	Genomic clone of *HXK2* with 592 bp upstream of ATG and 373 bp downstream of the stop and a C-terminal fusion to GFP; CEN *HIS3*	This study.
pRS315-Hxk2-G238V-GFP	Genomic clone of *HXK2* with 592 bp upstream of ATG and 373 bp downstream of the stop and a C-terminal fusion to GFP; the G238V mutation was introduced by site-directed mutagenesis; CEN *HIS3*	This study.
pRS315-Hxk2-3V5	Genomic clone of *HXK2* with 592 bp upstream of ATG and 373 bp downstream of the stop and a C-terminal fusion to 3V5; CEN *HIS3*	[224]
pRS315-Hxk2-G55V-3V5	Genomic clone of *HXK2* with 592 bp upstream of ATG and 373 bp downstream of the stop and a C-terminal fusion to 3V5; the G55V mutation was introduced by site-directed mutagenesis; CEN *HIS3*	[224]
pRS315-Hxk2-G238V-3V5	Genomic clone of *HXK2* with 592 bp upstream of ATG and 373 bp downstream of the stop and a C-terminal fusion to 3V5; the G238V mutation was introduced by site-directed mutagenesis; CEN *HIS3*	This study.

3.4.2 *In vitro* evolution and whole genome sequencing analysis

We used directed evolution to identify mutations that confer 2DG resistance to the ABC16-monster strain [439–442], which lacks sixteen ABC transporters. We evolved resistance via serial passaging in five independent replicates. In each passage, cultures were grown at 30°C in 30 mL of YPD (2% peptone, 1% yeast extract, 2% glucose) and 2DG, with shaking at 250 rpm. We stopped each passage when the growth reached saturation (OD ~3.0 per visual inspection) and examined the cultures under a microscope to verify that there was no contamination. We then placed 300 μL aliquots into a fresh supply of 30 mL YPD with 2DG (i.e., a 1:100 dilution into fresh media with drug) and repeated the process. In early passages, 0.05% 2DG was added, and growth to saturation required 4–5 days. As resistance developed, the time needed for saturation

shortened to roughly two days. To ensure evolved resistance at higher 2DG concentrations, we then increased the 2DG concentration to 0.2% and resumed serial passages. Each replicate required between eight and twelve passages total, at which point the growth rate of each had stabilized (per eighteen-hour growth curves calculated at multiple 2DG concentrations, 0.05–0.2%). To enable comparative genomics and growth-rate analyses, we also generated a no-drug control that involved passaging for the same time intervals but in medium containing no 2DG.

To determine the genomic changes associated with evolved 2DG resistance, we isolated the genomic DNA of both the resistant (passaged) and control strains using a glass-bead/phenol-extraction protocol [478]. We performed next generation sequencing on Illumina NextSeq500 machines. As detailed in Soncini et al. [224], sequencing libraries were prepared and multiplexed into single lanes for each strain to produce 151-bp paired end reads.

To identify potential resistance-conferring mutations, we followed the protocol described in Ellison et al. [479]. In brief, we used the Bowtie 2 software [480] to align the sequence reads to the S288C reference yeast genome. We then used Samtools 1.3.1 [481] to sort the alignments by their leftmost coordinates and to index the sorted alignments. BCFtools 1.3.1 [481] was used for variant calling (consensus calling model). VCFtools 0.1.14 [482] was used to identify variants that differed between the 2DG-resistant and no-drug control strains. Finally, we used SnpEff 4.3p [483] to annotate the identified variants (e.g., frameshift variants, missense variants, stop-gained variants, disruptive inframe insertions, putative impact high/moderate/low, etc.).

3.4.3 2-deoxyglucose resistance assays

We monitored resistance to 2DG in three different ways. First, to verify the 2DG resistance of the passaged strains, we performed serial dilution growth assays by plating serial dilutions of

yeast cells onto solid agar medium containing the indicated concentrations of 2DG and allowing cells to grow for the time indicated for each figure at 30°C. We compared the growth of the evolved yeast cells to the unpassaged, parental strain (ABC16-monster) or the parental strain that was passaged using medium lacking 2DG (naïve ABC16-monster). Serial dilution growth assays were performed as described in O'Donnell et al. [476]. In brief, we grew cells to saturation overnight in YPD or SC medium, measured the optical density of each culture, and initiated our dilution series with a cell density of A600 = 1.0 (or ~1 x 10^7 cells/mL). We then made five-fold serial dilutions of cells and pinned them onto solid YPD or SC with or without 2DG (0.05%, 0.2%, and 0.4%).

Second, we assessed our 2DG-resistant or control strains (parental ABC16-monster or naïve ABC16-monster, as indicated above) using growth curve analyses [484]. In brief, we grew cells to saturation in YPD or SC medium, washed cells into fresh medium, and inoculated in triplicate into flat-bottom 96-well plates at an A600 of 0.05 in the medium indicated (i.e., YPD or SC containing varying concentrations of 2DG). Prepared plates were incubated with shaking in a BioTek Cytation 5 plate reader (BioTek instruments; Winooski, VT, USA), and optical density measurements were taken every 30 minutes for 24 hours using the Gen5 software package. Optical densities measured over time are presented with a path-length correction (to report measurements in a 1 cm path length). We used these curves to calculate the doubling times of yeast cells via the following equation:

$$doubling\ time = \frac{\ln(2)}{\left(\frac{\ln(OD_2) - \ln(OD_1)}{t_2 - t_1}\right)}$$

Doubling times were calculated based on the mean growth curves of each strain by selecting two points that span the linear range of the logarithmic growth portion of the growth curve.

Third, we challenged cells with a range of 2DG concentrations, as described in Soncini et al. [224]. In this approach, overnight cultures are grown to saturation in either glucose (Figure 36A) or galactose (Figure 38D) as a carbon source, diluted to an A600 of 0.1, and grown in the absence or presence of 2DG (0.01%, 0.02%, 0.05%, 0.1%, or 0.2%) for 18 hours at 30°C with either 2% glucose (Figure 36A) or 2% galactose (Figure 38D) as a carbon source [224]. Each A600 was measured, and cell growth was normalized to growth in the absence of 2DG for each strain. The average of three replicate cultures is presented in Figure 36A, with statistical comparisons made using the Student's t-test for unpaired variables with equal variance. In this case, p-values are indicated as follows: * $p < 0.05$, ** $p < 0.01$, *** $p < 0.001$.

3.4.4 Immunoblotting to assess $Hxk2^{G238V}$ abundance and stability

To assess $Hxk2^{G238V}$ abundance in cells, we performed whole cell protein extracts using the trichloroacetic acid (TCA) method [403]. In brief, an equal density of mid-log phase cells was harvested by centrifugation, washed in water, and then resuspended in water with 0.25 M sodium hydroxide and 72 mM β-mercaptoethanol. Samples were then incubated on ice, and proteins were precipitated by the addition of TCA. After incubation on ice, proteins were collected as a pellet by centrifugation, the supernatant was removed, and the proteins were solubilized in 50 μL of TCA sample buffer (40 mM Tris-Cl [pH 8.0], 0.1 mM EDTA, 8M urea, 5% SDS, 1% β-mercaptoethanol, and 0.01% bromophenol blue). Samples were then heated to 37°C for 30 minutes, and the insoluble material was removed by centrifugation before resolving samples by SDS-PAGE. Proteins were transferred to a membrane support and detected with either anti-GFP antibodies (Santa Cruz Biotechnology) or an anti-V5 probe (Invitrogen), followed by goat anti-mouse IRDye 680 (Thermo) or goat anti-rabbit IRDye 800 (LiCor). Antibody complexes were

visualized using an Odyssey Infrared Imager (LiCor), and bands were quantified using the Odyssey software. REVERT (LiCor) total protein staining of membranes was used as a protein loading and membrane transfer control in immunoblotting.

3.4.5 Enzymatic assays for Hxk2 function

To verify that the *hxk2*^{G238V} mutation alone is sufficient to confer 2DG resistance, we used site-directed mutagenesis to introduce the *hxk2*^{G238V} mutation into a plasmid encoding the *HXK2* gene (Table 9). We performed DNA sequencing of the entire open reading frame to ensure that no unintentional changes were generated. We separately transformed plasmids expressing WT *HXK2* and *hxk2*^{G238V} into the *hxk1*Δ *hxk2*Δ *glk1*Δ triple deletion cells (Table 9) and measured the hexokinase activity associated with these two alleles, as described in Soncini et al. [224]. In summary, we prepared protein extracts using a glass-bead extraction protocol and assayed enzymatic activity by coupling the phosphorylation of glucose to its oxidation by glucose-6-phosphate dehydrogenase. The resulting production of NADPH, detected by measuring absorbance at 340 nm, correlates with hexokinase activity. For comparison, we used the same protocol to assess the enzymatic activity of WT Hxk2 (positive control). To measure the Michaelis-Menten constant (Km), we measured the reaction rate (v) at several glucose or 2DG concentrations ([S]) using a constant concentration of ATP (1 mM) and plotted the inverse of rate (1/v) against the inverse of concentration (1/[S]) (Lineweaver-Burk plot) [224]. To calculate the Km for ATP, we measured the reaction rate at several ATP concentrations, kept the glucose concentration constant (2 mM), and plotted the inverse rate against the inverse of the substrate concentration.

3.4.6 Invertase assays

The invertase activity of cells grown in 2% glucose, where expression of the *SUC2* gene that encodes invertase is repressed in an Hxk2-dependent manner, was measured as in Soncini et al. [224]. For this assay, three independent cultures were assessed using a colorimetric assay that measures Suc2 enzymatic function coupled to glucose oxidase [485]. The mean of these replicates is plotted with the standard error indicated by the error bars. Invertase activity is measured in units per OD of cells, where 1 unit is equal to 1 μmole of glucose released per minute. Student's t-test for unpaired variables with equal variance was used to compare the difference between *hxk2*Δ cells containing plasmids expressing WT *HXK2* vs. an empty vector or the *hxk2* mutant alleles. P-values are indicated as follows: * $p<0.05$, ** $p<0.01$, *** $p<0.001$.

3.4.7 Molecular dynamics simulations

To generate models of *apo* (ligand-absent) Hxk2, we downloaded a crystal structure of Hxk2 from the Protein Data Bank (PDB 1IG8 [80]). We used PDB2PQR 2.1.1 [416,417] to add hydrogen atoms per the PROPKA algorithm [418] (pH 7.0) and to optimize the hydrogen-bond network. To approximate an *in vivo* aqueous environment, we used the Ambertools18 program tleap [421] to (1) add a water box extending 10 Å beyond the protein in all directions, (2) add Na+ counter ions to achieve electrical neutrality, and (3) add additional Na+ and Cl- counter ions to approximate a 150 mM solution. A model of $Hxk2^{G238V}$ was prepared similarly, except the glycine at position 238 was first changed to valine using the Mutation-Wizard tool in PyMOL [486].

We similarly generated models of the holo (glucose-bound) systems. There is no crystal structure of glucose-bound *Sc*Hxk2, but the 2YHX structure [93] captures the binding pose of

ortho-toluoylglucosamine, a ligand with a glucose-like substructure. This substructure has the same orientation and position as glucose bound to *Sc*Hxk1 (yeast, PDB 3B8A [79]), *Hs*Hk2 (human, PDB 2NZT [89]), and *Hs*Hk1 (human, PDB 4FPB), suggesting that it correctly mimics the *Sc*Hxk2/glucose pose. Given this consistent binding mode, we modeled glucose bound to *Sc*Hxk2 by superimposing a crystallographic glucose bound to *Sc*Hxk1 (PDB 3B8A [79]) onto the *Sc*Hxk2 *apo* model. To prepare all systems for simulation, we used Ambertools18 to parameterize the protein and counter ions per the Amber ff14SB force field [419], and the water molecules per the TIP3P forcefield [420]. To parameterize the glucose molecule for the *holo* simulations, we used the GLYCAM_06j-1 force field [421].

To relax the geometries of both the WT Hxk2 and Hxk2^{G238V} systems, we applied four rounds of 5,000 minimization steps using NAMD [487,488]. Each round included progressively more atoms: (1) hydrogen atoms; (2) hydrogen atoms and water molecules; (3) hydrogen atoms, water molecules, and protein side chains; and (4) all atoms. We next equilibrated each *apo* system using five serial isothermal-isobaric (NPT, 310 K, 1 atm) MD simulations of 0.25 ns each. The first equilibration simulation had a time step of 1.0 fs, and the remaining had time steps of 2.0 fs. We applied progressively weaker restraining forces to the protein backbone atoms at each equilibration step (1.00, 0.75, 0.50, 0.25, and 0.00 kcal/mol/Å^2, respectively). The *holo* (glucose-bound) simulations were similarly equilibrated, except we used a single, unrestrained, one ns simulation with a 1.0 fs timestep.

Following minimization and equilibration, we started three independent isothermal-isobaric (NPT, 310 K, 1 atm) productive MD simulations of the WT Hxk2 *apo*, Hxk2^{G238V} *apo*, WT Hxk2 *holo*, and Hxk2^{G238V} *holo* systems, respectively (twelve simulations total, time steps of

2.0 fs). In each case, two of the simulations ran for roughly 250 ns, and the third ran for roughly 500 ns (Table 10).

Table 10. Simulation durations.

In all cases, we removed the initial five ns before subsequent analysis. For the sake of clarity, we list this removed segment first, followed by the larger segment used for analysis.

System	Simulation 1	Simulation 2	Simulation 3	Total
Hxk2 *apo*	5 ns + 274.79 ns	5 ns + 335.99 ns	5 ns + 495.15 ns	15 ns + 1105.93 ns
$Hxk2^{G238V}$ *apo*	5 ns + 275.55 ns	5 ns + 254.45 ns	5 ns + 511.76 ns	15 ns + 1041.76 ns
Hxk2 *holo*	5 ns + 245.00 ns	5 ns + 245.00 ns	5 ns + 507.13 ns	15 ns + 997.13 ns
$Hxk2^{G238V}$ *holo*	5 ns + 245.00 ns	5 ns + 245.00 ns	5 ns + 495.00 ns	15 ns + 985.00 ns

3.4.8 Confirming that the simulations had fully equilibrated

For each simulation, we aligned trajectory frames taken every ten ps to the corresponding first frame by their backbone heavy atoms. We then used MDAnalysis (V 1.0.0) [489] to calculate the corresponding backbone-heavy-atom RMSD. Plotting these twelve sets of RMSD values over simulation time (Figure 47) suggested that the simulations had not fully equilibrated before beginning the productive runs. We discarded the initial five ns pre-equilibrated portions of each simulation. Unless otherwise noted, all subsequent analyses focused only on the equilibrated (retained) portions of the productive runs, using the same 10-ps stride and backbone alignment.

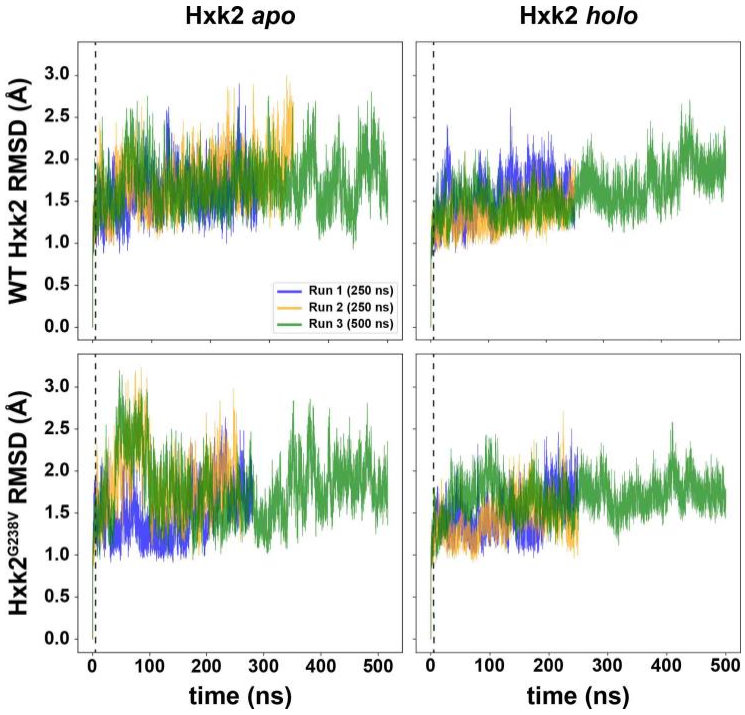

Figure 47. The heavy-atom backbone RMSD values between the first and subsequent frames of each simulation. We aligned trajectory frames taken every ten ps to the corresponding first frame and calculated the backbone-heavy-atom RMSD. Plotting RMSD values over simulation time suggested that the simulations had not fully equilibrated during the beginning portions of the production runs. We discarded the initial five ns preequilibrated portions of each simulation. Subsequent analyses focused on the remaining portions.

3.4.9 Root-mean-square-fluctuation (RMSF) analyses

To assess the per-residue dynamics of individual amino-acid residues, we used MDAnalysis [489] to calculate the RMSF values of residue centers of geometry, considering trajectory frames taken every ten ps.

3.4.10 Radius of gyration

To assess the opening and closing of the small and large subdomains (Figure 33), we used MDAnalysis [489] to calculate the protein RoG throughout the simulations. For comparison's sake, we similarly calculated the crystallographic radii of gyration of *Sc*Hxk2 in the open conformation (PDB 1IG8 [80]) and the closely related *K. lactis* Hxk1 in the closed conformation (PDPB 3O8M [83]).

3.4.11 Dynamic cross correlation

We calculated DCC matrices using MD-TASK [490]. Values in a DCC matrix describe to what degree the motions of all pairs of Cα are correlated (i.e., 1 indicates perfectly correlated motions, and -1 indicates anti-correlated motions). The matrix is calculated as follows:

$$C_{ij} = \frac{(\Delta r_i \cdot \Delta r_j)}{\sqrt{\langle \Delta \mathrm{r_i^2} \rangle} \cdot \sqrt{\langle \Delta \mathrm{r_j^2} \rangle}}$$

where ⟨⟩ denotes time averages over the whole trajectory (frames taken every ten ps), and Δr_i is the displacement of atom i from its average position.

To identify changes in correlated motions due to Hxk2^{G238V}, we calculated the element-wise difference between DCC matrices.

3.4.12 Betweenness centrality

We used MD-TASK to calculate the amino-acid BC values of simulation frames extracted every ten ps [457]. In brief, we represent protein conformations as graphs composed of nodes and

edges. The nodes (n_i) are the amino-acid Cβ atoms (or Cα in the case of glycine), and the edges ($e_{i,j}$) connect any two nodes (n_i and n_j) that are within 6.7 Å of each other. By considering all pairs of nodes, one can construct a complete set of the shortest paths between node pairs. The BC of a given node is simply the number of shortest paths from this set that pass through that node. Applying this same calculation to multiple conformations extracted from an MD simulation yields an ensemble-average BC value for each amino-acid node. We calculated these time-average per-residue BC values for each simulation i, $\langle BC_i \rangle$, to account for protein dynamics. Finally, we calculated $\langle BC_i \rangle$ differences between systems. To assess the effect size of these differences, we used Cohen's d with an in-house script.

3.4.13 Figure generation

To generate protein-structure images, we set up molecular representations in VMD [415] and imported them into the computer-graphics program Blender using the BlendMol plugin [424]. Select images also include QR codes that encode ProteinVR URLs [491] to enable visualization in stereoscopic 3D (virtual reality).

3.5 Acknowledgements

We thank Dr. Paulette Vincent-Ruz for support with the statistical analysis, and Dr. Frederick Roth for providing the ABC16-monster yeast strain. We also acknowledge the Microbial Genome Sequencing Center for whole genome sequencing and the University of Pittsburgh Center for Research Computing for computing resources.

4.0 Hexokinase 2 mutants confer cancer drug resistance by altering protein dynamics and perturbing glucose-dependent subcellular localization

4.1 Introduction

Glucose is a fundamental carbon source used to generate cellular energy in the form of ATP. Glucose enters the cell through glucose transporters (e.g., hexose transporters or HXTs in *S. cerevisiae* and glucose transporters or GLUTs in mammals) [2]. Glucose metabolism begins with the action of a hexokinase, which transfers the gamma phosphate from ATP to the C6 carbon of glucose to form glucose-6-phosphate (G6P). Subsequently, G6P can be converted via glycolysis into two pyruvate molecules; pyruvate can be further metabolized through aerobic oxidative phosphorylation (OXPHOS) or anaerobic fermentation to yield cellular energy. In addition, G6P is a substrate for reductive biosynthesis, primarily through the pentose phosphate pathway [3], which produces NADPH and ribose-5-phosphate as essential building blocks for macromolecules like nucleic and fatty acids [4].

Given their central metabolic role, modulation of hexokinases has critical ramifications on cellular health. Importantly, cancer cells often upregulate hexokinase expression to facilitate the increased uptake and turnover of glucose through glycolysis and other biosynthetic pathways that drive cellular proliferation [4,140]. For cancer cells, this shift in metabolism away from oxidative phosphorylation and towards anaerobic fermentation is referred to as the Warburg effect. This central role of hexokinases in this transition has made them a target for pharmaceutical intervention, with many anti-cancer strategies targeted to disrupt hexokinase function or, more

generally, glycolysis. The necessarily high glycolytic flux of Warburg-shifted cancer cells makes them more susceptible to downmodulation of this pathway [129,137,179].

One glycolytic inhibitor, called 2-deoxyglucose (2DG), has been used in anti-cancer clinical trials as a hexokinase and glycolytic inhibitor [322,330,337,338]. This toxic analog of glucose lacks the hydroxyl group on the C2 carbon of glucose and so, even though it is phosphorylated by hexokinases, it cannot be utilized in the glycolytic pathway by subsequent enzymes. This is thought to lead to an accumulation of phosphorylated 2DG in the form of 2-deoxyglucose-6-phosphate (2DG6P), which acts as a noncompetitive and competitive inhibitor of hexokinase and phosphoglucose isomerase, respectively, to further reduce glycolytic flux and thereby starve cancer cells of their predominant means to generate ATP [271,492]. Generation of 2DG6P consumes ATP during the energy investment phase of glycolysis, depleting ATP reserves without returning energy during the payoff phase [266,277,493].

In addition to blocking glycolysis, 2DG6P appears to be toxic via other distinct mechanisms. 2DG6P can be condensed with GTP to form GDP-2DG (GDP-2-deoxymannose), and this product can be incorporated into N-linked glycans during protein glycosylation, leading to protein folding defects, ER stress, and activation of the unfolded protein response (UPR) [294,295]. Activation of these ER and protein folding stress pathways appears to be a major contributor to the toxicity of 2DG in oxygenated cancer cells [294,295,320]. In addition, 2DG and its derivatives impact glycogen storage, glycolipid metabolism, and, in yeast cells, maintenance of the cell wall [266].

Our studies focus on hexokinases and how structural alterations in this class of enzymes impact their function. Broadly speaking, hexokinases are comprised of two subdomains: a predominantly α-helical large subdomain and a palm-shaped α/β small subdomain [77,78]. When

glucose binds to the catalytic pocket, hexokinases undergo dynamic structural changes [79–89]. To permit glucose binding, the hexokinase initially adopts an open conformation, with the large and small subdomains separated, leaving the enzymatic pocket solvent exposed [80,82]. Once glucose is bound, it triggers an induced fit conformational change initiated in the enzymatic pocket, which causes the large and small subdomains to approach and rotate relative to each other (Figure 48A) [79,83,84,93]. This transition collapses the enzymatic pocket (Figure 48A), rendering it inaccessible to the solvent and enveloping the glucose molecule via an "embracing" mechanism [79,101,430]. ATP binds adjacent to glucose in the enzymatic cleft, inducing further conformational changes that position the γ-phosphate next to the glucose C6 hydroxyl group [81,85,90,94]. A conserved aspartic acid residue acts as a catalytic base that removes hydrogen from that hydroxyl, enabling the conjugation of the ATP γ-phosphate to this site [87]. The negative charges between the resulting G6P and ADP repel each other, driving the two products apart, leading to product release.

The ability of 2DG to halt cell proliferation prompted its use in clinical trials —alone or in combination with other drugs—as a treatment for highly glycolytic cancers such as glioblastoma [322,330,337,338]. 2DG monotherapy has had limited efficacy, but combining 2DG with other drugs remains promising [322,330,337,338]. As with many drug therapies, resistance with prolonged treatment of 2DG has been documented [327,354,355,358]. However, 2DG derivatives remain in development and clinical trials, highlighting the importance of understanding these cellular resistance mechanisms [342].

To define cellular resistance mechanisms to 2DG, we and others have used the budding yeast *S. cerevisiae*. Yeast is an excellent model system for studying glycolytic cancers because it primarily ferments glucose even when oxygen is present, similar to the Warburg shift in some

cancers [28]. Indeed, studies of 2DG resistance in yeast date back to the 1970s and have played a crucial role in revealing fundamental aspects of cell metabolism [344,346,347,494]. More recently, we and others have performed genetic screens and laboratory evolution studies to identify 2DG-resistance-causing mutations in yeast, mirroring the spontaneous resistance that arises in cancer cells [224,227,245,287,307]. These studies define several critical mechanisms that cause 2DG resistance, including: (1) hyperactivation of the yeast AMPK ortholog Snf1 [224,245,307]; (2) loss-of-function in Glc7 or Reg1 subunits of the PP1 phosphatase, which negatively regulates Snf1 [224,287,307]; (3) increased expression or cell surface retention of glucose transporters [272,316]; (4) upregulation of the 2DG6P phosphatases Dog1 and Dog2 [287,307], and (5) multiple missense mutations in hexokinase 2 (Hxk2) [224,227,287]. Interestingly, no mutations were found in the other yeast hexokinases, Hxk1 and Glk1, despite their ability to phosphorylate 2DG and increased expression in response to 2DG [224]. One possible reason why only mutations in Hxk2 were observed is that Hxk2 has additional activities beyond its role in glucose phosphorylation that are not yet fully understood. As an example, we recently found that Hxk2 translocates to the nucleus under glucose-starvation conditions; however, the role of nuclear Hxk2 is unclear [232]. Prior studies suggested that Hxk2 may act as a transcriptional repressor, but our work demonstrates that Hxk2 is not a major transcriptional regulator and suggests that any transcriptional changes linked to loss of Hxk2 are due to compensation for altered cell metabolism [232,236,238,261]. These findings are in agreement with a recent paper that demonstrated human HK2 when expressed in yeast as the sole hexokinase also has no impact on transcriptional regulation [225]. Hxk2 also functions as an intracellular glucose sensor that activates glucose repression [228,233–235,389,495].

In the current study, we provide an in-depth analysis of the Hxk2 mutations linked to 2DG resistance (Figure 48B). We validate that six of the eight previously reported 2DG-resistant Hxk2 mutants do indeed improve growth on 2DG. Further, we find that five of these six 2DG-resistant Hxk2 mutants break the glucose-restricted nuclear localization and become nuclear localized in glucose-rich and glucose-depleted conditions. Many of the 2DG-resistant mutations line the catalytic pocket and impair Hxk2 enzymatic function, as evidenced by the inability of these alleles of Hxk2 to support growth on glucose as a carbon source when they are the only hexokinase expressed in the cell. However, one key mutant–Hxk2^{G55V}—stands out amongst these as it does not reside within the catalytic cleft, yet it confers 2DG resistance, increases Hxk2 nuclear propensity, but provides growth on glucose. We sought to determine how G55V impacts the Hxk2 enzyme through a combination of biochemical analysis and molecular dynamics (MD) simulations. We find that though G55V is removed from the catalytic pocket, it results in an enzyme that dwells predominantly in a "closed" conformation that would preclude glucose binding. This closed conformation appears to be due to disruption of tertiary structural interactions that disrupt the hinge point between the small and large subunits of Hxk2. Based on our MD simulations, we posited that the G55V allele may produce an unstable protein that does not bind glucose as well as the WT Hxk2 enzyme. Using protein thermal stability shift assays, we find that this is indeed the case; G55V is less thermally stable than WT Hxk2. Finally, we considered the possibility that in cells, G55V may become misfolded and be more prone to degradation than WT Hxk2. This idea is supported by the fact that the G55V protein is less abundant than WT Hxk2 and has higher proteolytic cleavage products when extracted from cells. Taken together, we propose that mutations of Hxk2 that destabilize this enzyme promote 2DG resistance. This may further

explain why so many of these 2DG-resistant Hxk2 alleles enter the nucleus aberrantly, as this may be part of their itinerary as they are managed by protein quality control machinery in the cell.

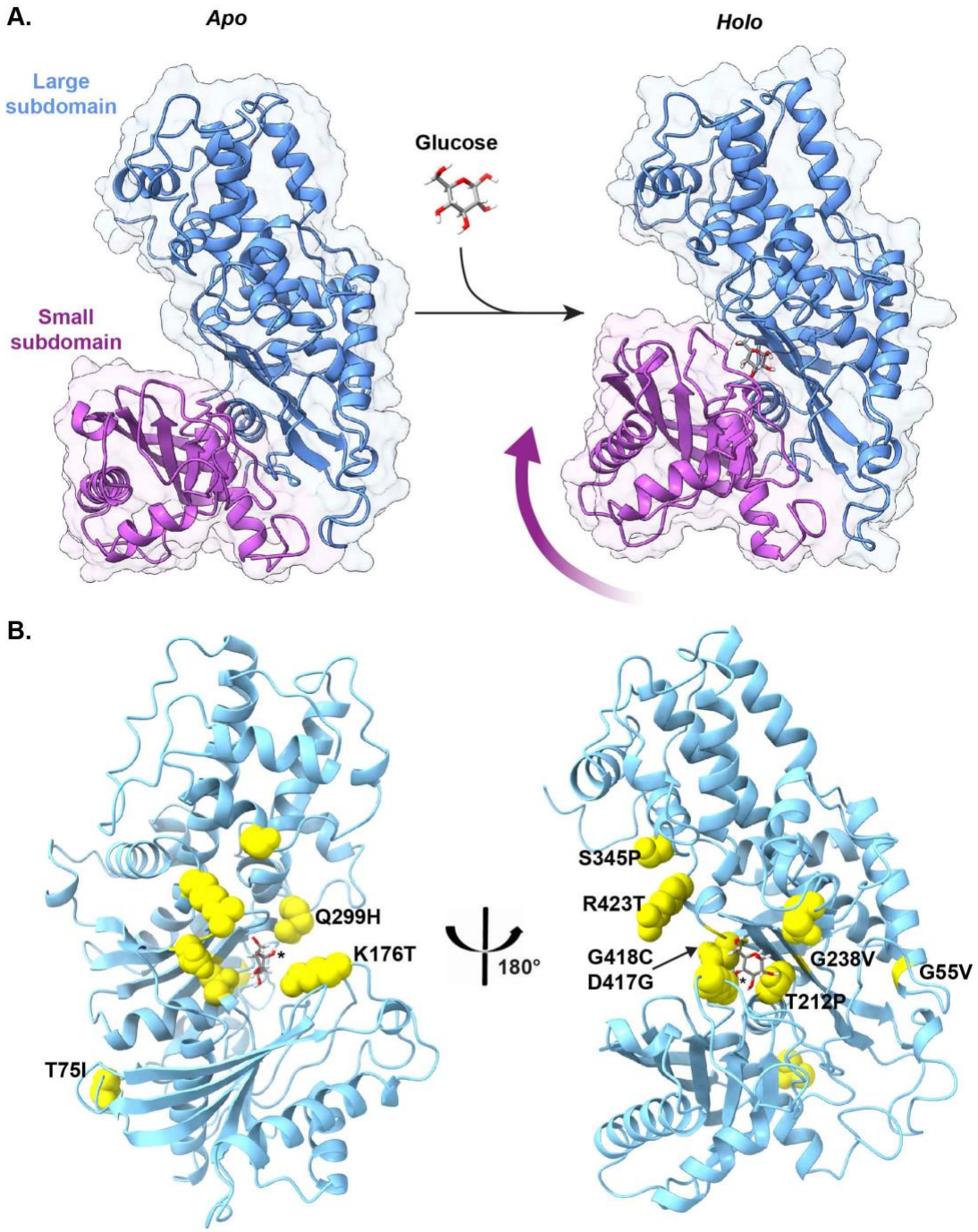

Figure 48. Hxk2 structural dynamics and the location of known 2DG-resistance mutations.

(A) Three-dimensional structure of Hxk2 (homology model constructed previously [232]) in ribbon and surface representation. The glucose-free (*apo*) and glucose-bound (*holo*) conformations captured in all-atom simulations (this study) are depicted. Blue and purple regions show the large and small subdomains, respectively. The curved arrow shows the approximate motion of domain closure. (B) Three-dimensional structure of Hxk2 as predicted by AlphaFold

(accession: P04807). Backbone carbon atoms are represented as light-blue ribbons. Sidechains of previously identified 2DG-resistance-conferring mutations are depicted as yellow spheres. To indicate the location of the glucose binding pocket, we superimposed crystallographic glucose (location denoted with an asterisk) from a *Hs*HK1 structure (PDB 4FPB).

4.2 Results

4.2.1 Hxk2 mutants confer differing degrees of 2DG resistance, but most retain the ability to phosphorylate glucose

2-deoxyglucose (2DG) has been extensively investigated in many anti-cancer clinical trials, and an acetylated pro-drug is currently undergoing testing [331,342], but its efficacy has been thwarted by spontaneous resistance mutations [327,354,355,358]. We and others have conducted extensive screens for 2DG-resistant mutants using *Saccharomyces cerevisiae* as a model system [224,227,245,287,307]. From these screens, nine loss-of-function mutations in the *HXK2* gene that confer 2DG resistance were isolated [224,227,287]. Notably, Hxk2 deletion confers 2DG resistance [245]; indeed, this particular hexokinase is responsible for phosphorylating 2DG upon cell entry [224,245]. Due to this connection, further analysis to confirm the causative role of these Hxk2 mutants in 2DG resistance was not extensively pursued. In this study, we use these 2DG-resistant mutants as a tool to gain insights into Hxk2 biology and its mechanistic role in 2DG resistance.

To establish the relationship between catalytic activity and 2DG resistance, we expressed each Hxk2 mutant in cells lacking the chromosomal copy of the *HXK2* gene. Next, we compared the growth of cells expressing each Hxk2 mutant to that of an empty vector control in serial dilution

growth assays and growth curve analysis (Figure 49). As expected, *hxk2*Δ cells expressing WT Hxk2 were sensitive to 2DG, while cells with an empty vector control had robust 2DG resistance (Figure 49A, C). Most of the Hxk2 mutants tested conferred resistance to 2DG (Figure 49A, C), except for the $Hxk2^{T75I/S345P}$ mutant. These results confirm that nearly all the Hxk2 mutations linked to 2DG resistance in past screens can confer 2DG resistance even when expressed in the presence of Hxk1 and Glk1.

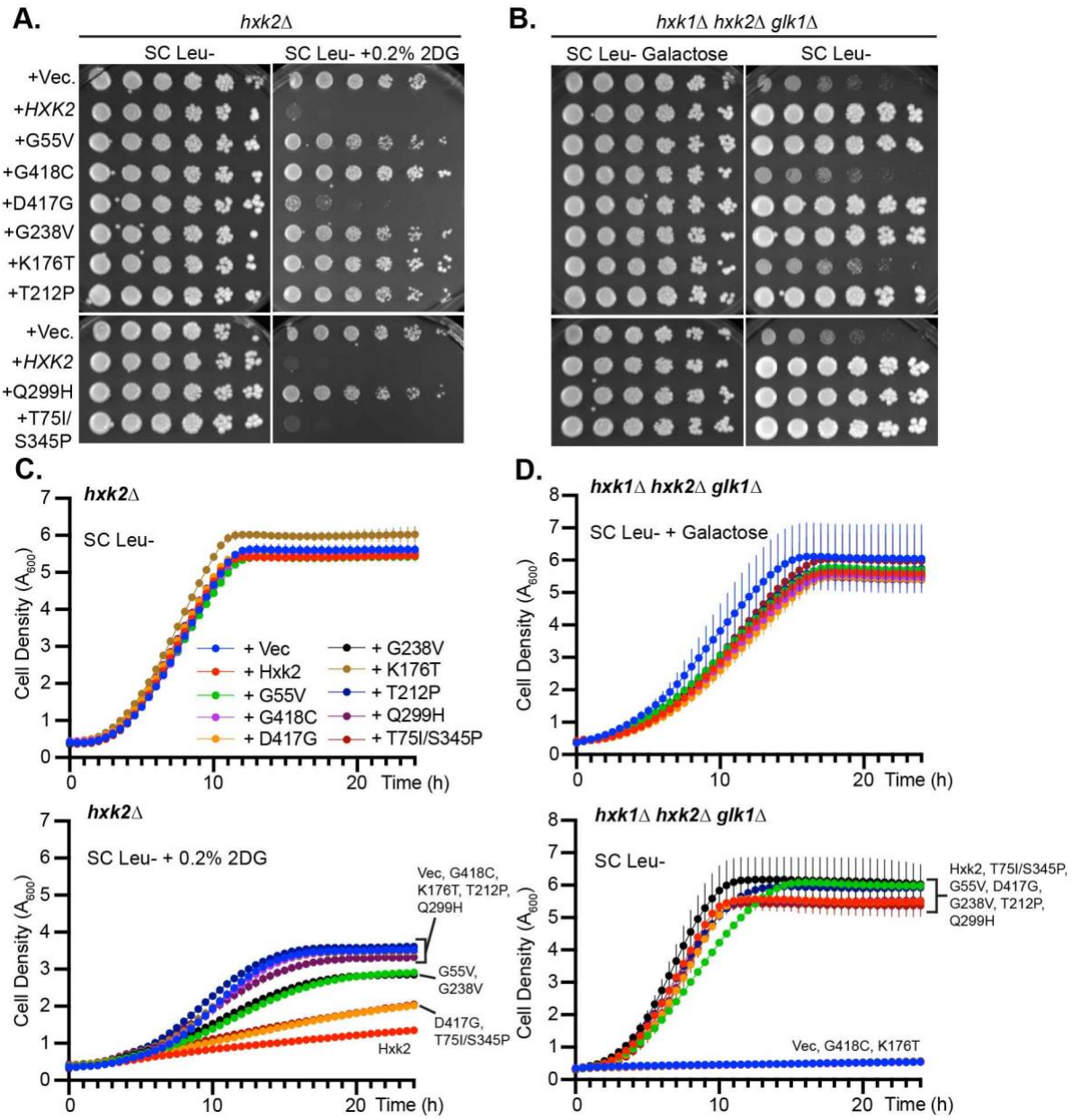

Figure 49. Hxk2 mutants confer varying degrees of 2DG resistance, yet most still promote growth on glucose.

(A and B) Images of serial dilution growth plates of *hxk2*Δ or *hxk1*Δ *hxk2*Δ *glk1*Δ cells containing the indicated plasmid (pRS315-*HXK2pr-HXK2*^{allele}) after three days of growth at 30°C. The medium is SC Leu- containing 2% glucose (panels A and B, far right) or 2% galactose (panel B, far left), with the addition of 0.2% 2DG where indicated. (C and D) The cell density (A_{600}) changes over time for cells grown in SC Leu-, SC Leu- with 0.2% 2DG, or SC Leu- with 2% galactose are plotted. Curves depict the average A_{600} of three technical replicates, while vertical lines

extending from each data point illustrate the +/- SD, occasionally being too minimal to extend beyond the data point itself.

We previously showed that some Hxk2 mutants (*e.g.,* Hxk2^{G55V}, Hxk2^{D417G}, and Hxk2^{G238V}) encode hexokinases with impaired catalytic activity, resulting in reduced glucose phosphorylation [224,227]. To further investigate the functional impact of these Hxk2 alleles, we examined their ability to support growth on glucose when they are the only hexokinase in cells. We expressed each Hxk2 mutant in *hxk1*Δ *hxk2*Δ *glk1*Δ cells, which cannot grow efficiently on glucose as a carbon source unless a functional hexokinase is introduced [228]. These cells were initially tested for growth on galactose-containing medium. Galactokinases, rather than hexokinases, are required under these conditions, providing a control for hexokinase-independent growth. The absence or presence of WT Hxk2 did not impact the growth of *hxk1*Δ *hxk2*Δ *glk1*Δ cells on galactose and neither did any of the 2DG resistant mutants (Figure 49B, D). On glucose, we found that *hxk1*Δ *hxk2*Δ *glk1*Δ cells expressing WT Hxk2 grew well (Figure 49B, D), as did cells expressing any other Hxk2 variant except for Hxk2^{G418C} and Hxk2^{K176T} (Figure 49B, D). This finding was unexpected, given that extracts from cells expressing Hxk2^{G55V} or Hxk2^{D417G} as the sole hexokinase have nearly undetectable catalytic activity [224]. It may be that the catalytic activity of some Hxk2 2DG-resistant mutants is sufficient to support growth on glucose yet falls below the detection threshold of *in vitro* assays. The observation that Hxk2^{G418C} and Hxk2^{K176T} mutants do not confer growth on glucose suggests they cannot phosphorylate glucose, thus mimicking the phenotype of an *hxk1*Δ *hxk2*Δ *glk1*Δ (Figure 49B, D).

4.2.2 Hxk2 2DG-resistance mutants alter glucose-dependent subcellular localization

We showed that Hxk2 undergoes nuclear localization during glucose starvation, a phenomenon also observed in mammalian hexokinases [65,66,68,71,232]. Our observations present a paradigm shift from a long-standing model that proposed Hxk2 enters the nucleus under glucose starvation [236–238,254,259–261]. Nuclear-localized mammalian hexokinases are thought to regulate chromatin structure, gene expression, stem cell pluripotency, glycogen storage, and oxidative stress response [65,66,68,71,232]. The function of nuclear Hxk2 in yeast remains unclear, and we are only beginning to unravel the features that allow Hxk2 nuclear retention/accumulation [232].

We assessed the nuclear localization of WT Hxk2 and 2DG-resistant mutants in glucose-replete conditions (2% glucose, "high" glucose), after 2 hours of acute glucose starvation (0.05% glucose, "low" glucose), and in glucose-replete conditions with the addition of 2DG (2% glucose with 0.2% 2DG, "2DG"). We used live-cell confocal microscopy and an AI-assisted image quantification pipeline to assess nuclear co-localization, as we have done in past studies to define Hxk2 nuclear translocation [232].

Consistent with our previous findings, WT Hxk2 was predominantly cytosolic under glucose-replete conditions, with a fraction translocating to the nucleus upon glucose starvation (Figure 50A). In the presence of 2DG, Hxk2 remained cytosolic. Surprisingly, several 2DG-resistant mutations showed an altered localization pattern, either promoting constitutive nuclear localization ($Hxk2^{G55V}$, $Hxk2^{K176T}$, $Hxk2^{T212P}$, and $Hxk2^{D417G}$) or completely abolishing nuclear localization ($Hxk2^{G418C}$) under all three media conditions (Figure 50A). Other mutants ($Hxk2^{G238V}$, $Hxk2^{Q299H}$, and $Hxk2^{T75I/S345P}$) had WT-like localization patterns (Figure 51A).

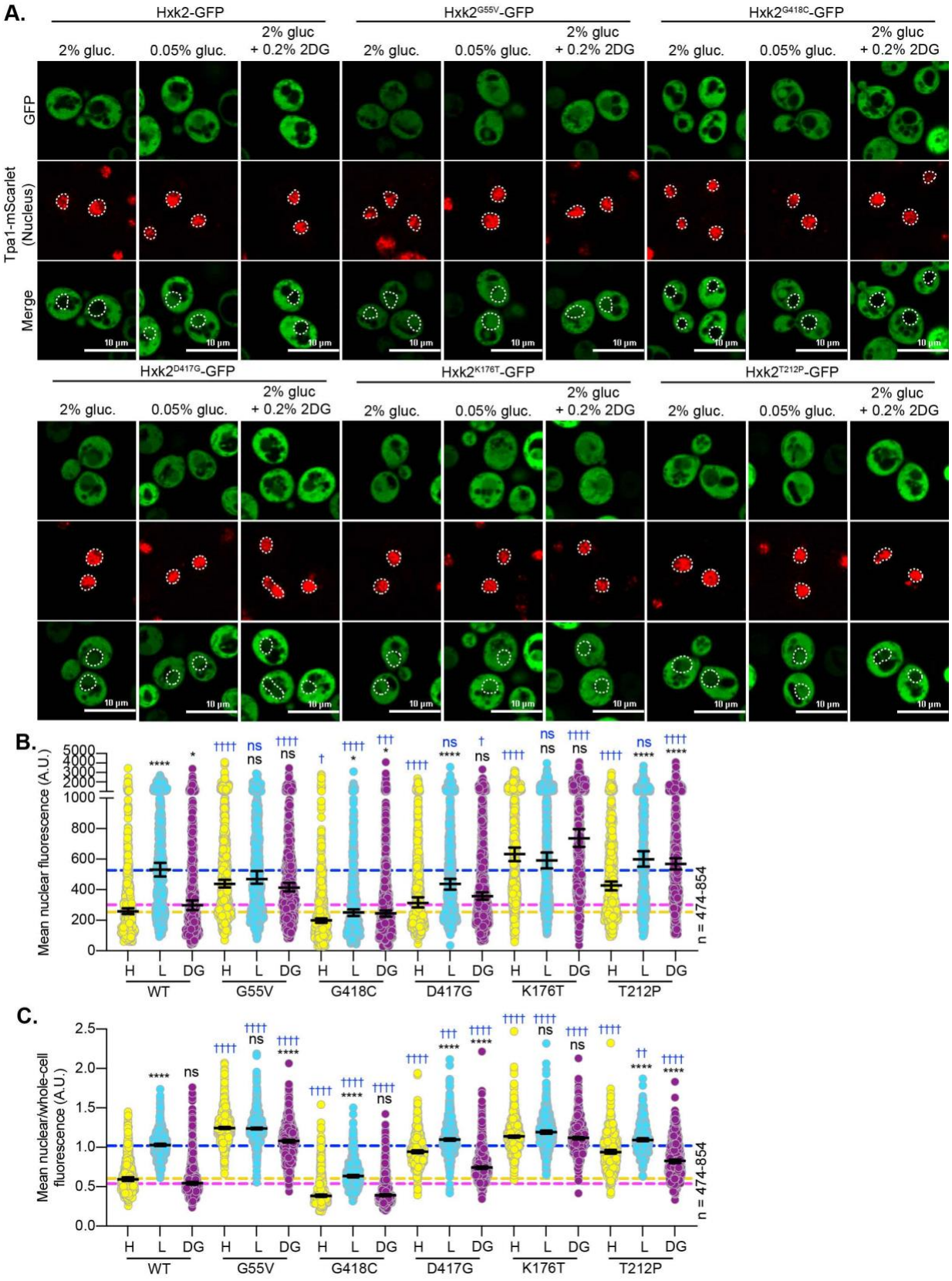

Figure 50. Hxk2 2DG-resistance mutants alter glucose-dependent subcellular localization.

(A) Confocal microscopy images of GFP-tagged WT Hxk2 and the indicated 2DG-resistance mutants expressed in *hxk2*Δ cells from pRS315-*HXK2pr-HXK2*^{allele} plasmids. The Tpa1-mScarlet nuclear marker is used to determine co-localization with the nucleus. A dashed, white line was traced around the mScarlet-marked nucleus and superimposed onto the GFP channel to indicate its relative position. (B and C) Images in panel A were analyzed using AI-assisted quantification (Nikon.*ai* and GA3 analyses), where (B) shows the mean nuclear fluorescence and (C) shows the mean nuclear fluorescence over the mean whole-cell fluorescence ratio for each Hxk2 variant. Diagrams to the left of each graph depict regions of the cell that were measured. Red dashed lines filled with black dots depict the area for nuclear fluorescence measurements (B), and the blue dashed line filled with grid lines shows the area for whole-cell fluorescence measurements (C). Horizontal bars represent the median, while the error bars indicate the 95% confidence interval. Dashed yellow, blue, and purple lines indicate the median value for WT Hxk2-GFP cells in high glucose, low glucose, and high glucose with 0.2% 2DG, respectively. Statistical analyses were performed using a Kruskal-Wallis test with Dunn's post hoc correction. This statistical test was done to compare the mean nuclear fluorescence or mean nuclear/whole-cell-fluorescence ratio across conditions of high and low glucose, as well as high glucose with 0.2% 2DG. Black asterisks denote statistical comparisons between low and high glucose conditions or high glucose with 0.2% 2DG and high glucose conditions for a particular *HXK2* allele. Blue daggers indicate comparisons between mutant alleles and the respective wild-type Hxk2 within identical medium conditions.

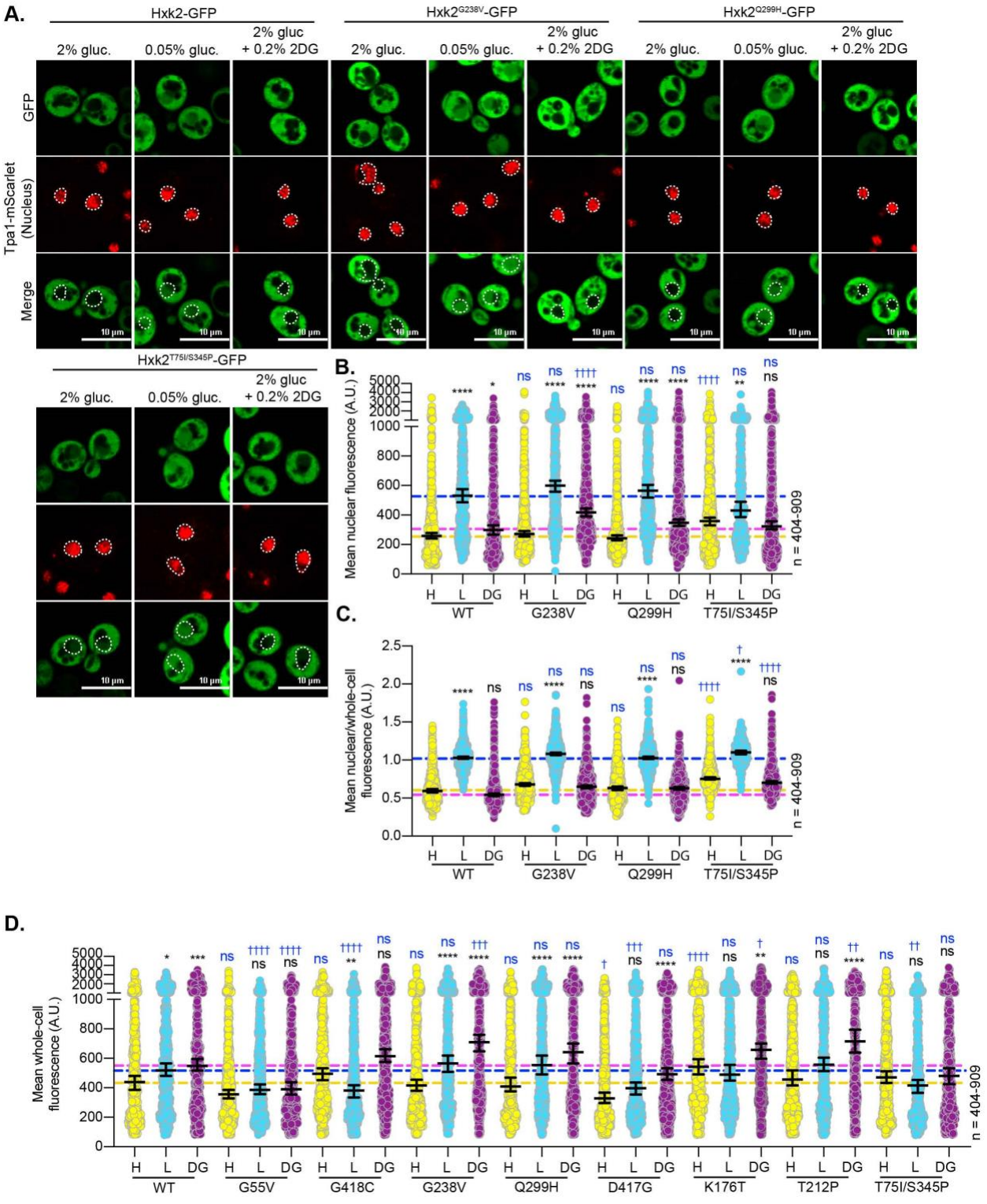

Figure 51. Several Hxk2 2DG-resistance mutants do not alter glucose-dependent subcellular localization.

(A) Confocal microscopy images of GFP-tagged WT Hxk2 and indicated 2DG-resistance mutants expressed in *hxk2*Δ cells from CEN plasmids under control of the endogenous *HXK2* promoter. The Tpa1-mScarlet nuclear marker is used

to determine co-localization with the nucleus. A dashed, white line was traced around the mScarlet-marked nucleus and superimposed onto the GFP channel to indicate its relative position. (B-D) Images in panel A were analyzed using AI-assisted quantification (Nikon.*ai* and GA3 analyses), where (B) shows the mean nuclear fluorescence, (C) shows the mean nuclear fluorescence over the mean whole-cell fluorescence ratio, and (D) shows the mean whole-cell fluorescence intensity for each Hxk2 variant. The diagram at the top left of panel D depicts the region of the cell that was measured. The blue dashed line filled with grid lines depicts the area for whole-cell fluorescence measurements. Horizontal bars depict the median, with error bars representing the 95% confidence interval. Dashed yellow, blue, and purple lines indicate the median value for WT Hxk2-GFP cells in high glucose, low glucose, and high glucose with 0.2% 2DG, respectively. Statistical analyses were performed using a Kruskal-Wallis test with Dunn's post hoc correction. This was done to compare the mean nuclear fluorescence or mean nuclear/whole-cell-fluorescence ratio across conditions of high and low glucose, as well as high glucose with 0.2% 2DG. Black asterisks denote statistical comparisons between low and high glucose conditions or high glucose with 0.2% 2DG and high glucose conditions for a particular *HXK2* allele. Blue daggers indicate comparisons between mutant alleles and the respective wild-type Hxk2 within identical medium conditions.

For each Hxk2 mutant, we next quantified (1) the mean nuclear fluorescence, (2) the mean whole-cell fluorescence, and (3) the mean nuclear-to-whole-cell fluorescence ratio. These measurements aimed to assess the relative contribution of the nuclear signal to the overall cellular fluorescence. Automated quantification revealed that WT Hxk2 had elevated mean nuclear fluorescence and nuclear-to-whole-cell ratio under glucose starvation conditions. In contrast, both high-glucose and 2DG conditions resulted in lower values (Figure 50B, C), consistent with our previous studies [232]. Visual inspection and automated quantification showed a similar trend in Hxk2 mutants that did not have altered nuclear propensity ($Hxk2^{G238V}$, $Hxk2^{Q299H}$, $Hxk2^{T75I/S345P}$; Figure 50B, C, Figure 51B, C).

Of the mutants with constitutive nuclear localization, $Hxk2^{G55V}$, $Hxk2^{T212P}$, and $Hxk2^{K176T}$ had elevated mean nuclear and nuclear-to-whole-cell fluorescence ratios across all experimental

conditions (Figure 50B, C). Conversely, the mean nuclear fluorescence of the Hxk2^{D417G} mutant was dampened in all conditions, though its mean nuclear-to-whole-cell ratio remained elevated. This reduction in nuclear fluorescence can be attributed to the lower whole-cell fluorescence of Hxk2^{D417G}, which explains the observed decrease despite its higher cytosolic-to-nuclear fluorescence ratio compared to WT Hxk2 (Figure 51D). This example underscores the importance of considering the nuclear and cytosolic fluorescence ratio as a readout, as changes in overall Hxk2 abundance do not confound it.

The mean nuclear and nuclear-to-cytosolic-fluorescence ratio of the Hxk2^{G418C} mutant—which did not localize to the nucleus in response to glucose-replete conditions, glucose-starvation, or glucose-replete conditions with 2DG—did not increase in any of these conditions, remaining significantly lower than that of the WT Hxk2 (Figure 50B, C). These findings collectively show, for the first time, that several 2DG-resistant Hxk2 mutants alter the subcellular distribution of this enzyme. Among these mutants, Hxk2^{G55V} has the most pronounced effect. Consequently, we next sought to determine how this seemingly modest Hxk2 mutation alters enzyme dynamics and stability.

4.2.3 Hxk2^{G55V} encodes an unstable protein product

Most Hxk2 2DG-resistance mutations line the glucose-binding (Hxk2^{T212P}, Hxk2^{K176T}, and Hxk2^{Q299H}) or ATP-binding (Hxk2^{D417G}, Hxk2^{R423T}, Hxk2^{G418C}, and Hxk2$^{T75I/S345P}$) pockets (Figure 48B). These mutations likely prevent 2DG phosphorylation by directly interfering with ATP or 2DG binding. However, the G55V mutation is notably distant from the catalytic pocket (~20 Å). Despite the substitution of a small isopropyl group at this site, it has a pronounced impact on the localization of Hxk2 (Figure 50A-C). Additionally, automated quantification revealed that

the mean whole-cell fluorescence intensity of Hxk2^{G55V} was consistently, lower than that of the wild-type (Figure 51D). We found that levels of full-length Hxk2^{G55V}-GFP were slightly lower compared to wild-type in cells grown under glucose-abundant, glucose-deficient, and 2DG-exposed conditions (Figure 52A, B). However, Hxk2^{G55V} was the only mutant that had two breakdown products around 50 and 25 kDa (Figure 52A). We hypothesized that Hxk2^{G55V} is an unstable enzyme, which could explain its lack of catalytic activity [224]. In cells grown at 37°C, the abundance of full-length Hxk2^{G55V}-GFP decreased further, and the breakdown product remained (Figure 52C). Interestingly, *hxk1*Δ *hxk2*Δ *glk1*Δ cells expressing Hxk2^{G55V} had a slight growth defect when grown at 30°C on glucose, and this defect was exacerbated at 37°C, suggesting that elevated temperatures may somewhat impair its catalytic activity. Collectively, these results suggest that Hxk2^{G55V} may indeed be an unstable enzyme.

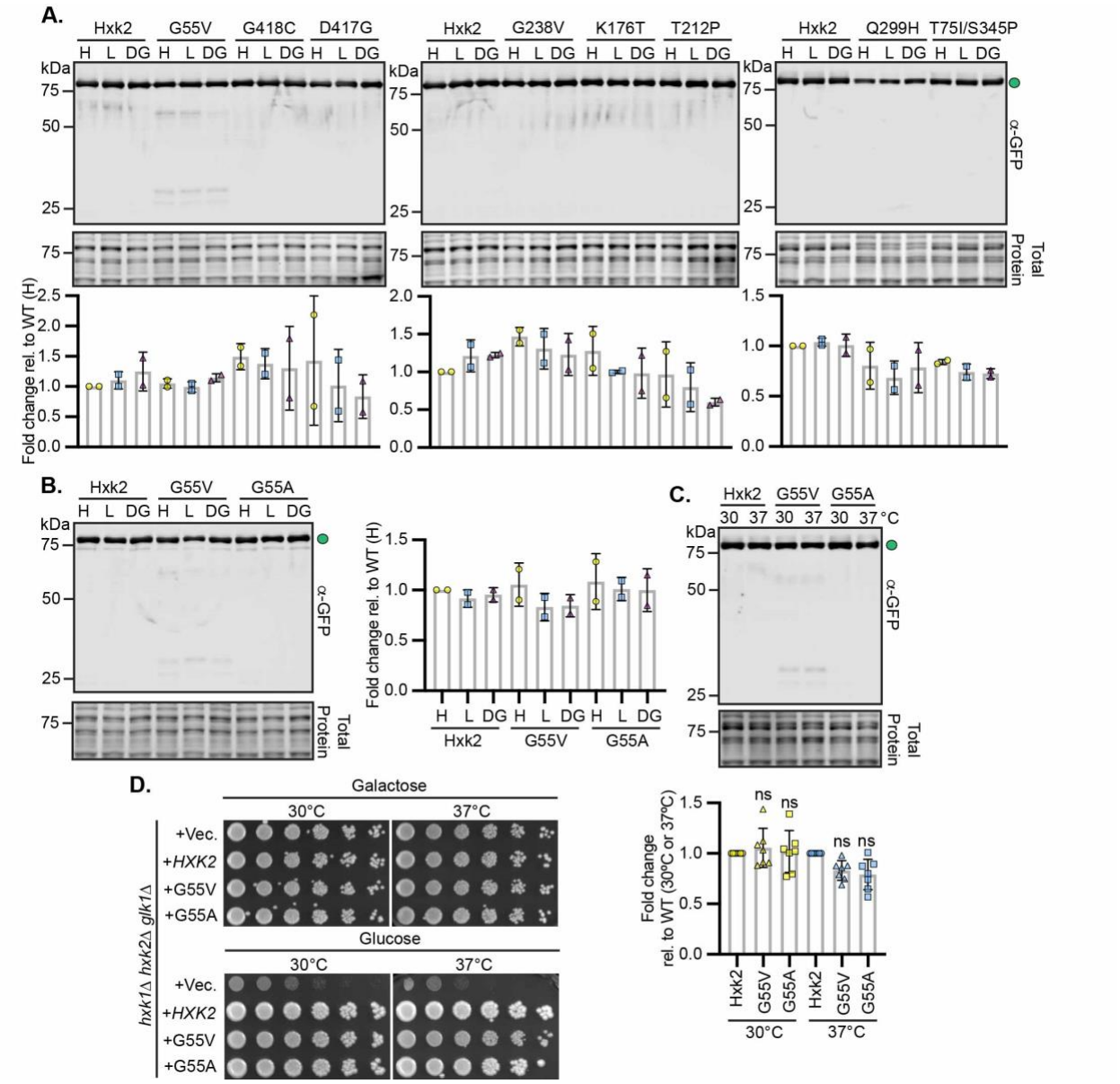

Figure 52. Hxk2^{G55V} may encode an unstable enzyme.

(A-B) Immunoblots showing Hxk2-GFP derived from whole-cell protein extracts obtained from cells cultured in high glucose or shifted to low glucose or high glucose supplemented with 0.2% 2DG for 2 hours. REVERT total protein stain is used as a loading control. Quantification of the full-length Hxk2-GFP signal as shown in panel A and B for two experimental replicates. The abundance of Hxk2-WT in high glucose conditions was normalized to 1 in each experiment. All other values represent the relative fold change. (C) Immunoblots showing Hxk2-GFP derived from whole-cell protein extracts obtained from cells cultured at 30°C or 37°C for 2 hours. REVERT total protein stain is used as a loading control. Quantification of the full-length Hxk2-GFP signal as shown in panel A and B for seven

experimental replicates (four of the seven replicates were performed by Annette Chiang). The abundance of Hxk2-WT at 30°C and 37°C were normalized to 1 in each experiment. All other values represent the relative fold change to wild-type at the same temperature. A one-way ANOVA was used to determine if the abundance of Hxk2^{G55V} ort Hxk2^{G55A} were different from the abundance of Hxk2-WT. (D) Images of serial dilution growth plates of *hxk1*Δ *hxk2*Δ *glk1*Δ cells containing the indicated plasmid (pRS315-*HXK2pr-HXK2*^{allele}) after three days of growth at 30°C or 37°C. The growth medium is SC Leu- containing 2% glucose (bottom two panels) or 2% galactose (top two panels).

The substitution of an isopropyl group at position 55 may seem modest, but it has a substantial impact on protein stability. Glycine is unique because it lacks a side chain, allowing for enhanced conformational flexibility at these sites. Indeed, hexokinases have several glycines at the terminal ends of secondary structures, likely to allow for crucial conformational changes required for glucose and ATP binding [80]. We hypothesize that substituting a valine isopropyl sidechain would restrict conformational flexibility at this site by increasing collisions with neighboring residues.

To further investigate the impact of a more subtle mutation at this position, we also generated an Hxk2^{G55A} mutant. We found that Hxk2^{G55A} most likely retains WT-like levels of catalytic activity as it does not confer resistance to 2DG. Moreover, it supports growth on glucose in *hxk1*Δ *hxk2*Δ *glk1*Δ cells (Figure 53A-D). In contrast to Hxk2^{G55V}, Hxk2^{G55A} does not exhibit clear breakdown products and maintains similar levels of full-length protein as the wild-type in glucose-rich, glucose-deficient, and glucose-rich conditions with 2DG (Figure 52B). The abundance of Hxk2^{G55A} remains unchanged in *hxk2*Δ cells grown at 37°C, and *hxk1*Δ *hxk2*Δ *glk1*Δ cells expressing this mutant show comparable growth to those expressing wild-type Hxk2 while growing at 37°C on glucose (Figure 52C, D).

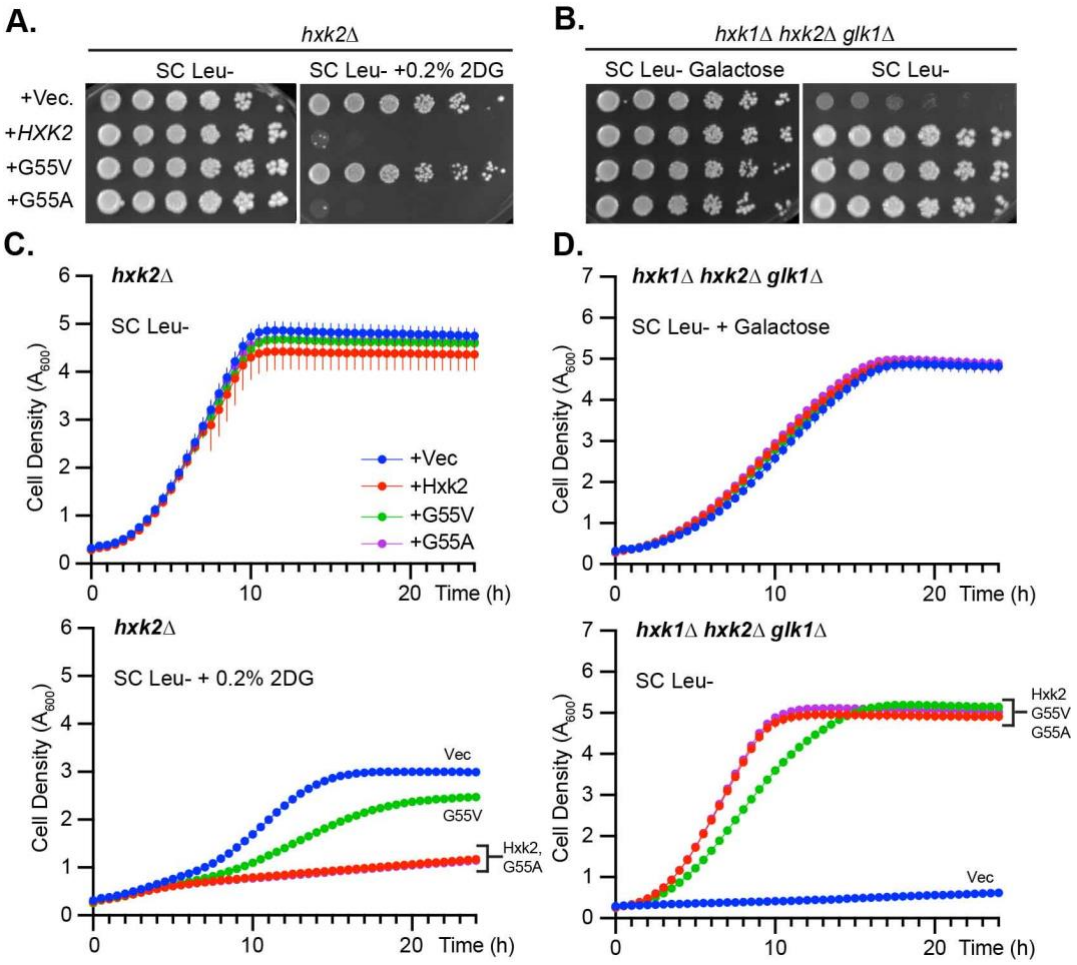

Figure 53. Hxk2^{G55A} does not confer 2DG resistance and facilitates growth on glucose.

(A and B) Images of serial dilution growth plates of *hxk2*Δ or *hxk1*Δ *hxk2*Δ *glk1*Δ cells containing the indicated plasmid (pRS315-*HXK2pr-HXK2*^{allele}) after three days of growth at 30°C. The growth medium is SC Leu- containing 2% glucose (panels A and B, far right) or 2% galactose (panel B, far left), with the addition of 0.2% 2DG where indicated. (C and D) The cell density (A_{600}) changes over time for cells grown in SC Leu-, SC Leu- with 0.2% 2DG, or SC Leu- with 2% galactose are plotted. Curves depict the average A_{600} of three technical replicates, while vertical lines extending from each data point illustrate the +/- SD, occasionally being too minimal to extend beyond the data point itself.

We investigated whether the Hxk2^{G55A} mutation has a similar impact on nuclear shuttling as the Hxk2^{G55V} mutation. Upon visual inspection, we observed that Hxk2^{G55A} predominantly

localized to the nucleus only under low-glucose conditions, while no discernable nuclear signal was detected in glucose-rich media and glucose-rich media supplemented with 2DG (Figure 54A). Our automated quantification analysis supported these observations, revealing that Hxk2^{G55A} had elevated mean nuclear fluorescence and mean nuclear-to-whole-cell ratio under glucose-starvation conditions (Figure 54B, C). In contrast, both high-glucose and 2DG conditions resulted in lower levels (Figure 54B, C). Overall, our data show that substituting a methyl group at position 55 does not recapitulate the phenotype observed in the Hxk2^{G55V} mutant but rather resembles the behavior of the wild-type enzyme.

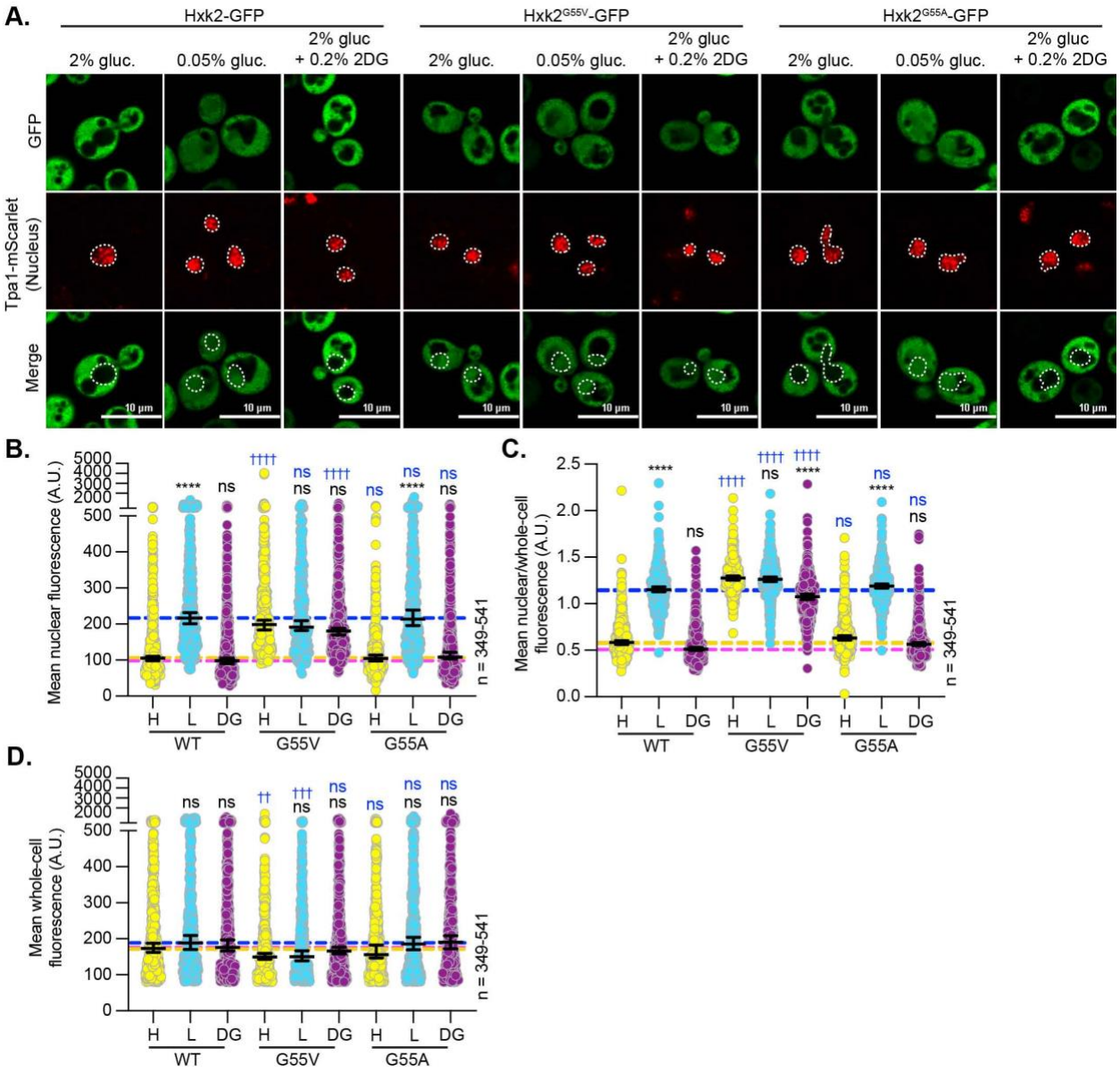

Figure 54. Hxk2^{G55A} does not impact nuclear propensity.

(A) Confocal microscopy images of GFP-tagged WT Hxk2 and the indicated 2DG-resistance mutants expressed in *hxk2*Δ cells from pRS315-*HXK2pr-HXK2*^{allele} plasmids. The Tpa1-mScarlet nuclear marker is used to determine co-localization with the nucleus. A dashed, white line was traced around the mScarlet-marked nucleus and superimposed onto the GFP channel to indicate its relative position. (B-D) Images in panel A were analyzed using AI-assisted quantification (Nikon.*ai* and GA3 analyses), where (B) shows the mean nuclear fluorescence, (C) shows the mean nuclear fluorescence over the mean whole-cell fluorescence ratio, and (D) shows the mean whole-cell fluorescence intensity for each Hxk2 variant. Horizontal bars depict the median, with error bars representing the 95% confidence

interval. Dashed yellow, blue, and purple lines indicate the median value for WT Hxk2-GFP cells in high glucose, low glucose, and high glucose with 0.2% 2DG, respectively. Statistical analyses were performed using a Kruskal-Wallis test with a Dunn's post hoc correction. This test was done to compare the mean nuclear fluorescence or mean nuclear/whole-cell fluorescence ratio, and mean whole-cell fluorescence intensities across high and low glucose, and high glucose with 0.2% 2DG conditions. Black asterisks denote statistical comparisons between low and high glucose conditions or high glucose with 0.2% 2DG and high glucose conditions for a particular *HXK2* allele. Blue daggers indicate comparisons between mutant alleles and the respective wild-type Hxk2 within identical medium conditions.

4.2.4 Molecular dynamics simulations reveal that Hxk2^{G55V} impairs large-scale conformational changes required to bind glucose and may prevent substrate binding

We further investigated the impact of Hxk2^{G55V} using molecular dynamics (MD) simulations. This work was motivated by our recent use of MD to predict the structural and functional defects of the Hxk2^{G238V} mutation [227]. Like Hxk2^{G55V}, the Hxk2^{G238V} mutation does not directly line the enzymatic cleft, yet it significantly impacts enzymatic-cleft, catalytic-residue, and overall dynamics. The prior study demonstrated that even minor alterations in protein structure can significantly impact function through allosteric mechanisms [227].

To investigate whether Hxk2^{G55V} impairs enzymatic activity through a similar allosteric mechanism, we performed all-atom MD simulations of six different systems: (1) Hxk2-WT *apo* (glucose-free), (2) Hxk2-WT *holo* (glucose-bound), (3) Hxk2^{G55V} *apo*, (4) Hxk2^{G55V} *holo*, (5) Hxk2^{G55A} *apo*, and (6) Hxk2^{G55A} *holo*. For each of the six systems, we performed three simulations of ~250 ns, ~250 ns, and ~500 ns, with the exception of the *holo* Hxk2^{G55V} system (~1μS for each system, ~6 μS total, summarized in Table 11). Unless otherwise noted, we treated the three simulations associated with each system as one for subsequent analysis.

Table 11. Summary of molecular dynamics simulations.

System	Simulation 1	Simulation 2	Simulation 3	Aggregate
Hxk2 *apo*	238.3 ns	255.7 ns	493.9 ns	987.9 ns
Hxk2 *holo*	249.1 ns	259.9 ns	529.5 ns	1038.5 ns
$Hxk2^{G55V}$ *apo*	256.0 ns	258.8 ns	507.7 ns	1022.5 ns
$Hxk2^{G55V}$ *holo*	563.6 ns	595.8 ns	500.4 ns	1659.8 ns
$Hxk2^{G55A}$ *apo*	263.7 ns	269.9 ns	519.9 ns	1053.5 ns
$Hxk2^{G55A}$ *holo*	257.7 ns	255.6 ns	519.9 ns	1033.0 ns

We assessed equilibration and large-scale structural changes by calculating the root-mean-square deviation (RMSD) per backbone heavy atom relative to the simulation's first (minimized) frame. We excluded the N-terminal tail (residues V2-A17) from these analyses because it is highly dynamic (disordered) in the monomeric form, which could overshadow the contributions of other regions to the RMSD. After approximately 10 ns of simulation time, the RMSDs of each simulation reached a plateau, indicating equilibration during the production runs. The average RMSD remained consistently below 3 Å for all wild-type simulations, suggesting only minor conformational changes. Notably, the RMSD remained consistently fluctuating during both $Hxk2^{G55V}$ and $Hxk2^{G55A}$ simulations, often reaching or exceeding 3 Å or higher regardless of glucose presence, indicating greater structural flexibility (Figure 55).

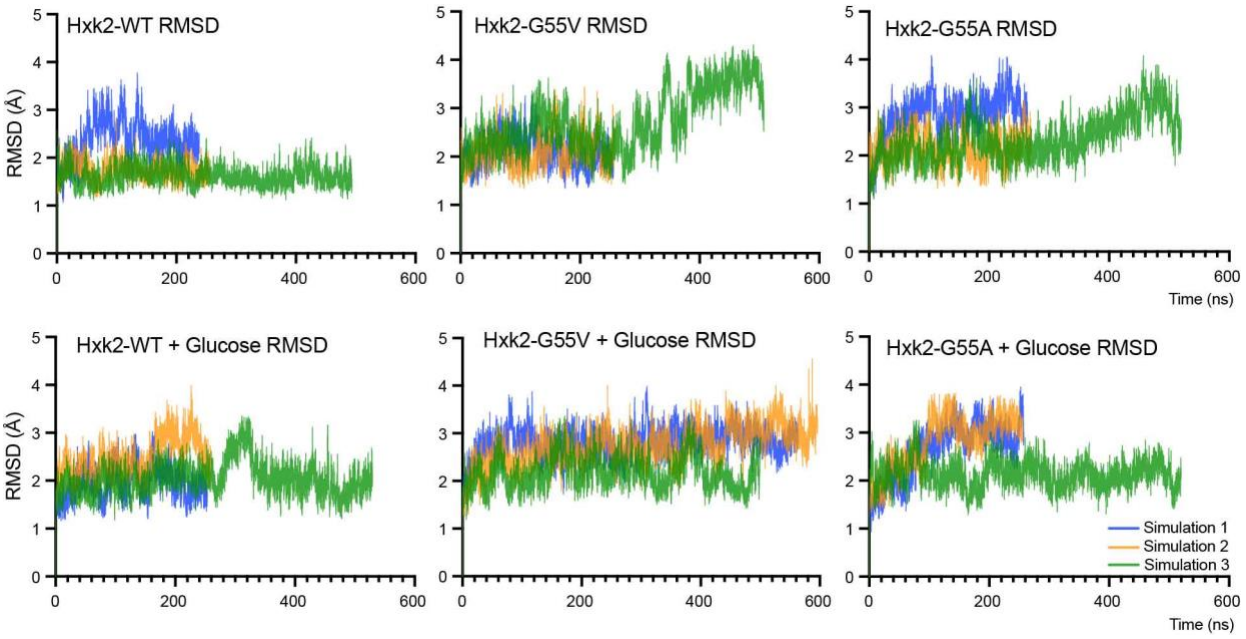

Figure 55. Hxk2^{G55V} may promote moderate overall structural change.

Line graphs showing the protein backbone heavy atom root-mean-square deviations (RMSD) over simulation time in each of the three simulations performed: Hxk2-WT *apo*, Hxk2-WT *holo*, Hxk2^{G55V} *apo*, Hxk2^{G55V} *holo*, Hxk2^{G55A} *apo*, Hxk2^{G55A} *holo*. Aligned trajectory frames were taken every 20 ps to conduct the analysis. The simulations did not achieve full equilibration during the beginning portions of each production run; therefore, we excluded the initial 10 ns of the pre-equilibrated portions of the production runs.

Prior to glucose binding, Hxk2 primarily adopts an open conformation characterized by the positioning of its large and small subdomains, allowing for accessibility of the enzymatic cleft to the surrounding solvent. Upon substrate binding, a conformational change occurs where the two domains transition to a closed state through rotational movement relative to each other, resulting in the collapse of the cleft and envelopment of the glucose molecule [79,80,83]. To assess the potential impact of G55 mutations on these domain-level conformational changes, we calculated the protein radius of gyration (RoG) throughout the six simulations (Figure 56A), again excluding the N-terminal residues. Larger RoG values indicate Hxk2 is in the open conformation (Figure

56A, red dotted line), and smaller RoG values indicate Hxk2 is in the closed conformation (Figure 56A, green dotted line).

The WT *apo* RoG averaged ~24.3 Å, consistent with a previously reported open-conformation structure (PDB 1IG8). This value significantly (P-value < 0.0001 per Kruskal-Wallis test) decreased to an average of ~24 Å in the WT *holo* simulations, approaching the RoG of a published closed-conformation structure (< 23.5 Å; PDB 3O8M, *K. Lactis* Hxk1). However, we did not observe a fully closed conformation in any simulations, consistent with our previous studies [227]. It may be that additional factors are required for further domain closure (e.g., ATP binding, which may be required to induce further conformational changes) [81].

In contrast to WT Hxk2, the Hxk2^{G55V}-mutant RoG was generally lower in both the *holo* and *apo* simulations (P-value < 0.0001 in both cases per Kruskal-Wallis test) (Figure 56A). This suggests the mutant is less prone to adopt an open conformation when glucose is absent. Notably, the same trend was observed for the Hxk2^{G55A} mutant (Figure 56A).

To further assess the impact of Hxk2^{G55V} on large-scale open-to-closed motions, we measured the distance between the Cα atoms of two hydrophobic, internal residues—one in the large subdomain (L314) and the other in the small subdomain (A132) (Figure 56B). As Hxk2 transitions to the closed conformation, the distance between these residues should decrease, indicating domain closure (Figure 56B). Our analysis revealed that both mutant *apo* (glucose-absent) simulations had a more closed conformation than the WT protein, even in the absence of glucose (average distances of 41.7 Å, 41.7 Å, and 43.6 Å for G55V, G55A, and WT Hxk2, respectively, compared to 45.2 Å for the 1IG8 open crystal structure). This analysis corroborates the RoG results mentioned earlier (Figure 56C). As expected, the distances in the WT *holo* simulation decreased (42.3 Å), indicating domain closure. But, since G55V and G55A already had

a more closed conformation in the absence of glucose, the average distances for their *holo* simulations remained relatively unchanged (41.6 Å and 42.0 Å for G55V and G55A, respectively, compared to 38.6 Å for the 3O8M closed crystal structure) (Figure 56D). Notably, for G55A and G55V, domain closure occurs independently of glucose binding, potentially affecting their ability to bind glucose.

Based on the results above, we hypothesize that Hxk2^{G55V} hinders the enzyme's ability to adopt a fully open conformation, which could create an unfavorable environment for glucose binding. Notably, in the third G55V *holo* simulation (500 ns), glucose completely dissociated from the enzymatic cleft, supporting this hypothesis (Table 12 and Supplemental Movie 4, available in OneDrive link: Supplemental Thesis Movies). That said, glucose dissociated in only one simulation, even after extending the duration of the other two simulations to 500 ns each. Nonetheless, these findings suggest a compelling mechanistic hypothesis that may explain how the Hxk2^{G55V} mutation attenuates Hxk2 activity, compatible with our enzymatic [224] and phenotypic assays (Figure 49A-D).

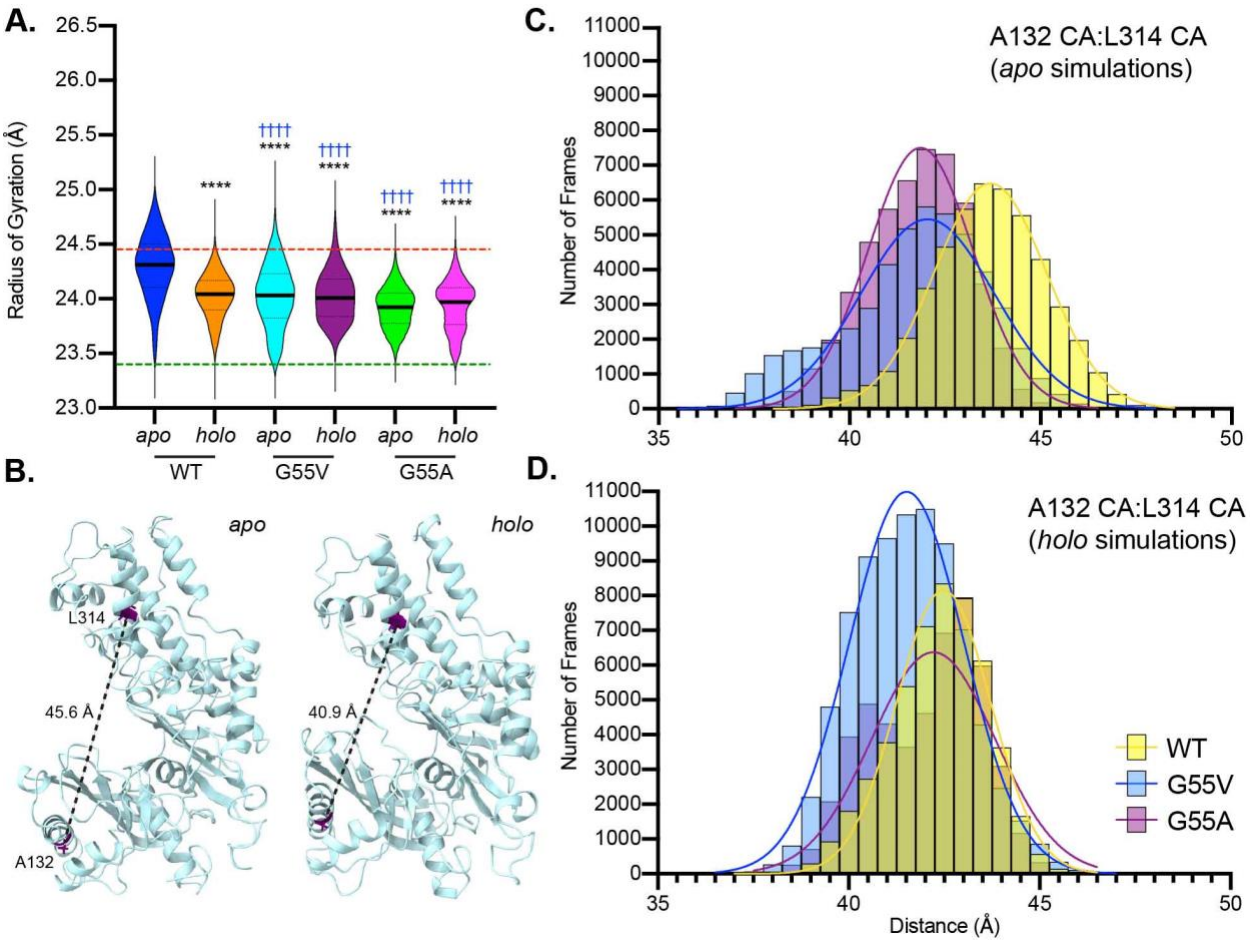

Figure 56. Hxk2^{G55V} impairs large-scale conformations required to bind glucose.

(A) RoG distributions for each of the indicated simulations are shown as violin plots. Bold and dashed horizontal lines indicate the median and interquartile range, respectively. Red and green dashed lines provide reference, showing the respective values of the 1IG8 (*Sc*Hxk2, open) and 3O8M (*Kl*Hxk1, closed) crystal structures, respectively. Black asterisks represent statistical comparisons between WT *apo* simulations and all other simulations, and blue daggers represent statistical comparisons between WT *holo* simulations and all other mutant simulations. A Kruskal-Wallis statistical test with a Dunn's post-hoc correction was used to compare the means of each simulation. Each simulation differs statistically from the means of all others (p-value < 0.0001 in all cases, indicated by **** or ††††). (B) *Sc*Hxk2 structure with backbone carbon atoms depicted as light-blue ribbons. To further assess domain closures, distances (dashed, black lines) between the α-carbons of two internal hydrophobic residues (purple) were measured over the duration of each simulation. (C and D) The distribution of distances between the α-carbons of A132 and L314 is

shown as frequency histograms (bin width 0.5 Å). The data were fitted to a Gaussian least square model, and the resulting curves were plotted over each set of histograms, shown as yellow, blue, and purple lines.

Table 12. Results of glucose heavy atom RMSD analysis.

System	Simulation 1	Simulation 2	Simulation 3	Aggregate
Hxk2 *holo*	1.71 ± 0.66 Å	2.64 ± 0.74 Å	1.99 ± 0.83 Å	2.11 Å
$Hxk2^{G55V}$ *holo*	1.94 ± 0.44 Å	3.11 ± 1.02 Å	21.48 ± 26.06 Å	8.84 Å
$Hxk2^{G55A}$ *holo*	2.41 ± 0.96 Å	1.44 ± 0.47 Å	1.41 ± 0.38 Å	1.75 Å

4.2.5 $Hxk2^{G55V}$ impacts the correlation of movements between the large and small subdomains, but conserved signaling hubs remain intact

We used dynamic cross-correlation (DCC) analysis to compare the motions of each Hxk2 residue to every other residue [490]. In the WT *apo* simulation, we observed high anti-correlation between the small and large subdomains (Figure 57A). This high degree of anti-correlation indicates that the two domains move in opposite directions, compatible with the observation that the enzyme samples open and closed conformations (i.e., the large and small subdomains repeatedly come together and separate). Upon glucose binding (*holo* simulations), the degree of anti-correlation decreased, likely due to the enzyme's reduced flexibility as it fully embraced the glucose molecule (Figure 57B).

In contrast, the large and small subdomains also had a high degree of anti-correlation in the G55V *apo* simulations, suggesting greater conformational flexibility in the absence of glucose (Figure 57C). This observation aligns with our RoG analysis, which showed a broader distribution of RoG values, suggesting both semi-open and -closed conformations (Figure 56A). The G55V *holo* simulation was less orderly, with localized regions showing both high correlation and anti-

correlation between the two domains (Figure 57D). Strikingly, both G55A simulations (*holo* and *apo*) showed a similar trend to the WT *holo* simulations and showed less flexibility as the degree of anti-correlation was lower (Figure 57E, F).

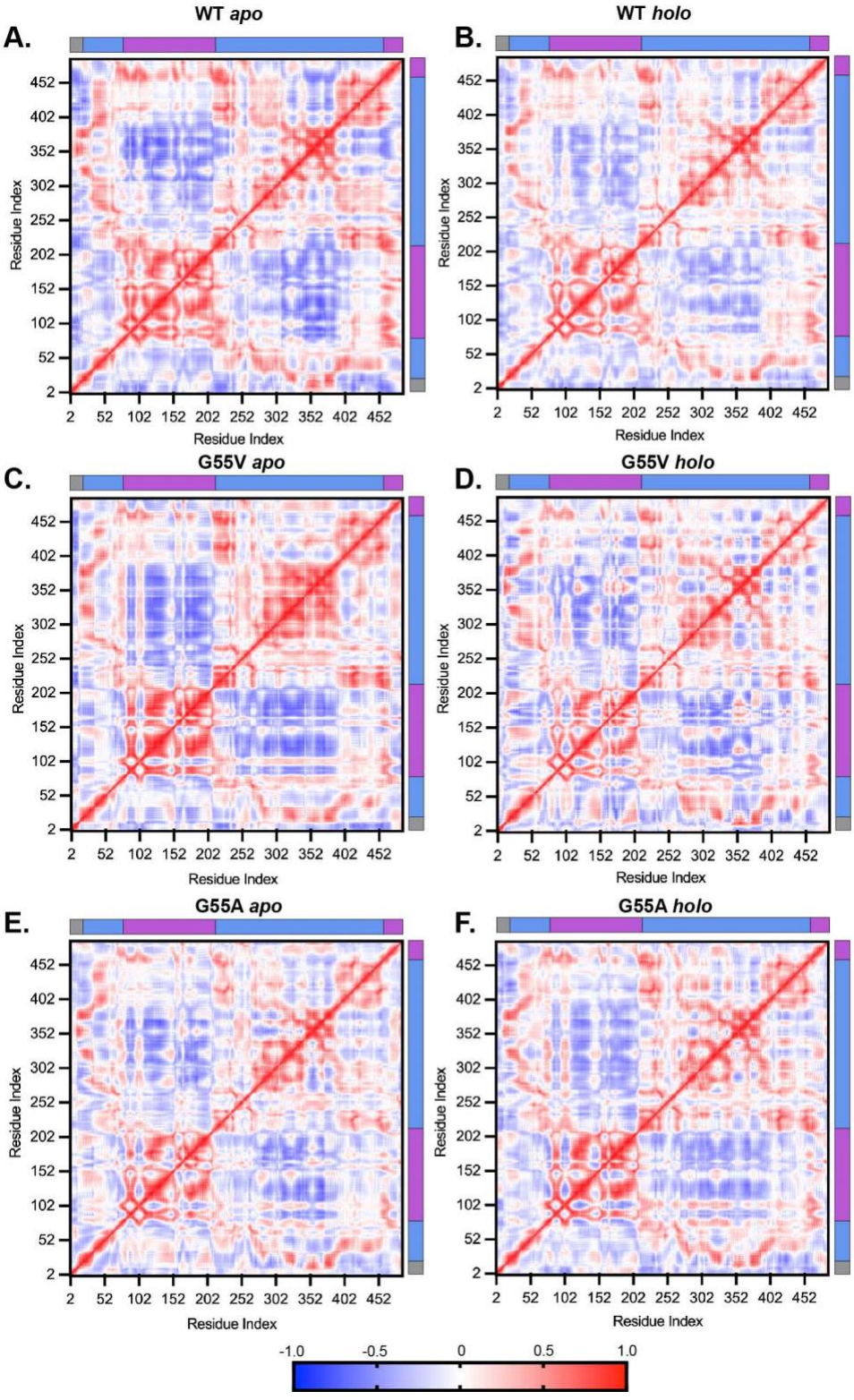

Figure 57. Hxk2^{G55V} changes the degree of correlation between small and large subdomains.

(A-F) NxN dynamic cross-correlation (DCC) matrices for the indicated MD simulations. A DCC value for a residue-residue pair of -1 (blue) indicates anticorrelated motions (opposite directions), and a value of 1 (red) indicates correlated motions (same direction).

The G55V mutation also impacts the propagation of residue-residue communication pathways within the protein, leading to the observed large-scale conformational changes. We calculated each residue's betweenness centrality (BC), which measures its importance in intra-protein communication [490]. Consistent with our previous study [227], several conserved regions surrounding the catalytic cleft have the greatest influence on intra-protein communication (Figure 58A-D). Notably, the residues forming the cleft-lining β9-β10 hairpin (I231-N237) and the α5 helix (I209-T215), which houses the catalytic residue D211, have the most substantial impact (Figure 58C). Our BC analysis revealed that these key signaling hubs remained unchanged regardless of the presence of glucose. Importantly, the G55V and G55A mutants did not noticeably perturb the BC values of these regions, indicating their continued importance in intra-protein communication. These results suggest that Hxk2^{G55V} maintains critical intra-protein signaling pathways during our simulations. Rather than disrupting these pathways, Hxk2^{G55V} may exploit them to propagate signals throughout the protein and promote the closed conformation.

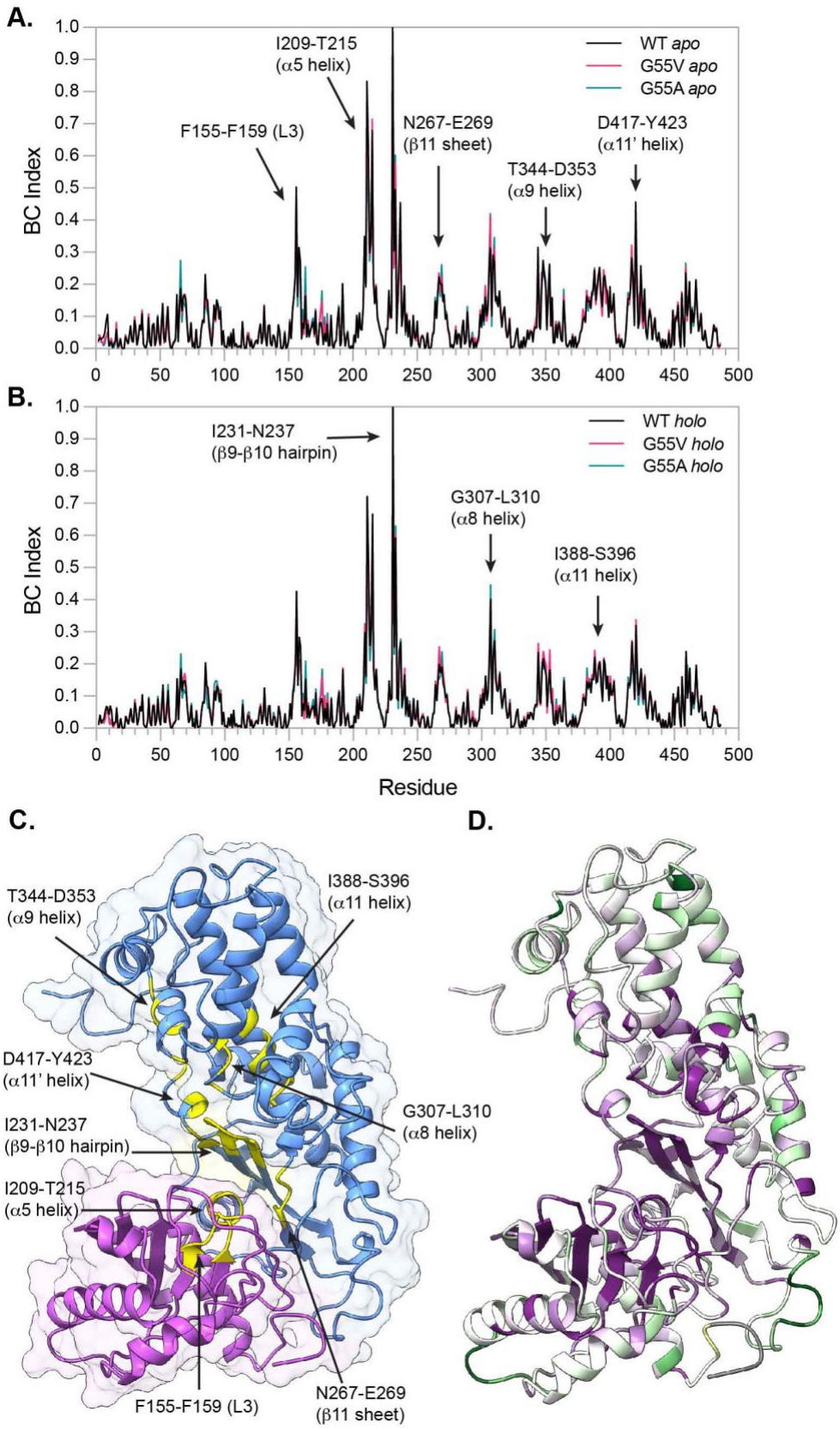

Figure 58. Betweennes centrality reveals putative communication hubs.

(A and B) Betweenness centrality (BC) index profiles of all three glucose-absent (*apo*; A) and glucose-bound (*holo*; B) simulations revealing potential communication hubs. (C) Three-dimensional structure of Hxk2 (homology model constructed previously [232]) in ribbon and surface representation. Blue and purple regions show the large and small subdomains, respectively. Notable regions with higher BC indices as indicated in (A and B) are colored yellow. (D) Structure of Hxk2 in ribbon representation colored according to residue conservation based on results using CONSURF [496]. Residues are colored on a 1 (green) to 9 (purple) scale, with 1 meaning poorly conserved and 9 being highly conserved.

4.2.6 Hxk2^{G55V} disrupts the stability of a molecular "hinge" point and residues of the enzymatic cleft

4.2.6.1 Impact of Hxk2^{G55V} on local dynamics and a molecular "hinge" point

To evaluate the impact of the G55V mutation on Hxk2 dynamics, we calculated the average root-mean-square fluctuations (RMSF) of each residue over the course of each simulation (Figure 59, 60). By plotting a heatmap of the ΔRMSF (G55V-WT) values of each residue onto the Hxk2 structure (Figure 59A, B, Figure 60A, B), we noticed the G55V mutation had a substantial impact on local dynamics. In the *apo* simulations, G55V increased the flexibility of nearby residues, including V55-G60 and D246-Q251 in the α5' helix (Figure 59A, Figure 60C). The increased flexibility at these two regions was further exacerbated in the *holo* simulations (Figure 59B, Figure 60D). Notably, the V55-G60 region forms the initial segment of an extended loop region spanning 24 residues from G55 to E78, commonly referred to as connecting loop I in studies of human glucokinase. This loop is a pivotal "hinge" point that dictates glucokinase's range of motion during its catalytic cycle and regulates catalytic turnover [88,102]. It is plausible that the altered dynamics of this loop, induced by the G55V mutation, restrict Hxk2's range of motion, thus encouraging a more closed conformation, as discussed above.

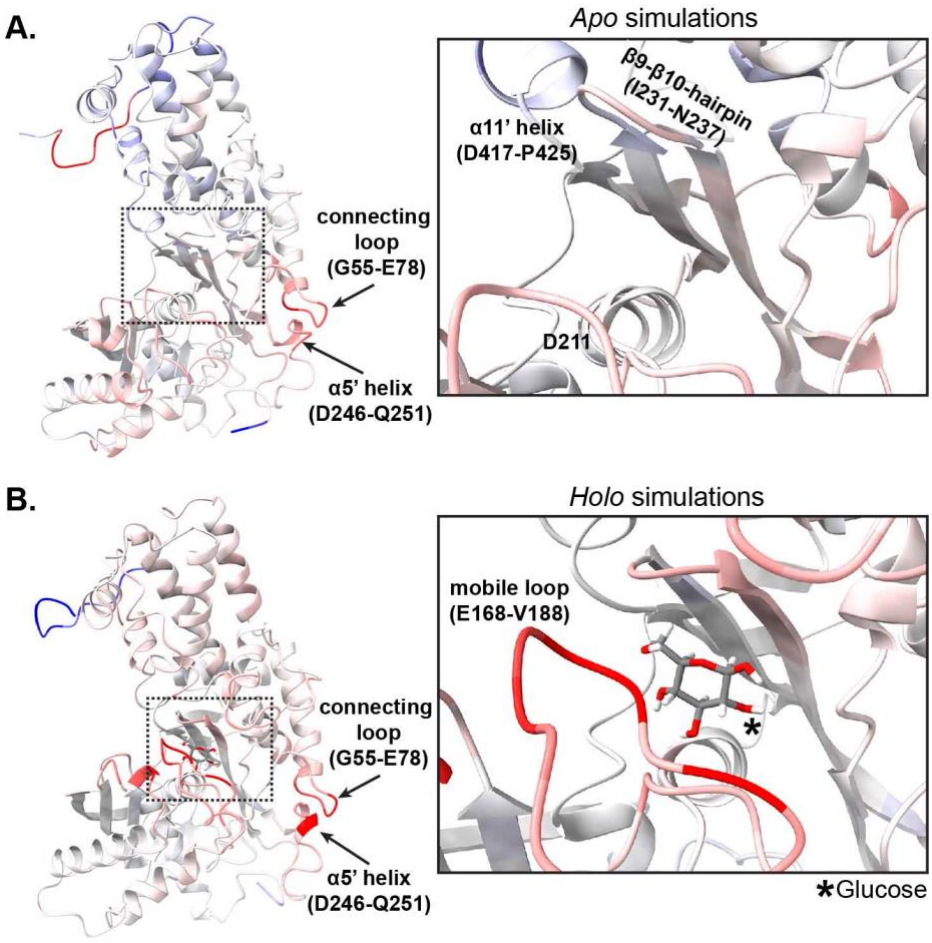

Figure 59. Hxk2^{G55V} alters protein dynamics locally and distally.

(A and B) Structural conformations of *Sc*Hxk2 taken from WT *apo* (panel A) and *holo* (panel B) simulations. Both Hxk2 structures (ribbon) are colored by ΔRMSF values (G55V-WT) calculated for each residue. In any given region, blue indicates that the G55V simulation was less flexible (ΔRMSF ≤ -2.00 Å), and red indicates that the G55V simulation was more flexible (ΔRMSF ≥ 2.00 Å). Zoomed-in views of the *Sc*Hxk2 glucose binding pocket are shown on the right in black boxes. In panel B, glucose atoms are depicted as cylinders, and their locations are marked with an asterisk.

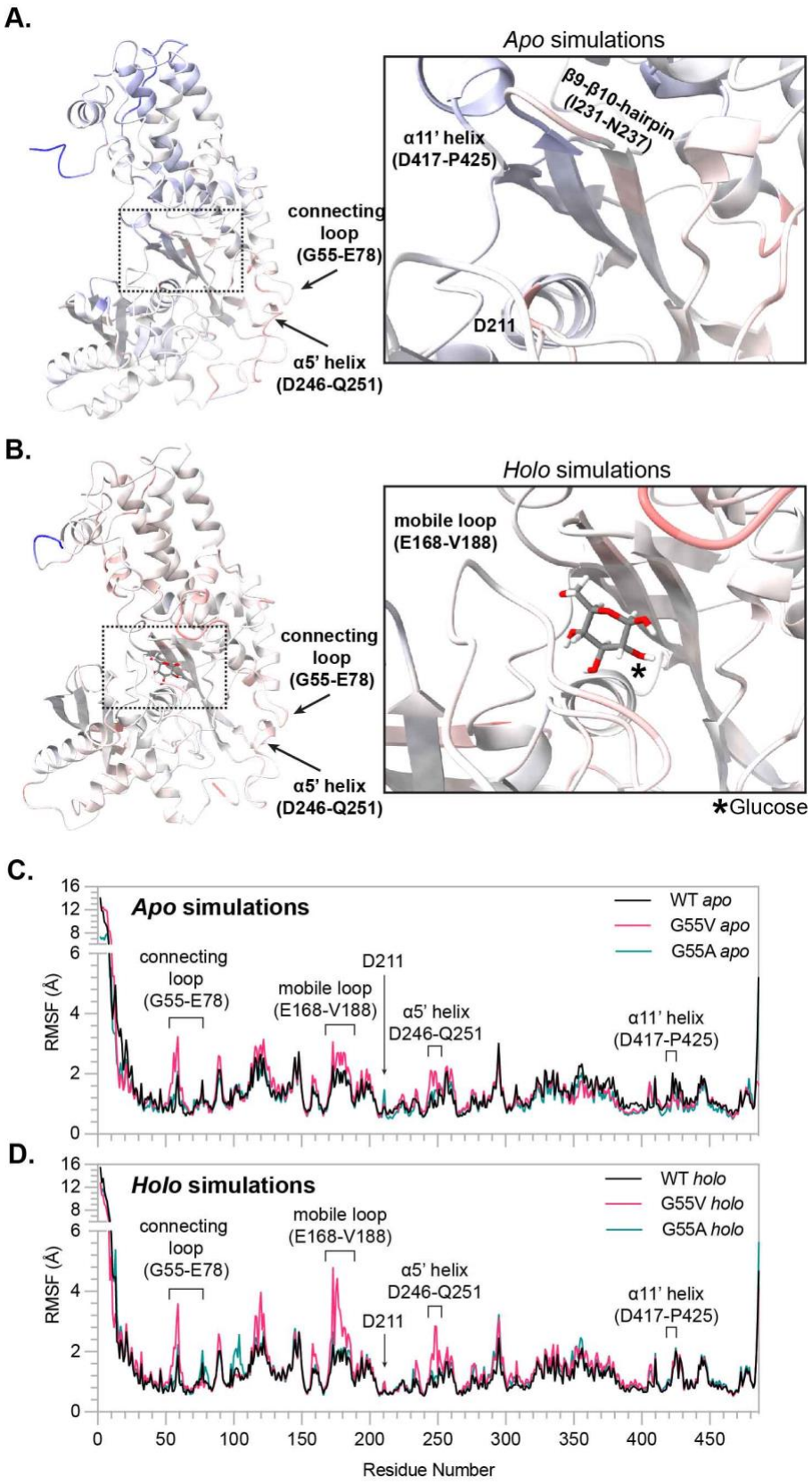

Figure 60. Hxk2^{G55A} does not dramatically alter protein dynamics.

(A and B) Structural conformations of *Sc*Hxk2 taken from WT *apo* (panel A) and *holo* (panel B) simulations. Both Hxk2 structures (ribbon) are colored according to ΔRMSF values (G55A-WT) calculated for each residue. In any given region, blue indicates that the G55A simulation was less flexible (ΔRMSF ≤ -2.00 Å), and red indicates that the G55A simulation was more flexible (ΔRMSF ≥ 2.00 Å). Zoomed-in views of the *Sc*Hxk2 glucose binding pocket are shown on the right in black boxes. In panel B, glucose atoms are depicted as cylinders (marked with an asterisk). (C and D) Line graphs showing root-mean-square fluctuations (RMSF) of each residue's center of geometry across all three *apo* (panel C) and *holo* (panel D) simulations.

Interestingly, a portion of the connecting loop undergoes a displacement away from the α5' helix in the *apo* and *holo* G55V simulations that induces a forward tilt of the large subdomain followed by an upward swing of the small subdomain that collapses the enzymatic cleft (Supplemental Movies 3 and 4, available in OneDrive link: Supplemental Thesis Movies). In contrast, the connecting loop remains associated with the α5' helix in the WT and G55A simulations as the protein transitions to the closed conformation. Importantly, key electrostatic and hydrogen-bonding interactions occur at this site, involving D246 (α5' helix) with K406 or R407 (α11 helix) and K58 (connecting loop) with E248 or Q251 (α5' helix) (Figure 61A).

We hypothesize that G55V may indirectly impact these interactions, causing defects in this site's tertiary structure. To test this hypothesis, we counted the number of simulation frames that captured these interactions (≤ 3.5 Å for the K58:Q251 hydrogen bond and ≤ 5 Å for salt bridges). We found that the G55V mutation induces several rearrangements amongst residue pairs (Figure 61B, Figure 62). For example, the D246:K406 electrostatic interaction occurred less frequently in the G55V simulations (82% *apo*/79.3% *holo* in WT vs. 23.9% *apo*/8.9% *holo* in G55V). Conversely, the D246:R407 electrostatic interaction became more prevalent (Figure 61B and Figure 62A-D). The K58:Q251 hydrogen bond was less prevalent (23% *apo*/23.9% *holo* in WT vs. 12.2% *apo*/10.3% *holo* in G55V), and the K58:E248 electrostatic interaction was more

prevalent in the G55V simulations (15.3% *apo*/10.2% *holo* in WT vs. 30.6% *apo*/35% *holo* in G55V; Figure 61B and Figure 62E-H). We did not observe the same displacement of the connecting loop in the G55A simulation, yet we still observed identical rearrangements of residue pairs as in the G55V simulations (Figure 61B, Figure 62). Collectively, these findings suggest that the G55V mutation may destabilize the local tertiary structure by altering the interaction preferences between residue pairs rather than completely disrupting all interactions.

A.

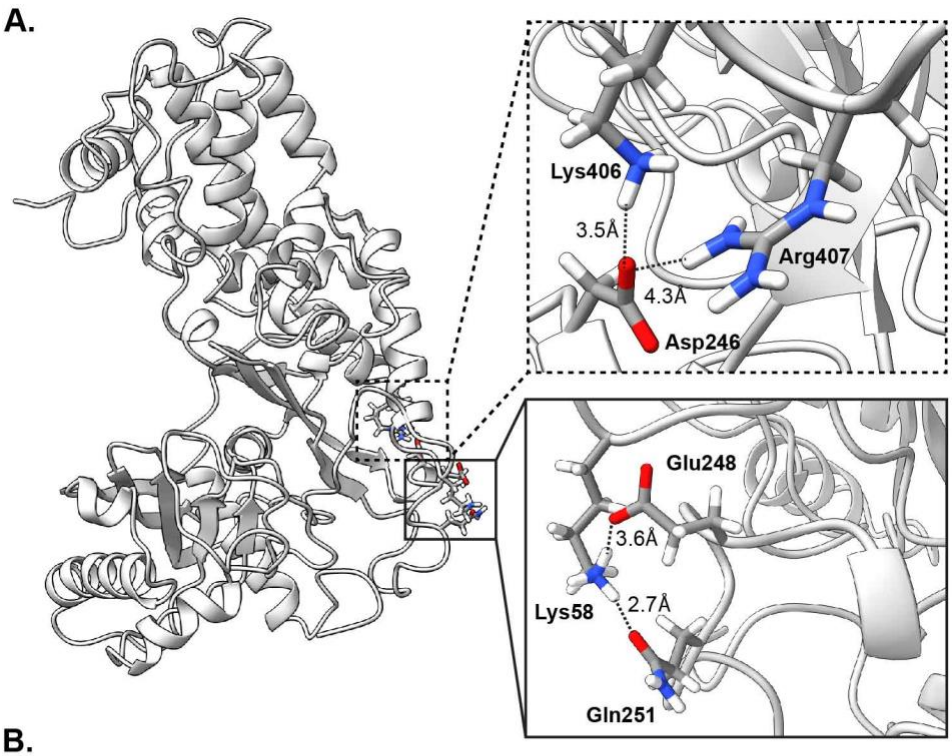

B.

Residue-residue interaction	Mutant	Percentage of frames within cutoff	
		apo	*holo*
D246 CG:K406 NZ (salt bridge)	WT	82.0%	79.3%
	G55V	23.9%	8.9%
	G55A	22.6%	36.7%
D246 CG:R407 CZ (salt bridge)	WT	4.2%	9.3%
	G55V	18.3%	47.7%
	G55A	39.9%	49.7%
K58 NZ:E248 CD (salt bridge)	WT	15.3%	10.2%
	G55V	30.6%	35.0%
	G55A	20.0%	21.8%
K58 NZ:Q251 OE1 (Hydrogen bond)	WT	23.0%	23.9%
	G55V	12.2%	10.3%
	G55A	12.8%	14.2%

Figure 61. Hxk2^{G55V} alters local dynamics by disrupting nearby electrostatic and hydrogen-bonding networks. (A) *Sc*Hxk2 structure (homology model constructed previously [232]; ribbon) showing key salt-bridge and hydrogen-bonding residues with sidechains depicted as cylinders. Zoomed-in images in black solid and dashed boxes depict the interacting residue sidechains connected with dashed lines. (B) Table summarizing the proportion of simulation frames where specific sidechain atom pairs interacted. We assumed a residue sidechain interaction occurred if the distances were ≤ 5.0 Å for salt bridge interactions and ≤ 3.5 Å for hydrogen bonds. See Materials and Methods for more information.

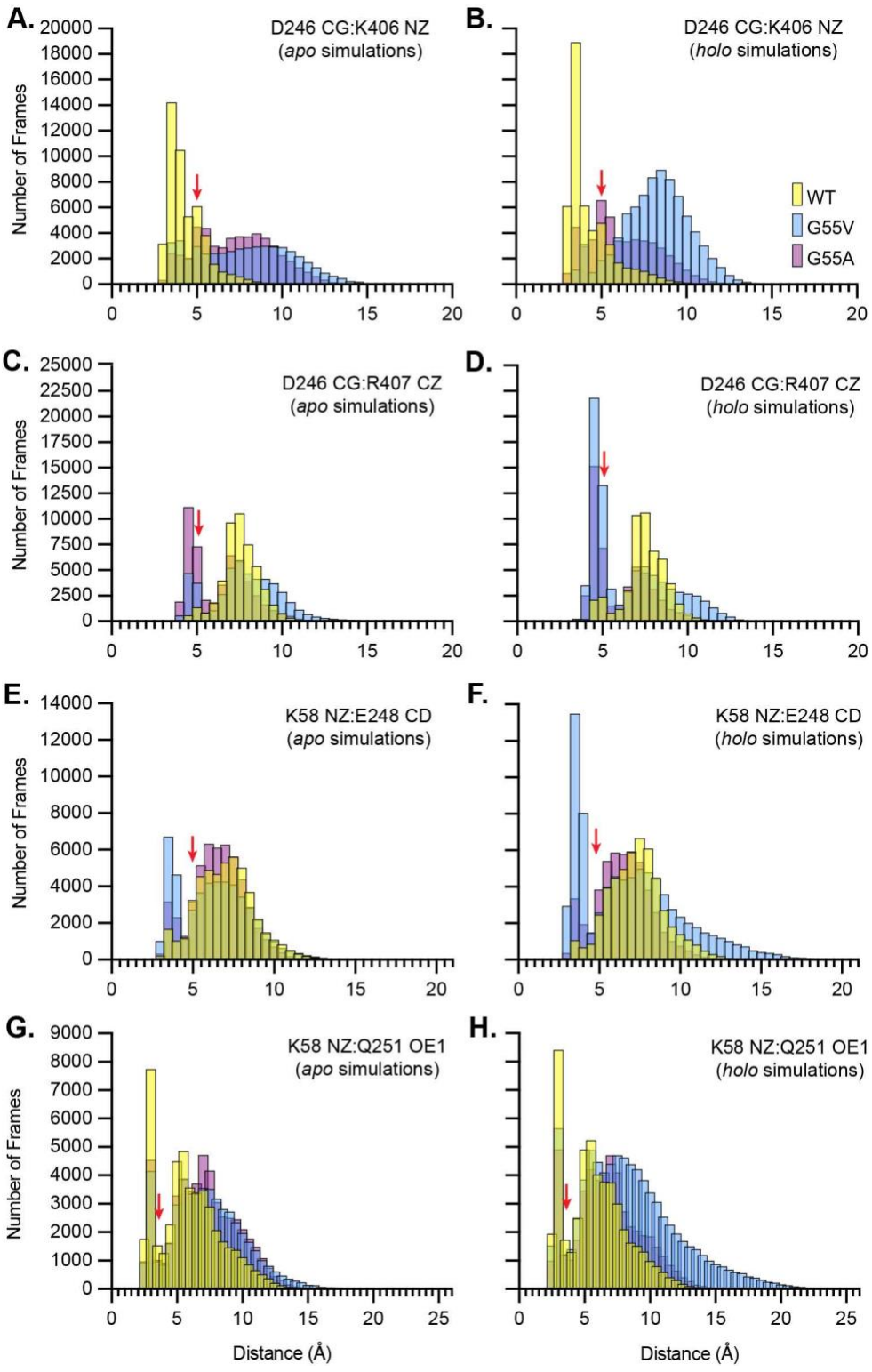

Figure 62. Hxk2^{G55V} promotes domain closure without glucose present.

(A-H) Distribution of distances between indicated residue sidechain atom-pairs as frequency histograms. We assumed a residue sidechain interaction occurred if the distances were ≤ 5.0 Å for salt bridge interactions (A-F) and ≤ 3.5 Å for

hydrogen bonds (G-H). See Materials and Methods for more information. Red arrows above each graph indicate these cutoffs.

4.2.7 Impact on stability of the enzymatic cleft and distant regions

From our analyses, the impact of G55V on local dynamics appeared to propagate and affect stability in other areas of Hxk2 (Figure 59, Figure 60). During the *apo* simulations (Figure 59A, Figure 60C), the mutation increased the flexibility of several loops and α-helices throughout the small subdomain, including the active site mobile loop (E168-V188) that includes the glucose binding residues T175 and K176. It is possible that a less stable small subdomain may contribute to the G55V variant's propensity to adopt a semi-closed conformation, possibly due to subtle but rapid conformational changes. Simulations of the *holo* systems demonstrated more pronounced changes in protein flexibility, specifically at enzymatic cleft-lining residues. For example, G55V increased the flexibility of the highly conserved β9/β10 hairpin, which lines the enzymatic cleft and houses an ATP binding residue (T234) (Figure 59B, Figure 60D). Additionally, the active site mobile loop containing the T175 and K176 glucose binding residues, dramatically increased flexibility in the glucose-bound simulations (Figure 59B, Figure 60D). In fact, during the *holo* G55V simulations, this loop flipped away from the catalytic pocket (~530 ns into simulation 2), disrupting the interactions of T175 and K176 with glucose. However, this event did not lead to the glucose dissociation event discussed above (see Table 12). Finally, a partial helical region (P114-T120) adjacent to the active site mobile loop was notably more flexible in the G55V *holo* simulations, and its instability may have contributed to the dissociating mobile loop region (Figure 59B, Figure 60D). Though G55A similarly causes rearrangement of local tertiary structures like G55V, we did not observe substantial changes in flexibility in either the *apo* or *holo* simulations

(Figure 60A-D). These results collectively illustrate that the G55V mutation affects local structural dynamics, consequently influencing the stability of residues that are crucial for catalysis.

4.2.8 Structurally unstable Hxk2 mutants localize to the nucleus and form intranuclear puncta

Our previous work revealed that Hxk2 accumulates in the nucleus under glucose-starvation conditions [232]. However, the purpose of this change in subcellular localization remains unknown. Our data demonstrate that Hxk2^{G55V} is structurally unstable and has impaired glucose binding. Interestingly, this causes the enzyme to accumulate in the nucleus as if the cells were glucose-starved. Aside from Hxk2^{G55V}, we have found three other mutants that similarly demonstrate constitutive nuclear localization (Hxk2^{T212P}, Hxk2^{K176T}, Hxk2^{D417G}) regardless of the condition tested. Interestingly, all three impact glucose- or ATP-binding residues and so may compromise substrate-binding stability. Given this pattern, we hypothesize that the absence of substrate binding triggers Hxk2 nuclear accumulation in glucose-deficient conditions.

To investigate this hypothesis, we constructed two Hxk2 mutants (Hxk2^{4A} [L23A, I27A, F30A, I33A] and Hxk2^{5A} [L310A, I313A, L314A, L316A, L318A]) with the goal of disrupting two α-helices believed to be crucial for maintaining the structure of the large subdomain (Figure 63E). We found that Hxk2^{4A} confers 2DG resistance and supported growth on glucose-containing medium when expressed in *hxk2*Δ and *hxk1*Δ *hxk2*Δ *glk1*Δ cells, respectively (Figure 63A-D). This observation suggests that Hxk2^{4A} retains the ability to phosphorylate glucose. In contrast, Hxk2^{5A} promotes 2DG resistance when expressed in *hxk2*Δ cells but fails to rescue the growth of *hxk1*Δ *hxk2*Δ *glk1*Δ cells on glucose medium, suggesting impaired catalytic activity (Figure 63A-D). The contrasting results between these two mutants may be attributed to the fact that a mutation within

Hxk2^{5A} (L310A) neighbors conserved residues that impact intra-protein signaling (Figure 58C-D). Conversely, the helix targeted by the mutagenesis in Hxk2^{4A} is not highly conserved and may not play a critical role in residue-residue signaling pathways (Figure 58C-D).

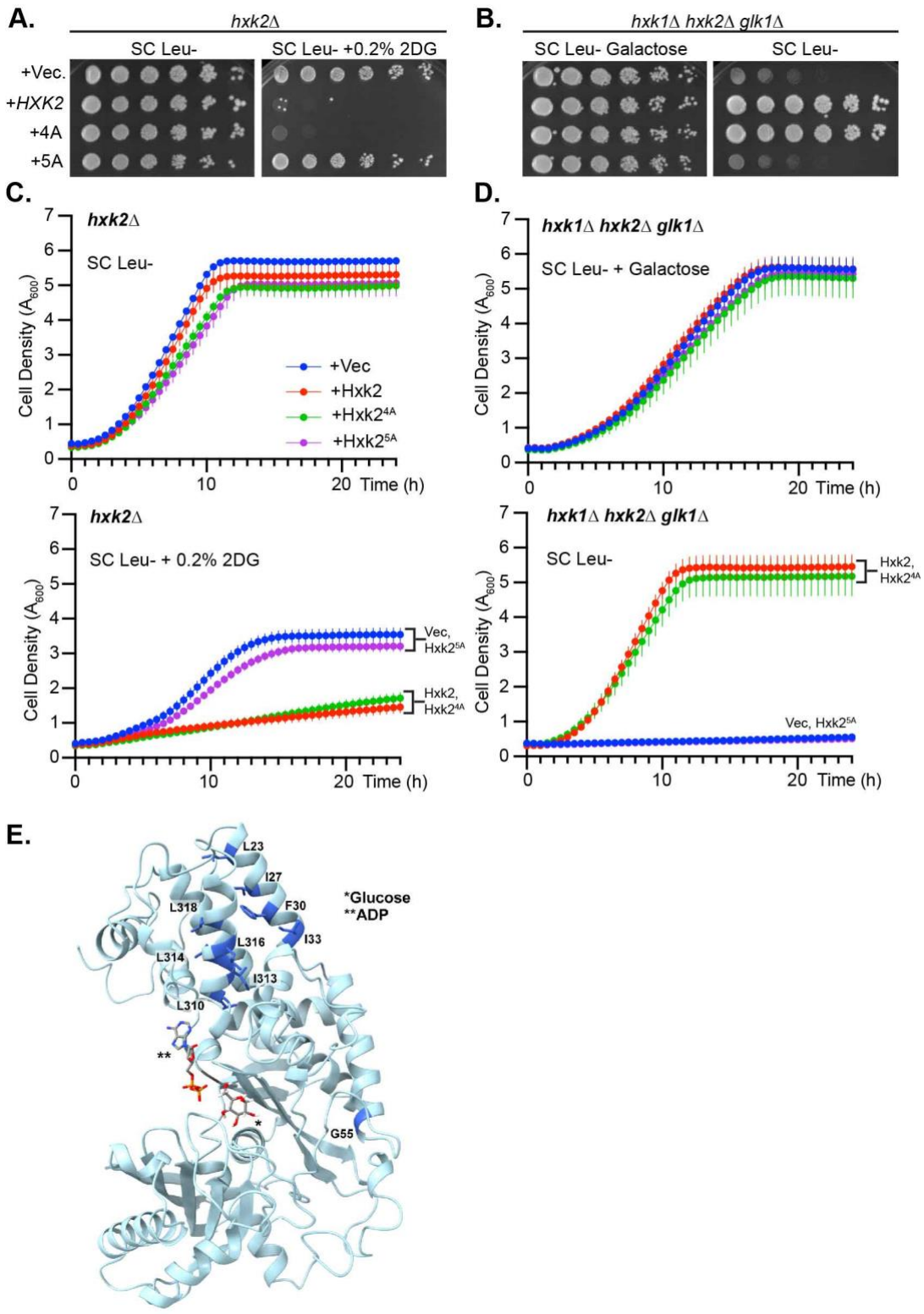

Figure 63. Hxk2^{4A} mutant does not confer 2DG resistance and is catalytically active whereas Hxk2^{5A} confers resistance and is catalyically deficient.

(A and B) Images of serial dilution growth plates of *hxk2*Δ or *hxk1*Δ *hxk2*Δ *glk1*Δ cells containing the indicated plasmid (pRS315-*HXK2pr-HXK2*^{allele}) after three days of growth at 30°C. Media contains 2% glucose (panels A and B, far right) or 2% galactose (panel B, far left), with the addition of 0.2% 2DG where indicated. (C and D) The cell density (A_{600}) changes over time for cells grown in SC Leu-, SC Leu- with 0.2% 2DG, or SC Leu- with 2% galactose are plotted. Curves represent the average A_{600} of three technical replicates, and vertical lines from each data point represent +/- SD, which was sometimes so small that it did not expand beyond the data point itself. (E) *Sc*Hxk2 structure (ribbon) showing the residues (dark blue sticks) that were mutated to construct the Hxk2^{4A} and Hxk2^{5A} mutants. To indicate the location of the glucose and ATP binding sites, we superimposed crystallographic glucose (*) from a *Hs*HK1 structure (PDB 4FPB) and crystallographic ADP (**) from an *Os*Hxk6 (PDB 6JJ8) structure.

To observe the impact of these mutants on Hxk2 nuclear translocation, we next imaged *hxk2*Δ cells expressing GFP-tagged Hxk2^{4A} and Hxk2^{5A}. These experiments revealed a substantial decrease in the abundance of both mutants compared to the wild-type, in high and low glucose conditions (Figure 64A). Automated quantification of the mean whole-cell fluorescence intensity supported this observation (Figure 64D). Nuclear pools of Hxk2^{4A} and Hxk2^{5A} were present in both high and low glucose conditions (Figure 64A). Further, quantifying both mutants revealed an elevated mean nuclear-to-whole-cell fluorescence ratio for both mutants in the tested conditions (Figure 64C). This effect was not evident in the mean nuclear fluorescence quantification alone due to low fluorescence throughout the entire cell (Figure 64B). Consistent with these observations, the full-length protein abundance of Hxk2^{4A} and Hxk2^{5A} was lower than that of the wild-type when expressed in *hxk2*Δ cells grown in abundant glucose (Figure 64E). This disparity was further exacerbated when these cells were incubated in glucose-depleted medium (Figure 64E).

Our imaging showed that both Hxk2^{4A} and Hxk2^{5A} mutants tended to form bright puncta (Figure 64A) that often overlapped with the bright inclusions of our nuclear marker. However, due

to the limitations of our chosen imaging approach, it was challenging to determine whether these were intra- or juxtanuclear puncta. Additionally, we observed some puncta in regions of the cytosol away from the nucleus (Figure 64A). These results suggest that Hxk2^{4A} and Hxk2^{5A} are misfolded and sequestered into distinct cellular compartments depending on their intracellular localization. Once misfolded cytosolic or nuclear proteins segregate, they are susceptible to clearance by protein quality control pathways such as INQ in the nucleus [497–499] or JUNQ and IPOD in the cytosol [500,501]. Hxk2^{4A} and Hxk2^{5A}, and perhaps wild-type, could be substrates for either of these pathways. Future work will attempt to shed light on this interesting possibility.

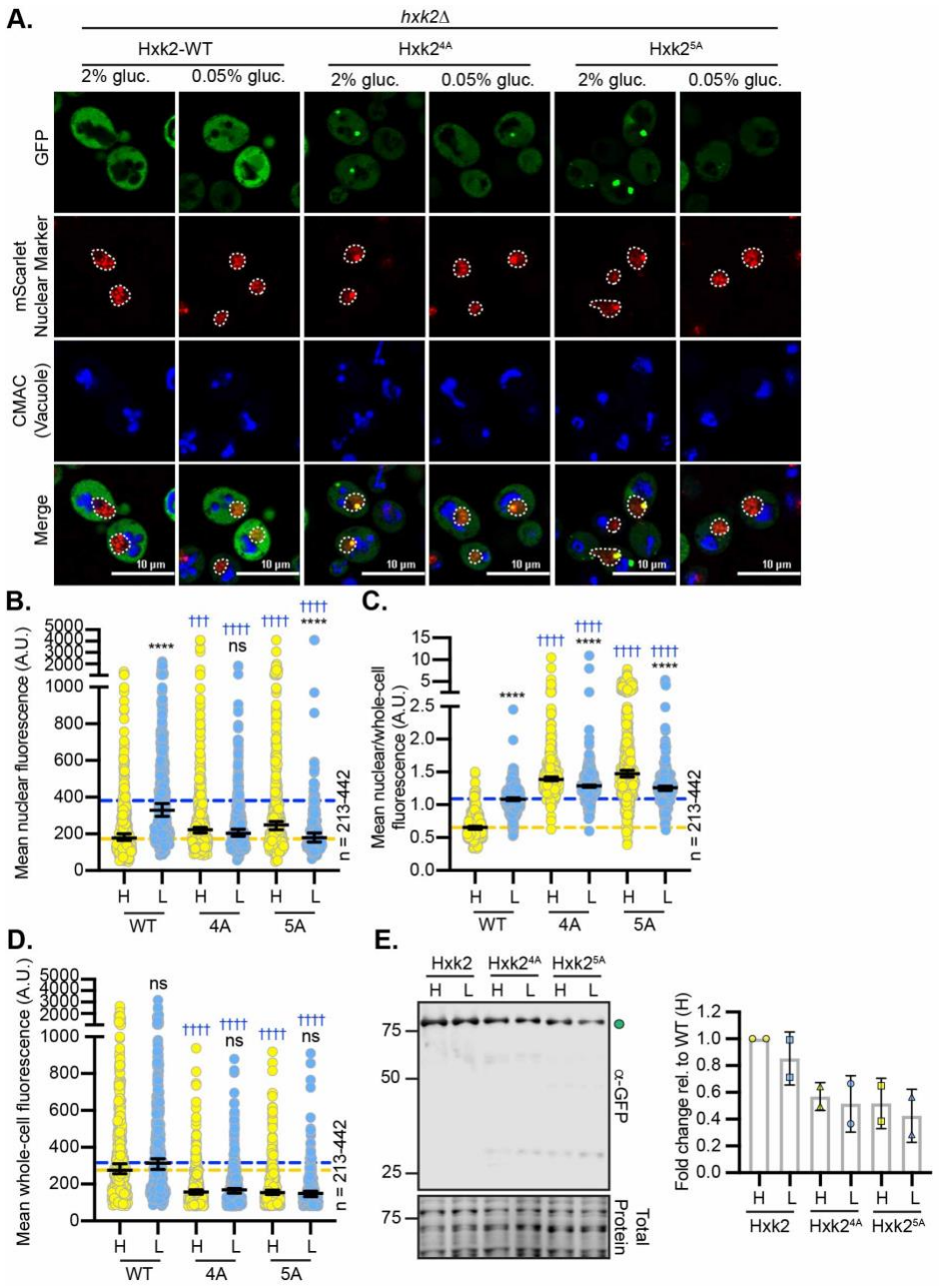

Figure 64. Structurally unstable Hxk2 mutants constitutively localize to the nucleus and form intranuclear puncta.

(A) Confocal microscopy images of GFP-tagged WT Hxk2 and the indicated 2DG-resistance mutants expressed in *hxk2*Δ cells from pRS315-*HXK2pr-HXK2*^{allele} plasmids. Co-localization with the nucleus is determined based on overlap with the Tpa1-mScarlet nuclear marker (dashed white line indicates the nucleus). CMAC stain was used to mark the location of the vacuole. (B-D) Automated quantification (using Nikon.*ai* and GA3 analyses) of the images shown in panel A where (B) shows the mean nuclear fluorescence, (C) shows the mean nuclear fluorescence over the

mean whole-cell fluorescence ratio, and (D) shows the mean whole-cell fluorescence intensity for each Hxk2 variant. Horizontal bars indicate the median, and error bars indicate the 95% confidence interval. Dashed yellow, blue, and purple lines represent the median value for WT Hxk2-GFP cells in high glucose, low glucose, and high glucose with 0.2% 2DG, respectively. Kruskal-Wallis statistical analyses with Dunn's posthoc test were performed to compare the mean nuclear fluorescence, mean nuclear/whole-cell fluorescence ratio, and mean whole-cell fluorescence intensities between high and low glucose, and high glucose with 0.2% 2DG conditions. Black asterisks represent statistical comparisons between low and high glucose for a specific *HXK2* allele, and blue daggers represent statistical comparisons between mutant alleles and the corresponding wild-type Hxk2 in the same medium condition. (E) Immunoblots showing Hxk2-GFP from whole-cell protein extracts made from cells grown in high glucose or shifted to low glucose for 2 hours. REVERT total protein stain serves as a loading control. Quantification of the full-length Hxk2-GFP signal as shown in panel E for two experimental replicates. The abundance of Hxk2-WT in high glucose conditions was normalized to 1 in each experiment. All other values represent the relative fold change.

4.3 Discussion

2DG presents a promising mechanism of action to inhibit the growth of highly glycolytic cancer cells, including glioblastoma. It has shown limited efficacy in clinical trials [322,330,337,338], and resistance to 2DG has been observed in cancer cells [327,354,355,358], confounding its potential as a cancer treatment. Still, 2DG derivatives remain in development, such as an acetylated pro-drug of 2DG that recently received the FDA's Orphan Drug designation for use against glioblastoma multiforme [342]. This designation has renewed interest in understanding how cancer cells respond and acquire resistance to 2DG.

In the present work, we examined all Hxk2 mutations linked to 2DG resistance and sought to define the structural changes that can cause 2DG resistance. Taken together, our data support a model where complete loss of Hxk2 activity is not required to generate 2DG resistance, which is

consistent with earlier studies [224,227,287]. Indeed, most of the mutants tested here demonstrate at least some retained catalytic activity, evidenced by the fact that five of the six mutants that confer resistance were still able to support growth of *hxk1*Δ *hxk2*Δ *glk1*Δ cells on glucose. In most cases, glucose growth of these Hxk2 mutants (i.e., Hxk2^{G55V}, Hxk2^{D417G}, Hxk2^{G238V}, Hxk2^{T212P}, Hxk2^{Q299H}, Hxk2$^{T75I/S345P}$) was equivalent to that observed when WT Hxk2 was similarly expressed. This finding was somewhat unexpected, as our previous *in vitro* hexokinase enzymatic assays using whole-cell protein extracts of *hxk1*Δ *hxk2*Δ *glk1*Δ cells revealed that cells expressing Hxk2^{G55V} and Hxk2^{D417G} had very little detectible hexokinase activity [224]. In another study, we demonstrated that Hxk2^{G238V} had reduced but measurable enzymatic activity towards glucose, while it did not detectably phosphorylate 2DG, unlike wild-type [227]. Despite these observations, all three mutants supported robust growth on glucose in the present study. These findings may highlight the fact that very little hexokinase activity is needed *in vivo* to support growth on a rich glucose source, or it could indicate that the enzymatic assays from cell culture are unable to recapitulate what is captured *in vivo*. For example, a mutant version of Hxk2 that confers growth on glucose may be aided by chaperones to fold *in vivo*, yet in the *in vitro* assay, it may become misfolded and lose its function. From a biological standpoint, reduced hexokinase activity may sufficiently limit 2DG phosphorylation while maintaining enough glucose phosphorylation to sustain life, perhaps because 2DG is present at a 10-fold lower concentration than glucose in our growth conditions.

We focused our studies on the Hxk2^{G55V} mutant, as this mutation does not line the catalytic pocket and encodes a minor isopropyl group substitution (G to V) yet imparts robust 2DG resistance. Hxk2^{G55V} is an unstable enzyme, as evidenced by the reduced protein abundance and increase in proteolytic breakdown products in protein extracts from cells expressing this allele.

Hxk2^{G55V} appears thermally unstable because its abundance slightly decreased, and the level of breakdown increased at elevated temperatures (Figure 52C). Hxk2^{G55V} did rescue growth on glucose-containing medium in *hxk1*Δ *hxk2*Δ *glk1*Δ cells, though it was noticeably less efficient than wild-type at 37°C (Figure 52D). These results suggest that Hxk2^{G55V} is structurally unstable or could be unfolding at elevated temperatures. In addition, biochemical analysis demonstrates that G55V elutes as a broad peak from size exclusion chromatography, and this defect is only improved when glucose is added to the preparation. Consistent with this observation, we find that purified recombinant G55V is thermally less stable than WT Hxk2 but becomes more stable with the addition of glucose. Thus, it appears that G55V destabilizes Hxk2, resulting in a hypomorphic mutant that can be stabilized by glucose. This, too, may explain the discrepancy between our *in vivo* studies, where G55V can support growth of cells on glucose when expressed as the only hexokinases, and our *in vitro* studies, where G55V extracts from cells have very little catalytic activity [224]. Our future studies will focus on defining the molecular pathway by which G55V, and possibly other Hxk2 mutants, are degraded in cells.

Our MD simulations suggest that Hxk2^{G55V} impacts large-scale conformational changes via an allosteric mechanism. RoG analyses showed that the mutant is more likely to adopt a closed conformation not typically associated with substrate binding (Figure 56A). This observation suggests Hxk2^{G55V} may benefit survival in the presence of 2DG by impeding its binding and subsequent phosphorylation.

Our RoG analysis suggests we did not capture a fully closed conformation (Figure 56A). Several possibilities could explain this discrepancy. First, classical all-atom MD simulations often struggle to capture conformational changes that occur on longer timescales [502,503]. Proteins can become trapped in local energy minima, requiring the system to overcome substantial energy

barriers to explore different regions of conformational space [502,503]. Enhanced sampling methods such as WESTPA or coarse-grained MD simulations could help overcome these limitations [504,505]. Second, structural studies suggest that ATP binding induces further domain closure, as required to bring the gamma phosphate closer to the C6 glucose hydroxyl group [81]. To capture the full closed conformation, it may be necessary to simulate bound ATP. That said, previous experimental work suggests that the RoG of Hxk2 decreases by 0.96 +/- 0.24 angstroms upon glucose binding alone [99]. In contrast, the RoG of our wild-type simulations decreases by only ~0.3 angstroms. Regardless, future MD studies should investigate the impact of ATP binding on the Hxk2 structure by performing simulations with both glucose and ATP present in the active site.

Hxk2^{G55V} impacts the dynamics of a key molecular "hinge point." All hexokinases have a connecting loop (G55 to E78 in Hxk2) that serves as a junction between the large and small subdomains. Studies of human GCK have shown that this region contributes to the positive cooperativity observed with glucose (i.e., glucose binding to the active site induces the binding of more glucose), suggesting it influences glucose-induced conformational changes. Indeed, mutagenesis of this region decreases the cooperativity between GCK and glucose [88,102]. Here, we present evidence that the connecting loop also dictates a conformational change in Hxk2. In our Hxk2^{G55V} simulations (both *apo* and *holo*), we saw a portion of the connecting loop (G55 to G60) separate from the α5' helix (Supplemental Movies 3 and 4, available in OneDrive link: Supplemental Thesis Movies). This displacement likely resulted from the rearrangement of local non-covalent interactions that maintain the tertiary structure in this region and steric hindrance introduced by the valine sidechain (Figure 61A, B). These results suggest the destabilization of the connecting loop prevents the open conformation, thereby impeding substrate binding.

Hxk2^{G55V} may destabilize glucose binding residues, thus discouraging substrate binding. In the second Hxk2^{G55V} *holo* simulation, we observed the active site mobile loop dissociate from the enzymatic pocket. This region houses two glucose-binding residues, T175 and K176. Because we only captured this event in one of three simulations, it is difficult to interpret whether the dissociation resulted from the mutation. It is interesting to point out that no crystal structure of human GCK to date resolves the region unless glucose is bound to the active site, suggesting that the mobile loop may be disordered but quickly stabilized upon glucose interaction [88,506,507]. Contrary to this observation, in most Hxk2 structures (and in those of other hexokinases in mammals and other yeasts), this region is consistently resolved regardless of substrate interaction with the enzymatic pocket, suggesting this loop may instead be stably associated with the enzymatic cleft [79–89]. Therefore, we cannot decipher if the event observed in our simulations results from the mutation. In the third Hxk2^{G55V} simulation, glucose dissociated from the enzymatic pocket, but its correlation with the disengagement of the mobile loop remains unclear. Still, this interesting observation presents a compelling hypothesis that the mutation may allosterically influence the conformation of important functional sites.

Counter to the long-standing yeast models, our recent study demonstrated that Hxk2 accumulates in the nucleus upon glucose starvation, as has been observed for mammalian cells [64–70,215]. However, the role or purpose of nuclear Hxk2 in yeast remains uncertain. The answer to this question remains to be addressed; however, our studies suggest a new possibility. Many of the 2DG-resistant Hxk2 mutants have increased nuclear propensity (Hxk2^{G55V}, Hxk2^{K176T}, Hxk2^{T212P}, Hxk2^{D417G}), entering the nucleus even in glucose-rich conditions (Figure 50). Since most of these mutants line the Hxk2 catalytic pocket, it led us to posit that perhaps enzymatically non-functional Hxk2 proteins enter the nucleus. There are several ways to lose enzymatic function,

but these mutations can be accompanied by loss of protein stability and misfolding. This is the case for G55V, which is less stable than WT Hxk2 and appears to become misfolded in the absence of glucose. To eliminate misfolded proteins and maintain optimal cellular proteostasis, the cell employs the ubiquitin-proteosome system that degrades these proteins that could harm the cell. The nucleus houses the necessary machinery for proteostasis in this compartment, termed the Nuclear Protein Quality Control pathway (NPQC) [508]. Indeed, the nucleus is rich with proteosomes and contains several ubiquitin-conjugating enzymes that mark misfolded proteins for degradation by NPQC, including San1, Asi1, and Doa10 in yeast [509–513] and UBR1, HUWE1, ZNF598, and UHRF1/2 in mammalian cells [514,515]. There is growing evidence to support the hypothesis that cytosolic proteins are targeted to the nucleus under conditions of impaired protein homeostasis and that critical factors involved with this process are heat shock proteins like Hsp70 chaperones and Hsp40 co-chaperones [498,499,509,516,517]. Of great interest to our future work will be to investigate whether Hxk2 or unstable Hxk2 mutants are substrates for chaperone-mediated nuclear transport and if NPQC pathways are involved in Hxk2 turnover. If so, it would be the newest example of a cytosolic protein entering the nucleus for degradation.

Reports suggest mammalian hexokinases are substrates for protein quality control pathways. For example, the GCK isoform undergoes regulation by the unfolded protein response (UPR) system in pancreatic β-cells, where it is ubiquitinated and degraded by the proteosome upon misfolding [518]. In response to MG132 treatment, GCK forms cytoplasmic aggregates, highlighting its flexibility and susceptibility to misfolding, thereby undermining the need for its control through the UPS system. Though GCK enters the nucleus of pancreatic β-cells and liver hepatocytes when blood glucose levels are low, it is unknown if nuclear degradation pathways regulate GCK turnover. The HK2 isozyme is also found within the mammalian nucleus [64–

66,68,70]. UBR5, a nuclear-localized E3 ubiquitin ligase known for its role in down regulating transcription factors and signaling molecules, was identified as a potential interacting partner with HK2 in the nucleus, suggesting it targets HK2 for degradation there [66]. However, more work is needed to decipher if nuclear degradation pathways regulate hexokinase turnover in mammalian cells. If future studies identify such a pathway in yeast, it would reveal a new pathway through which hexokinases are turned over and could motivate future work in mammalian systems.

Our studies are significant because hexokinases are associated with cancer progression. In the context of the Warburg effect, the HK2 isoform is commonly upregulated to help promote rapid glucose phosphorylation and turnover for energy production, making HK2 an attractive anti-cancer drug target [129,135,137,139,519,520]. Given that Hxk2 and HK2 share remarkable sequence conservation (~33% similarity according to Clustal Omega alignment), we suspect that HK2 mutations similar to those discussed in this work may also help cancer cells evade 2DG toxicity. For four of the 2DG-resistant Hxk2 mutants we characterized here, analogous variants exist in the Catalogue of Somatic Mutations in Cancer (COSMIC) database [472] for human HK2. Specifically, G414D, K173M, and A236S/T in the N-terminal domain are analogous to G418C, K176T, and G238V in yeast. Also, D861Y and A684V in the C-terminal domain are analogous to D417G and G238V in yeast. These human mutations are associated with impaired catalytic activity and were identified in patient tumor samples.

The identification of these analogous disease-linked HK2 mutations raises the question of whether they might also confer resistance to 2DG in cancer cells. While this remains to be defined, there are interesting links between hexokinase activity and 2DG resistance. In 1962, researchers isolated a 2DG-resistant HeLa cell line after prolonged exposure to 2DG [354]. These 2DG-resistant HeLa cells had reduced hexokinase activity towards both glucose and 2DG, suggesting

that these cells may harbor an HK2 loss-of-function mutation. In addition, a pig kidney cell line was isolated with reduced capacity to phosphorylate 2DG, suggesting a possible hexokinase mutation [355]. Taken together, these findings suggest that in mammalian cells, 2DG resistance may similarly arise due to loss of select hexokinase function. Determining whether HK2 mutants confer 2DG resistance in cancer cells is crucial, and further experimentation may reveal variants that predispose tumors to 2DG resistance.

4.4 Materials & Methods

4.4.1 Yeast strains, plasmids, and growth conditions

The yeast strains used in this study are detailed in Table 13. Strains were cultured in either YPD (2% peptone, 1% yeast extract, 2% glucose) or synthetic complete medium (following O'Donnell et al. [476]), which lacked specific amino acids required for plasmid maintenance. Information on the plasmids used here can be found in Table 14. The lithium acetate method [398] was used to introduce plasmids into yeast. In instances where specified, SC medium containing 2% glucose was supplemented with 2DG at the indicated final concentration (% w/v)**,** with 0.2% 2DG used predominantly in this work. A stock solution of 2% w/v 2DG (Sigma-Aldrich, St. Louis, MO) was prepared in water and subsequently filter-sterilized. Unless indicated otherwise, cells were grown at 30°C. For experiments involving glucose depletion, cells were washed into 0.05% glucose medium (referred to as low glucose medium), resuspended in this medium, and subsequently cultured at 30°C for 2 hours. For 2DG treatments (SC with 2% glucose and 0.2%

2DG), a 2% 2DG stock solution was spiked into mid-logarithmic cultures to a final concentration of 0.2%, followed by incubation at 30°C for 2 hours.

Table 13. Yeast strains used in this study.

Strain	Genotype	Source
BY4742	*MAT α his3Δ1 leu2Δ0 lys2Δ0 ura3Δ0*	[477]
AFO3935	*MAT α ura3Δ0 leu2Δ0 his3Δ1 hxk2Δ::KANMX4 TPA1-mScarlet::HYGRO*	[232]
AFO3936	*MAT α ura3Δ0 leu2Δ0 his3Δ1 met15Δ0 hxk1Δ::KAN hxk2Δ::KAN glk1Δ::KAN TPA1-mScarlet::HYGRO*	[232]

Table 14. Plasmids used in this study.

Name	Description	Source
pRS315	CEN *LEU2*	[401]
pRS315-Hxk2-GFP	Genomic clone of *HXK2* with 592 bp upstream of ATG and 373 bp downstream of the stop and a C-terminal fusion to EGFP; CEN *LEU2*	[227]
pRS315-Hxk2^{G55V}-GFP	The pRS315-Hxk2-GFP plasmid listed above had the G55V mutation introduced by site-directed mutagenesis with primers (Fwd: GGAAAAGGTTCTTTCGAAGAAGGGTGGTAACATTC; Rev: CCCTTCTTCGAAAGAACCTTTTCCAATTCGGAAA). CEN *LEU2*	This study.
pRS315-Hxk2^{G418C}-GFP	The pRS315-Hxk2-GFP plasmid listed above had the G418C mutation introduced by site-directed mutagenesis with primers (Fwd: CTGCAGACTGTTCCGTTTACAACAGATACC Rev: GTAAACGGAACAGTCTGCAGCGATGTG). CEN *LEU2*	This study.
pRS315-Hxk2^{D417G}-GFP	The pRS315-Hxk2-GFP plasmid listed above had the D417G mutation introduced by site-directed mutagenesis with primers (Fwd: ATCGCTGCTGGCGGTTCCGTTTACAACAG; Rev: CGGAACCGCCAGCGATGTGACCGGT). CEN *LEU2*	This study.
pRS315-Hxk2^{G238V}-GFP	The pRS315-Hxk2-GFP plasmid listed above had the G238V mutation introduced by site-directed mutagenesis with primers (Fwd: TGGTGTCAATGTCGCTTACTACGATGTTTG; Rev: TAAGCGACATTGACACCAGTACCGAAGATA). CEN *LEU2*	This study.
pRS315-Hxk2^{K176T}-GFP	The pRS315-Hxk2-GFP plasmid listed above had the K176T mutation introduced by site-directed mutagenesis with primers (Fwd: AAGATGGACTACCGGTTTTGATATTCCAAACATT; Rev: CAAAACCGGTAGTCCATCTTTGCAAGATACC). CEN *LEU2*	This study.
pRS315-Hxk2^{Q299H}-GFP	The pRS315-Hxk2-GFP plasmid listed above had the Q299H mutation introduced by site-directed mutagenesis with primers (Fwd: ACCAGGCCAACATACCTTTGAAAAAATGTC; Rev: AAAGGTATGTTGGCCTGGTCTTGGAGATTC). CEN *LEU2*	This study.
pRS315-Hxk2^{T75I,S345P}-GFP	The pRS315-Hxk2-GFP plasmid listed above had the T75I and S345P mutations were introduced by site-directed mutagenesis with primers (Fwd: GATTTCCCAATTGGTAAGGAATCCGGTGA, GACACTCCATACCCAGCCAGAATCGAG; Rev: TCCTTACCAATTGGGAAATCCATAACCCAAC, CTGGGTATGGAGTGTCCATGACGAAAGG). CEN *LEU2*	This study.

pRS315-Hxk2^{T212P}-GFP	The pRS315-Hxk2-GFP plasmid listed above had the T212P mutation introduced by site-directed mutagenesis with primers (Fwd: TTGATAAACGACCCAACCGGTACTTTGGTT; Rev: CCGGTTGGGTCGTTTATCAAAGCAACAA). CEN *LEU2*	This study.
pRS315-Hxk2^{4A}-GFP	The pRS315-Hxk2-GFP plasmid listed above had the L23A, I27A, F30A, and I33A mutations were introduced by site-directed mutagenesis with primers (Fwd: TGTGCCAAAGGAAGCGATGCAACAAGCTGAGAATGCTGAAAAAGCTTTC; Rev: TCAGTTGGAACAGTGAAAGCTTTTTCAGCATTCTCAGCTTGTTGCATCGC). CEN *LEU2*	This study.
pRS315-Hxk2^{5A}-GFP	The pRS315-Hxk2-GFP plasmid listed above had the L310A, I313A, L314A, L316A, and L318A mutations were introduced by site-directed mutagenesis with primers (Fwd: AATGTCTTCTGGTTACTACGCAGGTGAAGCTGCGCGTGCGGCCGCGATGG; Rev: CCTTGTTTGTACATGTCCATCGCGGCCGCACGCGCAGCTTCACCTGCGTA). CEN *LEU2*	This study.

4.4.2 Defining mutant Hxk2 function *in vivo*

To verify that previously reported Hxk2 mutants are the cause of 2DG resistance, we transformed pRS315-based plasmids (CEN; low copy) with either WT or mutant Hxk2s expressed from the Hxk2 promoter (592 bp upstream of ATG) into cells lacking the chromosomal Hxk2 (*hxk2*Δ). We then assessed 2DG sensitivity in two different ways. First, serial dilution growth assays were performed by inoculating yeast cells onto solid agar medium supplemented with specified concentrations of 2DG, followed by incubation at 30°C, in accordance with the procedure described in reference [476]. Cells were cultured to saturation overnight in either YPD or SC medium. Subsequently, the optical density of each culture was measured, and a dilution series was commenced with a cell density of A_{600} = 1.0 (equivalent to 1.0 x 10^7 cells/mL). A series of five-fold serial dilutions was prepared, and cells were pinned onto solid SC medium with or without 2DG (at concentrations of 0.05%, 0.2%, and 0.4%). We compared the growth of mutant-expressing cells to that of *hxk2*Δ cells expressing either an empty vector or complemented with a WT *HXK2*.

We next tested our Hxk2 mutant or control cells using growth curve analysis [484]. Cells were cultured to saturation overnight in SC medium, then washed and transferred into fresh SC medium. Next, cells were inoculated in triplicate into flat-bottom 96-well plates at an initial A_{600} of 0.05, using the specified medium (SC supplemented with varying concentrations of 2DG). 96-well plates were placed in a BioTek Cytation 5 plate reader (BioTek Instruments; Winooski, WT, USA) and subjected to incubation with shaking. Optical density readings were recorded every 30 minutes for a duration of 24 hours using Gen5 software. Optical density values obtained over time were adjusted for path length (to standardize measurements to a 1 cm path length) and are presented accordingly.

Finally, to define the ability of Hxk2 mutants to support growth on glucose, we employed *hxk1*Δ *hxk2*Δ *glk1*Δ cells. We transformed these cells with our pRS315-*HXK2pr-HXK2* expression plasmids and grew transformants on a galactose-containing medium, which does not require hexokinase 2 function. We grew cells to saturation overnight in SC medium supplemented with galactose. Subsequently, the optical density of each culture was measured, and a dilution series was initiated with a cell density of A_{600} = 1.0 (equivalent to 1.0 x 10^7 cells/mL). A series of five-fold serial dilutions was prepared, and cells were pinned onto solid SC medium supplemented with glucose or galactose. We compared the growth of mutant-expressing cells to that of *hxk1*Δ *hxk2*Δ *glk1*Δ cells expressing either an empty vector or complemented with WT *HXK2*. We also evaluated our Hxk2 mutant or control strains using growth curve analysis. Cells were prepared and tested exactly as described in the preceding paragraph in the medium indicated (SC containing glucose or galactose as the carbon source).

4.4.3 Immunoblotting to assess the abundance of Hxk2 mutants

We assessed the abundance of Hxk2 mutants in cells by performing whole-cell protein extractions and SDS-PAGE. The trichloroacetic acid (TCA) method [403] was used to generate whole-cell protein extracts. First, an equivalent density of mid-logarithmic phase cells was collected via centrifugation, washed with water, and reconstituted in a solution comprising 0.25 M sodium hydroxide and 72 mM b-mercaptoethanol. Following incubation on ice, proteins were precipitated using 50% TCA. After an additional incubation period on ice, proteins were pelleted through centrifugation, and the remaining supernatant was discarded. Next, protein pellets were dissolved in 120 µL of sample buffer (40 mM Tris-Cl [pH 8.0], 0.1 mM EDTA, 8 M urea, 5% SDS, 1% b-mercaptoethanol, and 0.01% bromophenol blue). Before being resolved by SDS-PAGE, protein samples were incubated at 37°C for 15 minutes and centrifuged to remove any remaining insoluble material. Proteins were transferred to polyvinylidene difluoride (PVDF) membrane support and probed with an anti-GFP antibody (Santa Cruz Biotechnology, Dallas, TX, USA), followed by goat anti-mouse IRDye 800 (LI-COR Biotechnologies, Lincoln, NB, USA). Antibody complexes were detected using an Odyssey Clx Infrared Imager (LI-COR). REVERT (LI-COR) total protein stain was used as a loading control and to verify successful transfer. Protein bands were quantified using ImageStudio software (LI-COR). In brief, boxes were drawn around each band, and the total pixel intensity was measured. A box was drawn at the membrane periphery to measure background fluorescence, and this value was subtracted from each measurement. The pixel intensities of GFP-containing bands were then adjusted using a correction factor derived from the total pixel intensity of the REVERT total protein stain, ensuring control for loading variability. All resulting values were normalized to the control.

4.4.4 Fluorescence microscopy

Localization of GFP-tagged Hxk2 proteins was detected using confocal fluorescence microscopy. First, saturated overnight cultures grown in SC medium containing 2% glucose were reinoculated into fresh SC medium at an OD_{600} of 0.3. Cells were then allowed to grow at 30°C until they reached mid-logarithmic phase (usually 4-5 hours; OD_{600} ~0.8). For shifts to low glucose (using SC with 0.05% glucose), cells were washed and incubated using the same procedure as detailed earlier. For 2DG treatments, a 2% 2DG stock was spiked into mid-logarithmic yeast cultures, and cells were incubated as described above. Prior to imaging, cells were plated onto 35 mm glass bottom microwell dishes (MatTek Corporation, Ashland, MA) coated with 15 µL (0.2 mg/mL) of concanavalin A (Sigma-Aldrich, St. Louis, MO, USA). Imaging to detect the GFP-tagged Hxk2 proteins was performed using a Nikon Eclipse Ti2 A1R inverted microscope (Nikon, Chiyoda, Tokyo, Japan) equipped with a 100 x oil immersion objective lens (NA 1.49). GaAsP or multi-alkali photomultiplier tube detectors were utilized for image capture, with acquisition controlled by NIS-Elements software (Nikon). Uniform settings were employed for all image acquisitions. Images were uniformly adjusted and cropped utilizing NIS-Elements software.

4.4.5 Image quantification and statistical analyses

We utilized Nikon General Analysis 3 software (Nikon) to quantify nuclear and whole-cell fluorescence intensities, incorporating segmentation facilitated by NIS-Elements.*ai* (Artificial Intelligence) software (Nikon). Whole-cell fluorescence quantification involved training NIS.ai software on a reference dataset of samples, manually segmented based on DIC channel images. The NIS.*ai* software underwent iterative training until it achieved a training loss threshold of

<0.02, a value that indicates excellent agreement between the output produced by the software and the initial ground truth. To ascertain the mean nuclear fluorescence, the NIS.*ai* software was trained to utilize a chromosomally tagged Tpa1-mScarlet nuclear marker, with training based on manually defined nuclear segmentations. Confocal microscopy images were segmented into individual whole-cell and nuclear objects using General Analysis 3 software, using the DIC and 561 nm (mScarlet) channels. A parent-child relationship was established to align individual nuclear objects (child) with their appropriate whole-cell (parent) and consolidate them as single objects. Incomplete cells at the edge of an image were excluded along with their child objects. Mean whole-cell or mean nuclear fluorescence intensities for each parent or child object were determined in the GFP (488 nm) channel. All imaging quantification in this study adhered to this methodology.

Prism (GraphPad Software, San Diego, CA) was used to carry out all statistical analyses of the resulting fluorescence quantification. Kruskal-Wallis statistical tests were conducted, followed by Dunn's post hoc correction for multiple comparisons. Significant p-values from these analyses are denoted as * p-value<0.1, ** p-value<0.01, *** p-value<0.001, and **** p-value<0.0001, while non-significant results (p-value>0.1) were labeled as "ns". In cases involving multiple comparisons, the † symbol might substitute * to signify the same p-values relative to a different reference sample (refer to the figure legends for details).

4.4.6 Molecular dynamics simulations

Molecular dynamics (MD) simulations of six systems were performed: 1) *apo* Hxk2-WT, 2) *holo* Hxk2-WT, 3) *apo* Hxk2^{G55V}, 4) *holo* Hxk2^{G55V}, 5) *apo* Hxk2^{G55A}, and 6) *holo* Hxk2^{G55A} systems. In this work, a homology model structure of monomeric Hxk2 we constructed previously

[232] was used. The G55V and G55A mutations were introduced to the Hxk2 structure using the rotamers tool in ChimeraX [521]. For each simulation, we used tleap (AmberTools18 [421]) to solvate the protein in a 10 $Å^3$ water box. Na+ ions were introduced to neutralize negative charges and maintain electrical neutrality. Further Na+ and Cl- ions were added to approximate a 150 mM solution. Parameterization of protein, counter ions, water molecules, and glucose molecules was carried out using the Amber ff14SB, TIP3P, and GLYCAM_06j-1 force fields, respectively.

To alleviate artificial steric clashes, four rounds of minimization were conducted by employing the Amber MD engine [422,423]. First, all hydrogen atoms underwent minimization for 5,000 steps. Second, both hydrogen atoms and water molecules were minimized for 5,000 steps. Third, all hydrogen atoms, water molecules, and protein side chains were minimized for 5,000 steps. Finally, all atoms within each system underwent minimization for 10,000 steps.

Following minimization, we equilibrated each system using three rounds of simulation. Initially, a brief simulation in the canonical ensemble (NVT, total duration of 0.02 ns) was conducted, with a restraining force of 1.0 kcal/mol/$Å^2$ applied to the backbone atoms. Using the same backbone restraints, we continued the simulation in the isothermal-isobaric ensemble (NPT, 1 atm, total duration of 1.0 ns). Finally, equilibration (NPT, 1 atm, total duration of 1.0 ns) was completed without any restraints. Throughout each phase, a timestep of 2 fs and a temperature of 310 K were maintained.

Finally, we ran three isothermal-isobaric (NPT, 310 K, 1 atm) productive simulations of the *apo* Hxk2-WT, *holo* Hxk2-WT, *apo* $Hxk2^{G55V}$, *holo* $Hxk2^{G55V}$, *apo* $Hxk2^{G55A}$, and *holo* $Hxk2^{G55A}$ (250 ns, 250 ns, and 500 ns for each system, with the exception of the *holo* Hxk2-G55V system) systems. Minimization and equilibration steps were performed before each triplicate simulation; therefore, each simulation began with a different initial conformation.

4.4.7 Confirming full equilibration of simulations

For each individual simulation, trajectory frames extracted every 20 ps were aligned to their respective first frame using their backbone heavy atoms. MDAnalysis (V 1.0.0) [489] was used to calculate the RMSD of the residue backbone heavy atoms. The N-terminal tail (residues V2-A17) was excluded from these analyses because it is highly dynamic (disordered) in the monomeric form, which could overshadow the contributions of other regions to the RMSD. Upon plotting the resulting eighteen sets of RMSD values against simulation time, it became evident that the simulations did not achieve full equilibration before the commencement of production runs. Consequently, we discarded the initial 10 ns, pre-equilibrated segments from each simulation, focusing solely on the equilibrated section of the productive runs for all subsequent analyses. Throughout this process, a 20 ps stride and backbone alignment were maintained consistently.

4.4.8 Root-mean-square fluctuation (RMSF) analyses

We used MDAnalysis [489] to assess the flexibility of each amino acid and calculated the RMSF values of each residue's center of geometry. We performed this analysis taking frames every 20 ps.

4.4.9 Atom-atom distances

We used VMD [415] to calculate the distance between select atoms in frames taken every 20 ps of the simulation. For all salt bridges (D246 CG:K406 NZ, D246 CG:R407 CZ, and K58 NZ:E248 CD), we assumed two atoms were interacting if the distance between them was ≤ 5.0 Å.

We chose this cutoff rather than ≤ 4 Å for a typical salt bridge because we measured from the terminal carbon (CZ) in the bulky R407 sidechain. All other residue pairs were given the same cutoff for fair comparison. For the K58 NZ:Q251 OE1 hydrogen bond, we assumed the two atoms were interacting if the distance between them was ≤ 3.5 Å.

4.4.10 Dynamic cross-correlation (DCC) analysis

Using MD-TASK [490], we calculated the DCC values of every residue-residue pair and plotted the resulting NxN matrices. A DCC value quantifies the extent to which the motions of a specific pair of Cα atoms are correlated (where a value of 1 signifies perfect correlation and -1 indicates anti-correlation). The matrices are calculated according to the following expression:

$$C_{ij} = \frac{(\Delta r_i \cdot \Delta r_j)}{\sqrt{\langle \Delta r_i^2 \rangle} \cdot \sqrt{\langle \Delta r_j^2 \rangle}}$$

where Δr_i represents the displacement of atom i from its average position and ⟨⟩ denotes time averages across the entire trajectory (with frames extracted every 20 ps).

4.4.11 Betweenness centrality

We calculated per-residue BC values in simulation frames extracted every 20 ps using MD-TASK [490]. Briefly, protein conformations are represented as graph nodes and edges. The nodes (n_i) are the amino acid Cβ atoms (Cα in the case of glycine), and the edges ($e_{i,j}$) connect any two nodes ($\underline{n_i}$ and n_j) within a specified cutoff distance (6.7 Å). By considering all node pairs, a comprehensive set of shortest paths is established. The BC value assigned to a node corresponds to the count of shortest paths that pass through that particular node. This calculation was performed

on conformations extracted every 1000 frames from each MD simulation. To accommodate protein dynamics, time-averaged BC values per residue, denoted as $\langle BC_i \rangle$, were calculated for each simulation *i*. Changes in $\langle BC_i \rangle$ between systems were then evaluated. Furthermore, all BC data were normalized relative to each simulation's maximum value. The resulting data are depicted in Figure 58.

4.4.12 Radius of gyration

To evaluate the dynamics of the small and large subdomains' opening and closing, we used MDAnalysis [489] to calculate the protein RoG in simulation frames extracted every 20 ps. The N-terminal tail (residues V2-A17) was excluded from these analyses because it exhibits high disorder in the monomeric form, potentially masking the contributions of the remaining protein to the RoG.

4.4.13 Molecular visualization

Movies and images were generated using VMD [415] and ChimeraX [521], respectively.

5.0 Conclusions and future directions

In the following section, I have summarized how my research advances the understanding of the regulatory mechanisms governing hexokinase nuclear translocation in yeast and describe the structural and conformational features that govern hexokinase-mediated resistance to 2DG. Additionally, I discuss various questions that arise from this work and suggest potential directions for future research in these areas.

5.1 Significance of these studies

5.1.1 Major Conclusions

We re-visited a long-standing model defining the regulation and function of Hxk2 nuclear shuttling in yeast. We demonstrate that almost all aspects of the old model are incorrect and propose a new model explaining the *cis* and *trans* regulatory elements that control the starvation-induced nuclear accumulation of Hxk2. Using high-resolution quantitative fluorescence microscopy, we demonstrate that Hxk2 is excluded from the nucleus when cells are glucose-fed and accumulates in the nucleus under glucose starvation conditions. These observations are in line with the trend of nuclear accumulation seen in mammalian cells but contradict two decades of work defining a previously established model of Hxk2 nuclear shuttling. The major tenets of the old model are summarized in section 1.2.3.3 and so we will not belabor the differences here but will rather focus on summarizing our new findings. Previous work proposed that Hxk2 nuclear

shuttling requires an NLS sequence in the N-terminal tail located between K6 and K13. We found that this site does not function as an NLS as previously assumed. Instead, it plays a crucial role in facilitating the glucose-dependent nuclear exclusion of Hxk2 and promoting its dimerization. Specifically, we pinpointed K13 as essential for both the glucose-dependent nuclear exclusion of Hxk2 and its dimerization. Additionally, we made a mutation of D106, the residue responsible for forming a salt bridge with K13 at the Hxk2 dimer interface. The Hxk2^{D106A} mutant prevented Hxk2 dimerization but retained normal nuclear-cytosolic partitioning. This implies that simply breaking the Hxk2 dimer is not sufficient to induce nuclear translocation and supports a model where a post-translation modification or other aspect of K13 is required for glucose-dependent regulation of Hxk2 nuclear accumulation. Consistent with many past studies, we found that though S15 phosphorylation is required for regulating the Hxk2 dimer-to-monomer transition, it is dispensable for regulating nuclear shuttling. Our results suggest that dimerization is important for the overall nuclear shuttling mechanism, but an additional input is required to induce nuclear accumulation. Interestingly, we identified Tda1, a NUAK family kinase and major S15-phosphorylating enzyme that controls Hxk2 dimer-monomer propensity, as indispensable for starvation-induced nuclear accumulation of Hxk2. To the best of our knowledge, this implicates a new role for NUAK family kinases in regulating the subcellular distribution of metabolic enzymes. Interestingly, both S15D and K13A mutations, which prevent dimer formation, overcome the nuclear shuttling defect in *tda1*Δ cells. This suggests that Tda1's role in inducing Hxk2 nuclear accumulation is partially through promoting dimer dissociation. Snf1 and Mig1 were dispensable for Hxk2 nuclear shuttling, also contradicting previous work. Finally, we used RNAseq analyses to demonstrate that deletion of the *HXK2* gene does not affect global transcriptional profiles, refuting the idea that

Hxk2 controls transcription in the nucleus. These studies reveal a new mechanism for Hxk2 nuclear shuttling and open the door to future studies deciphering the role of Hxk2 in the nucleus.

Using lab evolution and whole-genome sequencing, we identified a novel mutation in the yeast *HXK2* gene ($Hxk2^{G238V}$) that confers resistance to 2DG. We showed this allele is sufficient alone to confer 2DG resistance when expressed in *hxk2*Δ cells. Our western blot and phenotypic analyses demonstrate that $Hxk2^{G238V}$ encodes a stable protein product. By expressing $Hxk2^{G238V}$ in a *hxk1*Δ *hxk2*Δ *glk1*Δ strain, we demonstrated that it can phosphorylate glucose to some degree as it permits growth on glucose in these cells that lack any other hexokinase activity. We also grew these cells on galactose-containing medium with added 2DG, making it the only available substrate for hexokinases. This experiment showed that $Hxk2^{G238V}$ can still phosphorylate 2DG to some extent but still confers less sensitivity than cells expressing wild-type Hxk2. Our kinetic analyses also showed decreased activity of this mutant toward glucose and 2DG. The altered residue is located on a highly conserved central β-hairpin structure but does not line the catalytic pocket or interact directly with substrates. Yet $Hxk2^{G238V}$ has higher K_m values toward glucose and 2DG. We wondered if the mutation could impair substrate binding by impacting Hxk2 structural dynamics. Using MD simulations, we showed that $Hxk2^{G238V}$ influences Hxk2 structure and conformations through an allosteric mechanism. First, the mutant alters the flexibility of the enzymatic cleft, which could increase the entropic penalty of substrate binding. Second, $Hxk2^{G238V}$ affects the conformational changes of a neighboring residue on the β-hairpin (V236) that may be required to facilitate domain closures required for catalysis. Third, the mutation impacts the dynamics of the D211 catalytic residue that often points away from the catalytic cleft and therefore makes it unable to engage the incoming glucose molecule. Finally, the sum of these structural changes promotes changes in large-scale domain closures required for substrate binding. Our

simulations showed the Hxk2^{G238V} mutant interferes with domain closure by promoting the enzyme to adopt a semi-closed conformation rendering the protein less able to bind substrates. These studies present the first atomic-resolution model describing how Hxk2 mutations confer 2DG resistance.

Through lab evolution and genetic screens to isolate spontaneous 2DG-resistant mutants, we identified many loss-of-function Hxk2 mutations (Hxk2^{G55V}, Hxk2^{G238V}, Hxk2^{D417G}, and Hxk2^{R423T}), emphasizing the importance of hexokinase activity as a key regulatory point in 2DG toxicity [224,227,287]. However, a handful of mutations were discovered by another group in yeast 2DG screens designed to identify genetic variants that increased the expression of the DOG phosphatases. Only *HXK2* and *REG1* genes were sequenced in resistant cells that increased *DOG1* and *DOG2* expression [287]. Without whole-genome sequencing, it is not clear whether the observed resistance phenotype was largely due to the Hxk2 mutations identified here or other mutagenic events. This highlighted a need for our studies, where we performed a comprehensive follow-up study to confirm the causal relationship of each Hxk2 mutant and 2DG resistance. We confirmed that 6 of 8 mutations tested were sufficient to confer 2DG resistance when expressed alone in *hxk2*Δ cells. Our phenotypic analyses suggest that most of the Hxk2 mutations retain some level of enzymatic activity, contrary to our initial belief that all such mutations abolish catalytic activity completely. These results highlight a dichotomy the cell reaches where they reduce hexokinase activity to limit 2DG phosphorylation, but also retain enough glucose phosphorylation to sustain life.

Like the Hxk2^{G238V} mutant, we observed that another mutation (Hxk2^{G55V}), altered a residue far from the Hxk2 enzymatic pocket. Our biochemical and phenotypic analyses suggest Hxk2^{G55V} may be somewhat unstable. We performed MD simulations to assess the impact of this

mutation on Hxk2 structural dynamics and stability. We found Hxk2^{G55V} affected substrate-dependent domain closures and forced the enzyme to remain in the closed conformation even in the *holo* simulations. The mutation caused the dissociation of the active site loop containing glucose binding residues from the enzymatic cleft, an event that would likely promote substrate dissociation. RMSF analyses revealed Hxk2^{G55V} increased the flexibility of neighboring regions. This was caused by the disruption of salt bridge networks, which destabilized local tertiary structures. Specifically, Hxk2^{G55V} disrupted the stability of the connecting loop which is a region that connects the small and large subdomains and has been shown to regulate the domain closures of mammalian GCK [88,102]. This likely promotes the large-scale changes on enzyme conformation we observed here. These findings suggest that Hxk2^{G55V} allosterically impacts the conformation of functionally critical sites.

Our confocal microscopy experiments revealed a subset of resistance-conferring Hxk2 mutations with altered nuclear propensity compared to wild-type. The most common phenotype was constitutive nuclear localization regardless of glucose availability and this trend was typically seen in mutants that affected glucose or ATP binding sites (Hxk2^{K176T}, Hxk2^{T212P}, Hxk2^{D417G}). However, unlike these other mutants that increase nuclear localization, the Hxk2^{G55V} mutant is not close to the catalytic pocket, yet it too drives constitutive nuclear localization. In addition, we found that G55V mutant encodes an unstable protein product with reduced capacity to phosphorylate glucose. Given that *hxk2*Δ cells are also resistant to 2DG, it is not so surprising that a mutation that produces an unfolded, hypomorph of Hxk2 would similarly give rise to 2Dg resistance. Based on these findings we posit that reduced substrate binding or structural instability (in the case of Hxk2^{G55V}) may trigger nuclear accumulation of Hxk2. To confirm this trend, we further assessed two highly unstable Hxk2 mutants (Hxk2^{4A} and Hxk2^{5A}) that disrupt structurally

critical α-helices in the large subdomain of Hxk2 (Figure 61E). Fluorescence microscopy of these mutants revealed that 4A and 5A mutants; 1) accumulated in the nucleus in glucose-rich and glucose-depleted conditions, 2) had decreased whole-cell abundance, and 3) formed aggregates either in the cytosol and the nucleus, some of which were very large. Interestingly, the nuclear aggregates often formed adjacent to the vacuole that were reminiscent of those formed by a newly described nuclear protein quality control pathway [499]. Defining how nuclear translocation of Hxk2 is regulated and the role of this transition in Hxk2 biological function is a long-term goal of the O'Donnell lab. The fact that misfolded mutants of Hxk2 access the nucleus, irrespective of growth medium conditions, leads us to the hypothesis that Hxk2 mutants may enter the nucleus to be degraded by protein quality control machinery. This will be tested further in the lab, beyond the completion of my degree.

5.1.2 Limitations of these studies

Though the results discussed here advance our understanding of cellular resistance mechanisms to 2DG and define the regulatory components surrounding Hxk2 nuclear shuttling, there remain some limitations that must be considered. Though our studies thoroughly demonstrate the accumulation of Hxk2 pools inside the nucleus upon energy stress, we sought to provide evidence this was in fact due to the accumulation of the full-length Hxk2-GFP constructs used in these studies and not just free GFP. Indeed, our FRAP and media shift time course analyses showed a slow and regulated accumulation of Hxk2-GFP in the nucleus whereas free GFP diffuses freely and recovers in the nucleus almost instantly (Figure 10D). It would prove beneficial to verify by western blot that the nuclear Hxk2 pools represent full-length protein on top of these analyses. Indeed, we attempted a nuclear fractionation protocol, developed by Keogh et al. [522], to address

this very question. However, we quickly found that like all other yeast nuclear fractionation protocols available, this method proved unreliable for our applications. Nuclear fractionation of yeast requires zymolyase digestion of the cell wall before lysis and this induces a stress response in yeast [523]. Consistent with this, nuclear shuttling of Hxk2 was always induced and we would detect full-length Hxk2-GFP in the nuclear fraction regardless of glucose availability (unpublished observations). We tried to overcome this by adding glucose to the zymolyase digest buffer, but we found that glucose inhibited zymolyase activity (unpublished observations). Though nuclear fractionation could not be used to verify the presence of full-length nuclear Hxk2-GFP, our FRAP and media shift timecourse assays demonstrated nuclear diffusion properties that differed significantly from free GFP, suggesting that they represent the full length Hxk2-GFP protein.

Another important caveat is ours and others' methods that isolated 2DG resistance-conferring mutations in Hxk2 were performed using haploid yeast cells [224,227,287]. As such, Hxk2 mutations conferring 2DG resistance have only been isolated in haploid yeast, suggesting they do not confer a growth advantage in diploid cells that would become heterozygous at the *HXK2* locus. Indeed, for diploid yeast, it appears that they obtain 2DG resistance through other strategies, independent of altering Hxk2 activity, that involve the use of large-scale chromosomal rearrangements and aneuploidy [307]. It is likely that human cells gain resistance through similar means, rather than by mutations in hexokinase. In diploids, upregulation of the hexose transporters (HXTs) or the DOG phosphatases, which counter Hxk2's activity, were defined as causing 2DG resistance [307]. These findings may impact the importance of hexokinases in modulating 2DG toxicity in human cancers as they are already prone to genome rearrangements and instability as they respond to changing tumor environments and pressures [524,525]. These experiments may

reveal that hexokinase loss-of-function mutants would only confer resistance in homozygous individuals.

Another shortcoming of these studies is Hxk2 is expressed so abundantly in the cell. This made it difficult to detect protein abundance changes in our western blot analyses. An issue we encountered is the Hxk2-GFP band intensities often reached saturation making it difficult to observe expected protein abundance changes in our quantification. To counteract this, we performed a titration of our whole-cell protein extracts and found we needed to load $1/15^{th}$ the original concentration of protein to have Hxk2-GFP band intensities lie within the linear range of detection for the LiCOR-Clx Odessey scanner we used. A related caveat, is that our experiments in Figures 8 and 9, suggest that though in our plasmid-borne system we express Hxk2 from its native promoter, we are still driving greater expression of Hxk2-GFP that we would observe from the chromosomal locus. From these experiments, it was clear that nuclear fluorescence of an endogenous mNG-tagged Hxk2 in low glucose conditions reached only ~15% that of the plasmid-expressed Hxk2-GFP construct. Still, this comparison involves two distinct fluorophores, and there may be additional factors beyond just protein expression that could contribute to differences in fluorescence. For example, is there equal signal intensity between the two? Do the fluorescent tags fold equivalently? Is the RNA equally stable? None of our data rule out the possibility that a small fraction of Hxk2 accumulates in the nucleus in high glucose conditions, but that this still doubles in response to low glucose conditions. This would suggest nuclear shuttling still occurs at basal levels in high glucose conditions and this is greatly amplified in low glucose. Therefore, in future studies we should consider the use of endogenously tagged Hxk2 and Hxk2 mutants.

An additional consideration is we currently do not know if post-translational modifications are associated with inducing Hxk2 nuclear shuttling. We showed that though phosphorylation at

S15 is important in regulating dimer-to-monomer transition, it does not influence Hxk2 nuclear shuttling in low glucose, contrasting earlier reports. These results suggested another input was required to induce nuclear shuttling. We found that the N-terminal tail and specifically K13 was required to maintain glucose-dependent nuclear exclusion of Hxk2. We also made a mutation to D106, a residue that forms a salt bridge with K13 at the Hxk2 dimer interface. The D106A mutant maintained normal Hxk2 nuclear-cytosolic shuttling regulation but could not form dimers *in vivo*. These results suggest that K13 does not regulate Hxk2 through its role in stabilizing the dimer interface. Interestingly, K13 is reported to be sumoylated or dimethylated in Hxk2 but ubiquitinated in Hxk1 which shares 100% sequence homology at the N-terminal tail with Hxk2. Our results would suggest that the absence of a post-translational modification or another aspect of K13 is required for the glucose-dependent regulation of Hxk2 nuclear propensity. As Hxk2 is modified at this site and many others, it would prove beneficial to perform mass spectrometry to identify if any sites are differentially modified between high and low glucose conditions.

Hxk1 and Hxk2 are closely related paralogs and share remarkable amino acid sequence identity (77%) and similarity (89%). However, as discussed in Chapter 2, we do not detect Hxk1 nuclear accumulation. The N-terminal tail that seems to be critical for regulating Hxk2 nuclear localization is 100% conserved in Hxk1. To determine if this region is also important for its nuclear exclusion (Chapter 2, Figure 23), we made analogous Hxk1 N-terminal tail mutations to those studied in Hxk2. To our surprise, none of the Hxk1 mutants tested accumulated in the nucleus in glucose-fed or -starved conditions. With these findings, a question for future work is what differences between the Hxk1 and Hxk2 paralogs make them behave so differently? One key difference could lie within their post-translational modifications. Interestingly, both enzymes are identically modified at the N-terminal tail with one exception. For Hxk2, K13 is believed to be

sumoylated or dimethylated while the same residue on Hxk1 is believed to be sumoylated or ubiquitinated [375,377]. Whether ubiquitination at this site explains the nuclear exclusion of Hxk1 is unknown. However, if this were the case, then mutation of the K13 residue (Figure 23) would have induced nuclear localization of Hxk1. It is likely that regions of sequence variability and differences in post-translational modifications explain the discrepancy in nuclear localization between Hxk1 and Hxk2. While Hxk1 and Hxk2 share high sequence similarity and exhibit common modifications at analogous sites, both enzymes show variability at several surface-exposed residues and are reported to have unique modifications from each other [249,375,377,381–383,526,527]. As an example, Hxk1 is reported to be sumoylated at the surface-exposed K148, whereas the corresponding residue on Hxk2 is a serine and is not reported to be modified [375]. Whether such differences in sequence and sites of modification explain the discrepancy between Hxk1 and Hxk2 will be an important question to address in future work.

From our computational results, our MD simulations did not capture the fully closed conformation of Hxk2 (Figure 54). This observation likely points to a classic shortcoming of MD in that some protein conformations occur on timescales that are currently inaccessible. To overcome this, we would need to extend our simulations or use alternative methods that allow us to accelerate the exploration of conformational space. Fortunately, we could utilize weighted ensemble (WE) path sampling approaches including WESTPA (WE Simulation Toolkit with Parallelization and Analysis) to generate pathways for long-timescale processes like Hxk2 conformation changes [504]. We have recently used WESTPA to simulate Hxk2 conformation change and captured a wider range of conformations relative to traditional MD simulations, including those more reminiscent of closed conformation crystal structures (3O8M, [528]). We

will likely use this method in future investigations studying glucose-induced conformation change in hexokinases.

The MD simulations discussed in Chapters 3 and 4 presented a model for how the Hxk2^{G238V} and Hxk2^{G55V} alleles may impact enzymatic structure and function. Our methods predict that both mutations are likely to introduce steric hindrance at their respective sites and, through distinct allosteric mechanisms, they destabilize local residue-residue interactions, which then propagate to impact enzyme conformation changes required for catalysis. Hxk2^{G55V} likely decreases enzymatic function by disrupting the stability of the connecting loop, an important molecular hinge point for hexokinases [102]. Specifically, our MD simulations predict Hxk2^{G55V} disrupts residue sidechain interactions between the connecting loop and the α5' helix. However, experimental follow-up is needed to see if these changes in structure occur in cells and understand how they impact substrate binding and function. Based on our findings, we anticipate that mutagenesis of interacting residue pairs between the connecting loop and the α5' helix would also disrupt the association of these two regions, resulting in effects like those observed with Hxk2^{G55V}. Based on our MD simulations in Chapter 4, residues K58, E248, Q251, D246, K406, and R407 contribute to hydrogen bonding and salt bridge networks holding the connecting loop and α5' helix in place. We are yet to generate mutants at these sites to see if they have similar impact as Hxk2^{G55V}. If these mutants exhibit behavior similar to Hxk2^{G55V}, it would validate our MD simulation predictions, suggesting that Hxk2^{G55V} likely impairs enzymatic function by disrupting local tertiary structures.

5.2 Future directions

Following the results discussed in these studies, there are several avenues for further research. I discuss some of these possibilities below.

5.2.1 Short term

Our work in Chapter 4 (Figure 48) demonstrated that 2DG resistance mutations that affected glucose binding residues or impacted substrate binding (Hxk2^{T212P}, Hxk2^{K176T}, Hxk2^{D417G}, Hxk2^{G55V}) induced nuclear translocation of Hxk2 regardless of whether glucose was abundant or not. It was unclear exactly what the driver was for this change in nuclear propensity. Here, we showed that monomerization of Hxk2 through Tda1-dependent phosphorylation, which is itself activated in low glucose, is required for nuclear translocation of wild-type Hxk2 in low glucose (Chapter 2, Figure 23). It is not clear if there is a connection between these factors and the constitutive nuclear localization of this subset of Hxk2 mutants. A logical step would be to perform imaging of these mutants in a *tda1*Δ background and assess the impact this has on their nuclear localization. We wonder if the diminished catalytic activity of these mutants could signal the activation of Tda1 thereby driving their own nuclear accumulation. Western blotting should be performed to assess the abundance and phosphorylation state of Tda1 in response to cells expressing Hxk2 2DG resistance mutants. Co-IP experiments like those performed in this study, or native PAGE experiments using protocols that have resolved Hxk2 dimers in the past [247], should be used to test if dimer propensity is decreased in mutants demonstrating constitutive nuclear localization in vivo.

Until now, we have only tested Hxk2 nuclear shuttling in the context of acute and prolonged glucose starvation, conditions that would require cells to lift glucose repression and begin to generate energy through alternative carbon sources and respiration. Therefore, one obvious route of future study is to test the nuclear translocation of Hxk2 in response to other carbon sources. Such experiments could cover both fermentable (fructose, mannose, sucrose, galactose, etc.) and non-fermentable (glycerol, ethanol, acetate, lactate, etc.) carbon sources. We hypothesize that Hxk2 will not translocate to the nucleus upon the addition of fructose or mannose, as they are themselves preferential carbon sources that are phosphorylated by Hxk2 and readily enter glycolysis. We predict that any non-Hxk2 substrate will promote its nuclear localization. This is supported by the fact that Snf1, and presumably its downstream target, Tda1, becomes active when unpreferred carbon sources and non-Hxk2 substrates, are introduced [29]. Therefore, any non-preferential carbon source would activate Tda1 and drive nuclear accumulation of Hxk2. Results in agreement with these hypotheses would show that the subcellular localization of Hxk2 can be dictated by the carbon source available.

The work herein reverses a long-standing belief in the field that Hxk2 translocates to the nucleus in high glucose conditions and forms a transcription regulatory complex [230,236–238,254,257–261]. Following this, we are left without a potential role or purpose for its nuclear accumulation. Studies to decipher the nuclear function or role of Hxk2 could start broad and aim to identify the Hxk2 interactome using pulldown-based assays or BioID. These experiments should be performed in glucose-rich conditions and in response to acute starvation. Such an approach has been used to generate insights on the role of nuclear hexokinases in mammalian systems [66,67]. Resulting mass spectrometry hits can then drive further targeted investigations.

Another area of future investigation is to understand how Hxk2 enters the nucleus. Studies in mammalian cells suggest HK2 uses nuclear importin and exportin machinery to enter and exit the nucleus [64,65]. Investigations in yeast also proposed that Hxk2 nuclear transport requires the Kap60/Kap95 α/β importins and the exportin protein, Crm1 [259,260]. However, our work herein contradicts almost all aspects of the old Hxk2 nuclear shuttling model and emphasizes a need to re-visit this topic. In addition, work from a renowned lab studying Crm1 demonstrated that the putative nuclear export sequences in Hxk2 needed to bind Crm1 fail to do so *in vitro* and do not fit the Crm1 binding consensus motif well [262]. These findings call into question the role of Crm1 in regulating Hxk2 nuclear export. Alternative to the nuclear import/export machinery suggested by earlier studies is the idea that Hxk2 may enter the nucleus using a "piggy-backing", mechanism similar to mammalian GCK that binds to GKRP and translocates to the nucleus [69]. In support of this idea, we searched extensively for nuclear localization sequences in Hxk2 but the two candidates we tested were not involved in Hxk2 nuclear shuttling (Chapter 2, Figures 19 and 20) and there were no other possible lysine-rich regions on the surface of the protein. If Hxk2 contains an NLS to control its own nuclear translocation, it is a non-canonical one. No yeast equivalent to GKRP has been identified, but through the use of Alphafold [529] we have identified structurally similar proteins in yeast that could fill this role. It will be interesting to see if such a mechanism of nuclear entry presents an interesting question for future experiments. This emphasizes the need for a targeted mass spectrometry experiment to discover previously unknown Hxk2 binding partners and determine if these hits impact its nuclear shuttling.

The constitutive nuclear accumulation and intranuclear puncta formed by the Hxk2^{4A} and Hxk2^{5A} mutants are reminiscent of intranuclear quality control (INQ) compartments that sequester misfolded nuclear or cytosolic proteins that have been transported to the nucleus [497–499]. This

makes us curious if these mutants, and possibly wild-type, are substrates for nuclear protein quality control (NucPQC) pathways. Future work should be directed toward identifying whether any of these players are involved. A recent study identified a novel degradation pathway that occurs at nuclear-vacuolar contact sites termed, nuclear-vacuolar junctions (NVJ), formed by Vac8 and Nvj1 expressed on the vacuolar and nuclear membranes, respectively [499]. This pathway involves the assembly of juxtanuclear quality control (JUNQ) and INQ compartments formed by aggregation-prone cytosolic and nuclear proteins, respectively across from one another at the NVJ [499]. At these sites, nuclear INQ protrusions extend into the vacuole in an ESCRT-dependent manner and are cleared in a Vps4-dependent manner [499]. Confocal microscopy experiments should be performed to test if Hxk2^{4A} and Hxk2^{5A} intranuclear puncta align with a fluorescently tagged Nvj1 which is routinely used to mark these contact sites [530]. We also did not assess the dynamics of the Hxk2^{4A} and Hxk2^{5A} puncta. Therefore, it would prove beneficial to perform time-course imaging experiments to understand how quickly these puncta are cleared. If these results are positive, we could assess the impact of removing essential components of the NVJ-dependent degradation pathway on the formation of these puncta. This would include Vps4 and the vacuolar proteases Pep4 and Prb1 to eliminate vacuolar engulfment and degradation, removal of Nvj1 to prevent NVJ assembly, and removal of ESCRT proteins Chm7, Vps23, Vps34, and Vps15 to prevent convergence of INQ and JUNQ. If Hxk2 is a substrate for this pathway, then we expect perturbations here to prevent clearance of Hxk2 puncta and perhaps promote toxicity in these cells. Positive results would identify Hxk2 as a novel substrate for the NVJ-dependent degradation pathway.

It remains unclear if ubiquitination of misfolded client proteins is required for access to the novel NVJ-dependent degradation pathway [499]. Still, because the Hxk2^{G55V} allele represents an

unstable mutant that constitutively localizes to the nucleus, we wonder if Hxk2 or unstable Hxk2 mutants could be subject to proteasomal degradation in the nucleus. This would make sense as a means to degrade Hxk2 in the absence of glucose when the enzyme is not required or when it becomes misfolded. Also, hexokinases become unstable when glucose is absent, further supporting the need to degrade them in these conditions [89,531]. Indeed, the 26S proteasome is the main proteolytic degradation machinery in the cytosol and nucleus and is enriched inside the nucleus [532–537]. Several ubiquitin ligases localize to the nucleus in yeast and regulate proteasomal targeting of nuclear proteins. These include San1, the main soluble ubiquitin ligase involved in NucPQC, and the inner nuclear membrane (INM)-bound Asi1 and Doa10 associated with inner nuclear membrane-associated degradation (INMAD) [538–540]. San1 is a nucleoplasmic Ub ligase that recognizes exposed hydrophobic residues which often occurs when proteins unfold [540–542]. Asi1 regulates proteasomal targeting of misfolded or mislocalized INM-bound proteins and is a branch of the endoplasmic reticulum-associated degradation pathway (ERAD) [539]. Doa10 is localized to the INM and the ER where it plays dual roles in INMAD and ERAD pathways [539]. It therefore can target soluble proteins in the nucleus and cytosol as well as ER membrane- and INM-bound proteins [543–545]. Future experiments should involve chase assays using MG132 to assess the contribution of the proteasome to Hxk2 degradation. The contribution of each E3 ligase mentioned above should also be assessed. These experiments would involve deleting the *SAN1*, *ASI1*, and *DOA10* genes, followed by cycloheximide (CHX) chase assays to determine their contribution to Hxk2 degradation over time. If Hxk2 is a target of any of these factors, then Hxk2 protein abundance would remain more stable. Confocal imaging could be paired with this approach to understand how the nuclear pool of Hxk2 is affected. Removal of any E3 ligase that targets Hxk2 may result in enrichment or even aggregation of Hxk2 in the nucleus due

to impaired clearance. If Hxk2 is targeted for NucPQC-dependent degradation, we would expect San1 to play a major role due to its nucleoplasmic distribution and its significant role in regulating NucPQC [540,541]. Doa10 may also play a role as it has been shown to target soluble nuclear proteins [543–545]. These experiments would help to establish the Hxk2 degradation profile which has never been defined. Identification of Hxk2 as a substrate for NucPQC would provide another example of cytosolic proteins transported to the nucleus for degradation.

Another topic worthy of future pursuit is to determine whether loss-of-function mutations in human hexokinases can confer 2DG resistance. As discussed in Chapter 4, decreased hexokinase activity has been reported in a 2DG-resistant HeLa cell line [354], however, it has never been investigated whether loss-of-function mutations in a hexokinase gene can give rise to 2DG resistance in human cells. In the short-term, we could begin by expressing human hexokinases in yeast cells to preliminarily test their capacity to confer resistance. A recent study successfully humanized the entire yeast glycolysis pathway, and it was shown that the HK1, HK2, and GCK human isozymes effectively complement yeast Hxk2 [225]. Though GCK readily complemented Hxk2, HK1 and HK2 were only complementary after a brief lag phase and systemic occurrence of single amino acid substitutions at the G6P product inhibitory site [225]. We recently received these plasmid constructs and tests can begin immediately. These studies would most likely focus on the HK2 isoform as it has the greatest cancer implications and would be the most likely clinical target of 2DG in patients. We could mutagenize HK2 with the corresponding yeast Hxk2 2DG resistance mutations tested in Chapter 4. The COSMIC database documents several Hxk2-resistance-mutant-equivalent HK2 mutations, including four in the N-terminal catalytic domain (A236S, A236T, K173M, G414D) and two in the C-terminal domain (A684V and D861Y) that have been identified in patient tumor samples. These mutations would likely impact HK2 catalytic activity and ability

to phosphorylate 2DG given their respective locations and conservation with yeast Hxk2. We would additionally generate these mutations in HK2. After transformation into yeast, we would then confirm expression of the HK2 protein via western blotting, and then subject these cells to identical growth assays as performed in Chapter 4. Identification of 2DG-resistant cells would motivate our lab to move these studies into mammalian cells and test if loss-of-function HK2 mutations could similarly confer resistance.

If resistance-conferring HK2 mutations are identified, then another avenue could be to perform MD simulations to understand the impact of these mutations on HK2 conformational change in a similar fashion to our studies in Chapters 2 and 4. This would be of particular interest because the structures of these isozymes are different than that of yeast, with communication that takes place between the two catalytic lobes of HK1 and HK2. Indeed, the HK1 N-terminal domain acts as an allosteric site that regulates activity of the C-terminal domain [86,90,91,114,115]. Also, though both catalytic lobes of HK2 are active, the N-terminal lobe appears to regulate the stability of the whole enzyme [89]. Such studies would provide further insight into HK2 structure and conformational change and the impact of loss-of-function mutations.

5.2.2 Long term

The future directions discussed above represents work that can be accomplished soon, however, the results discussed throughout raise more long-term questions. Although we have identified several important factors that regulate yeast Hxk2 nuclear accumulation, we lack an understanding of the signals and mechanisms that regulate the nuclear shuttling of mammalian hexokinases, making it an interesting avenue for our future work. Our studies would exclude GCK, since the regulation and roles of its nuclear shuttling is well-established [213]. Current literature

suggests that HK2 nuclear shuttling is induced in response to metabolic stress including glucose starvation and 2DG treatment in cancer cells [64,65]. AKT phosphorylates HK2 and promotes its mitochondrial localization [181]. Upon pharmacological inactivation of AKT, HK2 dissociates from the mitochondria and accumulates in the nucleus [65]. However, mitochondrial dissociation alone is not sufficient to induce nuclear accumulation, suggesting other signals must be required [65]. Since the yeast NUAK family kinase, Tda1, is required for Hxk2 nuclear accumulation in low glucose it would be interesting if either of the two NUAK kinases in humans, NUAK1 or NUAK2, similarly induces HK2 nuclear shuttling. NUAK1 is a downstream target of AKT in response to nutrient deprivation where it promotes cell survival by regulating p53 activity [546]. It is an interesting question for future work whether the AKT-NUAK1 signaling pathway is required to induce nuclear shuttling of HK2.

Another option for future work is uncovering the function or purpose of hexokinase nuclear shuttling in mammalian cells. Using a BioID screen, one group identified the HK2 interactome in AML and normal haematopoietic stem cells and proposed that HK2 influences gene expression through direct interaction with proteins involved in chromatin organization and structure (CTR9. MAX, SPIN1), transcriptional regulation (IWS1), and DNA-damage responses (SIRT1, UBR5) [66]. Another group also found that nuclear HK2 interacts with the transcription factor NRF2, to upregulate redox homeostasis genes in glioma cells [68]. The proposed gene regulatory function was independent of HK2 catalytic function, suggesting this is a non-canonical function. One caveat of the above BioID screen is this was performed in cells overexpressing HK2 tagged with either a c-Myc or SV40 nuclear localization signal, but the authors did not provide rationale for this approach [66]. In the future, follow-up studies could be performed to confirm HK2 interaction with these BioID hits. Also, these experiments could be repeated without overexpressing HK2 and

after glucose starvation which readily promotes its nuclear accumulation. Given the great complexity of mammalian tissues in comparison to yeast cells, it is highly likely the role of nuclear HK2 and interactome would differ across cell types. Therefore, multiple HK2-enriched cell types could be tested in this way. HK3 also accumulates in the nucleus in AML and hematopoietic stem cell lines leaving the door open for these studies to extend to this isozyme and respective cell types [67].

If we find that yeast Hxk2 is a substrate for NucPQC pathways, an interesting future direction would be to investigate if mammalian hexokinases are also subject to NucPQC pathways. The BioID experiments discussed above provide a starting point to address this question. These studies identified UBR5, a nuclear-localized E3 ubiquitin ligase that so far has only been shown to downregulate transcription factors and signaling molecules [547,548], as a potential interacting partner with HK2 in the nucleus, suggesting it modifies and potentially targets HK2 for degradation there [66]. It would be interesting to test the impact of UBR5 knockdown on HK2 stability using CHX chase assays. Several other E3 ligases localize to the mammalian nucleus and could also be tested in these experiments [514,515].

As another possible avenue, our work should shift toward understanding how cancer cells can gain resistance to 2DG treatment. After testing their ability to confer 2DG resistance in yeast cells, it would be interesting to test if the HK2 mutations discussed in section 5.2.1, can promote resistance in cancer cells. Pilot studies could be performed where we first make mutations and test for resistance in an "easy-to-use" cell line such as HEK293 or CHO cells. Next, we could move these studies into HeLa cell lines. Finally, since 2DG derivatives are still being clinically tested as a treatment against GBM, we could make HK2 mutations and test resistance in GBM lines. It would be beneficial to test multiple GBM lines, such as U87, C6, U251, and LN229, to understand

if resistance varies in different genetic backgrounds and simulate the heterogeneity of tumors that 2DG derivatives would encounter. Given that the Hxk2 mutations and likely the HK2 mutations are recessive, mutations would need to be made in both alleles of these cell lines. Resistance conferred by any of the HK2 variants discussed thus far may suggest that current 2DG derivatives would have limited efficacy in patients expressing these alleles. Alternatively, we could use an unbiased approach and allow cancer cells to develop resistance after continuous treatment. Such an approach was used in early studies that isolated a 2DG-resistant HeLa cell line with decreased hexokinase activity [354]. Since modern sequencing technologies were unavailable at the time, it is not certain whether mutations in hexokinase contributed. Here, we could perform whole-genome sequencing of 2DG-resistant cells to identify potential variants that contribute to the resistance phenotype. Identification of HK2 mutations would demonstrate that hexokinase activity is also a critical regulatory point in cancer cells in modulating 2DG toxicity.

Finally, it would be interesting to test if our subset of HK2 mutations could promote resistance to other reported hexokinase inhibitors. Virtual and high-throughput screening have led to the discovery of a variety of HK2 inhibitors that could be promising avenues for cancer treatment [549]. Outside of 2DG, benserazide and benitrobenrazide bind to the HK2 glucose binding site where they act as potent inhibitors [550,551]. Metformin and several other compounds inhibit HK2 by acting as G6P-mimics [549,552]. Most HK2 mutations we would be testing here impact residues that directly bind to glucose and/or G6P. These mutations are likely to reduce the efficacy of these compounds in killing cancer cells by impairing their ability to bind to the enzymatic cleft. Several other compounds exist that target HK2 through various mechanisms such as 3-bromopyruvate, that inhibits binding of HK2 to VDAC1 [553]. Imatinib targets tyrosine kinases, but decreases the expression of HK2 [554,555]. Lonidamine also inhibits hexokinases and

glycolysis in cancers, though the effect on hexokinase seems to be indirect [556]. These additional compounds, may provide other exciting possibilities in future experiments.

Appendix A : Identifying regions of Hxk2 required for regulating nuclear shuttling and resistance to 2DG

Appendix A.1 Introduction

In the Spring 2023 semester, I helped organize and lead an undergraduate research course (BIOSC0352 – Introduction to Molecular Genetics) alongside Dr. O'Donnell. Here, we exposed the students to a real laboratory investigation by incorporating central questions from my research. Our objective was to develop a comprehensive suite of Hxk2 mutations (Figure 65) that impacted substrate binding residues and sites of post-translational modification to assess their contribution to 2DG resistance and the regulation of Hxk2 nuclear shuttling.

We included all known glucose-binding residues to understand their contribution to Hxk2 function and 2DG resistance, but also their impact on nuclear shuttling. We were particularly interested in the latter purpose, as our work in Chapter 4 revealed a trend: 2DG resistance mutants affecting substrate binding regions led to a significant impact on the nuclear propensity of Hxk2, mostly by promoting constitutive nuclear accumulation. In Chapter 3, we presented evidence showing that S15 phosphorylation was dispensable for regulating Hxk2 nuclear shuttling and that K13 is somehow required for glucose-dependent nuclear exclusion perhaps through PTMs including sumoylation or ubiquitination at this site. While our studies cover a narrow scope of PTM sites, Hxk2 has numerous other reported PTM sites that have never been examined for functional roles. Therefore, we included sites of ubiquitination and sumoylation in our analyses as both modifications are associated with regulating hexokinase turnover, stability, and nuclear shuttling in mammalian cells [213,220,221,557,558]. We also included two phosphorylation sites:

S158 reported to be an autophosphorylation site that regulates Hxk2 activity [246,253,559] and S419 located within an ATP-binding helix. Our initial list of mutations also included Hxk2 alleles with synonymous mutations sequenced in the HK2 gene of patient tumor samples at sites previously shown to confer 2DG resistance in yeast when mutated (see Chapter 5, section 5.2.1). As discussed in Chapter 4, we revealed that one 2DG resistance-conferring Hxk2 mutation ($Hxk2^{G55V}$) causes structural instability and impairs enzymatic activity, in part by impacting the dynamics of a key "hinge-point" called the connecting loop. We included the initial six residues of this structure as part of our mutation list to understand the contribution of this region to Hxk2 enzymatic activity, stability, and nuclear shuttling with the hope of recapitulating the effects of $Hxk2^{G55V}$. From this list, we covered a wide range of residues, each with functional or structural significance.

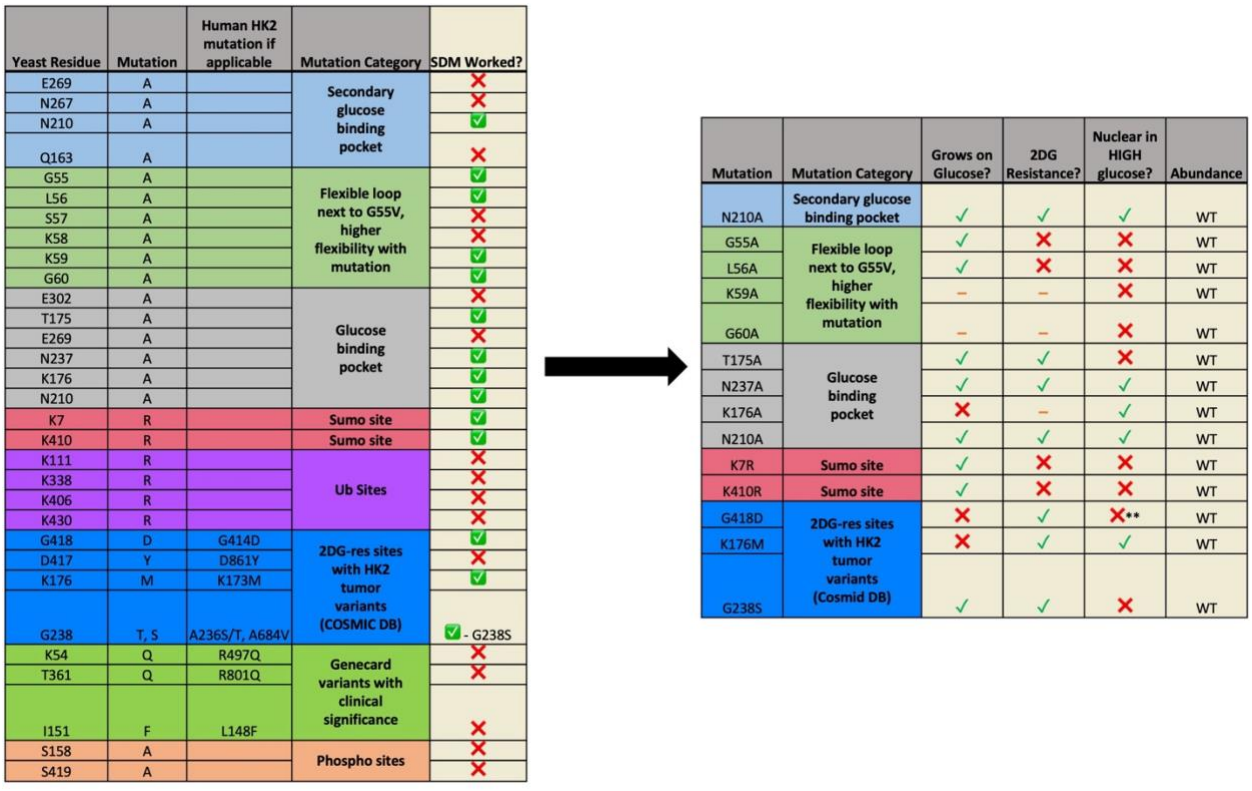

Yeast Residue	Mutation	Human HK2 mutation if applicable	Mutation Category	SDM Worked?
E269	A		Secondary glucose binding pocket	✗
N267	A			✗
N210	A			✓
Q163	A			✗
G55	A		Flexible loop next to G55V, higher flexibility with mutation	✓
L56	A			✓
S57	A			✗
K58	A			✗
K59	A			✓
G60	A			✓
E302	A		Glucose binding pocket	✗
T175	A			✓
E269	A			✗
N237	A			✓
K176	A			✓
N210	A			✓
K7	R		Sumo site	✓
K410	R		Sumo site	✓
K111	R		Ub Sites	✗
K338	R			✗
K406	R			✗
K430	R			✗
G418	D	G414D	2DG-res sites with HK2 tumor variants (COSMIC DB)	✓
D417	Y	D861Y		✗
K176	M	K173M		✓
G238	T, S	A236S/T, A684V		✓ - G238S
K54	Q	R497Q	Genecard variants with clinical significance	✗
T361	Q	R801Q		✗
I151	F	L148F		✗
S158	A		Phospho sites	✗
S419	A			✗

Mutation	Mutation Category	Grows on Glucose?	2DG Resistance?	Nuclear in HIGH glucose?	Abundance
N210A	Secondary glucose binding pocket	✓	✓	✓	WT
G55A	Flexible loop next to G55V, higher flexibility with mutation	✓	✗	✗	WT
L56A		✓	✗	✗	WT
K59A		–	–	✗	WT
G60A		–	–	✗	WT
T175A	Glucose binding pocket	✓	✓	✗	WT
N237A		✓	✓	✓	WT
K176A		✗	–	✓	WT
N210A		✓	✓	✓	WT
K7R	Sumo site	✓	✗	✗	WT
K410R	Sumo site	✓	✗	✗	WT
G418D	2DG-res sites with HK2 tumor variants (Cosmid DB)	✗	✓	✗**	WT
K176M		✗	✓	✓	WT
G238S		✓	✓	✗	WT

Figure 65. Hxk2 mutants generated in the BIOSC0352 course.

The left-hand table represents the original set of Hxk2 mutants we sought to generate through site-directed mutagenesis. The right-hand table lists successfully generated Hxk2 mutants and results of downstream experiments. Green check marks indicate positive data associated with each mutant, red crosses indicate negative results, and orange dashes represent conflicting results between pairs of groups.

In the course, we guided students through an experimental workflow to address a central question (Figure 66): Which regions of Hxk2 confer 2DG resistance? The students played an active part in generating the Hxk2 mutants through site-directed mutagenesis and subsequent validation steps. Next, I developed a module introducing the students to computational modeling. For this, I assembled an Hxk2 structure with glucose and ATP docked in the enzymatic pocket. Then, using ChimeraX software [413], the students performed a series of analyses to locate their assigned mutation, calculate their distances from glucose or ATP, and make a prediction on their impact on substrate binding. Next, the students transformed two different yeast strains (*hxk2*Δ and *hxk1*Δ *hxk2*Δ *glk1*Δ) with their assigned Hxk2 mutant plasmids. From this point forward, each group was assigned two Hxk2 mutants for further testing. Since the course was split into two sections, each pair of mutants was assigned to two groups, providing us an opportunity for two replicates in each experiment. Next, we assessed the impact of the Hxk2 mutants on nuclear localization in *hxk2*Δ cells and performed live-cell confocal imaging in high and low glucose conditions. Then, the students tested the ability of each mutant to confer 2DG resistance on solid media with glucose and 2DG added at a range of concentrations. At the same time, they also tested each mutant's capacity to promote growth on glucose in *hxk1*Δ *hxk2*Δ *glk1*Δ cells. Finally, the students performed whole-cell protein extractions on glucose-fed yeast cells and assessed whether the Hxk2 mutants impacted full-length protein abundance. Though follow-up experiments will be required to

confirm the results collected in this course, we nonetheless obtained promising results that will help guide future studies in our lab.

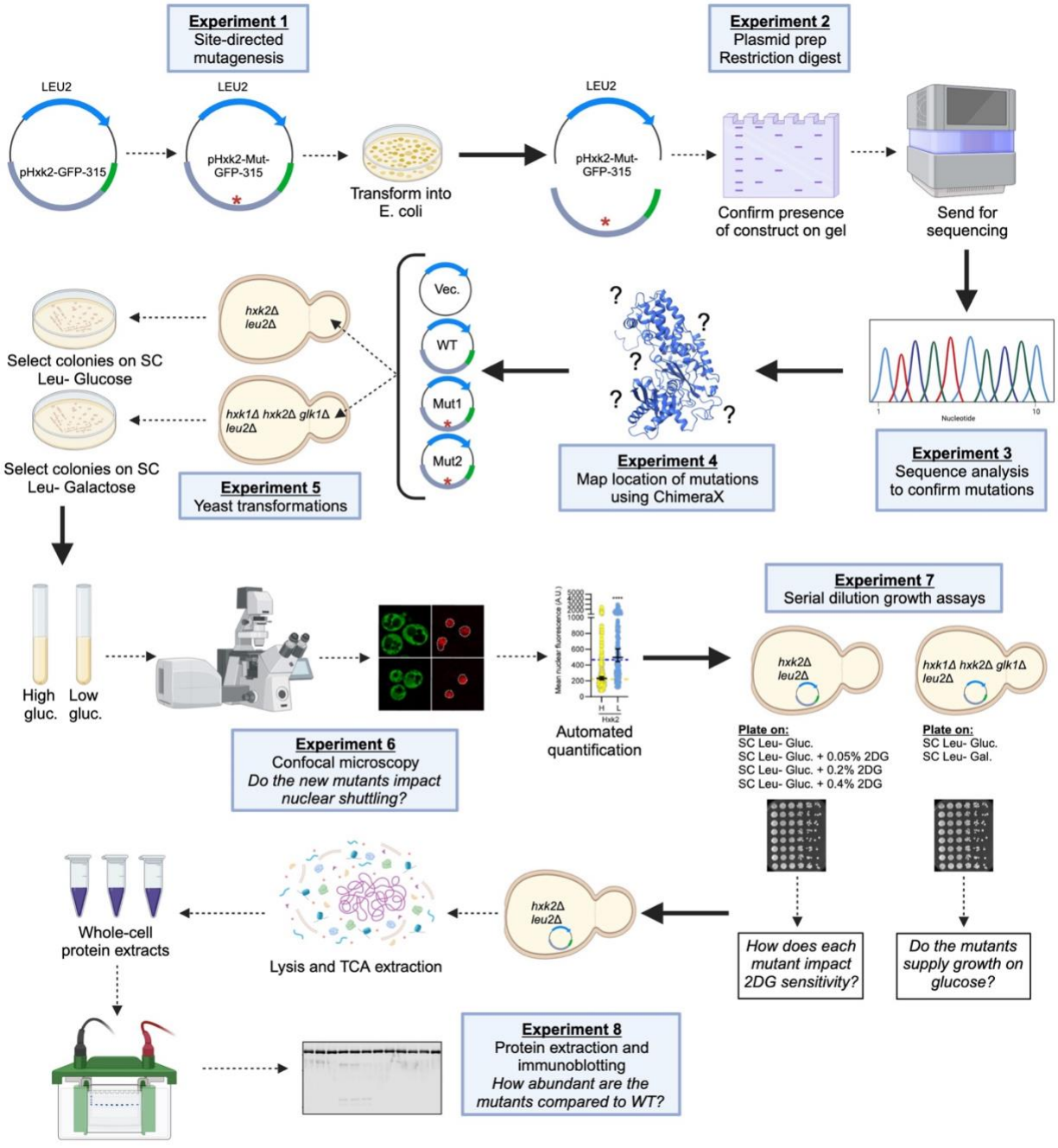

Figure 66. Flowchart summarizing the experimental workflow of the course.

Appendix A.2 Materials and methods

Appendix A.2.1 Yeast strains, plasmids, and growth conditions

Yeast strains in this investigation are detailed in Table 15. Strains lacking the native *HXK2* gene were grown in synthetic complete (SC) medium that lacks the specific amino acids necessary for plasmid maintenance [397]. Cells that are deficient for the *HXK1*, *HXK2*, and *GLK1* genes were cultured on SC medium supplemented with 2% galactose. The plasmids utilized throughout this study are outlined in Table 16 and were introduced into yeast cells via lithium acid transformation [398].

For 2DG resistance assays, SC medium containing 2% glucose was supplemented with 2DG to a final concentration of 0.05%, 0.2%, and 0.4% (% w/v). A 2% w/v stock of 2DG (Sigma-Aldrich, St. Louis, MO) was prepared in water and subsequently filter-sterilized. Yeast cells were cultivated at 30°C. When shifting to low glucose conditions, cells were washed into medium containing 0.05% glucose (low glucose medium), resuspended in this medium, and then incubated for 2 hours at 30°C.

Table 15. Yeast strains used in this study.

Strain	Genotype	Source
AFO3935	*MAT α ura3Δ0 leu2Δ0 his3Δ1 hxk2Δ::KANMX4 TPA1-mScarlet::HYGRO*	[232]
AFO3936	*MAT α ura3Δ0 leu2Δ0 his3Δ1 met15Δ0 hxk1Δ::KAN hxk2Δ::KAN glk1Δ::KAN TPA1-mScarlet::HYGRO*	[232]

Table 16. Plasmids used in this study.

Name	Description	Source
pRS315	CEN *LEU2*	[401]
pRS315-Hxk2-GFP	Genomic clone of *HXK2* with 592 bp upstream of ATG and 373 bp downstream of the stop and a C-terminal fusion to EGFP; CEN *LEU2*	[227]

pRS315-Hxk2^{N210A}-GFP	The pRS315-Hxk2-GFP plasmid listed above had the N210A mutation introduced by site-directed mutagenesis with primers (Fwd: GAATATCCCAATTGAAGTTGTTGCTTTGATAGCCGACACTACCGG; Rev: AGAAGCAACCAAAGTACCGGTAGTGTCGGCTATCAAAGCAACAAC). CEN *LEU2*	This study.
pRS315-Hxk2^{G55A}-GFP	The pRS315-Hxk2-GFP plasmid listed above had the G55A mutation introduced by site-directed mutagenesis with primers (Fwd: CAAGCATTTCATTTCCGAATTGGAAAAGGCTTTGTCCAAGAAGGG; Rev: TTGGAATGTTACCACCCTTCTTGGACAAAGCCTTTTCCAATTCGG). CEN *LEU2*	This study.
pRS315-Hxk2^{L56A}-GFP	The pRS315-Hxk2-GFP plasmid listed above had the L56A mutation introduced by site-directed mutagenesis with primers (Fwd: GCATTTCATTTCCGAATTGGAAAAGGGTGCGTCCAAGAAGGGTGG; Rev: CATTGGAATGTTACCACCCTTCTTGGACGCACCCTTTTCCAATTC). CEN *LEU2*	This study.
pRS315-Hxk2^{K59A}-GFP	The pRS315-Hxk2-GFP plasmid listed above had the K59A mutation introduced by site-directed mutagenesis with primers (Fwd: TTCCGAATTGGAAAAGGGTTTGTCCAAGGCGGGTGGTAACATTCC; Rev: CAACCTGGAATCATTGGAATGTTACCACCCGCCTTGGACAAACCC). CEN *LEU2*	This study.
pRS315-Hxk2^{G60A}-GFP	The pRS315-Hxk2-GFP plasmid listed above had the G60A mutation introduced by site-directed mutagenesis with primers (Fwd: GAATTGGAAAAGGGTTTGTCCAAGAAGGCTGGTAACATTCCAATG; Rev: CCAACCTGGAATCATTGGAATGTTACCAGCCTTCTTGGACAAACC). CEN *LEU2*	This study.
pRS315-Hxk2^{T175A}-GFP	The pRS315-Hxk2-GFP plasmid listed above had the T175A mutation introduced by site-directed mutagenesis with primers (Fwd: CAATGAAGGTATCTTGCAAAGATGGGCTAAAGGTTTTGATATTCC; Rev: TGGTTTTCAATGTTTGGAATATCAAAACCTTTAGCCCATCTTTGC). CEN *LEU2*	This study.
pRS315-Hxk2^{N237A}-GFP	The pRS315-Hxk2-GFP plasmid listed above had the N237A mutation introduced by site-directed mutagenesis with primers (Fwd: GATGGGTGTTATCTTCGGTACTGGTGTCGCTGGTGCTTACTACGA; Rev: CGATATCGGAACAAACATCGTAGTAAGCACCAGCGACACCAGTAC). CEN *LEU2*	This study.
pRS315-Hxk2^{K176A}-GFP	The pRS315-Hxk2-GFP plasmid listed above had the K176A mutation introduced by site-directed mutagenesis with primers (Fwd: CAATGAAGGTATCTTGCAAAGATGGACTGCAGGTTTTGATATTCC; Rev: TGGTTTTCAATGTTTGGAATATCAAAACCTGCAGTCCATCTTTGC). CEN *LEU2*	This study.
pRS315-Hxk2^{K7R}-GFP	The pRS315-Hxk2-GFP plasmid listed above had the K7R mutation introduced by site-directed mutagenesis with primers (Fwd: GTTCATTTAGGTCCACGAAAACCACAAGCCAGAAAGGGTTCCATG; Rev: CACATCGGCCATGGAACCCTTTCTGGCTTGTGGTTTTCGTGGACC). CEN *LEU2*	This study.

pRS315-Hxk2^{K410R}-GFP	The pRS315-Hxk2-GFP plasmid listed above had the K410R mutation introduced by site-directed mutagenesis with primers (Fwd: TGCTGCTATCTGTCAAAAGAGAGGTTACCGGACCGGTCACATCGC; Rev: GGAACCGTCTGCAGCGATGTGACCGGTCCGGTAACCTCTCTTTTG). CEN *LEU2*	This study.
pRS315-Hxk2^{G418D}-GFP	The pRS315-Hxk2-GFP plasmid listed above had the G418D mutation introduced by site-directed mutagenesis with primers (Fwd: GGTTACAAGACCGGTCACATCGCTGCAGACGATTCCGTTTACAAC; Rev: GAAACCTGGGTATCTGTTGTAAACGGAATCGTCTGCAGCGATGTG). CEN *LEU2*	This study.
pRS315-Hxk2^{K176M}-GFP	The pRS315-Hxk2-GFP plasmid listed above had the K176M mutation introduced by site-directed mutagenesis with primers (Fwd: CAATGAAGGTATCTTGCAAAGATGGACTATGGGTTTTGATATTCC; Rev: GTGGTTTTCAATGTTTGGAATATCAAAACCCATAGTCCATCTTTG). CEN *LEU2*	This study.
pRS315-Hxk2^{G238S}-GFP	The pRS315-Hxk2-GFP plasmid listed above had the G238S mutation introduced by site-directed mutagenesis with primers (Fwd: GGTGTTATCTTCGGTACTGGTGTCAATAGTGCTTACTACGATGTT; Rev: GATATCGGAACAAACATCGTAGTAAGCACTATTGACACCAGTACC). CEN *LEU2*	This study.

Appendix A.2.2 2DG resistance assays and defining mutant Hxk2 function *in vivo*

We evaluated the sensitivity of yeast cells expressing each of the class mutants to 2DG through serial dilution growth assays. The cells were plated onto solid agar medium supplemented with 2DG at the concentrations specified earlier and allowed to grow at 30°C. In brief, cells were cultured to saturation overnight in SC medium, and their optical densities were measured. Next, a dilution series was initiated, starting with a density of A_{600} = 1.0 (equivalent to 1.0 x 10^7 cells/mL). Five-fold serial dilutions of cells were prepared and then pinned onto solid SC medium with or without 2DG. Growth of the mutant-expressing cells was compared to that of *hxk2*Δ cells expressing either an empty vector (pRS315) or WT *HXK2* (pRS315-Hxk2-GFP).

To assess the capability of each Hxk2 mutant to support growth on glucose, we used a *hxk1*Δ *hxk2*Δ *glk1*Δ strain. These cells lack the hexokinases necessary for glucose phosphorylation, rendering them unable to grow on glucose-containing media, as glucose phosphorylation is

essential for initiating glycolysis [228]. The cells were cultured to saturation overnight in SC medium supplemented with galactose, and the optical density of each culture was measured. Next, a dilution series was prepared, starting with a density of A_{600} = 1.0 (equivalent to 1.0 x 10^7 cells/mL). Five-fold serial dilutions of cells were then made and pinned onto solid SC medium supplemented with either glucose or galactose. The growth of mutant-expressing cells was compared to that of *hxk1*Δ *hxk2*Δ *glk1*Δ cells expressing either an empty vector (pRS315) or WT *HXK2* (pRS315-Hxk2-GFP).

Appendix A.2.3 Fluorescence microscopy

We examined the subcellular localization of Hxk2^{mutant}-GFP fusion proteins by culturing *hxk2*Δ cells in SC medium with 2% glucose overnight. The culture was then re-inoculated to an optical density (OD_{300}) of 0.3 into fresh SC medium containing 2% glucose and grown until reaching mid-logarithmic phase at 30°C with aeration. For transitions to low glucose medium (SC with 0.05% glucose), cells were washed and incubated in the same manner as described above. In preparation for imaging, cells were plated onto 35 mm glass bottom microwell dishes (MaTek Corporation, Ashland, MA), which were coated with 15 μL (0.2 mg/mL) of concanavalin A (Sigma-Alrich, St. Louis, MO, USA). Imaging was performed using a Nikon Eclipse Ti2 A1R inverted confocal microscope (Nikon, Chiyoda, Tokyo, Japan) equipped with 100X oil immersion objective (NA 1.49). Images were captured using GaAsP or multi-alkali photomultiplier tube detectors, and acquisition was controlled using NIS-Elements software (Nikon). To ensure consistency, all images were acquired using identical settings, and adjustments were made uniformly using NIS-Elements software. Additionally, images were cropped using the same software.

Appendix A.2.4 Image quantification and statistical analyses

The quantification of nuclear fluorescence and whole-cell fluorescence intensity was conducted using Nikon General Analysis 3 software (Nikon) in conjunction with segmentation from NIS-Elements.*ai* (Artificial Intelligence) software (Nikon). For the quantification of whole-cell fluorescence, the NIS.*ai* software underwent a training process using a ground-truth set of images where cells had been manually segmented using DIC images. The NIS.*ai* software was iteratively trained until it reached a training loss threshold of <0.02, indicating a high level of agreement between the initial ground truth and the output produced by the NIS.*ai* software. To determine the mean nuclear fluorescence, the NIS.*ai* software was trained to identify the nucleus utilizing the chromosomally tagged Tpa1-mScarlet nuclear marker. This training involved a ground truth set of images captured through confocal microscopy, wherein individual whole-cell and nuclear objects in a field of view were segmented using the DIC and 561 nm (mScarlet) channels. A parent-child relationship was applied to individual nuclear objects (child) within the same cell (parent) to aggregate them as single objects and associate them with the appropriate whole cell. Any partial cells at the image edges were removed along with their child objects. Subsequently, the mean fluorescence intensity of each parent or child object was determined in the appropriate channel. All quantification graphs derived from imaging were generated using this method.

Statistical analyses for fluorescence quantification were conducted using Prism software (GraphPad Software, San Diego, CA). Kruskal-Wallis statistical tests were performed with Dunn's post hoc correction for multiple comparisons. Significant p-values from these tests are denoted as follows: * p-value<0.1; ** p-value<0.01; ***p-value<0.001; ****p-value<0.0001; and "not significant" (ns) for p-value>0.1. In cases when multiple comparisons were made, the symbol †

may replace * to signify the same p-values relative to a different reference sample (refer to the figure legends for details).

Appendix A.2.5 Immunoblotting to assess the abundance of Hxk2 mutants

To evaluate the abundance of the Hxk2 mutants within cells, we conducted whole-cell protein extractions using the trichloroacetic acid (TCA) method [403]. Briefly, mid-logarithmic cells of equal densities (OD_{300} 3.0) were harvested by centrifugation, washed in water, and resuspended in a solution containing 0.25 M sodium hydroxide and 72 mM β-mercaptoethanol. The samples were then incubated on ice, and protein precipitation was carried out by the addition of 50% TCA. After further incubation on ice, the proteins were pelleted by centrifugation. The supernatant was discarded, and the proteins were solubilized in 120 μL of TCA sample buffer (composed of 40 mM Tris-Cl [pH 8.0], 0.1 mM EDTA, 8 M urea, 5% SDS, 1% β-mercaptoethanol, and 0.01% bromophenol blue). Following a 30-minute incubation at 37°C, insoluble material was removed by centrifugation before resolving the samples by SDS-PAGE. The proteins were subsequently transferred to a PVDF membrane support and probed with an anti-GFP antibody (Santa Cruz Biotechnology, Dallas, TX, USA), followed by a goat anti-mouse IRDye 800 secondary antibody (LI-COR Biotechnologies, Lincoln, NB, USA). Detection of antibody complexes was performed using an Odyssey Clx Infrared Imager (LI-COR). For protein loading and membrane transfer control in immunoblotting, REVERT (LI-COR) total protein staining of the membranes was employed.

Appendix A.3 Results and discussion

From the class, we successfully generated 13 of the initial 32 mutations for Hxk2, covering a diverse range of functional sites. Though follow-up experiments are required to confirm the results collected here, we still obtained further insight into the regulation of Hxk2 nuclear shuttling and 2DG resistance while assembling a toolbox that will drive future work in the lab. The results of the class experiments are summarized in Figure 63.

Most mutants conferred growth of *hxk1*Δ *hxk2*Δ *glk1*Δ cells on glucose-containing medium except K176A, K176M, and G418D. These results are in agreement with our experiments in Chapter 4 (Figure 49, 67) where the K176T and G418C mutants also did not promote growth in these conditions. This suggests the three mutants here cannot phosphorylate substrate. In line with this, K176A, K176M, and G418D conferred 2DG resistance implying that they do not generate 2DG6P.

Excitingly, all mutations that impacted glucose binding residues conferred 2DG resistance. All of these mutants (N210A, T175A, N237A), except for the two mutations at K176, still promoted growth on glucose. From a basic biology perspective, this shows that these sites may be dispensable for enzymatic activity and contribute negligibly to glucose binding, whereas K176 appears to be required for substrate interactions. *In vitro* catalytic assays will be important in our follow-up studies to fully assess the contribution of each residue to enzymatic function.

We could not fully evaluate the impact of mutants affecting the Hxk2 connecting loop in our phenotypic assays. In agreement with our experiments in Chapter 4 (Figure 53) $Hxk2^{G55A}$ did not appear to affect enzymatic function as it facilitated growth on glucose and did not confer 2DG resistance. $Hxk2^{L56A}$ also demonstrated no effect in these assays. It should be noted that both sites lie at the C-terminal end of the Hxk2 α2 helix and substitution of alanines at both sites introduces

amino acids more conducive to helix formation and could therefore have a stabilizing effect on structure with no consequence to enzymatic function. The results of Hxk2^{K59A} and Hxk2^{G60A} were inconclusive due to a lack of agreement between results collected by student groups. Emphasis will be placed on re-testing these mutants and generating the remaining mutants of this region to see if any can recapitulate the phenotypes of Hxk2^{G55V} as discussed in Chapter 4. Positive results would indeed suggest this stretch of residues is important for catalytic function and subcellular localization.

In Chapter 4, we noticed that all 2DG resistance mutations that immediately impacted residues involved with substrate binding altered Hxk2 nuclear propensity. We were excited to observe that most glucose-binding residue mutations generated here produced mutants which also impacted Hxk2 nuclear shuttling, mostly by promoting nuclear accumulation even in the presence of glucose. Though independent follow-up is required, this observation strengthens our hypothesis that the inability or lack of substrate binding acts as a trigger to induce Hxk2's nuclear accumulation. It's worth noting that in both high and low glucose conditions, the Hxk2^{G418D} mutant did not accumulate in the nucleus, similar to the Hxk2^{G418C} 2DG resistance mutant (as shown in Chapter 4, Figure 49). However, the reason behind this distinction is currently unknown.

Finally, we did not detect protein abundance changes in either mutant tested in the class. As discussed in Chapter 5, section 5.1.2 – Limitations of these studies, full-length Hxk2-GFP from our plasmid-borne constructs is highly expressed, making the corresponding bands on a western blot sensitive to over-saturation, and detection of abundance changes difficult. The experiments performed in this class were done before realizing that reduced amounts whole-cell extract should be loaded to avoid these issues. Therefore, the abundance of each mutant will be re-tested using our new western blotting approach for detecting Hxk2-GFP bands.

In summary, this class project helped us to generate an additional set of Hxk2 mutants that we will utilize in future studies. We hope this new suite of mutants as part of the growing collection of alleles we have tested (Figure 67) will provide further insight on the important regions that contribute to enzymatic function and impact sensitivity to 2DG, but also Hxk2 nuclear propensity.

Mutation	Mutation Category/Location	Grows on Glucose?	2DG Resistance?	Nuclear in HIGH glucose?	Abundance	Citation if applicable
N210A	Secondary glucose binding pocket	✓	✓	✓	WT	UG Course 2023
G55A	Flexible loop next to G55V, higher flexibility with mutation	✓	✗	✗	WT	UG Course 2023
G55V		✓	✓	✓	Less abundant	Soncini et al., 2020
L56A		✓	✗	✗	WT	UG Course 2023
K59A		–	–	✗	WT	UG Course 2023
G60A		–	–	✗	WT	UG Course 2023
T175A	Glucose binding pocket	✓	✓	✗	WT	UG Course 2023
T212P		✓	✓	✓	WT	Defenouillere et al., 2019
N237A		✓	✓	✓	WT	UG Course 2023
K176A		✗	–	✓	WT	UG Course 2023
K176M		✗	✓	✓	WT	COSMIC database; UG Course 2023
K176T		✗	✓	✓	WT	Defenouillere et al., 2019
N210A		✓	✓	✓	WT	UG Course 2023
G238V	Adj. to Gluc. binding pocket	✓	✓	✗	WT	Walker, 2022
G238S		✓	✓	✗	WT	COSMIC database; UG Course 2023
Q299H		✓	✓	✗	WT	Defenouillere et al., 2019
G418C	ATP binding site	✗	✓	✗*	WT	Defenouillere et al., 2019
G418D		✗	✓	✗*	WT	COSMIC database; UG Course 2023
D417G		✓	✓	✓	WT	Soncini et al., 2020
K410R	Sumo site	✓	✗	✗	WT	UG Course 2023
T75I/S345P	Both NOT adjacent to enzymatic sites	✓	✗	✗	WT	Defenouillere et al., 2019
K13A	N-terminal tail mutants	✓	✗	✓	WT	N/A
K13R		✓	✗	✓	WT	N/A
Δ7-16		✓	✗	✓	WT	N/A
K7, 8, 13A		✓	✗	✓	WT	N/A
D106A	K13 binding partner	✓	✗	✗	WT	N/A
NES1 (L23A, I27A, F30A, I33A)	Nuclear export sites	✓	✓	✓	Less abundant	Paleaz et al., 2009
NES2 (L310A, I313A, L314A, L316A, L318A)		✗	✓	✓	Less abundant	Paleaz et al., 2009
K54A, K58A, K59A	2nd potential NLS ID'ed by Ally	✓	–	✗	WT	N/A

Figure 67. Effects of all Hxk2 mutants examined in this dissertation on growth, 2DG resistance, nuclear shuttling, and protein abundance.

Green check marks indicate positive data associated with each mutant, red crosses indicate negative results, and orange dashes represent conflicting results between pairs of groups. The sources of each mutant, where applicable, are indicated in the far-right column. Asterisks (*) represent mutants that did not enter the nucleus in either glucose-replete or glucose-depleted conditions.

Bibliography

1. Pavlova NN, Zhu J, Thompson CB. The hallmarks of cancer metabolism: Still emerging. Cell Metab. 2022;34: 355–377. doi:10.1016/J.CMET.2022.01.007
2. Özcan S, Johnston M. Function and Regulation of Yeast Hexose Transporters. Microbiology and Molecular Biology Reviews. 1999;63: 554–569. doi:10.1128/MMBR.63.3.554-569.1999
3. Bouché C, Serdy S, Kahn CR, Goldfine AB. The Cellular Fate of Glucose and Its Relevance in Type 2 Diabetes. Endocr Rev. 2004;25: 807–830. doi:10.1210/ER.2003-0026
4. Pavlova NN, Thompson CB. The Emerging Hallmarks of Cancer Metabolism. Cell Metab. 2016;23: 27–47. doi:10.1016/j.cmet.2015.12.006
5. Paneque A, Fortus H, Zheng J, Werlen G, Jacinto E. The Hexosamine Biosynthesis Pathway: Regulation and Function. Genes 2023;14: 933. doi:10.3390/GENES14040933
6. Röder P V., Wu B, Liu Y, Han W. Pancreatic regulation of glucose homeostasis. Experimental & Molecular Medicine 2016;48: e219–e219. doi:10.1038/emm.2016.6
7. Boucher J, Kleinridders A, Ronald Kahn C. Insulin Receptor Signaling in Normal and Insulin-Resistant States. Cold Spring Harb Perspect Biol. 2014;6: a009191. doi:10.1101/CSHPERSPECT.A009191
8. Schultze SM, Hemmings BA, Niessen M, Tschopp O. PI3K/AKT, MAPK and AMPK signalling: protein kinases in glucose homeostasis. Expert Rev Mol Med. 2012;14: e1. doi:10.1017/S1462399411002109
9. Bryant NJ, Govers R, James DE. Regulated transport of the glucose transporter GLUT4. Nature Reviews Molecular Cell Biology 2002 3:4. 2002;3: 267–277. doi:10.1038/nrm782

10. Cong LN, Chen H, Li Y, Zhou L, McGibbon MA, Taylor SI, et al. Physiological Role of Akt in Insulin-Stimulated Translocation of GLUT4 in Transfected Rat Adipose Cells. Molecular Endocrinology. 1997;11: 1881–1890. doi:10.1210/MEND.11.13.0027

11. Beg M, Abdullah N, Thowfeik FS, Altorki NK, McGraw TE. Distinct Akt phosphorylation states are required for insulin regulated Glut4 and Glut1-mediated glucose uptake. Elife. 2017;6. doi:10.7554/ELIFE.26896

12. Bergsma DJ, Ai Y, Skach WR, Nesburn K, Anoia E, Van Horn S, et al. Fine structure of the human galactokinase GALK1 gene. Genome Res. 1996;6: 980–985. doi:10.1101/GR.6.10.980

13. Hayward BE, Bonthron DT. Structure and alternative splicing of the ketohexokinase gene. Eur J Biochem. 1998;257: 85–91. doi:10.1046/J.1432-1327.1998.2570085.X

14. Janah L, Kjeldsen S, Galsgaard KD, Winther-Sørensen M, Stojanovska E, Pedersen J, et al. Glucagon Receptor Signaling and Glucagon Resistance. International Journal of Molecular Sciences 2019, Vol 20, Page 3314. 2019;20: 3314. doi:10.3390/IJMS20133314

15. Galsgaard KD, Pedersen J, Knop FK, Holst JJ, Albrechtsen NJW. Glucagon receptor signaling and lipid metabolism. Front Physiol. 2019;10: 431942. doi:10.3389/FPHYS.2019.00413

16. González A, Hall MN, Lin SC, Hardie DG. AMPK and TOR: The Yin and Yang of Cellular Nutrient Sensing and Growth Control. Cell Metab. 2020;31: 472–492. doi:10.1016/J.CMET.2020.01.015

17. Alfatah M, Cui L, Jie C, Goh H, Lewis J, Poh WJ, et al. Metabolism of glucose activates TORC1 through multiple mechanisms in Saccharomyces cerevisiae. Cell Rep. 2023;42. doi:10.1016/j.celrep.2023.113205

18. González A, Hall MN. Nutrient sensing and TOR signaling in yeast and mammals. EMBO J. 2017;36: 397–408. doi:10.15252/EMBJ.201696010

19. Liu GY, Sabatini DM. mTOR at the nexus of nutrition, growth, ageing and disease. Nat Rev Mol Cell Biol. 2020;21: 183–203. doi:10.1038/s41580-019-0199-y

20. Steinberg GR, Hardie DG. New insights into activation and function of the AMPK. Nature Reviews Molecular Cell Biology 2022;24: 255–272. doi:10.1038/S41580-022-00547-X

21. Lin SC, Hardie DG. AMPK: Sensing Glucose as well as Cellular Energy Status. Cell Metab. 2018;27: 299–313. doi:10.1016/j.cmet.2017.10.009

22. Shaw RJ, Kosmatka M, Bardeesy N, Hurley RL, Witters LA, DePinho RA, et al. The tumor suppressor LKB1 kinase directly activates AMP-activated kinase and regulates apoptosis in response to energy stress. Proc Natl Acad Sci U S A. 2004;101: 3329–3335. doi:10.1073/PNAS.0308061100

23. Woods A, Johnstone SR, Dickerson K, Leiper FC, Fryer LGD, Neumann D, et al. LKB1 Is the Upstream Kinase in the AMP-Activated Protein Kinase Cascade. Current Biology. 2003;13: 2004–2008. doi:10.1016/J.CUB.2003.10.031

24. Herzig S, Shaw RJ. AMPK: Guardian of metabolism and mitochondrial homeostasis. Nat Rev Mol Cell Biol. 2018;19: 121–135. doi:10.1038/nrm.2017.95

25. Zhang CS, Hawley SA, Zong Y, Li M, Wang Z, Gray A, et al. Fructose-1,6-bisphosphate and aldolase mediate glucose sensing by AMPK. Nature. 2017;548: 112–116. doi:10.1038/nature23275

26. Ma T, Tian X, Zhang B, Li M, Wang Y, Yang C, et al. Low-dose metformin targets the lysosomal AMPK pathway through PEN2. Nature. 2022. doi:10.1038/s41586-022-04431-8

27. Zhang CS, Jiang B, Li M, Zhu M, Peng Y, Zhang YL, et al. The lysosomal v-ATPase-ragulator complex is a common activator for AMPK and mTORC1, acting as a switch between catabolism and anabolism. Cell Metab. 2014;20: 526–540. doi:10.1016/j.cmet.2014.06.014

28. Diaz-Ruiz R, Rigoulet M, Devin A. The Warburg and Crabtree effects: On the origin of cancer cell energy metabolism and of yeast glucose repression. Biochim Biophys Acta Bioenerg. 2011;1807: 568–576. doi:10.1016/j.bbabio.2010.08.010

29. Conrad M, Schothorst J, Kankipati HN, Van Zeebroeck G, Rubio-Texeira M, Thevelein JM. Nutrient sensing and signaling in the yeast Saccharomyces cerevisiae. FEMS Microbiol Rev. 2014;38: 254–299. doi:10.1111/1574-6976.12065

30. Pfeiffer T, Morley A. An evolutionary perspective on the Crabtree effect. Front Mol Biosci. 2014;1: 108877. doi:10.3389/FMOLB.2014.00017

31. Jouhten P, Ponomarova O, Gonzalez R, Patil KR. Saccharomyces cerevisiae metabolism in ecological context. FEMS Yeast Res. 2016;16: 80. doi:10.1093/FEMSYR/FOW080

32. Hedbacker K, Carlson M. SNF1/AMPK pathways in yeast. Frontiers in bioscience. 2008;13: 2408–2420. doi:10.2741/2854

33. Coccetti P, Nicastro R, Tripodi F. Conventional and emerging roles of the energy sensor Snf1/AMPK in Saccharomyces cerevisiae. Microbial Cell. 2018;5: 482. doi:10.15698/MIC2018.11.655

34. Schmidt MC, McCartney RR. beta-subunits of Snf1 kinase are required for kinase function and substrate definition. EMBO J. 2000;19: 4936–4943. doi:10.1093/emboj/19.18.4936

35. Vincent O, Townley R, Kuchin S, Carlson M. Subcellular localization of the Snf1 kinase is regulated by specific β subunits and a novel glucose signaling mechanism. Genes Dev. 2001;15: 1104–1114. doi:10.1101/GAD.879301

36. Chandrashekarappa DG, McCartney RR, O'Donnell AF, Schmidt MC. The β subunit of yeast AMP-activated protein kinase directs substrate specificity in response to alkaline stress. Cell Signal. 2016;28: 1881–1893. doi:10.1016/j.cellsig.2016.08.016

37. Hong SP, Carlson M. Regulation of Snf1 protein kinase in response to environmental stress. Journal of Biological Chemistry. 2007;282: 16838–16845. doi:10.1074/jbc.M700146200

38. McCartney RR, Schmidt MC. Regulation of Snf1 Kinase. Activation requires phosphorylation of threonine 210 by an upstream kinase as well as a distinct step mediated by the Snf4 subunit. Journal of Biological Chemistry. 2001;276: 36460–36466. doi:10.1074/jbc.M104418200

39. Kayikci Ö, Nielsen J. Glucose repression in Saccharomyces cerevisiae. FEMS Yeast Res. 2015;15: 1–8. doi:10.1093/femsyr/fov068

40. McCartney RR, Garnar-Wortzel L, Chandrashekarappa DG, Schmidt MC. Activation and inhibition of Snf1 kinase activity by phosphorylation within the activation loop. Biochim Biophys Acta Proteins Proteom. 2016;1864: 1518–1528. doi:10.1016/j.bbapap.2016.08.007

41. Rubenstein EM, McCartney RR, Zhang C, Shokat KM, Shirra MK, Arndt KM, et al. Access denied: Snf1 activation loop phosphorylation is controlled by availability of the phosphorylated threonine 210 to the PP1 phosphatase. Journal of Biological Chemistry. 2008;283: 222–230. doi:10.1074/jbc.M707957200

42. Wilson WA, Hawley SA, Hardie DG. Glucose repression/derepression in budding yeast: SNF1 protein kinase is activated by phosphorylation under derepressing conditions, and this

correlates with a high AMP:ATP ratio. Current Biology. 1996;6: 1426–1434. doi:10.1016/S0960-9822(96)00747-6

43. Sutherland CM, Hawley SA, McCartney RR, Leech A, Stark MJR, Schmidt MC, et al. Elm1p is one of three upstream kinases for the Saccharomyces cerevisiae SNF1 complex. Current Biology. 2003;13: 1299–1305. doi:10.1016/S0960-9822(03)00459-7

44. Hong SP, Leiper FC, Woods A, Carling D, Carlson M. Activation of yeast Snf1 and mammalian AMP-activated protein kinase by upstream kinases. Proc Natl Acad Sci U S A. 2003;100: 8839–8843. doi:10.1073/pnas.1533136100

45. Nath N, McCartney RR, Schmidt MC. Yeast Pak1 Kinase Associates with and Activates Snf1. Mol Cell Biol. 2003;23: 3909. doi:10.1128/MCB.23.11.3909-3917.2003

46. Mayer F V., Heath R, Underwood E, Sanders MJ, Carmena D, McCartney RR, et al. ADP regulates SNF1, the saccharomyces cerevisiae homolog of AMP-activated protein kinase. Cell Metab. 2011;14: 707–714. doi:10.1016/j.cmet.2011.09.009

47. Ludin K, Jiang R, Carlson M. Glucose-regulated interaction of a regulatory subunit of protein phosphatase 1 with the Snf1 protein kinase in Saccharomyces cerevisiae. Proc Natl Acad Sci U S A. 1998;95: 6245–6250. doi:10.1073/PNAS.95.11.6245

48. Tu J, Carlson M. REG1 binds to protein phosphatase type 1 and regulates glucose repression in Saccharomyces cerevisiae. EMBO Journal. 1995;14: 5939–5946. doi:10.1002/J.1460-2075.1995.TB00282.X

49. Sanz P, Alms GR, Haystead TAJ, Carlson M. Regulatory Interactions between the Reg1-Glc7 Protein Phosphatase and the Snf1 Protein Kinase. Mol Cell Biol. 2000;20: 1321–1328. doi:10.1128/mcb.20.4.1321-1328.2000

50. Treitel MA, Kuchin S, Carlson M. Snf1 Protein Kinase Regulates Phosphorylation of the Mig1 Repressor in Saccharomyces cerevisiae. Mol Cell Biol. 1998;18: 6273–6280. doi:10.1128/mcb.18.11.6273

51. Smith FC, Davies SP, Wilson WA, Carling D, Hardie DG. The SNF1 kinase complex from Saccharomyces cerevisiae phosphorylates the transcriptional repressor protein Mig1p in vitro at four sites within or near regulatory domain 1. FEBS Lett. 1999;453: 219–223. doi:10.1016/S0014-5793(99)00725-5

52. Östling J, Ronne H. Negative control of the Mig1p repressor by Snf1p-dependent phosphorylation in the absence of glucose. Eur J Biochem. 1998;252: 162–168. doi:10.1046/J.1432-1327.1998.2520162.X

53. Shashkova S, Wollman AJM, Leake MC, Hohmann S. The yeast Mig1 transcriptional repressor is dephosphorylated by glucose-dependent and -independent mechanisms. FEMS Microbiol Lett. 2017;364: 133. doi:10.1093/FEMSLE/FNX133

54. DeVit MJ, Johnston M. The nuclear exportin Msn5 is required for nuclear export of the Mig1 glucose repressor of Saccharomyces cerevisiae. Current Biology. 1999;9: 1231–1241. doi:10.1016/S0960-9822(99)80503-X

55. Hedges D, Proft M, Entian K-D. CAT8, a New Zinc Cluster-Encoding Gene Necessary for Derepression of Gluconeogenic Enzymes in the Yeast Saccharomyces cerevisiae. Mol Cell Biol. 1995;15: 1915–1922. doi:10.1128/MCB.15.4.1915

56. Weinhandl K, Winkler M, Glieder A, Camattari A. Carbon source dependent promoters in yeasts. Microb Cell Fact. 2014;13: 1–17. doi:10.1186/1475-2859-13-5

57. Biddick RK, Law GL, Young ET. Adr1 and Cat8 Mediate Coactivator Recruitment and Chromatin Remodeling at Glucose-Regulated Genes. PLoS One. 2008;3: e1436. doi:10.1371/JOURNAL.PONE.0001436

58. Tachibana C, Biddick R, Law GL, Young ET. A Poised Initiation Complex Is Activated by SNF1. Journal of Biological Chemistry. 2007;282: 37308–37315. doi:10.1074/JBC.M707363200

59. Randez-Gil F, Bojunga N, Proft M, Entian K-D. Glucose Derepression of Gluconeogenic Enzymes in Saccharomyces cerevisiae Correlates with Phosphorylation of the Gene Activator Cat8p. Mol Cell Biol. 1997;17: 2502–2510. doi:10.1128/MCB.17.5.2502

60. Meyerhof O. Über die enzymatische Milchsäurebildung im Muskelextrakt. III. Mitteilung: Die Milchsäurebildung aus den gärfähigen Hexosen. Biochem Z. 1927;183: 176–215.

61. Cárdenas ML, Cornish-Bowden A, Ureta T. Evolution and regulatory role of the hexokinases. Biochimica et Biophysica Acta (BBA) - Molecular Cell Research. 1998;1401: 242–264. doi:10.1016/S0167-4889(97)00150-X

62. Rodríguez-Saavedra C, Morgado-Martínez LE, Burgos-Palacios A, King-Díaz B, López-Coria M, Sánchez-Nieto S. Moonlighting Proteins: The Case of the Hexokinases. Front Mol Biosci. 2021;8: 531. doi:10.3389/FMOLB.2021.701975

63. Roberts DJ, Miyamoto S. Hexokinase II integrates energy metabolism and cellular protection: Akting on mitochondria and TORCing to autophagy. Cell Death Differ. 2015;22: 248–257. doi:10.1038/cdd.2014.173

64. Neary CL, Pastorino JG. Nucleocytoplasmic shuttling of hexokinase II in a cancer cell. Biochem Biophys Res Commun. 2010;394: 1075–1081. doi:10.1016/j.bbrc.2010.03.129

65. Neary CL, Pastorino JG. Akt inhibition promotes hexokinase 2 redistribution and glucose uptake in cancer cells. J Cell Physiol. 2013;228: 1943–1948. doi:10.1002/jcp.24361

66. Thomas GE, Egan G, García-Prat L, Botham A, Voisin V, Patel PS, et al. The metabolic enzyme hexokinase 2 localizes to the nucleus in AML and normal haematopoietic stem and progenitor cells to maintain stemness. Nature Cell Biology 2022;24: 872–884. doi:10.1038/s41556-022-00925-9

67. Seiler K, Humbert M, Minder P, Mashimo I, Schläfli AM, Krauer D, et al. Hexokinase 3 enhances myeloid cell survival via non-glycolytic functions. Cell Death & Disease 2022 13:5. 2022;13: 1–14. doi:10.1038/s41419-022-04891-w

68. Sheikh T, Gupta P, Gowda P, Patrick S, Sen E. Hexokinase 2 and nuclear factor erythroid 2-related factor 2 transcriptionally coactivate xanthine oxidoreductase expression in stressed glioma cells. Journal of Biological Chemistry. 2018;293: 4767–4777. doi:10.1074/jbc.M117.816785

69. Brown KS, Kalinowski SS, Megill JR, Durham SK, Mookhtiar KA. Glucokinase regulatory protein may interact with glucokinase in the hepatocyte nucleus. Diabetes. 1997;46: 179–186. doi:10.2337/diab.46.2.179

70. Han CY, Patten DA, Kim SI, Lim JJ, Chan DW, Siu MKY, et al. Nuclear hkii–p-p53 (Ser15) interaction is a prognostic biomarker for chemoresponsiveness and glycolytic regulation in epithelial ovarian cancer. Cancers (Basel). 2021;13. doi:10.3390/cancers13143399

71. Agius L. The physiological role of glucokinase binding and translocation in hepatocytes. Adv Enzyme Regul. 1998;38: 303–331. doi:10.1016/S0065-2571(97)00001-0

72. Hussain S, Richardson E, Ma Y, Holton C, De Backer I, Buckley N, et al. Glucokinase activity in the arcuate nucleus regulates glucose intake. Journal of Clinical Investigation. 2015;125: 337–349. doi:10.1172/JCI77172

73. Rizzo MA, Magnuson MA, Drain PF, Piston DW. A Functional Link between Glucokinase Binding to Insulin Granules and Conformational Alterations in Response to Glucose and Insulin. Journal of Biological Chemistry. 2002;277: 34168–34175. doi:10.1074/JBC.M112478200

74. Toyoda Y, Shironoguchi H, Miwa I, Yoshie S. Glucokinase is concentrated in insulin-secretory granules of pancreatic B-cells. Histochem Cell Biol. 1999;112: 35–40. doi:10.1007/S004180050389

75. Toyoda Y, Yoshie S, Fujita T, Ito Y, Nonogaki T, Miwa I. Glucokinase is located in secretory granules of pancreatic D-cells. FEBS Lett. 1997;415: 281–284. doi:10.1016/S0014-5793(97)01139-3

76. Ciscato F, Filadi R, Masgras I, Pizzi M, Marin O, Damiano N, et al. Hexokinase 2 displacement from mitochondria-associated membranes prompts Ca 2+ -dependent death of cancer cells. EMBO Rep. 2020; 1–13. doi:10.15252/embr.201949117

77. Hurley JH. The Sugar Kinase/Heat Shock Protein 7O/Actin Superfamily: Implications of Conserved Structure for Mechanism. Annu Rev Biophys Biomol Struct. 1996;25: 137–62. Available: www.annualreviews.org

78. Bork P, Sander C, Valencia A. An ATPase domain common to prokaryotic cell cycle proteins, sugar kinases, actin, and hsp70 heat shock proteins. Proc Natl Acad Sci U S A. 1992;89: 7290–7294. doi:10.1073/PNAS.89.16.7290

79. Kuser P, Cupri F, Bleicher L, Polikarpov I. Crystal structure of yeast hexokinase PI in complex with glucose: A classical “induced fit” example revised. Proteins: Structure, Function and Genetics. 2008;72: 731–740. doi:10.1002/prot.21956

80. Kuser PR, Krauchenco S, Antunes OAC, Polikarpov I. The high resolution crystal structure of yeast hexokinase PII with the correct primary sequence provides new insights into its mechanism of action. Journal of Biological Chemistry. 2000;275: 20814–20821. doi:10.1074/jbc.M910412199

81. Shoham M, Steitz TA. Crystallographic Studies and Model Building of ATP at the Active Site of Hexokinase. J Mol Biol. 1980;140: 1–14.

82. Steitz TA, Shoham M, Bennett WS. Structural dynamics of yeast hexokinase during catalysis. Philosophical Transactions of the Royal Society of London B, Biological Sciences. 1981;293: 43–52. doi:10.1098/RSTB.1981.0058

83. Kuettner EB, Kettner K, Keim A, Svergun DI, Volke D, Singer D, et al. Crystal structure of hexokinase KlHxk1 of kluyveromyces lactis: A molecular basis for understanding the control of yeast hexokinase functions via covalent modification and oligomerization. Journal of Biological Chemistry. 2010;285: 41019–41033. doi:10.1074/jbc.M110.185850

84. He C, Chen J, Wang H, Wan Y, Zhou J, Dan Z, et al. Crystal structures of rice hexokinase 6 with a series of substrates shed light on its enzymatic mechanism. Biochem Biophys Res Commun. 2019;515: 614–620. doi:10.1016/J.BBRC.2019.05.139

85. Feng J, Zhao S, Chen X, Wang W, Dong W, Chen J, et al. Biochemical and structural study of Arabidopsis hexokinase 1. Acta Crystallogr D Biol Crystallogr. 2015;71: 367–375. doi:10.1107/S1399004714026091

86. Aleshin AE, Zeng C, Bourenkov GP, Bartunik HD, Fromm HJ, Honzatko RB. The mechanism of regulation of hexokinase: New insights from the crystal structure of recombinant human brain hexokinase complexed with glucose and glucose-6-phosphate. Structure. 1998;6: 39–50. doi:10.1016/S0969-2126(98)00006-9

87. Nishimasu H, Fushinobu S, Shoun H, Wakagi T. Crystal Structures of an ATP-dependent Hexokinase with Broad Substrate Specificity from the Hyperthermophilic Archaeon Sulfolobus tokodaii. Journal of Biological Chemistry. 2007;282: 9923–9931. doi:10.1074/JBC.M610678200

88. Kamata K, Mitsuya M, Nishimura T, Eiki JI, Nagata Y. Structural basis for allosteric regulation of the monomeric allosteric enzyme human glucokinase. Structure. 2004;12: 429–438. doi:10.1016/j.str.2004.02.005

89. Nawaz MH, Ferreira JC, Nedyalkova L, Zhu H, Carrasco-López C, Kirmizialtin S, et al. The catalytic inactivation of the N-half of human hexokinase 2 and structural and biochemical characterization of its mitochondrial conformation. Biosci Rep. 2018;38: 1–17. doi:10.1042/BSR20171666

90. Aleshin AE, Kirby C, Liu X, Bourenkov GP, Bartunik HD, Fromm HJ, et al. Crystal structures of mutant monomeric hexokinase I reveal multiple ADP binding sites and conformational changes relevant to allosteric regulation. J Mol Biol. 2000;296: 1001–1015. doi:10.1006/JMBI.1999.3494

91. Aleshin AE, Zeng C, Bartunik HD, Fromm HJ, Honzatko RB. Regulation of hexokinase I: crystal structure of recombinant human brain hexokinase complexed with glucose and phosphate. J Mol Biol. 1998;282: 345–357. doi:10.1006/JMBI.1998.2017

92. Mulichak AM, Wilson JE, Padmanabhan K, Michael Garavito R. The structure of mammalian hexokinase-1. Nature Structural Biology 1998;5: 555–560. doi:10.1038/811

93. Anderson CM, Stenkamp RE, Steitz TA. Sequencing a protein by X-ray crystallography: II. Refinement of yeast hexokinase B Co-ordinates and sequence at 2.1 Å resolution. J Mol Biol. 1978;123: 15–33. doi:10.1016/0022-2836(78)90374-1

94. Stoddard PR, Lynch EM, Farrell DP, dosey AM, diMaio F, Williams TA, et al. Polymerization in the actin ATPase clan regulates hexokinase activity in yeast. Science. 2020;367: 1039–1042. doi:10.1126/science.aay5359

95. Cho J Il, Ryoo N, Eom JS, Lee DW, Kim HB, Jeong SW, et al. Role of the rice hexokinases OsHXK5 and OsHXK6 as glucose sensors. Plant Physiol. 2009;149: 745–759. doi:10.1104/pp.108.131227

96. Rosano C, Sabini E, Rizzi M, Deriu D, Murshudov G, Bianchi M, et al. Binding of non-catalytic ATP to human hexokinase I highlights the structural components for enzyme-membrane association control. Structure. 1999;7: 1427–1437. doi:10.1016/S0969-2126(00)80032-5

97. Rose IA, Warms JVB. Mitochondrial Hexokinase: Release, Rebinding, and Location. Journal of Biological Chemistry. 1967;242: 1635–1645. doi:10.1016/S0021-9258(18)96139-9

98. Koshland DE. The Key–Lock Theory and the Induced Fit Theory. Angewandte Chemie International Edition in English. 1995;33: 2375–2378. doi:10.1002/ANIE.199423751

99. McDonald RC, Steitz TA, Engelman DM. Yeast Hexokinase in Solution Exhibits a Large Conformational Change upon Binding Glucose or Glucose 6-Phosphate. Biochemistry. 1979;18: 338–342. Available: https://pubs.acs.org/sharingguidelines

100. Steitz TA, Flatterick RJ, Anderson WF, Anderson CM. High resolution X-ray structure of yeast hexokinase, an allosteric protein exhibiting a non-symmetric arrangement of subunits. J Mol Biol. 1976;104: 197–222. doi:10.1016/0022-2836(76)90009-7

101. Jeong EJ, Park K, Joung HA, Lee CS, Seol DW, Chung BH, et al. Detection of glucose-induced conformational change in hexokinase II using fluorescence complementation assay. Biotechnol Lett. 2007;29: 797–802. doi:10.1007/S10529-007-9313-X

102. Martinez JA, Larion M, Conejo MS, Porter CM, Miller BG. Role of connecting loop I in catalysis and allosteric regulation of human glucokinase. Protein Science. 2014;23: 915–922. doi:10.1002/PRO.2473

103. Liu X, Kim CS, Kurbanov FT, Honzatko RB, Fromm HJ. Dual mechanisms for glucose 6-phosphate inhibition of human brain hexokinase. Journal of Biological Chemistry. 1999;274: 31155–31159. doi:10.1074/jbc.274.44.31155

104. Ferreira JC, Khrbtli AR, Shetler CL, Mansoor S, Ali L, Sensoy O, et al. Linker residues regulate the activity and stability of hexokinase 2, a promising anticancer target. Journal of Biological Chemistry. 2021;296: 100071. doi:10.1074/JBC.RA120.015293

105. Ning J, Purich DL, Fromm HJ. Studies on the Kinetic Mechanism and Allosteric Nature of Bovine Brain Hexokinase. Journal of Biological Chemistry. 1969;244: 3840–3846. doi:10.1016/S0021-9258(17)36426-8

106. Lueck JD, Fromm HJ. Kinetics, Mechanism, and Regulation of Rat Skeletal Muscle Hexokinase. J Biol Chem. 1974;249: 1341–1347.

107. Fromm HJ, Zewe V. Kinetic Studies of Yeast Hexokinase. J Biol Chem. 1962;237: 3027–3032.

108. Farooq Z, Ismail H, Bhat SA, Layden BT, Khan MW. Aiding Cancer's "Sweet Tooth": Role of Hexokinases in Metabolic Reprogramming. Life. 2023;13: 946. doi:10.3390/LIFE13040946

109. Guo D, Meng Y, Jiang X, Lu Z. Hexokinases in cancer and other pathologies. Cell Insight. 2023;2: 100077. doi:10.1016/J.CELLIN.2023.100077

110. Wilson JE. Isozymes of mammalian hexokinase: Structure, subcellular localization and metabolic function. Journal of Experimental Biology. 2003;206: 2049–2057. doi:10.1242/jeb.00241

111. Ardehali H, Yano Y, Printz RL, Koch S, Whitesell RR, May JM, et al. Functional Organization of Mammalian Hexokinase II. Journal of Biological Chemistry. 1996;271: 1849–1852. doi:10.1074/jbc.271.4.1849

112. Tsai HJ, Wilson JE. Functional Organization of Mammalian Hexokinases: Both N- and C-Terminal Halves of the Rat Type II Isozyme Possess Catalytic Sites. Arch Biochem Biophys. 1996;329: 17–23. doi:10.1006/ABBI.1996.0186

113. Ardehali H, Printz RL, Whitesell RR, May JM, Granner DK. Functional Interaction between the N- and C-terminal Halves of Human Hexokinase II. Journal of Biological Chemistry. 1999;274: 15986–15989. doi:10.1074/JBC.274.23.15986

114. White TK, Wilson JE. Isolation and characterization of the discrete N- and C-terminal halves of rat brain hexokinase: Retention of full catalytic activity in the isolated C-terminal half. Arch Biochem Biophys. 1989;274: 375–393. doi:10.1016/0003-9861(89)90451-7

115. Tsai HJ, Wilson JE. Functional Organization of Mammalian Hexokinases: Characterization of Chimeric Hexokinases Constructed from the N- and C-Terminal Domains of the Rat

Type I and Type II Isozymes. Arch Biochem Biophys. 1995;316: 206–214. doi:10.1006/ABBI.1995.1029

116. Heimberg H, De Vos A, Moens K, Quartier E, Bouwens L, Pipeleers D, et al. The glucose sensor protein glucokinase is expressed in glucagon-producing alpha-cells. Proceedings of the National Academy of Sciences. 1996;93: 7036–7041. doi:10.1073/PNAS.93.14.7036

117. Pusec CM, De Jesus A, Khan MW, Terry AR, Ludvik AE, Xu K, et al. Hepatic HKDC1 expression contributes to liver metabolism. Endocrinology. 2019;160: 313–330. doi:10.1210/en.2018-00887

118. Sui D, Wilson JE. Structural Determinants for the Intracellular Localization of the Isozymes of Mammalian Hexokinase: Intracellular Localization of Fusion Constructs Incorporating Structural Elements from the Hexokinase Isozymes and the Green Fluorescent Protein. Arch Biochem Biophys. 1997;345: 111–125. doi:10.1006/ABBI.1997.0241

119. Katzen HM, Schimke RT. Multiple forms of hexokinase in the rat: tissue distribution, age dependency, and properties. Proc Natl Acad Sci U S A. 1965;54: 1218–1225. doi:10.1073/PNAS.54.4.1218

120. White JA, Liu W, Wilson JE. Isolation of the Promoter for Type I Hexokinase from Rat. Arch Biochem Biophys. 1996;335: 161–172. doi:10.1006/ABBI.1996.0494

121. Zeng C, Aleshin AE, Hardie JB, Harrison RW, Fromm HJ. ATP-binding site of human brain hexokinase as studied by molecular modeling and site-directed mutagenesis. Biochemistry. 1996;35: 13157–13164. doi:10.1021/BI960750E

122. Zhang X, Alshakhshir N, Zhao L. Glycolytic Metabolism, Brain Resilience, and Alzheimer's Disease. Front Neurosci. 2021;15: 662242. doi:10.3389/FNINS.2021.662242

123. Heikkinen S, Suppola S, Malkki M, Deeb SS, Jänne J, Laakso M. Mouse hexokinase II gene: Structure, cDNA, promoter analysis, and expression pattern. Mammalian Genome. 2000;11: 91–96. doi:10.1007/S003350010019

124. Wasserman DH. Insulin, Muscle Glucose Uptake, and Hexokinase: Revisiting the Road Not Taken. Physiology. 2022;37: 115–127. doi:10.1152/PHYSIOL.00034.2021

125. Sebastian S, Horton JD, Wilson JE. Anabolic Function of the Type II Isozyme of Hexokinase in Hepatic Lipid Synthesis. Biochem Biophys Res Commun. 2000;270: 886–891. doi:10.1006/BBRC.2000.2527

126. Kaselonis GL, McCabe ERB, Gray SM. Expression of Hexokinase 1 and Hexokinase 2 in Mammary Tissue of Nonlactating and Lactating Rats: Evaluation by RT–PCR. Mol Genet Metab. 1999;68: 371–374. doi:10.1006/MGME.1999.2923

127. Osawa H, Sutherland C, Robey RB, Printz RL, Granner DK. Analysis of the Signaling Pathway Involved in the Regulation of Hexokinase II Gene Transcription by Insulin. Journal of Biological Chemistry. 1996;271: 16690–16694. doi:10.1074/JBC.271.28.16690

128. Bhaskar PT, Nogueira V, Patra KC, Jeon S-M, Park Y, Robey RB, et al. mTORC1 Hyperactivity Inhibits Serum Deprivation-Induced Apoptosis via Increased Hexokinase II and GLUT1 Expression, Sustained Mcl-1 Expression, and Glycogen Synthase Kinase 3β Inhibition. Mol Cell Biol. 2009;29: 5136–5147. doi:10.1128/MCB.01946-08

129. Patra KC, Wang Q, Bhaskar PT, Miller L, Wang Z, Wheaton W, et al. Hexokinase 2 is required for tumor initiation and maintenance and its systemic deletion is therapeutic in mouse models of cancer. Cancer Cell. 2013;24: 213–228. doi:10.1016/j.ccr.2013.06.014

130. Wolf A, Agnihotri S, Micallef J, Mukherjee J, Sabha N, Cairns R, et al. Hexokinase 2 is a key mediator of aerobic glycolysis and promotes tumor growth in human glioblastoma

multiforme. Journal of Experimental Medicine. 2011;208: 313–326. doi:10.1084/jem.20101470

131. Huang X, Liu M, Sun H, Wang F, Xie X, Chen X, et al. HK2 is a radiation resistant and independent negative prognostic factor for patients with locally advanced cervical squamous cell carcinoma. Int J Clin Exp Pathol. 2015;8: 4054. Available: /pmc/articles/PMC4466980/

132. Meng YM, Jiang X, Zhao X, Meng Q, Wu S, Chen Y, et al. Hexokinase 2-driven glycolysis in pericytes activates their contractility leading to tumor blood vessel abnormalities. Nature Communications 2021;12: 1–19. doi:10.1038/s41467-021-26259-y

133. Katagiri M, Karasawa H, Takagi K, Nakayama S, Yabuuchi S, Fujishima F, et al. Hexokinase 2 in colorectal cancer: a potent prognostic factor associated with glycolysis, proliferation and migration. Histol Histopathol. 2017;32: 351–360. doi:10.14670/HH-11-799

134. Liu Y, Wu K, Shi L, Xiang F, Tao K, Wang G. Prognostic significance of the metabolic marker hexokinase-2 in Various solid tumors: A meta-analysis. PLoS One. 2016;11: 1–13. doi:10.1371/journal.pone.0166230

135. Cui N, Li L, Feng Q, Ma HM, Lei D, Zheng PS. Hexokinase 2 Promotes Cell Growth and Tumor Formation Through the Raf/MEK/ERK Signaling Pathway in Cervical Cancer. Front Oncol. 2020;10: 581208. doi:10.3389/FONC.2020.581208

136. Li WC, Huang CH, Hsieh YT, Chen TY, Cheng LH, Chen CY, et al. Regulatory Role of Hexokinase 2 in Modulating Head and Neck Tumorigenesis. Front Oncol. 2020;10: 1–11. doi:10.3389/fonc.2020.00176

137. DeWaal D, Nogueira V, Terry AR, Patra KC, Jeon SM, Guzman G, et al. Hexokinase-2 depletion inhibits glycolysis and induces oxidative phosphorylation in hepatocellular carcinoma and sensitizes to metformin. Nat Commun. 2018;9: 1–14. doi:10.1038/s41467-017-02733-4

138. Perrin-cocon L, Vidalain P, Jacquemin C, Aublin-gex A, Olmstead K, Panthu B, et al. A hexokinase isoenzyme switch in human liver cancer cells promotes lipogenesis and enhances innate immunity. Commun Biol. 2021;4: 1–15. doi:10.1038/s42003-021-01749-3

139. Liu C, Wang X, Zhang Y. The Roles of HK2 on Tumorigenesis of Cervical Cancer. Technol Cancer Res Treat. 2019;18: 1–9. doi:10.1177/1533033819871306

140. Liberti M V, Locasale JW. The Warburg Effect: How Does it Benefit Cancer Cells? Trends Biochem Sci. 2016;41: 211–218. doi:10.1016/j.tibs.2016.01.004

141. Gwak GY, Yoon JH, Kim KM, Lee HS, Chung JW, Gores GJ. Hypoxia stimulates proliferation of human hepatoma cells through the induction of hexokinase II expression. J Hepatol. 2005;42: 358–364. doi:10.1016/J.JHEP.2004.11.020

142. Jiang S, Zhang LF, Zhang HW, Hu S, Lu MH, Liang S, et al. A novel miR-155/miR-143 cascade controls glycolysis by regulating hexokinase 2 in breast cancer cells. EMBO Journal. 2012;31: 1985–1998. doi:10.1038/EMBOJ.2012.45

143. Palmieri D, Fitzgerald D, Shreeve SM, Hua E, Bronder JL, Weil RJ, et al. Analyses of resected human brain metastases of breast cancer reveal the association between up-regulation of hexokinase 2 and poor prognosis. Molecular Cancer Research. 2009;7: 1438–1445. doi:10.1158/1541-7786.MCR-09-0234

144. Gong L, Cui Z, Chen P, Han H, Peng J, Leng X. Reduced survival of patients with hepatocellular carcinoma expressing hexokinase II. Medical Oncology. 2012;29: 909–914. doi:10.1007/s12032-011-9841-z

145. Lee HJ, Li CF, Ruan D, He J, Montal ED, Lorenz S, et al. Non-proteolytic ubiquitination of Hexokinase 2 by HectH9 controls tumor metabolism and cancer stem cell expansion. Nature Communications 2019;10: 1–16. doi:10.1038/s41467-019-10374-y

146. Wu J, Hu L, Wu F, Zou L, He T, Wu J, et al. Poor prognosis of hexokinase 2 overexpression in solid tumors of digestive system: a meta-analysis. Oncotarget. 2017;8: 32332–32344. doi:10.18632/ONCOTARGET.15974

147. Wilson DF, Cember ATJ, Matschinsky FM. The thermodynamic basis of glucose-stimulated insulin release: a model of the core mechanism. Physiol Rep. 2017;5. doi:10.14814/PHY2.13327

148. Matschinsky FM, Wilson DF. The central role of glucokinase in glucose homeostasis: A perspective 50 years after demonstrating the presence of the enzyme in islets of Langerhans. Front Physiol. 2019;10: 430287. doi:10.3389/FPHYS.2019.00148

149. Ashcroft FM, Lloyd M, Haythorne EA. Glucokinase activity in diabetes: too much of a good thing? Trends in Endocrinology and Metabolism. 2023;34: 119–130. doi:10.1016/j.tem.2022.12.007

150. Agius L. Hormonal and Metabolite Regulation of Hepatic Glucokinase. Annu Rev Nutr. 2016;36: 389–415. doi:10.1146/ANNUREV-NUTR-071715-051145

151. Gersing S, Cagiada M, Gebbia M, Gjesing AP, Coté AG, Seesankar G, et al. A comprehensive map of human glucokinase variant activity. Genome Biology 2023;24: 1–23. doi:10.1186/S13059-023-02935-8

152. Njølstad PR, Sagen J V., Bjørkhaug L, Odili S, Shehadeh N, Bakry D, et al. Permanent Neonatal Diabetes Caused by Glucokinase DeficiencyInborn Error of the Glucose-Insulin Signaling Pathway. Diabetes. 2003;52: 2854–2860. doi:10.2337/DIABETES.52.11.2854

153. Osbak KK, Colclough K, Saint-Martin C, Beer NL, Bellanné-Chantelot C, Ellard S, et al. Update on mutations in glucokinase (GCK), which cause maturity-onset diabetes of the young, permanent neonatal diabetes, and hyperinsulinemic hypoglycemia. Hum Mutat. 2009;30: 1512–1526. doi:10.1002/HUMU.21110

154. Cuesta-Muñoz AL, Huopio H, Otonkoski T, Gomez-Zumaquero JM, Näntö-Salonen K, Rahier J, et al. Severe Persistent Hyperinsulinemic Hypoglycemia due to a De Novo Glucokinase Mutation. Diabetes. 2004;53: 2164–2168. doi:10.2337/DIABETES.53.8.2164

155. Kim SH. Maturity-Onset Diabetes of the Young: What Do Clinicians Need to Know? Diabetes Metab J. 2015;39: 468–477. doi:10.4093/DMJ.2015.39.6.468

156. Bell GI, Polonsky KS. Diabetes mellitus and genetically programmed defects in β-cell function. Nature 2001 414:6865. 2001;414: 788–791. doi:10.1038/414788a

157. Wyatt E, Wu R, Rabeh W, Park HW, Ghanefar M, Ardehali H. Regulation and Cytoprotective Role of Hexokinase III. PLoS One. 2010;5: e13823. doi:10.1371/JOURNAL.PONE.0013823

158. Irwin DM, Tan H. Molecular evolution of the vertebrate hexokinase gene family: Identification of a conserved fifth vertebrate hexokinase gene. Comp Biochem Physiol Part D Genomics Proteomics. 2008;3: 96–107. doi:10.1016/J.CBD.2007.11.002

159. Guo C, Ludvik AE, Arlotto ME, Hayes MG, Armstrong LL, Scholtens DM, et al. Coordinated regulatory variation associated with gestational hyperglycaemia regulates

expression of the novel hexokinase HKDC1. Nat Commun. 2015;6: 4–11. doi:10.1038/ncomms7069

160. Zapater JL, Lednovich KR, Khan MW, Pusec CM, Layden BT. Hexokinase domain-containing protein-1 in metabolic diseases and beyond. Trends in Endocrinology and Metabolism. 2022;33: 72–84. doi:10.1016/j.tem.2021.10.006

161. Zapater JL, Lednovich KR, Layden BT. The Role of Hexokinase Domain Containing Protein-1 in Glucose Regulation During Pregnancy. Curr Diab Rep. 2021;21. doi:10.1007/s11892-021-01394-4

162. Ludvik AE, Pusec CM, Priyadarshini M, Angueira AR, Guo C, Lo A, et al. HKDC1 Is a Novel Hexokinase Involved in Whole-Body Glucose Use. Endocrinology. 2016;157: 3452–3461. doi:10.1210/EN.2016-1288

163. Larion M, Hansen AL, Zhang F, Bruschweiler-Li L, Tugarinov V, Miller BG, et al. Kinetic Cooperativity in Human Pancreatic Glucokinase Originates from Millisecond Dynamics of the Small Domain. Angewandte Chemie International Edition. 2015;54: 8129–8132. doi:10.1002/ANIE.201501204

164. Carl Whittington A, Larion M, Bowler JM, Ramsey KM, Brüschweiler R, Miller BG. Dual allosteric activation mechanisms in monomeric human glucokinase. Proc Natl Acad Sci U S A. 2015;112: 11553–11558. doi:10.1073/PNAS.1506664112

165. Storer AC, Cornish-Bowden A. Kinetics of Rat Liver Glucokinase Co-operative interactions with glucose at physiologically significant concentrations. 1976;159: 7–14.

166. Ghosh A, Ronner P, Cheong E, Khalid P, Matschinskys FM. The role of ATP and free ADP in metabolic coupling during fuel-stimulated insulin release from islet beta-cells in the

isolated perfused rat pancreas. Journal of Biological Chemistry. 1991;266: 22887–22892. doi:10.1016/S0021-9258(18)54437-9

167. Doliba NM, Qin W, Najafi H, Liu C, Buettger CW, Sotiris J, et al. Glucokinase activation repairs defective bioenergetics of islets of Langerhans isolated from type 2 diabetics. Am J Physiol Endocrinol Metab. 2012;302: 87–102. doi:10.1152/AJPENDO.00218.2011

168. Matschinsky F, Liang Y, Kesavan P, Wang L, Froguel P, Velho G, et al. Glucokinase as pancreatic beta cell glucose sensor and diabetes gene. J Clin Invest. 1993;92: 2092–2098. doi:10.1172/JCI116809

169. Moede T, Leibiger B, Vaca Sanchez P, Daré E, Köhler M, Muhandiramlage TP, et al. Glucokinase intrinsically regulates glucose sensing and glucagon secretion in pancreatic alpha cells. Scientific Reports 2020 10:1. 2020;10: 1–11. doi:10.1038/s41598-020-76863-z

170. Basco D, Zhang Q, Salehi A, Tarasov A, Dolci W, Herrera P, et al. α-cell glucokinase suppresses glucose-regulated glucagon secretion. Nature Communications 2018;9: 1–9. doi:10.1038/s41467-018-03034-0

171. Mayer SE, Mayfield AC, Haas JA. Heart Muscle Hexokinase: Subcellular Distribution and Inhibition by Glucose 6-Phosphate. Mol Pharmacol. 1966;2: 393–405.

172. Xie G, Wilson JE. Rat brain hexokinase: The hydrophobie N-terminus of the mitochondrially bound enzyme is inserted in the lipid bilayer. Arch Biochem Biophys. 1988;267: 803–810. doi:10.1016/0003-9861(88)90090-2

173. Azoulay-Zohar H, Israelson A, Abu-Hamad S, Shoshan-Barmatz V. In self-defence: hexokinase promotes voltage-dependent anion channel closure and prevents mitochondria-mediated apoptotic cell death. Biochemical Journal. 2004;377: 347–355. doi:10.1042/BJ20031465

174. Majewski N, Nogueira V, Bhaskar P, Coy PE, Skeen JE, Gottlob K, et al. Hexokinase-mitochondria interaction mediated by Akt is required to inhibit apoptosis in the presence or absence of Bax and Bak. Mol Cell. 2004;16: 819–830. doi:10.1016/J.MOLCEL.2004.11.014

175. Haloi N, Wen PC, Cheng Q, Yang M, Natarajan G, Camara AKS, et al. Structural basis of complex formation between mitochondrial anion channel VDAC1 and Hexokinase-II. Commun Biol. 2021;4: 1–12. doi:10.1038/s42003-021-02205-y

176. Camara AKS, Zhou YF, Wen PC, Tajkhorshid E, Kwok WM. Mitochondrial VDAC1: A key gatekeeper as potential therapeutic target. Front Physiol. 2017;8: 242373. doi:10.3389/FPHYS.2017.00460

177. John S, Weiss JN, Ribalet B. Subcellular Localization of Hexokinases I and II Directs the Metabolic Fate of Glucose. PLoS One. 2011;6: e17674. doi:10.1371/JOURNAL.PONE.0017674

178. Codocedo JF, Landreth GE. The intersection of metabolism and inflammation is governed by the intracellular topology of hexokinases and the metabolic fate of glucose. Immunometabolism (Cobham (Surrey, England). 2022;4: e00011. doi:10.1097/IN9.0000000000000011

179. Xu S, Herschman HR. A tumor agnostic therapeutic strategy for hexokinase 1–null/hexokinase 2–positive cancers. Cancer Res. 2019;79: 5907–5914. doi:10.1158/0008-5472.CAN-19-1789

180. De Jesus A, Keyhani-Nejad F, Pusec CM, Goodman L, Geier JA, Stoolman JS, et al. Hexokinase 1 cellular localization regulates the metabolic fate of glucose. Mol Cell. 2022;82: 1261-1277.e9. doi:10.1016/j.molcel.2022.02.028

181. Roberts DJ, Tan-Sah VP, Smith JM, Miyamoto S. Akt phosphorylates HK-II at Thr-473 and increases mitochondrial HK-II association to protect cardiomyocytes. Journal of Biological Chemistry. 2013;288: 23798–23806. doi:10.1074/jbc.M113.482026

182. McCommis KS, Douglas DL, Krenz M, Baines CP. Cardiac-specific Hexokinase 2 Overexpression Attenuates Hypertrophy by Increasing Pentose Phosphate Pathway Flux. Journal of the American Heart Association: Cardiovascular and Cerebrovascular Disease. 2013;2. doi:10.1161/JAHA.113.000355

183. Sun L, Shukair S, Naik TJ, Moazed F, Ardehali H. Glucose Phosphorylation and Mitochondrial Binding Are Required for the Protective Effects of Hexokinases I and II. Mol Cell Biol. 2008;28: 1007–1017. doi:10.1128/MCB.00224-07

184. Manning BD, Toker A. AKT/PKB Signaling: Navigating the Network. Cell. 2017;169: 381–405. doi:10.1016/J.CELL.2017.04.001

185. Pantic B, Trevisan E, Citta A, Rigobello MP, Marin O, Bernardi P, et al. Myotonic dystrophy protein kinase (DMPK) prevents ROS-induced cell death by assembling a hexokinase II-Src complex on the mitochondrial surface. Cell Death & Disease 2013 4:10. 2013;4: e858–e858. doi:10.1038/cddis.2013.385

186. Ciscato F, Ferrone L, Masgras I, Laquatra C, Rasola A. Hexokinase 2 in Cancer: A Prima Donna Playing Multiple Characters. Int J Mol Sci. 2021;22. doi:10.3390/ijms22094716

187. Chiara F, Castellaro D, Marin O, Petronilli V, Brusilow WS, Juhaszova M, et al. Hexokinase II detachment from mitochondria triggers apoptosis through the permeability transition pore independent of voltage-dependent anion channels. PLoS One. 2008;3. doi:10.1371/journal.pone.0001852

188. Pastorino JG, Shulga N, Hoek JB. Mitochondrial binding of hexokinase II inhibits Bax-induced cytochrome c release and apoptosis. Journal of Biological Chemistry. 2002;277: 7610–7618. doi:10.1074/jbc.M109950200

189. Da-Silva WS, Gómez-Puyou A, De Gómez-Puyou MT, Moreno-Sanchez R, De Felice FG, De Meis L, et al. Mitochondrial bound hexokinase activity as a preventive antioxidant defense. Steady-state ADP formation as a regulatory mechanism of membrane potential and reactive oxygen species generation in mitochondria. Journal of Biological Chemistry. 2004;279: 39846–39855. doi:10.1074/jbc.M403835200

190. Wu R, Wyatt E, Chawla K, Tran M, Ghanefar M, Laakso M, et al. Hexokinase II knockdown results in exaggerated cardiac hypertrophy via increased ROS production. EMBO Mol Med. 2012;4: 633–646. doi:10.1002/EMMM.201200240

191. Bauer TM, Murphy E. Role of Mitochondrial Calcium and the Permeability Transition Pore in Regulating Cell Death. Circ Res. 2020;126: 280–293. doi:10.1161/CIRCRESAHA.119.316306

192. Mailloux RJ, Dumouchel T, Aguer C, Dekemp R, Beanlands R, Harper ME. Hexokinase II acts through UCP3 to suppress mitochondrial reactive oxygen species production and maintain aerobic respiration. Biochemical Journal. 2011;437: 301–311. doi:10.1042/BJ20110571

193. Filadi R, Theurey P, Pizzo P. The endoplasmic reticulum-mitochondria coupling in health and disease: Molecules, functions and significance. Cell Calcium. 2017;62: 1–15. doi:10.1016/J.CECA.2017.01.003

194. Bernardi P, Rasola A. Calcium and cell death: The mitochondrial connection. Subcell Biochem. 2007;45: 481–506. doi:10.1007/978-1-4020-6191-2_18

195. Shangguan X, He J, Ma Z, zhang W, Ji Y, Shen K, et al. SUMOylation controls the binding of hexokinase 2 to mitochondria and protects against prostate cancer tumorigenesis. Nat Commun. 2021;12. doi:10.1038/s41467-021-22163-7

196. Martorana F, Motta G, Pavone G, Motta L, Stella S, Vitale SR, et al. AKT Inhibitors: New Weapons in the Fight Against Breast Cancer? Front Pharmacol. 2021;12: 662232. doi:10.3389/FPHAR.2021.662232

197. Li H, Lu S, Chen Y, Zheng L, Chen L, Ding H, et al. AKT2 phosphorylation of hexokinase 2 at T473 promotes tumorigenesis and metastasis in colon cancer cells via NF-κB, HIF1α, MMP2, and MMP9 upregulation. Cell Signal. 2019;58: 99–110. doi:10.1016/J.CELLSIG.2019.03.011

198. Miyamoto S, Murphy AN, Brown JH. Akt mediates mitochondrial protection in cardiomyocytes through phosphorylation of mitochondrial hexokinase-II. Cell Death & Differentiation 2008 15:3. 2007;15: 521–529. doi:10.1038/sj.cdd.4402285

199. Arzoine L, Zilberberg N, Ben-Romano R, Shoshan-Barmatz V. Voltage-dependent anion channel 1-based peptides interact with hexokinase to prevent its anti-apoptotic activity. Journal of Biological Chemistry. 2009;284: 3946–3955. doi:10.1074/jbc.M803614200

200. Chen Q, Feng J, Wu J, Yu Z, Zhang W, Chen Y, et al. HKDC1 C-terminal based peptides inhibit extranodal natural killer/T-cell lymphoma by modulation of mitochondrial function and EBV suppression. Leukemia 2020;34: 2736–2748. doi:10.1038/s41375-020-0801-5

201. Chen X, Lv Y, Sun Y, Zhang H, Xie W, Zhong L, et al. PGC1β regulates breast tumor growth and metastasis by SREBP1-mediated HKDC1 expression. Front Oncol. 2019;9: 453138. doi:10.3389/FONC.2019.00290

202. Khan MW, Terry AR, Priyadarshini M, Ilievski V, Farooq Z, Guzman G, et al. The hexokinase “HKDC1” interaction with the mitochondria is essential for liver cancer progression. Cell Death & Disease 2022;13: 1–17. doi:10.1038/s41419-022-04999-z

203. Boukouris AE, Zervopoulos SD, Michelakis ED. Metabolic Enzymes Moonlighting in the Nucleus: Metabolic Regulation of Gene Transcription. Trends Biochem Sci. 2016;41: 712–730. doi:10.1016/j.tibs.2016.05.013

204. Konings AWT. Glucose oxidation in nuclei isolated from rat thymus. Life Sci. 1969;8: 1009–1016. doi:10.1016/0024-3205(69)90208-2

205. Sundararaj KP, Wood RE, Ponnusamy S, Salas AM, Szulc Z, Bielawska A, et al. Rapid Shortening of Telomere Length in Response to Ceramide Involves the Inhibition of Telomere Binding Activity of Nuclear Glyceraldehyde-3-phosphate Dehydrogenase. Journal of Biological Chemistry. 2004;279: 6152–6162. doi:10.1074/JBC.M310549200

206. Hara MR, Agrawal N, Kim SF, Cascio MB, Fujimuro M, Ozeki Y, et al. S-nitrosylated GAPDH initiates apoptotic cell death by nuclear translocation following Siah1 binding. Nature Cell Biology 2005;7: 665–674. doi:10.1038/ncb1268

207. Popanda O, Fox G, Thielmann HW. Modulation of DNA polymerases α, δ and ε by lactate dehydrogenase and 3-phosphoglycerate kinase. Biochimica et Biophysica Acta - Gene Structure and Expression. 1998;1397: 102–117. doi:10.1016/S0167-4781(97)00229-7

208. Cieśla M, Mierzejewska J, Adamczyk M, Farrants AKÖ, Boguta M. Fructose bisphosphate aldolase is involved in the control of RNA polymerase III-directed transcription. Biochim Biophys Acta Mol Cell Res. 2014;1843: 1103–1110. doi:10.1016/J.BBAMCR.2014.02.007

209. Enzo E, Santinon G, Pocaterra A, Aragona M, Bresolin S, Forcato M, et al. Aerobic glycolysis tunes YAP/TAZ transcriptional activity. EMBO J. 2015;34: 1349–1370. doi:10.15252/EMBJ.201490379

210. Yalcin A, Clem BF, Simmons A, Lane A, Nelson K, Clem AL, et al. Nuclear targeting of 6-phosphofructo-2-kinase (PFKFB3) increases proliferation via cyclin-dependent kinases. Journal of Biological Chemistry. 2009;284: 24223–24232. doi:10.1074/JBC.M109.016816

211. Matsuda S, Adachi J, Ihara M, Tanuma N, Shima H, Kakizuka A, et al. Nuclear pyruvate kinase M2 complex serves as a transcriptional coactivator of arylhydrocarbon receptor. Nucleic Acids Res. 2016;44: 636–647. doi:10.1093/NAR/GKV967

212. Sutendra G, Kinnaird A, Dromparis P, Paulin R, Stenson TH, Haromy A, et al. A nuclear pyruvate dehydrogenase complex is important for the generation of Acetyl-CoA and histone acetylation. Cell. 2014;158: 84–97. doi:10.1016/j.cell.2014.04.046

213. Sternisha SM, Miller BG. Molecular and cellular regulation of human glucokinase. Arch Biochem Biophys. 2019;663: 199–213. doi:10.1016/j.abb.2019.01.011

214. Salgado M, Ordenes P, Villagra M, Uribe E, García-Robles M de los A, Tarifeño-Saldivia E. When a Little Bit More Makes the Difference: Expression Levels of GKRP Determines the Subcellular Localization of GK in Tanycytes. Front Neurosci. 2019;13. doi:10.3389/FNINS.2019.00275

215. Shiota C, Coffey J, Grimsby J, Grippo JF, Magnuson MA. Nuclear Import of Hepatic Glucokinase Depends upon Glucokinase Regulatory Protein, whereas Export Is Due to a Nuclear Export Signal Sequence in Glucokinase. Journal of Biological Chemistry. 1999;274: 37125–37130. doi:10.1074/JBC.274.52.37125

216. Beck T, Miller BG. Structural Basis for Regulation of Human Glucokinase by Glucokinase Regulatory Protein. Biochemistry. 2013;52: 6232–6239. doi:10.1021/bi400838t

217. Pautsch A, Stadler N, Löhle A, Rist W, Berg A, Glocker L, et al. Crystal structure of glucokinase regulatory protein. Biochemistry. 2013;52: 3523–3531. doi:10.1021/BI4000782

218. Anderka O, Boyken J, Aschenbach U, Batzer A, Boscheinen O, Schmoll D. Biophysical Characterization of the Interaction between Hepatic Glucokinase and Its Regulatory Protein. Journal of Biological Chemistry. 2008;283: 31333–31340. doi:10.1074/jbc.m805434200

219. van Schaftingen E. A protein from rat liver confers to glucokinase the property of being antagonistically regulated by fructose 6-phosphate and fructose 1-phosphate. Eur J Biochem. 1989;179: 179–184. doi:10.1111/J.1432-1033.1989.TB14538.X

220. Johansson BB, Fjeld K, Solheim MH, Shirakawa J, Zhang E, Keindl M, et al. Nuclear import of glucokinase in pancreatic beta-cells is mediated by a nuclear localization signal and modulated by SUMOylation. Mol Cell Endocrinol. 2017;454: 146–157. doi:10.1016/J.MCE.2017.06.020

221. Aukrust I, Bjorkhaug L, Negahdar M, Molnes J, Johansson BB, Müller Y, et al. SUMOylation of pancreatic glucokinase regulates its cellular stability and activity. Journal of Biological Chemistry. 2013;288: 5951–5962. doi:10.1074/jbc.M112.393769

222. Ma H, Bloom LM, Dakin SE, Walsh CT, Botstein D. The 15 N-terminal amino acids of hexokinase II are not required for in vivo function: Analysis of a truncated form of hexokinase II in Saccharomyces cerevisiae. Proteins: Structure, Function, and Bioinformatics. 1989;5: 218–223. doi:10.1002/prot.340050305

223. Lobo Z, Maitra PK. Physiological role of glucose-phosphorylating enzymes in Saccharomyces cerevisiae. Arch Biochem Biophys. 1977;182: 639–645. doi:10.1016/0003-9861(77)90544-6

224. Soncini SR, Chandrashekarappa DG, Augustine DA, Callahan KP, O'Donnell AF, SchmidtI MC. Spontaneous mutations that confer resistance to 2-deoxyglucose act through Hxk2 and Snf1 pathways to regulate gene expression and HXT endocytosis. PLoS Genet. 2020;16: 1–30. doi:10.1371/journal.pgen.1008484

225. Boonekamp FJ, Knibbe E, Vieira-Lara MA, Daran J-M, Bakker BM, Daran-Lapujade P, et al. Full humanization of the glycolytic pathway in Saccharomyces cerevisiae. CellReports. 2022;39: 111010. doi:10.1016/j.celrep.2022.111010

226. Umekawa M, Hamada K, Isono N, Karita S. The Emi2 Protein of Saccharomyces cerevisiae is a Hexokinase Expressed under Glucose Limitation. J Appl Glycosci (1999). 2020;67: 103–109. doi:10.5458/jag.jag.jag-2020_0007

227. Hellemann E, Walker JL, Lesko MA, Chandrashekarappa DG, Schmidt MC, et al. Novel mutation in hexokinase 2 confers resistance to 2-deoxyglucose by altering protein dynamics. PLoS Genet. 2022. doi:10.1371/journal.pcbi.1009929

228. De Winde JH, Crauwels M, Hohmann S, Thevelein JM, Winderickx J. Differential requirement of the yeast sugar kinases for sugar sensing in establishing the catabolite-repressed state. Eur J Biochem. 1996;241: 633–643. doi:10.1111/j.1432-1033.1996.00633.x

229. Herrero P, Galíndez J, Ruiz N, Martínez-Campa C, Moreno F. Transcriptional regulation of the Saccharomyces cerevisiae HXK1, HXK2 and GLK1 genes. Yeast. 1995;11: 137–144. doi:10.1002/YEA.320110205

230. Rodríguez A, De La Cera T, Herrero P, Moreno F. The hexokinase 2 protein regulates the expression of the GLK1, HXK1 and HXK2 genes of Saccharomyces cerevisiae. Biochemical Journal. 2001;355: 625–631. doi:10.1042/bj3550625

231. Young ET, Dombek KM, Tachibana C, Ideker T. Multiple Pathways Are Co-regulated by the Protein Kinase Snf1 and the Transcription Factors Adr1 and Cat8. Journal of Biological Chemistry. 2003;278: 26146–26158. doi:10.1074/JBC.M301981200

232. Lesko MA, Chandrashekarappa DG, Jordahl EM, Oppenheimer KG, Bowman RW, Shang C, et al. Changing course: Glucose starvation drives nuclear accumulation of Hexokinase 2 in S. cerevisiae. PLoS Genet. 2023;19: e1010745. doi:10.1371/JOURNAL.PGEN.1010745

233. Entian KD, Frohlich KU. Saccharomyces cerevisiae mutants provide evidence of hexokinase PII as a bifunctional enzyme with catalytic and regulatory domains for triggering carbon catabolite repression. J Bacteriol. 1984;158: 29–35. doi:10.1128/jb.158.1.29-35.1984

234. Sanz P, Nieto A, Prieto JA. Glucose repression may involve processes with different sugar kinase requirements. J Bacteriol. 1996;178: 4721–4723. doi:10.1128/jb.178.15.4721-4723.1996

235. Schmidt GW, Welkenhuysen N, Ye T, Cvijovic M, Hohmann S. Mig1 localization exhibits biphasic behavior which is controlled by both metabolic and regulatory roles of the sugar kinases. Molecular Genetics and Genomics. 2020;295: 1489–1500. doi:10.1007/s00438-020-01715-4

236. Ahuatzi D, Herrero P, De La Cera T, Moreno F. The Glucose-regulated Nuclear Localization of Hexokinase 2 in Saccharomyces cerevisiae Is Mig1-dependent. Journal of Biological Chemistry. 2004;279: 14440–14446. doi:10.1074/jbc.M313431200

237. Ahuatzi D, Riera A, Peláez R, Herrero P, Moreno F. Hxk2 regulates the phosphorylation state of Mig1 and therefore its nucleocytoplasmic distribution. Journal of Biological Chemistry. 2007;282: 4485–4493. doi:10.1074/jbc.M606854200

238. Vega M, Riera A, Fernández-Cid A, Herrero P, Moreno F. Hexokinase 2 Is an intracellular glucose sensor of yeast cells that maintains the structure and activity of mig1 protein repressor complex. Journal of Biological Chemistry. 2016;291: 7267–7285. doi:10.1074/jbc.M115.711408

239. Elbing K, Ståhlberg A, Hohmann S, Gustafsson L. Transcriptional responses to glucose at different glycolytic rates in Saccharomyces cerevisiae. Eur J Biochem. 2004;271: 4855–4864. doi:10.1111/J.1432-1033.2004.04451.X

240. Moreno F, Herrero P. The hexokinase 2-dependent glucose signal transduction pathway of Saccharomyces cerevisiae. FEMS Microbiol Rev. 2002;26: 83–90. doi:10.1016/S0168-6445(01)00077-8

241. Krogan NJ, Cagney G, Yu H, Zhong G, Guo X, Ignatchenko A, et al. Global landscape of protein complexes in the yeast Saccharomyces cerevisiae. Nature 2006 440:7084. 2006;440: 637–643. doi:10.1038/nature04670

242. Gavin AC, Bösche M, Krause R, Grandi P, Marzioch M, Bauer A, et al. Functional organization of the yeast proteome by systematic analysis of protein complexes. Nature. 2002 415:6868. 2002;415: 141–147. doi:10.1038/415141a

243. Uetz P, Glot L, Cagney G, Mansfield TA, Judson RS, Knight JR, et al. A comprehensive analysis of protein–protein interactions in Saccharomyces cerevisiae. Nature. 2000;403: 623–627. doi:10.1038/35001009

244. Yu H, Braun P, Yildirim MA, Lemmens I, Venkatesan K, Sahalie J, et al. High-quality binary protein interaction map of the yeast interactome network. Science. 2008;322: 104–110. doi:10.1126/SCIENCE.1158684

245. McCartney RR, Chandrashekarappa DG, Zhang BB, Schmidt MC. Genetic analysis of resistance and sensitivity to 2-deoxyglucose in Saccharomyces cerevisiae. Genetics. 2014;198: 635–646. doi:10.1534/genetics.114.169060

246. Kraakman LS, Winderickx J, Thevelein JM, De Winde JH. Structure-function analysis of yeast hexokinase: Structural requirements for triggering cAMP signalling and catabolite repression. Biochemical Journal. 1999;343: 159–168. doi:10.1042/0264-6021:3430159

247. Kaps S, Kettner K, Migotti R, Kanashova T, Krause U, Rödel G, et al. Protein kinase Ymr291w/Tda1 is essential for glucose signaling in Saccharomyces cerevisiae on the level of hexokinase isoenzyme ScHxk2 phosphorylation. Journal of Biological Chemistry. 2015;290: 6243–6255. doi:10.1074/jbc.M114.595074

248. Morales FC, Lucia Bianconi M. Influence of the oligomeric state of yeast hexokinase isozymes on inactivation and unfolding by urea. Biophys Chem. 2001;91: 183–190. doi:10.1016/S0301-4622(01)00170-3

249. Müller H, Lesur A, Dittmar G, Gentzel M, Kettner K. Proteomic consequences of TDA1 deficiency in Saccharomyces cerevisiae: Protein kinase Tda1 is essential for Hxk1 and Hxk2 serine 15 phosphorylation. Scientific Reports. 2022;12: 1–20. doi:10.1038/s41598-022-21414-x

250. Kettner K, Krause U, Mosler S, Bodenstein C, Kriegel TM, Rödel G. Saccharomyces cerevisiae gene YMR291W/TDA1 mediates the in vivo phosphorylation of hexokinase

isoenzyme 2 at serine-15. FEBS Lett. 2012;586: 455–458. doi:10.1016/j.febslet.2012.01.030

251. Randez-Gil F, Sanz P, Entian K-D, Prieto JA. Carbon Source-Dependent Phosphorylation of Hexokinase PII and Its Role in the Glucose-Signaling Response in Yeast. Mol Cell Biol. 1998;18: 2940–2948. doi:10.1128/mcb.18.5.2940

252. Golbik R, Naumann M, Otto A, Müller EC, Behlke J, Reuter R, et al. Regulation of phosphotransferase activity of hexokinase 2 from Saccharomyces cerevisiae by modification at serine-14. Biochemistry. 2001;40: 1083–1090. doi:10.1021/bi001745k

253. Behlke J, Heidrich K, Naumann M, Müller EC, Otto A, Reuter R, et al. Hexokinase 2 from Saccharomyces cerevisiae: Regulation of oligomeric structure by in vivo phosphorylation at serine-14. Biochemistry. 1998;37: 11989–11995. doi:10.1021/bi980914m

254. Fernańdez-García P, Peláez R, Herrero P, Moreno F. Phosphorylation of yeast hexokinase 2 regulates its nucleocytoplasmic shuttling. Journal of Biological Chemistry. 2012;287: 42151–42164. doi:10.1074/jbc.M112.401679

255. Oh S, Lee J, Swanson SK, Florens L, Washburn MP, Workman JL. Yeast nuakl phosphorylates histone h3 threonine 11 in low glucose stress by the cooperation of ampk and ck2 signaling. Elife. 2020;9: 1–20. doi:10.7554/ELIFE.64588

256. Schulze IT, Colowick SP. The modification of yeast hexokinases by proteases and its relationship to the dissociation of hexokinase into subunits. Journal of Biological Chemistry. 1969;244: 2306–2316. doi:10.1016/s0021-9258(19)78227-1

257. Moreno F, Ahuatzi D, Riera A, Palomino CA, Herrero P. Glucose sensing through the Hxk2-dependent signalling pathway. Biochem Soc Trans. 2005;33: 265–268. doi:10.1042/BST0330265

258. Peláez R, Herrero P, Moreno F. Functional domains of yeast hexokinase 2. Biochemical Journal. 2010;432: 181–190. doi:10.1042/BJ20100663

259. Peláez R, Herrero P, Moreno F. Nuclear export of the yeast hexokinase 2 protein requires the Xpo1 (Crm-1)-dependent pathway. Journal of Biological Chemistry. 2009;284: 20548–20555. doi:10.1074/jbc.M109.013730

260. Peláez R, Fernández-García P, Herrero P, Moreno F. Nuclear import of the yeast hexokinase 2 protein requires α/β-importin-dependent pathway. Journal of Biological Chemistry. 2012;287: 3518–3529. doi:10.1074/jbc.M111.317230

261. Herrero P, Martínez-Campa C, Moreno F. The hexokinase 2 protein participates in regulatory DNA-protein complexes necessary for glucose repression of the SUC2 gene in Saccharomyces cerevisiae. FEBS Lett. 1998;434: 71–76. doi:10.1016/S0014-5793(98)00872-2

262. Zhang M, Kong H, Yee H, Fung J, Fu S-C, Chook M. Nuclear export receptor CRM1 recognizes diverse conformations in nuclear export signals. Elife. 2017. doi:10.7554/eLife.23961.001

263. Rossi MJ, Kuntala PK, Lai WKM, Yamada N, Badjatia N, Mittal C, et al. A high-resolution protein architecture of the budding yeast genome. Nature. 2021;592: 309–314. doi:10.1038/s41586-021-03314-8

264. Kriegel TM, Kettner K, Rödel G, Sträter N. Regulatory Function of Hexokinase 2 in Glucose Signaling in Saccharomyces cerevisiae. Journal of Biological Chemistry. 2016;291: 16477. doi:10.1074/JBC.L116.735514

265. Cramer FB, Woodward GE. 2-Desoxy-D-glucose as an antagonist of glucose in yeast fermentation. J Franklin Inst. 1952;253: 354–360. doi:10.1016/0016-0032(52)90852-1

266. Laussel C, Léon S. Cellular toxicity of the metabolic inhibitor 2-deoxyglucose and associated resistance mechanisms. Biochem Pharmacol. 2020;182: 114213. doi:10.1016/j.bcp.2020.114213

267. Van Steveninck J. Transport and transport-associated phosphorylation of 2-deoxy-d-glucose in yeast. Biochimica et Biophysica Acta (BBA) - Biomembranes. 1968;163: 386–394. doi:10.1016/0005-2736(68)90123-5

268. Landau BR, Lubs HA. Animal Responses to 2-Deoxy-D-Glucose Administration. Exp Biol Med. 1958;99: 124–127. doi:10.3181/00379727-99-24268

269. Sols A, Crane RK. Substrate specificity of brain hexokinase. Journal of Biological Chemistry. 1954;210: 581–595. doi:10.1016/S0021-9258(18)65384-0

270. Woodward GE, Hudson MT. Phosphorylation of 2-deoxy-D-glucose by yeast hexokinase: Competition between 2-deoxy-d-glucose and glucose. J Franklin Inst. 1955;259: 543–547. doi:10.1016/0016-0032(55)90108-3

271. Wick AN, Drury DR, Nakada HI, Wolfe JB. Localization of the primary metabolic block produced by 2-deoxyglucose. Journal of Biological Chemistry. 1957;224: 963–969. doi:10.1016/S0021-9258(18)64988-9

272. Laussel C, Albanèse V, Javier F, Rodríguez G, Ballin A, Defenouillère Q, et al. 2-deoxyglucose transiently inhibits yeast AMPK signaling and triggers glucose transporter endocytosis, potentiating the drug toxicity. PLoS Genet. 2022;18: e1010169. doi:10.1371/JOURNAL.PGEN.1010169

273. Bissonnette P, Gagné H, Blais A, Berteloot A. 2-Deoxyglucose transport and metabolism in Caco-2 cells. American Journal of Physiology. 1996;270. doi:10.1152/AJPGI.1996.270.1.G153

274. Kipnis DM, Cori CF. Studies of Tissue Permeability: The penetration and phosphorylation of 2-deoxyglucose in the rat diaphragm. Journal of Biological Chemistry. 1959;234: 171–177. doi:10.1016/S0021-9258(18)70358-X

275. Chen W, Guéron M. The inhibition of bovine heart hexokinase by 2-deoxy-d-glucose-6-phosphate: characterization by 31P NMR and metabolic implications. Biochimie. 1992;74: 867–873. doi:10.1016/0300-9084(92)90070-U

276. Kuo SC, Lampen JO. Inhibition by 2-Deoxy-d-Glucose of Synthesis of Glycoprotein Enzymes by Protoplasts of Saccharomyces: Relation to Inhibition of Sugar Uptake and Metabolism. J Bacteriol. 1972;111: 419–429. doi:10.1128/JB.111.2.419-429.1972

277. Pietzke M, Zasada C, Mudrich S, Kempa S. Decoding the dynamics of cellular metabolism and the action of 3-bromopyruvate and 2-deoxyglucose using pulsed stable isotope-resolved metabolomics. Cancer & Metabolism 2014 2:1. 2014;2: 1–11. doi:10.1186/2049-3002-2-9

278. Schmidt MFG, Schwarz RT, Scholtissek C. Nucleoside-Diphosphate Derivatives of 2-Deoxy-d-glucose in Animal Cells. Eur J Biochem. 1974;49: 237–247. doi:10.1111/J.1432-1033.1974.TB03828.X

279. Jeon SM, Chandel NS, Hay N. AMPK regulates NADPH homeostasis to promote tumour cell survival during energy stress. Nature. 2012;485: 661–665. doi:10.1038/nature11066

280. Suzuki M, O'Dea JD, Suzuki T, Agar NS. 2-deoxyglucose as a substrate for glutathione regeneration in human and ruminant red blood cells. Comparative Biochemistry and Physiology Part B: Comparative Biochemistry. 1983;75: 195–197. doi:10.1016/0305-0491(83)90312-7

281. Rippa M, Signorini M, Dallocchio F. A Multiple Role for the Coenzyme in the Mechanism of Action of 6-Phosphogluconate Dehydrogenase: the oxidative decarboxylation of 2-

deoxy-6-phosphogluconate. Journal of Biological Chemistry. 1973;248: 4920–4925. doi:10.1016/S0021-9258(19)43652-1

282. Ralser M, Wamelink MM, Struys EA, Joppich C, Krobitsch S, Jakobs C, et al. A catabolic block does not sufficiently explain how 2-deoxy-D-glucose inhibits cell growth. Proc Natl Acad Sci U S A. 2008;105: 17807–17811. doi:10.1073/pnas.0803090105

283. Urakami K, Zangiacomi V, Yamaguchi K, Kusuhara M. Impact of 2-deoxy-D-glucose on the target metabolome profile of a human endometrial cancer cell line. Biomedical Research. 2013;34: 221–229. Available: http://vanted.ipk-gatersleben.de/

284. Biely P, Bauer Š. The formation of guanosine diphosphate-2-deoxy-d-glucose in yeast. Biochimica et Biophysica Acta (BBA) - General Subjects. 1968;156: 432–434. doi:10.1016/0304-4165(68)90281-X

285. Biely P, Bauer Š. The formation of uridine diphosphate-2-deoxy-d-glucose in yeast. Biochimica et Biophysica Acta (BBA) - General Subjects. 1966;121: 213–214. doi:10.1016/0304-4165(66)90379-5

286. Colwell DR, Higgins JA, Denyer GS. Incorporation of 2-deoxy-d-glucose into glycogen. Implications for measurement of tissue-specific glucose uptake and utilisation. Int J Biochem Cell Biol. 1996;28: 115–121. doi:10.1016/1357-2725(95)00110-7

287. Defenouillère Q, Verraes A, Laussel C, Friedrich A, Schacherer J, Léon S. The induction of HAD-like phosphatases by multiple signaling pathways confers resistance to the metabolic inhibitor 2-deoxyglucose. Sci Signal. 2019;12. doi:10.1126/scisignal.aaw8000

288. Johnson BF. Lysis of Yeast Cell Walls Induced by 2-Deoxyglucose at Their Sites of Glucan Synthesis. J Bacteriol. 1968;95: 1169–1172. doi:10.1128/JB.95.3.1169-1172.1968

289. Megnet R. Effect of 2-Deoxyglucose on Schizosaccharomyces pombe. J Bacteriol. 1965;90: 1032–1035. doi:10.1128/JB.90.4.1032-1035.1965

290. Zemek J, Farkaš V, Biely P, Bauer Š. Transglycosylic reactions of nucleotides of 2-deoxy-sugars II. 2-deoxyglucose incorporation into glycogen. Biochimica et Biophysica Acta (BBA) - General Subjects. 1971;252: 432–438. doi:10.1016/0304-4165(71)90145-0

291. Steiner MR, Somers K, Steiner S. Incorporation of [14C]-2 deoxy-D-glucose into the lipids of normal cells as compared to virus-transformed cells. Biochem Biophys Res Commun. 1974;61: 795–801. doi:10.1016/0006-291X(74)91027-4

292. Kavaliauskiene S, Skotland T, Sylvänne T, Simolin H, Klokk TI, Torgersen ML, et al. Novel actions of 2-deoxy-D-glucose: protection against Shiga toxins and changes in cellular lipids. Biochemical Journal. 2015;470: 23–37. doi:10.1042/BJ20141562

293. Hannun YA, Obeid LM. Sphingolipids and their metabolism in physiology and disease. Nature Reviews Molecular Cell Biology. 2017;19: 175–191. doi:10.1038/nrm.2017.107

294. Kurtoglu M, Maher JC, Lampidis TJ. Differential toxic mechanisms of 2-deoxy-D-glucose versus 2-fluorodeoxy-D-glucose in hypoxic and normoxic tumor cells. Antioxid Redox Signal. 2007;9: 1383–1390. doi:10.1089/ars.2007.1714

295. Kurtoglu M, Gao N, Shang J, Maher JC, Lehrman MA, Wangpaichitr M, et al. Under normoxia, 2-deoxy-D-glucose elicits cell death in select tumor types not by inhibition of glycolysis but by interfering with N-linked glycosylation. Mol Cancer Ther. 2007;6: 3049–3058. doi:10.1158/1535-7163.MCT-07-0310

296. Leung HJ, Duran EM, Kurtoglu M, Andreansky S, Lampidis TJ, Mesri EA. Activation of the unfolded protein response by 2-deoxy-D-Glucose Inhibits Kaposi's sarcoma-associated

herpesvirus replication and gene expression. Antimicrob Agents Chemother. 2012;56: 5794–5803. doi:10.1128/AAC.01126-12

297. Xi H, Kurtoglu M, Liu H, Wangpaichitr M, You M, Liu X, et al. 2-Deoxy-d-glucose activates autophagy via endoplasmic reticulum stress rather than ATP depletion. Cancer Chemother Pharmacol. 2011;67: 899–910. doi:10.1007/s00280-010-1391-0

298. Shinjo S, Mizotani Y, Tashiro E, Imoto M. Comparative Analysis of the Expression Patterns of UPR-Target Genes Caused by UPR-Inducing Compounds. Biosci Biotechnol Biochem. 2013;77: 729–735. doi:10.1271/BBB.120812

299. Xi H, Barredo JC, Merchan JR, Lampidis TJ. Endoplasmic reticulum stress induced by 2-deoxyglucose but not glucose starvation activates AMPK through CaMKKβ leading to autophagy. Biochem Pharmacol. 2013;85: 1463–1477. doi:10.1016/J.BCP.2013.02.037

300. Kovacs K, Decatur C, Toro M, Pham DG, Liu H, Jing Y, et al. 2-deoxy-glucose downregulates endothelial AKT and ERK via interference with N-linked glycosylation, induction of endoplasmic reticulum stress, and GSK3β activation. Mol Cancer Ther. 2016;15: 264–275. doi:10.1158/1535-7163.MCT-14-0315

301. Schmidt MFG, Schwarz RT, Scholtissek C. Interference of Nucleoside Diphosphate Derivatives of 2-Deoxy-d-glucose with the Glycosylation of Virus-Specific Glycoproteins in vivo. Eur J Biochem. 1976;70: 55–62. doi:10.1111/J.1432-1033.1976.TB10955.X

302. Nakamura K, Compans RW. Effects of glucosamine, 2-deoxyglucose, and tunicamycin on glycosylation, sulfation, and assembly of influenza viral proteins. Virology. 1978;84: 303–319. doi:10.1016/0042-6822(78)90250-7

303. Grahame Hardie D. Regulation of AMP-activated protein kinase by natural and synthetic activators. Acta Pharm Sin B. 2016;6: 1–19. doi:10.1016/J.APSB.2015.06.002

304. Bungard D, Fuerth BJ, Zeng PY, Faubert B, Maas NL, Viollet B, et al. Signaling kinase AMPK activates stress-promoted transcription via histone H2B phosphorylation. Science. 2010;329: 1201–1205. doi:10.1126/SCIENCE.1191241

305. Wang Q, Liang B, Shirwany NA, Zou MH. 2-Deoxy-D-Glucose Treatment of Endothelial Cells Induces Autophagy by Reactive Oxygen Species-Mediated Activation of the AMP-Activated Protein Kinase. PLoS One. 2011;6: e17234. doi:10.1371/JOURNAL.PONE.0017234

306. Wu Y, Sarkissyan M, Mcghee E, Lee S, Vadgama J V. Combined inhibition of glycolysis and AMPK induces synergistic breast cancer cell killing. Breast Cancer Res Treat. 2015. doi:10.1007/s10549-015-3386-3

307. Barney JB, Chandrashekarappa DG, Soncini SR, Schmidt MC. Drug resistance in diploid yeast is acquired through dominant alleles, haploinsufficiency, gene duplication and aneuploidy. PLoS Genet. 2021;17: e1009800. doi:10.1371/journal.pgen.1009800

308. Wu N, Zheng B, Shaywitz A, Dagon Y, Tower C, Bellinger G, et al. AMPK-Dependent Degradation of TXNIP upon Energy Stress Leads to Enhanced Glucose Uptake via GLUT1. Mol Cell. 2013;49: 1167–1175. doi:10.1016/j.molcel.2013.01.035

309. Vincent EE, Coelho PP, Blagih J, Griss T, Viollet B, Jones RG. Differential effects of AMPK agonists on cell growth and metabolism. Oncogene. 2014;34: 3627–3639. doi:10.1038/onc.2014.301

310. Trefts E, Shaw RJ. AMPK: restoring metabolic homeostasis over space and time. Mol Cell. 2021;81: 3677–3690. doi:10.1016/j.molcel.2021.08.015

311. Jiang W, Zhu Z, Thompson HJ. Modulation of the activities of AMP-activated protein kinase, protein kinase B, and mammalian target of rapamycin by limiting energy availability with 2-deoxyglucose. Mol Carcinog. 2008;47: 616–628. doi:10.1002/MC.20425

312. Wu H, Zhu H, Liu DX, Niu TK, Ren X, Patel R, et al. Silencing of elongation factor-2 kinase potentiates the effect of 2-deoxy-D-glucose against human glioma cells through blunting of autophagy. Cancer Res. 2009;69: 2453–2460. doi:10.1158/0008-5472.CAN-08-2872

313. Haar E Vander, Lee S il, Bandhakavi S, Griffin TJ, Kim DH. Insulin signalling to mTOR mediated by the Akt/PKB substrate PRAS40. Nature Cell Biology. 2007;9: 316–323. doi:10.1038/ncb1547

314. DiPaola RS, Dvorzhinski D, Thalasila A, Garikapaty V, Doram D, May M, et al. Therapeutic starvation and autophagy in prostate cancer: A new paradigm for targeting metabolism in cancer therapy. Prostate. 2008;68: 1743–1752. doi:10.1002/PROS.20837

315. Sahra I Ben, Laurent K, Giuliano S, Larbret F, Ponzio G, Gounon P, et al. Targeting cancer cell metabolism: The combination of metformin and 2-deoxyglucose induces p53-dependent apoptosis in prostate cancer cells. Cancer Res. 2010;70: 2465–2475. doi:10.1158/0008-5472.CAN-09-2782

316. O'Donnell AF, McCartney RR, Chandrashekarappa DG, Zhang BB, Thorner J, Schmidt MC. 2-Deoxyglucose Impairs Saccharomyces cerevisiae Growth by Stimulating Snf1-Regulated and α-Arrestin-Mediated Trafficking of Hexose Transporters 1 and 3. Mol Cell Biol. 2015;35: 939–955. doi:10.1128/mcb.01183-14

317. Warburg O, Wind F, Negelein E. The Metabolism of Tumors in the Body. Journal of General Physiology. 1927;8: 519–530. doi:10.1085/JGP.8.6.519

318. Strickland M, Stoll EA. Metabolic reprogramming in glioma. Front Cell Dev Biol. 2017;5: 260670. doi:10.3389/FCELL.2017.00043

319. Blum R, Kloog Y. Metabolism addiction in pancreatic cancer. Cell Death Dis. 2014;5. doi:10.1038/CDDIS.2014.38

320. Maher JC, Krishan A, Lampidis TJ. Greater cell cycle inhibition and cytotoxicity induced by 2-deoxy-D-glucose in tumor cells treated under hypoxic vs aerobic conditions. Cancer Chemother Pharmacol. 2004;53: 116–122. doi:10.1007/s00280-003-0724-7

321. Liu H, Hu YP, Savaraj N, Priebe W, Lampidis TJ. Hypersensitization of Tumor Cells to Glycolytic Inhibitors. Biochemistry. 2001;40: 5542–5547. doi:10.1021/BI002426W

322. Stein M, Lin H, Jeyamohan C, Dvorzhinski D, Gounder M, Bray K, et al. Targeting tumor metabolism with 2-deoxyglucose in patients with castrate-resistant prostate cancer and advanced malignancies. Prostate. 2010;70: 1388–1394. doi:10.1002/pros.21172

323. Ong LC, Jin Y, Song IC, Yu S, Zhang K, Chow PKH. 2-[18f]-2-deoxy-d-glucose (fdg) uptake in human tumor cells is related to the expression of glut-1 and hexokinase ii. Acta radiol. 2008;49: 1145–1153. doi:10.1080/02841850802482486

324. Maschek G, Savaraj N, Priebe W, Braunschweiger P, Hamilton K, Tidmarsh GF, et al. 2-Deoxy-d-glucose Increases the Efficacy of Adriamycin and Paclitaxel in Human Osteosarcoma and Non-Small Cell Lung Cancers In Vivo. Cancer Res. 2004;64: 31–34. doi:10.1158/0008-5472.CAN-03-3294

325. Kern KA, Norton JA. Inhibition of established rat fibrosarcoma growth by the glucose antagonist 2-deoxy-D-glucose. Surgery. 1987;102: 380–385. Available: http://www.surgjournal.com/article/0039606087902601/fulltext

326. Cay O, Radnell M, Jeppsson B, Ahren B, Bengmark S. Inhibitory effect of 2-deoxy-D-glucose on liver tumor growth in rats. Cancer Res. 1992;52: 5794–5796. Available: https://pubmed.ncbi.nlm.nih.gov/1394204/

327. Zhong D, Xiong L, Liu T, Liu X, Liu X, Chen J, et al. The glycolytic inhibitor 2-deoxyglucose activates multiple prosurvival pathways through IGF1R. Journal of Biological Chemistry. 2009;284: 23225–23233. doi:10.1074/jbc.M109.005280

328. Yamaguchi R, Janssen E, Perkins G, Ellisman M, Kitada S, Reed JC. Efficient Elimination of Cancer Cells by Deoxyglucose-ABT-263/737 Combination Therapy. PLoS One. 2011;6: e24102. doi:10.1371/JOURNAL.PONE.0024102

329. Bénéteau M, Zunino B, Jacquin MA, Meynet O, Chiche J, Pradelli LA, et al. Combination of glycolysis inhibition with chemotherapy results in an antitumor immune response. Proc Natl Acad Sci U S A. 2012;109: 20071–20076. doi:10.1073/PNAS.1206360109

330. Raez LE, Papadopoulos K, Ricart AD, Chiorean EG, Dipaola RS, Stein MN, et al. A phase i dose-escalation trial of 2-deoxy-d-glucose alone or combined with docetaxel in patients with advanced solid tumors. Cancer Chemother Pharmacol. 2013;71: 523–530. doi:10.1007/s00280-012-2045-1

331. Pajak B, Siwiak E, Sołtyka M, Priebe A, Zieliński R, Fokt I, et al. 2-Deoxy-D-Glucose and its analogs: From diagnostic to therapeutic agents. Int J Mol Sci. 2020;21. doi:10.3390/ijms21010234

332. Samuel SM, Satheesh NJ, Ghosh S, Büsselberg D, Majeed Y, Ding H, et al. Treatment with a Combination of Metformin and 2-Deoxyglucose Upregulates Thrombospondin-1 in Microvascular Endothelial Cells: Implications in Anti-Angiogenic Cancer Therapy. Cancers 2019, Vol 11, Page 1737. 2019;11: 1737. doi:10.3390/CANCERS11111737

333. Zhu J, Zheng Y, Zhang H, Sun H. Targeting cancer cell metabolism: The combination of metformin and 2-Deoxyglucose regulates apoptosis in ovarian cancer cells via p38 MAPK/JNK signaling pathway. Am J Transl Res. 2016;8: 4812. Available: /pmc/articles/PMC5126324/

334. Shafaee A, Pirayesh Islamian J, Zarei D, Mohammadi M, Nejati-Koshki K, Farajollahi A, et al. Induction of Apoptosis by a Combination of 2-Deoxyglucose and Metformin in Esophageal Squamous Cell Carcinoma by Targeting Cancer Cell Metabolism. Iran J Med Sci. 2019;44: 99. Available: /pmc/articles/PMC6423430/

335. Cheong JH, Park ES, Liang J, Dennison JB, Tsavachidou D, Nguyen-Charles C, et al. Dual inhibition of tumor energy pathway by 2-deoxyglucose and metformin is effective against a broad spectrum of preclinical cancer models. Mol Cancer Ther. 2011;10: 2350–2362. doi:10.1158/1535-7163.MCT-11-0497

336. Foretz M, Guigas B, Viollet B. Metformin: update on mechanisms of action and repurposing potential. Nature Reviews Endocrinology. 2023;19: 460–476. doi:10.1038/s41574-023-00833-4

337. Mohanti BK, Rath GK, Naranappa Anantha I, Kannan I V, Das BS, R Chandramouli BA, et al. Improving cancer radiotherapy with 2-deoxy-D-glucose: phase I/II clinical trials on human cerebral gliomas. International Journal of Radiation Oncology, Biology, Biophysics. 1996;35: 103–111.

338. Singh D, Banerji AK, Dwarakanath BS, Tripathi RP, Gupta JP, Mathew TL, et al. Optimizing cancer radiotherapy with 2-deoxy-D-glucose: Dose escalation studies in patients with glioblastoma multiforme. Strahlentherapie und Onkologie. 2005;181: 507–514. doi:10.1007/s00066-005-1320-z

339. Phelps ME. PET: The Merging of Biology and Imaging into Molecular Imaging. Journal of Nuclear Medicine. 2000;41: 661–681. Available: https://jnm.snmjournals.org/content/41/4/661

340. Lampidis TJ, Kurtoglu M, Maher JC, Liu H, Krishan A, Sheft V, et al. Efficacy of 2-halogen substituted D-glucose analogs in blocking glycolysis and killing "hypoxic tumor cells." Cancer Chemother Pharmacol. 2006;58: 725–734. doi:10.1007/S00280-006-0207-8

341. Piña Y, Houston SK, Murray TG, Koru-Sengul T, Decatur C, Scott WK, et al. Retinoblastoma treatment: impact of the glycolytic inhibitor 2-deoxy-d-glucose on molecular genomics expression in LHBETATAG retinal tumors. Clin Ophthalmol. 2012;6: 817. doi:10.2147/OPTH.S29688

342. Michel KA, Zielinski R, Walker CM, Le Roux L, Priebe W, Bankson JA, et al. Hyperpolarized pyruvate MR spectroscopy depicts glycolytic inhibition in a mouse model of glioma. Radiology. 2019;293: 168–173. doi:10.1148/radiol.2019182919

343. Heredia MF, Heredia CF. Saccharomyces cerevisiae acquires resistance to 2-deoxyglucose at a very high frequency. J Bacteriol. 1988;170: 2870–2872. doi:10.1128/jb.170.6.2870-2872.1988

344. Zimmermann FK, Scheel I. Mutants of Saccharomyces cerevisiae resistant to carbon catabolite repression. MGG Molecular & General Genetics. 1977;154: 75–82. doi:10.1007/BF00265579

345. Neigeborn L, Carlson M. Mutations causing constitutive invertase synthesis in yeast: Genetic interactions with snf mutations. Genetics. 1987;115: 247–253.

346. Bailey RB, Woodword A. Isolation and characterization of a pleiotropic glucose repression resistant mutant of Saccharomyces cerevisiae. MGG Molecular & General Genetics. 1984;193: 507–512. doi:10.1007/BF00382091

347. Schuller HJ, Entian KD. Extragenic suppressors of yeast glucose derepression mutants leading to constitutive synthesis of several glucose-repressible enzymes. J Bacteriol. 1991;173: 2045–2052. doi:10.1128/jb.173.6.2045-2052.1991

348. Zimmermann FK, Kaufmann I, Rasenberger H, Haußmann P. Genetics of carbon catabolite repression in Saccharomyces cerevisiae: genes involved in the derepression process. MGG Molecular & General Genetics. 1977;151: 95–103. doi:10.1007/BF00446918

349. Schmidt MC, Donnell AFO. "Sugarcoating" 2 - deoxyglucose: mechanisms that suppress its toxic effects. Curr Genet. 2020. doi:10.1007/s00294-020-01122-7

350. Randez-Gil F, Blasco A, Prieto JA, Sanz P. DOGR1 and DOGR2: Two genes from Saccharomyces cerevisiae that confer 2-deoxyglucose resistance when overexpressed. Yeast. 1995;11: 1233–1240. doi:10.1002/YEA.320111303

351. Kuznetsova E, Nocek B, Brown G, Makarova KS, Flick R, Wolf YI, et al. Functional Diversity of Haloacid Dehalogenase Superfamily Phosphatases from Saccharomyces cerevisiae: biochemical, structural, and evolutionary insights. Journal of Biological Chemistry. 2015;290: 18678–18698. doi:10.1074/JBC.M115.657916

352. Westholm JO, Nordberg N, Murén E, Ameur A, Komorowski J, Ronne H. Combinatorial control of gene expression by the three yeast repressors Mig1, Mig2 and Mig3. BMC Genomics. 2008;9: 1–15. doi:10.1186/1471-2164-9-601

353. Su Y, Xu C, Shea J, DeStephanis D, Su Z. Transcriptomic changes in single yeast cells under various stress conditions. BMC Genomics. 2023;24: 1–19. doi:10.1186/S12864-023-09184-W/FIGURES/7

354. Barban S. Studies on the Mechanism of Resistance to 2-Deoxy-D-glucose in Mammalian Cell Cultures. Journal of Biological Chemistry. 1962;237: 291–295. doi:10.3412/jsb.5.361

355. Bailey PJ, Harris M. Patterns of resistance to 2-deoxy-D-glucose in pig kidney cells. J Cell Physiol. 1968;71: 23–32. doi:10.1002/JCP.1040710105

356. Morrow J, De Carli L. The correlation of resistance to 2-deoxyglucose with alkaline phosphatase levels in a human cell line. Exp Cell Res. 1967;47: 1–11. doi:10.1016/0014-4827(67)90204-2

357. Barban S. Differential action of hormones on induced resistance to 2-deoxy-d-glucose in mammalian cell cultures. Biochimica et Biophysica Acta (BBA) - General Subjects. 1966;115: 197–204. doi:10.1016/0304-4165(66)90064-X

358. Maher JC, Wangpaichitr M, Savaraj N, Kurtoglu M, Lampidis TJ. Hypoxia-inducible factor-1 confers resistance to the glycolytic inhibitor 2-deoxy-D-glucose. Mol Cancer Ther. 2007;6: 732–741. doi:10.1158/1535-7163.MCT-06-0407

359. Singh N, Bhalla N. Moonlighting Proteins. Annu Rev Genet. 2020;54: 265–285. doi:10.1146/ANNUREV-GENET-030620-102906

360. Ow YLP, Green DR, Hao Z, Mak TW. Cytochrome c: functions beyond respiration. Nature Reviews Molecular Cell Biology 2008 9:7. 2008;9: 532–542. doi:10.1038/nrm2434

361. Jung DW, Kim WH, Williams DR. Chemical genetics and its application to moonlighting in glycolytic enzymes. Biochem Soc Trans. 2014;42: 1756–1761. doi:10.1042/BST20140201

362. Ma H, Bloom LM, Zhimin Z, Walsh CT, Botstein D. Isolation and Characterization of Mutations in the HXK2 Gene of Saccharomyces. Mol Cell Biol. 1989;9: 5630–5642. doi:10.1128/mcb.9.12.5630

363. Ahuatzi D, Herrero P, De La Cera T, Moreno F. The Glucose-regulated Nuclear Localization of Hexokinase 2 in Saccharomyces cerevisiae Is Mig1-dependent. Journal of Biological Chemistry. 2004;279: 14440–14446. doi:10.1074/jbc.M313431200

364. Adnan M, Zheng W, Islam W, Arif M, Abubakar YS, Wang Z, et al. Carbon Catabolite Repression in Filamentous Fungi. International Journal of Molecular Sciences 2018, Vol 19, Page 48. 2017;19: 48. doi:10.3390/IJMS19010048

365. Gancedo C, Flores CL, Gancedo JM. Evolution of moonlighting proteins: insight from yeasts. Biochem Soc Trans. 2014;42: 1715–1719. doi:10.1042/BST20140199

366. Cho YH, Yoo SD, Sheen J. Regulatory Functions of Nuclear Hexokinase1 Complex in Glucose Signaling. Cell. 2006;127: 579–589. doi:10.1016/j.cell.2006.09.028

367. Kriegel TM, Vojtek AB, Clifton D, Fraenkel DG, Rush J. In Vivo Phosphorylation Site of Hexokinase 2 in Saccharomyces cerevisiae. Biochemistry. 1994;33: 148–152. doi:10.1021/bi00167a019

368. Laurian R, Dementhon K, Doumèche B, Soulard A, Noel T, Lemaire M, et al. Hexokinase and glucokinases are essential for fitness and virulence in the pathogenic yeast Candida albicans. Front Microbiol. 2019;10: 1–18. doi:10.3389/fmicb.2019.00327

369. Timney BL, Raveh B, Mironska R, Trivedi JM, Kim SJ, Russel D, et al. Simple rules for passive diffusion through the nuclear pore complex. Journal of Cell Biology. 2016;215: 57–76. doi:10.1083/JCB.201601004

370. Schmidt JJ, Colowick SP. Identification of a peptide sequence involved in association of subunits of yeast hexokinases. Arch Biochem Biophys. 1973;158: 471–477. doi:10.1016/0003-9861(73)90538-9

371. Mortimer RK, Johnston JR. Genealogy of principal strains of the yeast genetic stock center. Genetics. 1986;113: 35–43. doi:10.1093/GENETICS/113.1.35

372. Prior C, Mamessier P, Fukuhara H, Jie Chen X, Wesolowski-louvel M. The hexokinase gene is required for transcriptional regulation of the glucose transporter gene RAG1 in Kluyveromyces lactis. Mol Cell Biol. 1993;13: 3882–3889. doi:10.1128/MCB.13.7.3882-3889.1993

373. Kellis M, Birren BW, Lander ES. Proof and evolutionary analysis of ancient genome duplication in the yeast Saccharomyces cerevisiae. Nature. 2004;428: 617–624. doi:10.1038/nature02424

374. Lu J, Wu T, Zhang B, Liu S, Song W, Qiao J, et al. Types of nuclear localization signals and mechanisms of protein import into the nucleus. Cell Communication and Signaling. 2021;19. doi:10.1186/S12964-021-00741-Y

375. Bhagwat N, Owens S, Ito M, Boinapalli J, Poa P, Ditzel A, et al. Sumo is a pervasive regulator of meiosis. Elife. 2021;10: 1–89. doi:10.7554/ELIFE.57720

376. Zhang Y, Pan Y, Liu W, Zhou YJ, Wang K, Wang L, et al. In vivo protein allylation to capture protein methylation candidates. Chemical Communications. 2016;52: 6689–6692. doi:10.1039/c6cc02386j

377. Swaney DL, Beltrao P, Starita L, Guo A, Rush J, Fields S, et al. Global analysis of phosphorylation and ubiquitylation cross-talk in protein degradation. Nat Methods. 2013;10: 676–682. doi:10.1038/nmeth.2519

378. Soulard A, Cremonesi A, Moes S, Schütz F, Jenö P, Hall MN. The rapamycin-sensitive phosphoproteome reveals that TOR controls protein kinase A toward some but not all substrates. Mol Biol Cell. 2010;21: 3475–3486. doi:10.1091/MBC.E10-03-0182

379. Ficarro SB, McCleland ML, Stukenberg PT, Burke DJ, Ross MM, Shabanowitz J, et al. Phosphoproteome analysis by mass spectrometry and its application to Saccharomyces cerevisiae. Nature Biotechnology. 2002;20: 301–305. doi:10.1038/nbt0302-301

380. Chen YC, Jiang PH, Chen HM, Chen CH, Wang YT, Chen YJ, et al. Glucose intake hampers PKA-regulated HSP90 chaperone activity. Elife. 2018;7. doi:10.7554/ELIFE.39925

381. Lanz MC, Yugandhar K, Gupta S, Sanford EJ, Faça VM, Vega S, et al. In-depth and 3-dimensional exploration of the budding yeast phosphoproteome. EMBO Rep. 2021;22: e51121. doi:10.15252/EMBR.202051121

382. MacGilvray ME, Shishkova E, Place M, Wagner ER, Coon JJ, Gasch AP. Phosphoproteome Response to Dithiothreitol Reveals Unique Versus Shared Features of Saccharomyces cerevisiae Stress Responses. J Proteome Res. 2020;19: 3405–3417. doi:10.1021/ACS.JPROTEOME.0C00253

383. Holt LJ, Tuch BB, Villen J, Johnson AD, Gygi SP, Morgan DO. Global analysis of cdk1 substrate phosphorylation sites provides insiqhts into evolution. Science. 2009;325: 1682–1686. doi:10.1126/SCIENCE.1172867

384. Ozcan S, Johnston M. Three different regulatory mechanisms enable yeast hexose transporter (HXT) genes to be induced by different levels of glucose. Mol Cell Biol. 1995;15: 1564–1572. doi:10.1128/mcb.15.3.1564

385. Liang H, Gaber RF. A novel signal transduction pathway in Saccharomyces cerevisiae defined by Snf3-regulated expression of HXT6. https://doi.org/101091/mbc7121953. 2017;7: 1953–1966. doi:10.1091/MBC.7.12.1953

386. Caligaris M, Nicastro R, Hu Z, Tripodi F, Hummel JE, Pillet B, et al. Snf1/AMPK fine-tunes TORC1 signaling in response to glucose starvation. Elife. 2023;12. doi:10.7554/eLife.84319

387. Douzery EJP, Snell EA, Bapteste E, Delsuc F, Philippe H. The timing of eukaryotic evolution: Does a relaxed molecular clock reconcile proteins and fossils? Proc Natl Acad Sci U S A. 2004;101: 15386–15391. doi:10.1073/PNAS.0403984101

388. Kachroo AH, Laurent JM, Yellman CM, Meyer AG, Wilke CO, Marcotte EM. Systematic humanization of yeast genes reveals conserved functions and genetic modularity. Science (1979). 2015;348: 921–925. doi:10.1126/SCIENCE.AAA0769

389. Hohmann S, Winderickx J, De Winde JH, Valckx D, Cobbaert P, Luyten K, et al. Novel alleles of yeast hexokinase PII with distinct effects on catalytic activity and catabolite repression of SUC2. Microbiology (N Y). 1999;145: 703–714. doi:10.1099/13500872-145-3-703

390. Ma H, Botstein D. Effects of null mutations in the hexokinase genes of Saccharomyces cerevisiae on catabolite repression. Mol Cell Biol. 1986;6: 4046–4052. doi:10.1128/MCB.6.11.4046-4052.1986

391. Agius L. Glucokinase and molecular aspects of liver glycogen metabolism. Biochemical Journal. 2008;414: 1–18. doi:10.1042/BJ20080595

392. Van Schaftingen E, Veiga-da-Cunha M, Niculescu L. The regulatory protein of glucokinase. Biochem Soc Trans. 1997;25: 136–140. doi:10.1042/BST0250136

393. Wissing S, Ludovico P, Herker E, Büttner S, Engelhardt SM, Decker T, et al. An AIF orthologue regulates apoptosis in yeast. Journal of Cell Biology. 2004;166: 969–974. doi:10.1083/JCB.200404138

394. Amigoni L, Frigerio G, Martegani E, Colombo S. Involvement of Aif1 in apoptosis triggered by lack of Hxk2 in the yeast Saccharomyces cerevisiae. FEMS Yeast Res. 2016;16: 16. doi:10.1093/FEMSYR/FOW016

395. Brandina I, Graham J, Lemaitre-Guillier C, Entelis N, Krasheninnikov I, Sweetlove L, et al. Enolase takes part in a macromolecular complex associated to mitochondria in yeast. Biochim Biophys Acta Bioenerg. 2006;1757: 1217–1228. doi:10.1016/J.BBABIO.2006.07.001

396. Renvoisé M, Bonhomme L, Davanture M, Valot B, Zivy M, Lemaire C. Quantitative variations of the mitochondrial proteome and phosphoproteome during fermentative and respiratory growth in Saccharomyces cerevisiae. J Proteomics. 2014;106: 140–150. doi:10.1016/J.JPROT.2014.04.022

397. Johnston GC, Pringle JR, Hartwell LH. Coordination of growth with cell division in the yeast Saccharomyces cerevisiae. Exp Cell Res. 1977;105: 79–98. doi:10.1016/0014-4827(77)90154-9

398. Gietz RD, Schiestl RH. High-efficiency yeast transformation using the LiAc/SS carrier DNA/PEG method. Nature Protocols 2007 2:1. 2007;2: 31–34. doi:10.1038/nprot.2007.13

399. Baker Brachmann C, Davies A, Cost GJ, Caputo E, Li J, Hieter P, et al. Designer Deletion Strains derived from Saccharomyces cerevisiae S288C: a Useful set of Strains and Plasmids for PCR-mediated Gene Disruption and Other Applications. Yeast. 1998;14: 115–132. doi:10.1002/(SICI)1097-0061(19980130)14:2

400. Meurer M, Duan Y, Sass E, Kats I, Herbst K, Buchmuller BC, et al. Genome-wide C-SWAT library for high-throughput yeast genome tagging. Nature Methods. 2018;15: 598–600. doi:10.1038/s41592-018-0045-8

401. Sikorski RS, Hieter P. A system of shuttle vectors and yeast host strains designed for efficient manipulation of DNA in Saccharomyces cerevisiae. Genetics. 1989;122: 19–27. doi:10.1093/GENETICS/122.1.19

402. Zhou C, Slaughter BD, Unruh JR, Guo F, Yu Z, Mickey K, et al. Organelle-Based Aggregation and Retention of Damaged Proteins in Asymmetrically Dividing Cells. Cell. 2014;159: 530–542. doi:10.1016/J.CELL.2014.09.026

403. Volland C, Urban-Grimal D, Gbraud G, Haguenauer-Tsapiss R. Endocytosis and Degradation of the Yeast Uracil Permease Under Adverse Conditions*. 1994;269: 9833–9841. doi:10.1016/S0021-9258(17)36959-4

404. Southern JA, Young DF, Heaney F, Baumgartner WK, Randall RE. Identification of an epitope on the P and V proteins of simian virus 5 that distinguishes between two isolates with different biological characteristics. Journal of General Virology. 1991;72: 1551–1557. doi:10.1099/0022-1317-72-7-1551

405. Phair RD, Scaffidi P, Elbi C, Vecerová J, Dey A, Ozato K, et al. Global Nature of Dynamic Protein-Chromatin Interactions In Vivo: Three-Dimensional Genome Scanning and Dynamic Interaction Networks of Chromatin Proteins. Mol Cell Biol. 2004;24: 6393–6402. doi:10.1128/MCB.24.14.6393-6402.2004

406. Bray NL, Pimentel H, Melsted P, Pachter L. Near-optimal probabilistic RNA-seq quantification. Nature Biotechnology. 2016;34: 525–527. doi:10.1038/nbt.3519

407. Bertoni M, Kiefer F, Biasini M, Bordoli L, Schwede T. Modeling protein quaternary structure of homo- and hetero-oligomers beyond binary interactions by homology. Scientific Reports. 2017;7: 1–15. doi:10.1038/s41598-017-09654-8

408. Studer G, Rempfer C, Waterhouse AM, Gumienny R, Haas J, Schwede T. QMEANDisCo—distance constraints applied on model quality estimation. Bioinformatics. 2020;36: 1765–1771. doi:10.1093/BIOINFORMATICS/BTZ828

409. Guex N, Peitsch MC, Schwede T. Automated comparative protein structure modeling with SWISS-MODEL and Swiss-PdbViewer: A historical perspective. Electrophoresis. 2009;30: S162–S173. doi:10.1002/ELPS.200900140

410. Bienert S, Waterhouse A, De Beer TAP, Tauriello G, Studer G, Bordoli L, et al. The SWISS-MODEL Repository—new features and functionality. Nucleic Acids Res. 2017;45: D313–D319. doi:10.1093/NAR/GKW1132

411. Waterhouse A, Bertoni M, Bienert S, Studer G, Tauriello G, Gumienny R, et al. SWISS-MODEL: homology modelling of protein structures and complexes. Nucleic Acids Res. 2018;46: W296–W303. doi:10.1093/NAR/GKY427

412. Bär D, Golbik R, Hübner G, Lilie H, Müller EC, Naumann M, et al. The unique hexokinase of Kluyveromyces lactis. Molecular and functional characterization and evaluation of a role in glucose signaling. Journal of Biological Chemistry. 2003;278: 39280–39286. doi:10.1074/jbc.M305706200

413. Pettersen EF, Goddard TD, Huang CC, Couch GS, Greenblatt DM, Meng EC, et al. UCSF Chimera—A visualization system for exploratory research and analysis. J Comput Chem. 2004;25: 1605–1612. doi:10.1002/JCC.20084

414. Roberts E, Eargle J, Wright D, Luthey-Schulten Z. MultiSeq: Unifying sequence and structure data for evolutionary analysis. BMC Bioinformatics. 2006;7: 1–11. doi:10.1186/1471-2105-7-382

415. Humphrey W, Dalke A, Schulten K. VMD: Visual molecular dynamics. J Mol Graph. 1996;14: 33–38. doi:10.1016/0263-7855(96)00018-5

416. Dolinsky TJ, Nielsen JE, McCammon JA, Baker NA. PDB2PQR: an automated pipeline for the setup of Poisson–Boltzmann electrostatics calculations. Nucleic Acids Res. 2004;32: W665–W667. doi:10.1093/NAR/GKH381

417. Dolinsky TJ, Czodrowski P, Li H, Nielsen JE, Jensen JH, Klebe G, et al. PDB2PQR: expanding and upgrading automated preparation of biomolecular structures for molecular simulations. Nucleic Acids Res. 2007;35: W522–W525. doi:10.1093/NAR/GKM276

418. Olsson MHM, SØndergaard CR, Rostkowski M, Jensen JH. PROPKA3: Consistent treatment of internal and surface residues in empirical pKa predictions. J Chem Theory Comput. 2011;7: 525–537. doi:10.1021/CT100578Z

419. Maier JA, Martinez C, Kasavajhala K, Wickstrom L, Hauser KE, Simmerling C. ff14SB: Improving the Accuracy of Protein Side Chain and Backbone Parameters from ff99SB. J Chem Theory Comput. 2015;11: 3696–3713. doi:10.1021/ACS.JCTC.5B00255

420. Jorgensen WL, Chandrasekhar J, Madura JD, Impey RW, Klein ML. Comparison of simple potential functions for simulating liquid water. J Chem Phys. 1998;79: 926. doi:10.1063/1.445869

421. Kirschner KN, Yongye AB, Tschampel SM, González-Outeiriño J, Daniels CR, Foley BL, et al. GLYCAM06: A generalizable biomolecular force field. Carbohydrates. J Comput Chem. 2008;29: 622–655. doi:10.1002/JCC.20820

422. Case DA, Cheatham TE, Darden T, Gohlke H, Luo R, Merz KM, et al. The Amber biomolecular simulation programs. J Comput Chem. 2005;26: 1668–1688. doi:10.1002/JCC.20290

423. Salomon-Ferrer R, Case DA, Walker RC. An overview of the Amber biomolecular simulation package. Wiley Interdiscip Rev Comput Mol Sci. 2013;3: 198–210. doi:10.1002/WCMS.1121

424. Durrant JD. BlendMol: advanced macromolecular visualization in Blender. Bioinformatics. 2019;35: 2323–2325. doi:10.1093/BIOINFORMATICS/BTY968

425. Pollard-Knight D, Cornish-Bowden A. Mechanism of liver glucokinase. Mol Cell Biochem. 1982;44: 71–80. doi:10.1007/BF00226892

426. Lunt SY, Vander Heiden MG. Aerobic Glycolysis: Meeting the Metabolic Requirements of Cell Proliferation. https://doi.org/101146/annurev-cellbio-092910-154237. 2011;27: 441–464. doi:10.1146/ANNUREV-CELLBIO-092910-154237

427. Pastorino J, Hoek J. Hexokinase II: The Integration of Energy Metabolism and Control of Apoptosis. Curr Med Chem. 2005;10: 1535–1551. doi:10.2174/0929867033457269

428. Feron O. Pyruvate into lactate and back: From the Warburg effect to symbiotic energy fuel exchange in cancer cells. Radiotherapy and Oncology. 2009;92: 329–333. doi:10.1016/j.radonc.2009.06.025

429. Gall JM, Wong V, Pimental DR, Havasi A, Wang Z, Pastorino JG, et al. Hexokinase regulates Bax-mediated mitochondrial membrane injury following ischemic stress. Kidney Int. 2011;79: 1207–1216. doi:10.1038/ki.2010.532

430. Shoham M, Steitz TA. The 6-hydroxymethyl group of a hexose is essential for the substrateinduced closure of the cleft in hexokinase. Biochimica et Biophysica Acta (BBA)

- Protein Structure and Molecular Enzymology. 1982;705: 380–384. doi:10.1016/0167-4838(82)90260-6

431. Guerra R, Bianconi ML. Increased Stability and Catalytic Efficiency of Yeast Hexokinase Upon Interaction with Zwitterionic Micelles. Kinetics and Conformational Studies. Biosci Rep. 2000;20: 41–49. doi:10.1023/A:1005583117296

432. Noat G, Ricard J, Borel M, Got C. Kinetic Study of Yeast Hexokinase. Eur J Biochem. 1968;5: 55–70. doi:10.1111/J.1432-1033.1968.TB00337.X

433. Granchi C, Fancelli D, Minutolo F. An update on therapeutic opportunities offered by cancer glycolytic metabolism. Bioorg Med Chem Lett. 2014;24: 4915–4925. doi:10.1016/J.BMCL.2014.09.041

434. Pelicano H, Martin DS, Xu RH, Huang P. Glycolysis inhibition for anticancer treatment. Oncogene. 2006;25: 4633–4646. doi:10.1038/sj.onc.1209597

435. Kratky Z, Biely P, Bauer Š. Mechanism of 2-Deoxy-d-glucose Inhibition of Cell-Wall Polysaccharide and Glycoprotein Biosyntheses in Saccharomyces cerevisiae. Eur J Biochem. 1975;54: 459–467. doi:10.1111/J.1432-1033.1975.TB04157.X

436. Berthe A, Zaffino M, Muller C, Foulquier F, Houdou M, Schulz C, et al. Protein N-glycosylation alteration and glycolysis inhibition both contribute to the antiproliferative action of 2-deoxyglucose in breast cancer cells. Breast Cancer Res Treat. 2018;171: 581–591. doi:10.1007/s10549-018-4874-z

437. Scatena R, Bottoni P, Pontoglio A, Mastrototaro L, Giardina B. Glycolytic enzyme inhibitors in cancer treatment. Expert Opin Investig Drugs. 2008;17: 1533–1545. doi:10.1517/13543784.17.10.1533

438. Dietz GW, Heppel LA. Studies on the Uptake of Hexose Phosphates. Journal of Biological Chemistry. 1971;246: 2881–2884. doi:10.1016/s0021-9258(18)62264-1

439. Goldgof GM, Durrant JD, Ottilie S, Vigil E, Allen KE, Gunawan F, et al. Comparative chemical genomics reveal that the spiroindolone antimalarial KAE609 (Cipargamin) is a P-type ATPase inhibitor. Scientific Reports 2016 6:1. 2016;6: 1–13. doi:10.1038/srep27806

440. Ottilie S, Goldgof GM, Cheung AL, Walker JL, Vigil E, Allen KE, et al. Two inhibitors of yeast plasma membrane ATPase 1 (ScPma1p): Toward the development of novel antifungal therapies. J Cheminform. 2018;10: 1–9. doi:10.1186/S13321-018-0261-3

441. Ottilie S, Goldgof GM, Calvet CM, Jennings GK, Lamonte G, Schenken J, et al. Rapid Chagas Disease Drug Target Discovery Using Directed Evolution in Drug-Sensitive Yeast. ACS Chem Biol. 2017;12: 422–434. doi:10.1021/ACSCHEMBIO.6B01037

442. Suzuki Y, Onge RPS, Mani R, King OD, Heilbut A, Labunskyy VM, et al. Knocking out multigene redundancies via cycles of sexual assortment and fluorescence selection. Nature Methods 2011 8:2. 2011;8: 159–164. doi:10.1038/nmeth.1550

443. Lang GI, Rice DP, Hickman MJ, Sodergren E, Weinstock GM, Botstein D, et al. Pervasive genetic hitchhiking and clonal interference in forty evolving yeast populations. Nature. 2013;500: 571–574. doi:10.1038/nature12344

444. Gidalevitz T, Prahlad V, Morimoto RI, Morimoto R, Selkoe D, Kelly J. The Stress of Protein Misfolding: From Single Cells to Multicellular Organisms. Cold Spring Harb Perspect Biol. 2011;3: a009704. doi:10.1101/CSHPERSPECT.A009704

445. Leuenberger P, Ganscha S, Kahraman A, Cappelletti V, Boersema PJ, Von Mering C, et al. Cell-wide analysis of protein thermal unfolding reveals determinants of thermostability. Science. 2017;355. doi:10.1126/SCIENCE.AAI7825

446. Slein M, Cori GT, Cori CF. A comparative study of hexokinase from yeast and animal tissues. Journal of Biological Chemistry. 1950;186: 763–780. Available: https://pubmed.ncbi.nlm.nih.gov/14794672/

447. Burley SK, Bhikadiya C, Bi C, Bittrich S, Chen L, Crichlow G V., et al. RCSB Protein Data Bank: powerful new tools for exploring 3D structures of biological macromolecules for basic and applied research and education in fundamental biology, biomedicine, biotechnology, bioengineering and energy sciences. Nucleic Acids Res. 2021;49: D437–D451. doi:10.1093/NAR/GKAA1038

448. Berman HM, Westbrook J, Feng Z, Gilliland G, Bhat TN, Weissig H, et al. The Protein Data Bank. Nucleic Acids Res. 2000;28: 235–242. doi:10.1093/NAR/28.1.235

449. Goujon M, McWilliam H, Li W, Valentin F, Squizzato S, Paern J, et al. A new bioinformatics analysis tools framework at EMBL–EBI. Nucleic Acids Researc. 2010;38: W695–W699. doi:10.1093/NAR/GKQ313

450. Sievers F, Wilm A, Dineen D, Gibson TJ, Karplus K, Li W, et al. Fast, scalable generation of high-quality protein multiple sequence alignments using Clustal Omega. Mol Syst Biol. 2011;7: 539. doi:10.1038/MSB.2011.75

451. Hansen DF, Kay LE. Determining valine side-chain rotamer conformations in proteins from methyl 13C chemical shifts: Application to the 360 kDa half-proteasome. J Am Chem Soc. 2011;133: 8272–8281. doi:10.1021/JA2014532

452. Dauber-Osguthorpe P, Osguthorpe DJ, Stern PS, Moult J. Low Frequency Motion in Proteins: Comparison of Normal Mode and Molecular Dynamics of Streptomyces Griseus Protease A. J Comput Phys. 1999;151: 169–189. doi:10.1006/JCPH.1999.6232

453. Kruskal WH, Wallis WA. Use of Ranks in One-Criterion Variance Analysis. J Am Stat Assoc. 1952;47: 583–621. doi:10.1080/01621459.1952.10483441

454. Conover WJ, Iman RL. Multiple-comparisons procedures. Informal report. Technical report, Los Alamos Scientific Laboratory. 1979. doi:10.2172/6057803

455. Durrant JD, Votapka L, Sørensen J, Amaro RE. POVME 2.0: An enhanced tool for determining pocket shape and volume characteristics. J Chem Theory Comput. 2014;10: 5047–5056. doi:10.1021/CT500381C

456. Durrant JD, De Oliveira CAF, McCammon JA. POVME: An algorithm for measuring binding-pocket volumes. J Mol Graph Model. 2011;29: 773–776. doi:10.1016/J.JMGM.2010.10.007

457. Brandes U. A Faster Algorithm for Betweenness Centrality. Journal of mathematical sociology. 2001;25: 163–177.

458. Gunasekaran K, Ma B, Nussinov R. Is allostery an intrinsic property of all dynamic proteins? Proteins: Structure, Function, and Bioinformatics. 2004;57: 433–443. doi:10.1002/PROT.20232

459. Nussinov R, Tsai CJ. Allostery without a conformational change? Revisiting the paradigm. Curr Opin Struct Biol. 2015;30: 17–24. doi:10.1016/J.SBI.2014.11.005

460. Zhang J, Wang S, Jiang B, Huang L, Ji Z, Li X, et al. C-Src phosphorylation and activation of hexokinase promotes tumorigenesis and metastasis. Nat Commun. 2017;8: 1–16. doi:10.1038/ncomms13732

461. Mathupala SP, Rempel A, Pedersen PL. Aberrant glycolytic metabolism of cancer cells: A remarkable coordination of genetic, transcriptional, post-translational, and mutational

events that lead to a critical role for Type II hexokinase. J Bioenerg Biomembr. 1997;29: 339–343. doi:10.1023/A:1022494613613

462. Phan LM, Yeung SCJ, Lee MH. Cancer metabolic reprogramming: importance, main features, and potentials for precise targeted anti-cancer therapies. Cancer Biol Med. 2014;11: 1. doi:10.7497/J.ISSN.2095-3941.2014.01.001

463. Teicher BA, Linehan WM, Helman LJ. Targeting Cancer Metabolism. Clinical Cancer Research. 2012;18: 5537–5545. doi:10.1158/1078-0432.CCR-12-2587

464. Denko NC. Hypoxia, HIF1 and glucose metabolism in the solid tumour. Nature Reviews Cancer. 2008;8: 705–713. doi:10.1038/nrc2468

465. Vander Heiden MG. Targeting cancer metabolism: a therapeutic window opens. Nature Reviews Drug Discovery. 2011;10: 671–684. doi:10.1038/nrd3504

466. Zhang XD, Deslandes E, Villedieu M, Poulain L, Duval M, Gauduchon P, et al. Effect of 2-Deoxy-D-glucose on Various Malignant Cell Lines In Vitro. Anticancer Res. 2006;26: 3561–3566. Available: https://ar.iiarjournals.org/content/26/5A/3561

467. Brenner C, Subramaniam K, Pertuiset C, Pervaiz S. Adenine nucleotide translocase family: four isoforms for apoptosis modulation in cancer. Oncogene. 2010;30: 883–895. doi:10.1038/onc.2010.501

468. Thangaraju M, Karunakaran SK, Itagaki S, Gopal E, Elangovan S, Prasad PD, et al. Transport by SLC5A8 with subsequent inhibition of histone deacetylase 1 (HDAC1) and HDAC3 underlies the antitumor activity of 3-bromopyruvate. Cancer. 2009;115: 4655–4666. doi:10.1002/CNCR.24532

469. Scott AJ, Wilkinson AS, Wilkinson JC. Basal metabolic state governs AIF dependent growth support in pancreatic cancer cells. BMC Cancer. 2016;16: 1–15. doi:10.1186/S12885-016-2320-3

470. Akins NS, Nielson TC, Le H V. Inhibition of Glycolysis and Glutaminolysis: An Emerging Drug Discovery Approach to Combat Cancer. Curr Top Med Chem. 2018;18: 494–504. doi:10.2174/1568026618666180523111351

471. O'donnell AF, Schmidt MC. AMPK-mediated regulation of alpha-arrestins and protein trafficking. Int J Mol Sci. 2019;20. doi:10.3390/ijms20030515

472. Forbes SA, Beare D, Boutselakis H, Bamford S, Bindal N, Tate J, et al. COSMIC: somatic cancer genetics at high-resolution. Nucleic Acids Res. 2017;45: D777–D783. doi:10.1093/NAR/GKW1121

473. Shihab HA, Gough J, Cooper DN, Day INM, Gaunt TR. Predicting the functional consequences of cancer-associated amino acid substitutions. Bioinformatics. 2013;29: 1504–1510. doi:10.1093/BIOINFORMATICS/BTT182

474. Bonatelli M, Silva ECA, Cárcano FM, Zaia MG, Lopes LF, Scapulatempo-Neto C, et al. The Warburg effect is associated with tumor aggressiveness in testicular germ cell tumors. Front Endocrinol (Lausanne). 2019;10: 458483. doi:10.3389/FENDO.2019.00417

475. Tang Z, Li C, Kang B, Gao G, Li C, Zhang Z. GEPIA: a web server for cancer and normal gene expression profiling and interactive analyses. Nucleic Acids Res. 2017;45: W98–W102. doi:10.1093/NAR/GKX247

476. O'Donnell AF, Huang L, Thorner J, Cyert MS. A calcineurin-dependent switch controls the trafficking function of α-arrestin Aly1/Art6. Journal of Biological Chemistry. 2013;288: 24063–24080. doi:10.1074/jbc.M113.478511

477. Winston F, Dollard C, Ricupero-Hovasse SL. Construction of a set of convenient saccharomyces cerevisiae strains that are isogenic to S288C. Yeast. 1995;11: 53–55. doi:10.1002/YEA.320110107

478. Hoffman CS, Winston F. A ten-minute DNA preparation from yeast efficiently releases autonomous plasmids for transformaion of Escherichia coli. Gene. 1987;57: 267–272. doi:10.1016/0378-1119(87)90131-4

479. Ellison MA, Walker JL, Ropp PJ, Durrant JD, Arndt KM. MutantHuntWGS: A pipeline for identifying Saccharomyces cerevisiae mutations. G3: Genes, Genomes, Genetics. 2020;10: 3009–3014. doi:10.1534/g3.120.401396

480. Langmead B, Salzberg SL. Fast gapped-read alignment with Bowtie 2. Nature Methods. 2012;9: 357–359. doi:10.1038/nmeth.1923

481. Li H, Handsaker B, Wysoker A, Fennell T, Ruan J, Homer N, et al. The Sequence Alignment/Map format and SAMtools. Bioinformatics. 2009;25: 2078–2079. doi:10.1093/BIOINFORMATICS/BTP352

482. Danecek P, Auton A, Abecasis G, Albers CA, Banks E, DePristo MA, et al. The variant call format and VCFtools. Bioinformatics. 2011;27: 2156–2158. doi:10.1093/BIOINFORMATICS/BTR330

483. Cingolani P, Platts A, Wang LL, Coon M, Nguyen T, Wang L, et al. A program for annotating and predicting the effects of single nucleotide polymorphisms, SnpEff. Fly (Austin). 2012;6: 80–92. doi:10.4161/FLY.19695

484. Minear S, O'Donnell AF, Ballew A, Giaever G, Nislow C, Stearns T, et al. Curcumin inhibits growth of saccharomyces cerevisiae through iron chelation. Eukaryot Cell. 2011;10: 1574–1581. doi:10.1128/EC.05163-11

485. Goldstein A, Oliver Lampen J. β-d-Fructofuranoside fructohydrolase from yeast. Methods Enzymol. 1975;42: 504–511. doi:10.1016/0076-6879(75)42159-0

486. DeLano W. Pymol: An open-source molecular graphics tool. CCP4 Newsletter On Protein Crystallography. 2002;40: 82–92.

487. Phillips JC, Braun R, Wang W, Gumbart J, Tajkhorshid E, Villa E, et al. Scalable molecular dynamics with NAMD. J Comput Chem. 2005;26: 1781–1802. doi:10.1002/JCC.20289

488. Kalé L, Skeel R, Bhandarkar M, Brunner R, Gursoy A, Krawetz N, et al. NAMD2: Greater Scalability for Parallel Molecular Dynamics. J Comput Phys. 1999;151: 283–312. doi:10.1006/JCPH.1999.6201

489. Michaud-Agrawal N, Denning EJ, Woolf TB, Beckstein O. MDAnalysis: A Toolkit for the Analysis of Molecular Dynamics Simulations. J Comput Chem. 2011;32: 2319–2327. doi:10.1002/jcc

490. Brown DK, Penkler DL, Amamuddy OS, Ross C, Atilgan AR, Atilgan C, et al. MD-TASK: A software suite for analyzing molecular dynamics trajectories. Bioinformatics. 2017;33: 2768–2771. doi:10.1093/bioinformatics/btx349

491. Cassidy KC, Šefcík J, Raghav Y, Chang A, Durrant JD. ProteinVR: Web-based molecular visualization in virtual reality. PLoS Comput Biol. 2020;16: e1007747. doi:10.1371/JOURNAL.PCBI.1007747

492. Chen W, Guéron M. The inhibition of bovine heart hexokinase by 2-deoxy-d-glucose-6-phosphate: characterization by 31P NMR and metabolic implications. Biochimie. 1992;74: 867–873. doi:10.1016/0300-9084(92)90070-U

493. Van Steveninck J. Transport and transport-associated phosphorylation of 2-deoxy-d-glucose in yeast. Biochimica et Biophysica Acta (BBA) - Biomembranes. 1968;163: 386–394. doi:10.1016/0005-2736(68)90123-5

494. Neigeborn L, Carlson M. Mutations causing constitutive invertase synthesis in yeast: Genetic interactions with snf mutations. Genetics. 1987;115: 247–253. doi:10.1093/genetics/115.2.247

495. Rose M, Albig W, Entian K -D. Glucose repression in Saccharomyces cerevisiae is directly associated with hexose phosphorylation by hexokinases PI and PII. Eur J Biochem. 1991;199: 511–518. doi:10.1111/J.1432-1033.1991.TB16149.X

496. Ashkenazy H, Abadi S, Martz E, Chay O, Mayrose I, Pupko T, et al. ConSurf 2016: an improved methodology to estimate and visualize evolutionary conservation in macromolecules. Nucleic Acids Res. 2016;44: W344–W350. doi:10.1093/NAR/GKW408

497. Yasuda S, Tsuchiya H, Kaiho A, Guo Q, Ikeuchi K, Endo A, et al. Stress- and ubiquitylation-dependent phase separation of the proteasome. Nature. 2020;578: 296–300. doi:10.1038/s41586-020-1982-9

498. Miller SB, Ho C, Winkler J, Khokhrina M, Neuner A, Mohamed MY, et al. Compartment-specific aggregases direct distinct nuclear and cytoplasmic aggregate deposition. EMBO J. 2015;34: 778–797. doi:10.15252/EMBJ.201489524

499. Sontag EM, Morales-Polanco F, Chen J-H, McDermott G, Dolan PT, Gestaut D, et al. Nuclear and cytoplasmic spatial protein quality control is coordinated by nuclear–vacuolar junctions and perinuclear ESCRT. Nature Cell Biology. 2023; 1–15. doi:10.1038/s41556-023-01128-6

500. Sontag EM, Samant RS, Frydman J. Mechanisms and functions of spatial protein quality control. Annu Rev Biochem. 2017;86: 97–122. doi:10.1146/ANNUREV-BIOCHEM-060815-014616

501. Kaganovich D, Kopito R, Frydman J. Misfolded proteins partition between two distinct quality control compartments. Nature. 2008;454: 1088–1095. doi:10.1038/NATURE07195

502. Hollingsworth SA, Dror RO. Molecular Dynamics Simulation for All. Neuron. 2018;99: 1129–1143. doi:10.1016/j.neuron.2018.08.011

503. Durrant JD, McCammon JA. Molecular dynamics simulations in drug discovery. BMC Biol. 2011;9. doi:10.1016/B978-0-12-809633-8.20154-4

504. Russo JD, Zhang S, Leung JMG, Bogetti AT, Thompson JP, Degrave AJ, et al. WESTPA 2.0: High-Performance Upgrades for Weighted Ensemble Simulations and Analysis of Longer-Timescale Applications. J Chem Theory Comput. 2022;18: 638–649. doi:10.1021/ACS.JCTC.1C01154

505. Souza PCT, Alessandri R, Barnoud J, Thallmair S, Faustino I, Grünewald F, et al. Martini 3: a general purpose force field for coarse-grained molecular dynamics. Nature Methods. 2021;18: 382–388. doi:10.1038/s41592-021-01098-3

506. Liu S, Ammirati MJ, Song X, Knafels JD, Zhang J, Greasley SE, et al. Insights into mechanism of glucokinase activation: Observation of multiple distinct protein conformations. Journal of Biological Chemistry. 2012;287: 13598–13610. doi:10.1074/JBC.M111.274126

507. Petit P, Antoine M, Ferry G, Boutin JA, Lagarde A, Gluais L, et al. The active conformation of human glucokinase is not altered by allosteric activators. Acta Crystallographica Section D. 2011;67: 929–935. doi:10.1107/S0907444911036729

508. Kumar A, Mathew V, Stirling PC. Nuclear protein quality control in yeast: the latest INQuiries. Journal of Biological Chemistry. 2022; 102199. doi:10.1016/J.JBC.2022.102199

509. Borgert L, Mishra S, den Brave F. Quality control of cytoplasmic proteins inside the nucleus. Comput Struct Biotechnol J. 2022;20: 4618–4625. doi:10.1016/J.CSBJ.2022.08.033

510. Enam C, Geffen Y, Ravid T, Gardner RG. Protein Quality Control Degradation in the Nucleus. Annu Rev Biochem. 2018;87: 725–749. doi:10.1146/ANNUREV-BIOCHEM-062917-012730

511. Russell SJ, Steger KA, Johnston SA. Subcellular localization, stoichiometry, and protein levels of 26 S proteasome subunits in yeast. Journal of Biological Chemistry. 1999;274: 21943–21952. doi:10.1074/jbc.274.31.21943

512. Pack CG, Yukii H, Toh-E A, Kudo T, Tsuchiya H, Kaiho A, et al. Quantitative live-cell imaging reveals spatio-temporal dynamics and cytoplasmic assembly of the 26S proteasome. Nature Communications. 2014;5: 1–10. doi:10.1038/ncomms4396

513. Laporte D, Salin B, Daignan-Fornier B, Sagot I. Reversible cytoplasmic localization of the proteasome in quiescent yeast cells. J Cell Biol. 2008;181: 737. doi:10.1083/JCB.200711154

514. Breckel CA, Hochstrasser M. Ubiquitin Ligase Redundancy and Nuclear-Cytoplasmic Localization in Yeast Protein Quality Control. Biomolecules 2021, Vol 11, Page 1821. 2021;11: 1821. doi:10.3390/BIOM11121821

515. Jones RD, Gardner RG. Protein quality control in the nucleus. Curr Opin Cell Biol. 2016;40: 81–89. doi:10.1016/J.CEB.2016.03.002

516. Park SH, Kukushkin Y, Gupta R, Chen T, Konagai A, Hipp MS, et al. PolyQ proteins interfere with nuclear degradation of cytosolic proteins by sequestering the Sis1p chaperone. Cell. 2013;154: 134–145. doi:10.1016/j.cell.2013.06.003

517. Prasad R, Xu C, Ng DTW. Hsp40/70/110 chaperones adapt nuclear protein quality control to serve cytosolic clients. Journal of Cell Biology. 2018;217: 2019–2032. doi:10.1083/JCB.201706091

518. Hofmeister-Brix A, Lenzen S, Baltrusch S. The ubiquitin–proteasome system regulates the stability and activity of the glucose sensor glucokinase in pancreatic β-cells. Biochemical Journal. 2013;456: 173–184. doi:10.1042/BJ20130262

519. Anderson M, Marayati R, Moffitt R, Yeh JJ. Hexokinase 2 promotes tumor growth and metastasis by regulating lactate production in pancreatic cancer. Oncotarget. 2017;8: 56081–56094. doi:10.18632/oncotarget.9760

520. Suh DH, Kim MA, Kim H, Kim MK, Kim HS, Chung HH, et al. Association of overexpression of hexokinase II with chemoresistance in epithelial ovarian cancer. Clin Exp Med. 2014. doi:10.1007/s10238-013-0250-9

521. Pettersen EF, Goddard TD, Huang CC, Couch GS, Greenblatt DM, Meng EC, et al. UCSF Chimera - A visualization system for exploratory research and analysis. J Comput Chem. 2004;25: 1605–1612. doi:10.1002/jcc.20084

522. Keogh MC, Kim JA, Downey M, Fillingham J, Chowdhury D, Harrison JC, et al. A phosphatase complex that dephosphorylates γH2AX regulates DNA damage checkpoint recovery. Nature 2005 439:7075. 2005;439: 497–501. doi:10.1038/nature04384

523. García R, Rodríguez-Peña JM, Bermejo C, Nombela C, Arroyo J. The high osmotic response and cell wall integrity pathways cooperate to regulate transcriptional responses to

zymolyase-induced cell wall stress in Saccharomyces cerevisiae. Journal of Biological Chemistry. 2009;284: 10901–10911. doi:10.1074/jbc.M808693200

524. Ben-David U, Amon A. Context is everything: aneuploidy in cancer. Nature Reviews Genetics. 2019;21: 44–62. doi:10.1038/s41576-019-0171-x

525. Gordon DJ, Resio B, Pellman D. Causes and consequences of aneuploidy in cancer. Nature Reviews Genetics. 2012;13: 189–203. doi:10.1038/nrg3123

526. Albuquerque CP, Smolka MB, Payne SH, Bafna V, Eng J, Zhou H. A multidimensional chromatography technology for in-depth phosphoproteome analysis. Molecular and Cellular Proteomics. 2008;7: 1389–1396. doi:10.1074/MCP.M700468-MCP200

527. Wang K, Zhou YJ, Liu H, Cheng K, Mao J, Wang F, et al. Proteomic analysis of protein methylation in the yeast Saccharomyces cerevisiae. J Proteomics. 2015;114: 226–233. doi:10.1016/j.jprot.2014.07.032

528. Hellemann E, Durrant JD. Worth the Weight: Sub-Pocket EXplorer (SubPEx), a Weighted Ensemble Method to Enhance Binding-Pocket Conformational Sampling. J Chem Theory Comput. 2023;19: 5677–5689. doi:10.1021/ACS.JCTC.3C00478

529. Jumper J, Evans R, Pritzel A, Green T, Figurnov M, Ronneberger O, et al. Highly accurate protein structure prediction with AlphaFold. Nature. 2021;596: 583–589. doi:10.1038/s41586-021-03819-2

530. Pan X, Roberts P, Chen Y, Kvam E, Shulga N, Huang K, et al. Nucleus-vacuole junctions in Saccharomyces cerevisiae are formed through the direct interaction of Vac8p with Nvj1p. Mol Biol Cell. 2000;11: 2445–2457. doi:10.1091/mbc.11.7.2445

531. Zelent B, Buettger C, Grimsby J, Sarabu R, Vanderkooi JM, Wand AJ, et al. Thermal stabilty of glucokinase (GK) as influenced by the substrate glucose, an allosteric

glucokinase activator drug (GKA) and the osmolytes glycerol and urea. Biochimica et Biophysica Acta (BBA) - Proteins and Proteomics. 2012;1824: 769–784. doi:10.1016/J.BBAPAP.2012.03.003

532. Pack CG, Yukii H, Toh-E A, Kudo T, Tsuchiya H, Kaiho A, et al. Quantitative live-cell imaging reveals spatio-temporal dynamics and cytoplasmic assembly of the 26S proteasome. Nature Communications. 2014;5: 1–10. doi:10.1038/ncomms4396

533. Laporte D, Salin B, Daignan-Fornier B, Sagot I. Reversible cytoplasmic localization of the proteasome in quiescent yeast cells. J Cell Biol. 2008;181: 737. doi:10.1083/JCB.200711154

534. Chen X, Htet ZM, L Opez-Alfonzo E, Martin A, Walters KJ, Martin CA, et al. Proteasome interaction with ubiquitinated substrates: from mechanisms to therapies. FEBS J. 2021;288: 5231–5251. doi:10.1111/FEBS.15638

535. Finley D, Chen X, Walters KJ. Gates, Channels, and Switches: Elements of the Proteasome Machine. Trends Biochem Sci. 2016;41: 77–93. doi:10.1016/J.TIBS.2015.10.009

536. Amm I, Sommer T, Wolf DH. Protein quality control and elimination of protein waste: The role of the ubiquitin–proteasome system. Biochimica et Biophysica Acta (BBA) - Molecular Cell Research. 2014;1843: 182–196. doi:10.1016/J.BBAMCR.2013.06.031

537. Russell SJ, Steger KA, Johnston SA. Subcellular Localization, Stoichiometry, and Protein Levels of 26 S Proteasome Subunits in Yeast. Journal of Biological Chemistry. 1999;274: 21943–21952. doi:10.1074/JBC.274.31.21943

538. Foresti O, Rodriguez-Vaello V, Funaya C, Carvalho P. Quality control of inner nuclear membrane proteins by the Asi complex. Science. 2014;346: 751–755. doi:10.1126/SCIENCE.1255638

539. Khmelinskii A, Blaszczak E, Pantazopoulou M, Fischer B, Omnus DJ, Dez G Le, et al. Protein quality control at the inner nuclear membrane. Nature. 2014;516: 410–413. doi:10.1038/nature14096

540. Dasgupta A, Ramsey HL, Smith JS, Auble DT. Sir Antagonist 1 (San1) is a ubiquitin ligase. Journal of Biological Chemistry. 2004;279: 26830–26838. doi:10.1074/jbc.M400894200

541. Gardner RG, Nelson ZW, Gottschling DE. Degradation-mediated protein quality control in the nucleus. Cell. 2005;120: 803–815. doi:10.1016/j.cell.2005.01.016

542. Fredrickson EK, Rosenbaum JC, Locke MN, Milac TI, Gardner RG. Exposed hydrophobicity is a key determinant of nuclear quality control degradation. Mol Biol Cell. 2011;22: 2384–2395. doi:10.1091/MBC.E11-03-0256

543. Carvalho P, Goder V, Rapoport TA. Distinct Ubiquitin-Ligase Complexes Define Convergent Pathways for the Degradation of ER Proteins. Cell. 2006;126: 361–373. doi:10.1016/j.cell.2006.05.043

544. Deng M, Hochstrasser M. Spatially regulated ubiquitin ligation by an ER/nuclear membrane ligase. Nature. 2006;443: 827–831. doi:10.1038/nature05170

545. Swanson R, Locher M, Hochstrasser M. A conserved ubiquitin ligase of the nuclear envelope/endoplasmic reticulum that functions in both ER-associated and Matα2 repressor degradation. Genes Dev. 2001;15: 2660–2674. doi:10.1101/GAD.933301

546. Suzuki A, Kusakai GI, Kishimoto A, Lu J, Ogura T, Lavin MF, et al. Identification of a novel protein kinase mediating Akt survival signaling to the ATM protein. Journal of Biological Chemistry. 2003;278: 48–53. doi:10.1074/jbc.M206025200

547. Kaisari S, Miniowitz-Shemtov S, Sitry-Shevah D, Shomer P, Kozlov G, Gehring K, et al. Role of ubiquitin-protein ligase UBR5 in the disassembly of mitotic checkpoint complexes. Proc Natl Acad Sci U S A. 2022;119: e2121478119. doi:10.1073/PNAS.2121478119

548. Mark KG, Kolla SDD, Aguirre JD, Garshott DM, Schmitt S, Haakonsen DL, et al. Orphan quality control shapes network dynamics and gene expression. Cell. 2023;186: 3460-3475.e23. doi:10.1016/J.CELL.2023.06.015

549. Shan W, Zhou Y, Tam KY. The development of small-molecule inhibitors targeting hexokinase 2. Drug Discov Today. 2022;27: 2574–2585. doi:10.1016/J.DRUDIS.2022.05.017

550. Li W, Zheng M, Wu S, Gao S, Yang M, Li Z, et al. Benserazide, a dopadecarboxylase inhibitor, suppresses tumor growth by targeting hexokinase 2. Journal of Experimental and Clinical Cancer Research. 2017;36: 1–12. doi:10.1186/S13046-017-0530-4

551. Zheng M, Wu C, Yang K, Yang Y, Liu Y, Gao S, et al. Novel selective hexokinase 2 inhibitor Benitrobenrazide blocks cancer cells growth by targeting glycolysis. Pharmacol Res. 2021;164: 105367. doi:10.1016/J.PHRS.2020.105367

552. Marini C, Salani B, Massollo M, Amaro A, Esposito AI, Orengo AM, et al. Direct inhibition of hexokinase activity by metformin at least partially impairs glucose metabolism and tumor growth in experimental breast cancer. Cell Cycle. 2013;12: 3490–3499. doi:10.4161/CC.26461

553. Chen Z, Zhang H, Lu W, Huang P. Role of mitochondria-associated hexokinase II in cancer cell death induced by 3-bromopyruvate. Biochimica et Biophysica Acta (BBA) - Bioenergetics. 2009;1787: 553–560. doi:10.1016/J.BBABIO.2009.03.003

554. Iqbal N, Iqbal N. Imatinib: A Breakthrough of Targeted Therapy in Cancer. Chemother Res Pract. 2014;2014: 1–9. doi:10.1155/2014/357027

555. Shima T, Taniguchi K, Tokumaru Y, Inomata Y, Arima J, Lee SW, et al. Glucose transporter-1 inhibition overcomes imatinib resistance in gastrointestinal stromal tumor cells. Oncol Rep. 2022;47: 1–13. doi:10.3892/OR.2021.8218/HTML

556. Nath K, Guo L, Nancolas B, Nelson DS, Shestov AA, Lee SC, et al. Mechanism of antineoplastic activity of lonidamine. Biochimica et Biophysica Acta (BBA) - Reviews on Cancer. 2016;1866: 151–162. doi:10.1016/J.BBCAN.2016.08.001

557. Xia H guang, Najafov A, Geng J, Galan-Acosta L, Han X, Guo Y, et al. Degradation of HK2 by chaperone-mediated autophagy promotes metabolic catastrophe and cell death. Journal of Cell Biology. 2015;210: 705–716. doi:10.1083/JCB.201503044

558. Jiao L, Zhang HL, Li DD, Yang KL, Tang J, Li X, et al. Regulation of glycolytic metabolism by autophagy in liver cancer involves selective autophagic degradation of HK2 (hexokinase 2). Autophagy. 2018;14: 671–684. doi:10.1080/15548627.2017.1381804

559. Heidrich K, Otto A, Behlke J, Rush J, Wenzel KW, Kriegel T. Autophosphorylation-inactivation site of hexokinase 2 in Saccharomyces cerevisiae. Biochemistry. 1997;36: 1960–1964. doi:10.1021/bi9623643